Technical Report Documentation Page

1. Report No. ABC-UTC-2013-C2-UNR04-Final	2. Government Accession No.	3. Recipient's Catalog No.	
4. Title and Subtitle **Shake Table Studies of a Bridge System with ABC Connections**		5. Report Date April 2019 6. Performing Organization Code	
7. Author(s) Elmira Shoushtari (0000-0002-0044-2314), M. Saiid Saiidi, Ahmad Itani (0000-0002-9813-6314), Mohamed A. Moustafa (0000-0002-1006-7685)		8. Performing Organization Report No.	
9. Performing Organization Name and Address Department of Civil and Environmental Engineering Florida International University 10555 West Flagler Street, EC 3680 Miami, FL 33174		10. Work Unit No. (TRAIS) 11. Contract or Grant No. DTRT13-G-UTC41	
12. Sponsoring Organization Name and Address Accelerated Bridge Construction University Transportation Center Florida International University 10555 W. Flagler Street, EC 3680 Miami, FL 33174		13. Type of Report and Period Covered Final Report (August 2015 to May 2019) 14. Sponsoring Agency Code	
15. Supplementary Notes Visit www.abc-utc.fiu.edu for other ABC reports.			
16. Abstract Accelerated bridge construction (ABC) reduces the onsite construction time by utilizing prefabricated elements. Connections between prefabricated elements are critical in high seismic areas to maintain the integrity of the bridge system. Various ABC connections have been investigated at the component level to build a solid understanding of their local seismic response. However, to confidently recommend ABC bridges for adoption in standard bridge design and construction, they should be tested as a system. This study was aimed at addressing this issue by conducting experimental and analytical investigations of a 0.35-scale two-span steel girder bridge system with six ABC connection types: (1) column-to-footing rebar hinge pocket connection, (2) column-to-hybrid cap beam grouted duct connection, (3) steel girder-to-cap beam connection, (4) girder-to-deck grouted pocket connection, (5) ultra-high performance concrete (UHPC)-filled joints between the deck panels, and (6) UHPC-filled joint over the pier. The bridge system was tested to failure on shake tables under successive motions simulating scaled versions of the 1994 Northridge-Sylmar earthquake. Results demonstrated that the performance of the bridge model was comparable to cast-in-place bridges as columns underwent 6.9% resultant drift ratio in a ductile manner while cap beam, deck, footing, and four ABC connections in the superstructure responded as capacity protected elements.			
17. Key Words Accelerated bridge construction, shake table test, steel girder, hybrid cap beam, grouted duct connection, rebar hinge pocket (socket) connection, full-depth precast deck panel, simple for dead continuous for live, ultra-high performance concrete		18. Distribution Statement No restrictions.	
19. Security Classification (of this report) Unclassified.	20. Security Classification (of this page) Unclassified.	21. No. of Pages 232	22. Price

Form DOT F 1700.7 (8-72) Reproduction of completed page authorized

(this page is intentionally left blank)

Shake Table Studies of a Bridge System with ABC Connections

Final Report

April 2019

Principal Investigator: M. Saiidi and A. Itani

Department of Civil and Environmental Engineering

Florida International University

Authors

Elmira Shoushtari

M. Saiid Saiidi

Ahmad Itani

Mohamed Moustafa

Sponsored by

Accelerated Bridge Construction University Transportation Center

A report from

University of Nevada, Reno

Department of Civil and Environmental Engineering, MS 258

1664 N. Virginia St.

Reno, NV 89557

www.unr.edu/cee

DISCLAIMER

The contents of this report reflect the views of the authors, who are responsible for the facts and the accuracy of the information presented herein. This document is disseminated in the interest of information exchange. The report is funded, partially or entirely, by a grant from the U.S. Department of Transportation's University Transportation Program. However, the U.S. Government assumes no liability for the contents or use thereof.

ABSTRACT

Accelerated bridge construction (ABC) reduces the onsite construction time by utilizing prefabricated elements. Connections between prefabricated elements are critical in high seismic areas to maintain the integrity of the bridge system. Various ABC connections have been investigated at the component level to build a solid understanding of their local seismic response. However, to confidently recommend ABC bridges for adoption in standard bridge design and construction, they should be tested as a system. This study was aimed at addressing this issue by conducting experimental and analytical investigations of a 0.35-scale two-span steel girder bridge system with six ABC connection types: (1) column-to-footing rebar hinge pocket connection, (2) column-to-hybrid cap beam grouted duct connection, (3) steel girder-to-cap beam connection, (4) girder-to-deck grouted pocket connection, (5) ultra-high performance concrete (UHPC)-filled joints between the deck panels, and (6) UHPC-filled joint over the pier. The bridge system was tested to failure on shake tables under successive motions simulating scaled versions of the 1994 Northridge-Sylmar earthquake. Results demonstrated that the performance of the bridge model was comparable to cast-in-place bridges as columns underwent 6.9% resultant drift ratio in a ductile manner while cap beam, deck, footing, and four ABC connections in the superstructure responded as capacity protected elements.

ACKNOWLEDGMENTS

This project was supported by the Accelerated Bridge Construction University Transportation Center (ABC-UTC at www.abc-utc.fiu.edu) at Florida International University (FIU), as lead institution, and Iowa State University (ISU) and the University of Nevada-Reno (UNR) as partner institutions. The authors would like to acknowledge the ABC-UTC support.

The author would like to extend special appreciation to the ABC-UTC and the U.S. Department of Transportation Office of the Assistant Secretary for Research and Technology for funding this project.

The authors would like to thank the Research Advisory Panel members: Bijan Khaleghi, Washington State DOT; Elmer Marx, Alaska DOT&PF; Tom Ostrom, Caltrans.

Several companies and organizations are thanked for various contributions to the project: Lafarge North America Inc. for donating UHPC material, C&K Johnson Industries for donating corrugated metal ducts, Reno Iron Works for fabrication of steel girders at a reduced cost, Utah Pacific Steel and NSBA for donating the steel girders, cross frames, and other steel accessories. Mr. Don Newman is thanked for his diligent efforts and meticulous attention to construction of the test model.

Thanks are due the UNR Earthquake Engineering Laboratory staff Dr. Patrick Laplace, Chad Lyttle, Todd Lyttle, and Mark Lattin for their unfailing support and assistance. The support and advice of ABC-UTC director, Dr. Atorod Azizinamini, is greatly appreciated. Thanks are due to Mojtaba Alian, Jose Benjumea Royero, Jared Jones, Amir Sadeghnezhad, Dr. Alireza Mohebbi, Dr. Ali Mehrsoroush, and Azin Ghaffari for their dedicated assistance along the course of this study. Amir Sadeghnezhad is especially thanked for development of the design guideline for SDCL connections, which is included in Appendix D.

CONTENTS

LIST OF FIGURES

LIST OF TABLES

CHAPTER 1: INTRODUCTION

1.1. Project Motivation

Bridge cast-in-place construction often leads to traffic delays, subjects highway workers and the traveling public to increased probability of accidents, and may affect the regional economy of the residents. By utilizing prefabricated bridge elements, accelerated bridge construction (ABC) shortens onsite construction time. Accordingly, ABC saves time and money for the traveling public and enhances the work-zone safety. Due to the fact that prefabricated components are built offsite and under controlled environmental conditions, ABC provides the opportunity to use novel materials and to increase the quality and durability of the components. ABC can also reduce the total duration of projects as prefabrication of bridge components can be performed simultaneously.

Connections between prefabricated elements (hereby referred to as ABC connections) play a crucial role in adequate performance of ABC bridges under moderate and strong earthquakes. ABC connections have to be practical and efficiently constructible and at the same time provide clear load path under vertical and lateral loading. When used for connecting columns to the adjoining members, ABC connections must allow for the energy dissipation in the column while maintaining the capacity and the integrity of the structural system.

Several researchers (Matsumoto et al. 2001; Restrepo et al. 2011; Tazarv and Saiidi 2014; Motaref et al. 2011; Mehrsoroush, et al. 2016; Mehraein and Saiidi 2016) have developed and investigated a variety of ABC connections and prefabricated elements in the past decade. These connections include but are not limited to grouted duct connections, pocket and socket connections, mechanical bar splices, simple for dead continuous for live (SDCL) connections of various configurations, and connections for partial or full precast deck panels. The primary intent of these studies was to assess the local behavior of ABC connections, formulate preliminary design guidelines, and build a certain level of confidence in utilizing ABC techniques. As such, experimental studies have been limited either to the component level or bridge subassembly. Another typical limitation of these studies was that they focused on connection behavior under uni-directional loading. For example, column cap-beam connections were studied in two-column pier models that were subjected only to in-plane loading.

While providing invaluable information on the local behavior of ABC connections, component tests do not provide confidence in the performance of the bridge systems when subjected to bi-directional loading. Therefore, to understand the holistic seismic behavior of ABC bridges ABC connections along with prefabricated elements should be integrated into a bridge system and studied under realistic bi-axial seismic loading.

1.2. Research, Objectives, and Tasks

Comprehensive analytical and experimental investigations of a large-scale two-span steel girder bridge model incorporating six ABC connection types subjected to bi-directional horizontal earthquake motions were conducted. The aforementioned ABC connections were: (1) column-to -footing rebar hinge pocket connection; (2) column-to-hybrid cap beam grouted duct connection; (3) simple for dead continuous for live (SDCL); (4) panel-

to-girder grouted pocket connection; (5) spliced deck panel rebars in the transverse panel-to-panel joints filled with ultra-high performance concrete (UHPC); and (6) spliced deck panel rebars in UHPC-filled panel-to-panel joint over the pier.

The primary objectives of this research project were to:

1. Investigate the system level seismic performance of six ABC connections under horizontal bi-directional seismic excitations at different limit states;
2. Determine the adequacy of the available design methods for ABC components and connections;
3. Evaluate the feasibility of the construction methods and identify construction issues in handling and connecting various prefabricated elements;

The following tasks were undertaken to meet the aforementioned objectives:

- *Task 1 – Literature review:* An in-depth literature search was conducted to identify the recent experimental and analytical studies of ABC bridge systems, their elements and connections under seismic loading.
- *Task 2 – Evaluate ABC connections and details:* The merit of a variety of ABC details were evaluated in terms of the seismic performance, ease of construction, time saving, cost, durability, and damage susceptibility. Different alternatives for prefabricated columns: solid, segmental, hollow, SCC (self-consolidating concrete) filled hollow columns, concrete-filled steel tubes, concrete-filled FRP (fiber-reinforced polymer) tubes were identified. Connections between columns and adjoining members include grouted duct connections, pocket or socket connections, mechanical bar splices, rebar hinge pocket connections, pipe pin connections were studied, etc. With respect to superstructure-to-bent cap connections, limited research has been reported on SDCL connections for steel girders under seismic loading. However, recent research at the Florida International University coordinated with the UNR research team could yield practical alternative connections.
- *Task 3 – Develop preliminary design for a two-span large-scale bridge model for shake table testing:* Select ABC connection details and prefabricated elements that were ranked at the top of the different alternatives were integrated in a, 0.35-scale, straight, two-span bridge model. All the components were prefabricated elements except for the portion of the girder to cap beam connection detail that utilized FIU's SDCL connection detail that required closure pours. The key details to be decided were column connection to the footing, column-pier cap connection, girder-cap beam connection, deck-girder connection, and connections between adjacent decks. All elements and connections were designed in accordance to the current design codes where applicable and previous studies on ABC connections.
- *Task 4 - Finalize bridge model details, construct and instrument the bridge model, and conduct shake table tests:* As part of task 4, various prefabricated components and connection types of the bridge model were constructed. To monitor the response of the bridge model, 280 channels of data were collected

from critical parts of the test model and the shake table. The shake table test as the core component of this research study was conducted afterward, which was expected to provide conclusive observations and recorded data to assess the response of the ABC bridge system and the six connection types and serve as an underlying foundation for the analytical phase including calibration and parametric studies.

- *Task 5- Process and interpret shake table test data and assess seismic performance of bridge model:* Shake table test results were processed and evaluated at the local and global levels. The global response parameters of interest were forces and displacements. The relationship between these parameters defined stiffness and its variation as nonlinearity developed in steel reinforcement and concrete. Other important global parameters were the effective stiffness and damping ratio of the bridge and its variation in the subsequent runs. Curvature and rotations were among the local responses of importance, which indicated the extent of section nonlinearity. Other local responses of interest were the strains in superstructure steel girders, steel reinforcement, and concrete at various critical sections of elements and connections.
- *Task 6 - Summarize the investigation and the results in final report:* The current document is the final report prepared meeting the RITA requirements for UTC funded projects. The content of the report contains a detailed summary of the results from the preceding tasks.

1.3. Research Advisory Panel (RAP)

The project work was done in collaboration with the Research Advisory Panel (RAP). The following people participated in the RAP:

- Tom Ostrom (California Department of Transportation)
- Bijan Khaleghi (Washington state DOT)
- Elmer Marx (Alaska DOT)

1.4. Report Overview

The current document is the first report of the two reports that cover experimental and analytical studies of the two-span steel girder bridge system. This report focuses on the experimental phase of the project while the next report entitled "Analytical investigations and design implications of seismic response of a two-span ABC bridge system" summarizes the undertaken analytical efforts, as well as the design implications and guidelines.

Chapter 1 includes the problem statement, objectives of the project, and the methodology to meet the objectives. Chapter 2 provides the literature review for the connection types incorporated in the research project. The final chapter describes a summary and conclusions of the research study (Chapter 5). Chapters 3 and 4 correspond to a stand-alone refereed journal paper constituting a separate portion of the study. However, for clarity and completeness, the articles include a summary of important background

information from the rest of the study. Consequently, chapters 3 and 4 are stand-alone documents that can be read in any order. At the time of this writing the paper at chapter 3 have been accepted for publication, and the one in chapter 4 is under review. The date of the initial submission and the name of the journal are noted at the beginning of each chapter.

To document detailed data and descriptive information that are included in the papers, two appendices (Appendix A-B) are included. Appendix A contains complete documentation of the design, construction, and testing of the two-span bridge model. Included in this appendix are the bridge model drawings, construction and test photos, material test data, instrumentation drawings, and loading protocol. Appendix B documents comprehensive results of the shake table test.

CHAPTER 2: PAST RELEVANT STUDIES

2.1. Introduction

Various earthquake-resistant connection types have been explored by researchers through experimental and analytical studies for possible adoption in ABC. These connections (referred to as "ABC connections") include but are not limited to grouted ducts, mechanical bar splice couplers, pocket and socket connections, pipe pin connections, and rebar hinge connections as well as the connection between bridge superstructures and cap beams. The objectives of these studies have been to develop a thorough understanding of the local response of the ABC connections. Due to limitation of test facilities and budget, experimental studies have been mostly limited either to the component level or bridge subassembly testing. Another limitation of these studies has been focused on connection behavior under uni-directional loading. However, to confidently recommend ABC bridges for incorporation in routine bridge design and construction in high seismic regions, investigating the effect of interaction and load distribution among components is essential.

To address this gap a large-scale two-span bridge system with steel superstructure and six ABC connections was investigated experimentally and analytically. The ABC connections used in the bridge model were: (1) column-to-footing rebar hinge pocket connection; (2) column-to-hybrid cap beam grouted duct connection; (3) simple for dead continuous for live (SDCL); (4) panel-to-girder grouted pocket connection; (5) spliced deck panel rebars in the transverse panel-to-panel joints filled with ultra-high performance concrete (UHPC); and (6) spliced deck panel rebars in UHPC-filled panel-to-panel joint over the pier.

This chapter presents a summary review of past studies on the aforementioned ABC connections. Because some of the connections are closely inter-related, the review of past research on connection types: panel-to-girder grouted pocket connection, spliced deck rebars in UHPC-filled transverse joints between adjacent panels and connection between deck panels over the pier.

2.2. Rebar Hinge Pocket/Socket Connections

2.2.1. Introduction

"Pin" or hinge connections are desirable for connecting columns to the footing as they result in smaller and more cost-effective foundations. They may also be used at top of the columns to reduce moment demand in outrigger cap beams. Two-way hinges are free to rotate in any directions and are commonly used in multi-column bents. Rebar hinge connection as a type of a two-way hinge comprises a reinforcement cage with smaller diameter compared to that of the column. A hinge throat (vertical gap) is provided at the interface of the adjoining members to improve the hinge rotational capacity. Rebar hinge is the most commonly used column hinge type in the United States. Although, hinges are intended to be moment free, some moment is developed in the rebar hinge due to the eccentricity of hinge bars relative to the concrete compression force that can be developed in the hinge.

To make the rebar hinge connection suitable for rapid construction, details of the rebar hinges can be combined with those of the pocket/socket connections. In rebar hinge pocket connection (Figure 2-1(a)), precast hinge element integrated with the precast column extended into a corrugated steel pipe embedded in the footing. The gap between the hinge and the pocket is filled with high-strength, non-shrink grout to make the connection monolithic. Another alternative is rebar hinge socket connection in which the hinge element consists of a rebar cage alone that extends from the column into a footing opening. The opening is filled with concrete with higher compressive strength compared to that of the footing concrete. This connection is called rebar hinge socket connection and is shown in Figure 2-1(b). Yet a third alternative is to leave an opening in the column core and install the column over hinge rebars that extend from the footing and fill the space with grout (Figure 2-1(c)).

Only a few experimental studies have incorporated rebar hinge pocket connections. However, pocket connections for full moment transfer and rebar hinge connections have been the focus of several studies, which are highlighted in this section.

2.2.2. Past Research on Pocket Connections

Pocket connection can be constructed by forming a pocket inside a precast footing or cap beam and extending either the precast column or the extruded reinforcement of the partially precast column into the pocket. In the former method, the gap between the column and the pocket is filled with grout, while in the latter method, the pocket is filled with concrete. Seismic performance of pocket connections has been investigated by several researchers in recent years.

Matsumoto et al. (2001) conducted four full-scale experiments on grout-pocket, grouted-duct, and bolted cap beam-column connections, and two full-scale experiments on bents. The authors reported similar strength and ductility capacity as CIP column-cap beam connections. It was concluded that these connections not only expedited construction, but also resulted in emulative response to that of the monolithic construction.

Restrepo et al. (2011), performed a series of 0.42 scale bent cap to column component tests including a CIP control specimen, a cap pocket full ductility specimen (CPFD), and a cap pocket limited ductility specimen (CPLD). The authors reported considerably more damage in the CPLD compared to the CPFD model. It was concluded that using corrugated steel pipe serving as joint shear reinforcement provided sufficient joint shear resistance when subjected to column overstrength demands. The test results showed that the longitudinal bars of the precast cap beams in the extreme layer yielded which is not acceptable in capacity protected elements.

Haraldsson et al. (2013) showed that the seismic performance of octagonal pocket connections with an embedment length ratio of 1.1 to the column diameter was as good as that of comparable cast-in-place (CIP) systems.

Motaref et al. (2011) conducted a shake table test of a 0.3-scale precast two-column bent. One of the columns comprised a glass fiber reinforced polymer (GFRP) tube filled with concrete. The other column employed ECC in the plastic hinge zone. Both columns were embedded in pockets left in the footing with an embedment length corresponding to 1.5

times the column diameter. Kavianipour and Saiidi (2013) conducted a shake table test of a quarter scale four-span bridge model in which one of the three bents consisted of precast columns constructed with GFRP concrete-filled tubes, embedded to a depth of 1.5 times the column diameter into the footing pockets. In both studies, the embedment length was found to be sufficient to develop the full moment capacity of the columns, while connections and the GFRP tube remained intact. Kavianipour and Saiidi (2013) reported minor surface concrete spalling in the footing area around the columns in the second study.

Mehrsoroush and Saiidi (2016), and Mehraein and Saiidi (2016) tested large-scale two-column bent models, in which columns were embedded in the cap beam pockets to a depth of 1.2 and 1.0 times the column diameter, respectively. Test results demonstrated column-to-cap beam pocket connections behaved as monolithic connections.

Mohebbi et al. (2018a, 2018b) conducted two 0.33-scale shake table tests on a precast bridge column and a precast two-column bent. Square columns were used in the test models. In the single-column model, Unbonded CFRP tendons were used to post-tension the single-column model and UHPC was used in the plastic hinge zone. Column was connected to the footing through a square pocket. The two-column bent model employed UHPC and ECC in the plastic hinges of the columns that were connected to the cap beam with pocket connections. The embedment length of the columns into the pockets was 1.0 times the column dimension. Results showed that the column-footing and column-cab beam pocket connections performed successfully and the integrity was maintained.

2.2.3. Past Research on Rebar Hinge Connections

More than fifty 1/20-scale and fourteen 1/5-scale cantilever columns incorporating rebar hinge detail were tested by Lim and McLean (1991) under cyclic loading. The authors concluded that two-way hinge connections can substantially reduce the moment transfer to the footing, but the moment is not negligible in contrast to design assumptions.

Four 1/6 scale one-way hinge specimens subjected to a constant axial load and variable lateral load were tested under both monolithic and cyclic loads by Saiidi and Straw (1993). Results demonstrated that even for specimens with very low aspect ratio, flexure and not shear controlled the strength of the hinges. It was also found that the concrete at the hinge throat region is capable of developing strains as high as nearly 0.03, and that its compressive strength is approximately 80 percent higher than the measured cylinder strength.

Haroun et al. (1993), tested six 0.4 scale, two-way hinge columns under reverse cyclic lateral loads. The failure mechanism in all specimens was flexural with a high ductility capacity. Pure shear was then applied to three other columns to assess the shear strength. The authors reported that the shear failure mechanism was diagonal tension failure of the entire column, and that the strength of the hinge section might be underestimated by beam shear design theory.

Further experimental research was conducted by Jiang and Saiidi (1995) on one-way hinges. It was concluded that the shear friction method (SFM) is not applicable to hinges

and that SFM underestimates the shear capacity of hinges. A preliminary method was hence developed for the design of one-way hinges under lateral load.

Saiidi et al. (2009), tested five one-third scale columns on a shake table under uni-directional loading. The columns incorporated two-way hinges at top. The test parameters were the hinge size, column longitudinal steel ratio, hinge steel ratio, column aspect ratio, and the axial load level. The authors reported that all columns exhibited stable hinging and ductile behavior, and that the classical shear friction mechanism in which two concrete segments slide parallel to each other was not observed in any specimens. It was concluded that under small deformations shear force is resisted by friction only in the compression zone of the hinge rather than the entire hinge. Under large deformations, dowel action of the hinge longitudinal bars provides shear resistance and prevents the total failure of the hinge. Moment-rotation, and shear-slippage models for two-way hinges were proposed.

Mehraein and Saiidi (2016), performed a shake table test on 1/3.75-scale two-column bent in which rebar hinges connected the column to the pile shaft. The precast hollow column was placed on top of the pile shafts around the rebar hinge, and was filled with SCC after the precast cap beam was placed over the columns. The design and the detailing of rebar hinge was believed to be successful for the connection of column to pile shaft, and led to the ductile behavior of the bent. The concrete at the hinge throat was damaged, but the column and pedestal reinforcement did not yield near the rebar hinge section.

2.2.4. Past Research on Rebar Hinge Pocket/Socket Connections

Mehrsoroush et al. (2016) tested a two-column bent with a combined detail of rebar hinge and pocket connection connecting one of the columns to the cap beam, while the other column was connected to the cap beam through one-piece pipe pin connection. The pier model was tested to failure on a shake table under unidirectional loading. The rebar hinge pocket connection was found to be successful even under high drift ratios.

Mohebbi et al. (2018b), conducted a shake table test on a two-column bent in which precast square columns were connected to the footing using circular rebar hinge pocket connections. A 1.0 in. (25.4 mm) vertical gap corresponding to 3.0 in. (25.4 mm) in a full-scale bridge was provided between the footing and the columns to allow for the rotation of columns. The authors reported that damage in the hinge section was limited to minor spalling of the cover concrete at the hinge gap, and no damage was detected around the rebar hinge pocket connection. Debonding the longitudinal bars of the rebar hinge for $2d_b$ each above and below the footing interface was believed to be effective in spreading yielding to prevent strain concentration and premature bar rupture at the interface.

2.3. Column to Hybrid Cap Beam Grouted Duct Connections

2.3.1. Introduction

In grouted duct connections, the longitudinal bars protruded from a precast or cast-in-place column are extended into individual ducts embedded in the adjoining member. The

ducts are then filled with high-strength grout or ultra-high performance concrete. Grouted duct connections are often used for joining columns to the cap beam.

One version of grouted duct connections consists of grouted ducts over part of the cap beam with the rest of bond for the column longitudinal steel provided in a cast-in-place portion. This is referred to as a hybrid grouted duct connection in this study. Hybrid connections allow for making the cap beam superstructure join integral. Only one past research has been conducted on hybrid cap beam connections. Therefore, the following section is mostly focused on grouted duct connections.

2.3.2. Past Research

Raynor et al. (2002) investigated the bond behavior of reinforcing bars of various sizes grouted in ducts subjected to cyclic loading. It was shown that grouted ducts provided enhanced bond strength compared to that of the conventional concrete. Furthermore, the duct provided adequate confinement for bars and thus prevented splitting of the grout.

Pang et al. (2008) tested three 0.4-scale precast columns that were connected to precast bent caps through grouted ducts. The results were compared with a typical cast-in-place (CIP) reference column with similar details. Longitudinal bars of two of the three columns were debonded over a length of $8d_b$ into the cap beam. Authors reported that precast columns showed comparable ductility capacity, lateral load capacity, and energy dissipation capacity to those of the reference CIP column. Debonding of the bars reduced the strain concentration, but did not delay the fracture of bars as intended.

Matsumoto (2008) conducted quasi-static cyclic loading on a 0.42-scale grouted duct column-cap beam connection (GD). No bar or duct pullout or splitting of the grout within the ducts were reported. The hysteretic force-displacement response of the connection resembled that of the reference CIP model up to 3.7% drift ratio. GD model exhibited higher lateral load capacity but lower drift ratio capacity compared to the CIP model.

Tazarv and Saiidi (2014) developed UHPC-filled duct connections to connect columns to shallow cap beam and footings. A half-scale precast column model connected to footing through the new grouted duct detail was tested under cyclic loading. The column was initially hollow but was filled with self-consolidating concrete (SCC) afterward. The performance of the model was satisfactory and emulative of the CIP alternate in terms of the lateral load capacity, drift ratio capacity, and strength and stiffness degradation. Tazarv and Saiidi further extended their studies to determine the bond strength of UHPC-filled ducts. The authors reported that bond strength of UHPC was eight times higher than that of the conventional concrete, and that the required embedment length of the bars in UHPC-filled ducts is at least 50% shorter other grouted duct connections.

Marsh, M. L. et al. (2010) developed a hybrid bent system aimed for integral connections with prestressed girders. The bent employed a two-stage cap beam comprising a lower precast and an upper-part cast-in-place segment. Column bars were partially anchored in the grout-filled ducts embedded in the precast cap beam. The pier model was tested under cyclic lateral loading. Test results were promising; however, the combined effect of the out-of-plane and in-plane loading on the connection was not investigated.

2.4. Simple for Dead, Continuous for Live (SDCL) connection

2.4.1. Introduction

The superstructure-to-substructure integral connection provides the load path to transfer the superstructure moment to the substructure. One advantage of the integral connections is that the cap beam soffit is at the same elevation as or close to the bottom of the girders, and as such larger under-clearance is provided for the bridge. Integral connections can also improve the seismic performance of the bridge through maintaining its integrity and reducing the weight of the superstructure.

Steel superstructures are considerably lighter than the concrete alternative. This can result in enhanced seismic behavior of steel bridges. However, non-integral connections and the need for heavy cap beams can offset the mass reduction provided through using steel girders (Wassef and Davis, 2004). The conventional integral steel girder bridge construction often involves the placement of the middle segment of the steel girders over the pier, connected to the end segments with bolted or welded field splices that requires temporary supports and increases the onsite construction time.

In the simple for dead and continuous for live load (SDCL) system, the girders span from pier to pier (or abutment to pier) within each span, and are spliced directly over the pier. Girders are simply supported before the deck is in place, but continuous for live load and superimposed dead loads such as the weight of barrier and wearing surface. Past studies on SDCL connection are presented in the following section.

2.4.2. Past Research

The idea of a simple span for dead load and continuous for live load was developed in the 1960's for precast prestressed concrete girders to prevent leakage through the deck joints in simple beam spans (Lampe et al., 2001). The same idea was pursued by researchers to use a pseudo-connection for steel bridges.

Three full-scale tests were carried out to study the behavior of proposed connections (Azizinamini et al. 2005). In the first experiment, the bottom flanges of two adjacent girders were welded over the pier centerline and end bearing plates were welded to the ends of the girders. In the second experiment, girders were simply embedded in the concrete diaphragm. The third specimen was similar to the first one but bottom flanges were not connected. A cyclic load test followed by an ultimate load test was conducted on the specimens. The authors reported that the ultimate moment capacity of the first and third specimens were almost the same and were 1.5 times of that of the second specimen. Ductility of the connections was the highest for the first specimen and the lowest for the second. In the first and third specimens, all tension reinforcement in the deck yielded before the concrete compressive failure of concrete in the diaphragm. However, in the second specimen, concrete compressive failure occurred before all the rebar yielded.

A seismic detail comprising an integral pier connection was proposed for the SDCL connection and its structural behavior and the force transfer mechanism was investigated through analytical studies at the Florida International University (Taghinezhadbilondy, 2016). The proposed connection was evaluated under push-up, push-down, reverse and axial loading. Figure 2-2 shows a schematic view of the connection. The authors

reported that under gravity loads, dowel bars and closed stirrups had no effect on the moment capacity of the system. When the FEM was loaded with concentrated push-up forces, the continuity of the bottom flange and tie bars played a major role. The vertical dowel bars were effective but not as much as the tie bars. Under reversal type loading, the only elements that affected the moment capacity were the dowel bars. These dowel bars corresponded to the vertical stirrups referred to as (A_s^{jv}) in Seismic Design Criteria Section 7.4.4.3. A simple design formula for the SDCL seismic detail was developed using a combination of moment-curvature analysis and the Winkler foundation method. Seismic performance of this connection was also tested under cyclic lateral loading. Test results confirmed that the connection was suitable for high seismic regions (Sadeghnejad and Azizinamini, 2017). The model did not include precast elements and also was tested only in one direction. Moreover, the combined effect of out-plane loading and in-plane rotation of the superstructure was not included in the study.

2.5. Deck Panel Connections

2.5.1. Full-depth precast deck panels

Full-depth precast deck panels have been appealing in bridge construction for more than thirty years because they reduce onsite and the total construction time significantly as deck forming, casting, and curing time are eliminated from the critical path of the project. As precast panels are built offsite and under controlled environmental conditions, they offer potential high-quality production, and less volume variations due to shrinkage and temperature during initial curing (Badie and Tadros, 2008). Furthermore, there is an opportunity for the deployment of advanced materials and thus noticeably enhancing the serviceability of deck panels. Although full-depth precast decks are usually more expensive compared to cast-in-place panels in terms of the construction and material, the additional cost is often offset by decreased construction time and less required maintenance (PCI, 2011).

2.5.2. Panel to Girder Pocket Connection

Composite action between the deck and the girder offers many advantages over the non-composite alternate as it leads to shallower depth of the superstructure, longer spans, smaller deflection and less vibration caused by moving traffic, and larger clearance. One of the challenges for the incorporation of prefabricated panels is to provide a full-composite (or sufficiently composite) action between the deck and the girders.

As a part of NCHRP 12-65 Project, Badie and Tadros (2008) proposed a new detail for connection between steel girder and precast panels, in which eight double-headed 1-1/4 in. studs at 48 in. spacing were welded to the girder top flanges. Figure 2-3 shows the connection details. The proposed detail was tested under gravity and lateral loading. Pockets were left in deck panels over the girder lines to accommodate studs. The authors reported that response of the connection was satisfactory in terms of the strength and fatigue capacity. Hollow structural steel (HSS) tubes that were used around the studs were found to be effective in confining the grout surrounding the studs. In addition, it was shown that the 48-in. spacing of the cluster of studs (instead of the 24 in. that is currently specified in AASHTO (2012), Section 6, was adequate to provide a composite

action. Furthermore, it was concluded that Article 5.8.4.1 in the AASHTO (2012) can reasonably estimate the horizontal shear capacity of the proposed panel-to girder detail.

Shrestha et al. (2018) conducted a mix of experimental and analytical studies to develop and design prefabricated bridge decks with composite connection to precast girders. A series of pullout and shear tests with various details were undertaken to determine the shear and axial stiffness and strength of headed anchors. Figure 2-4(a) and (b) show the typical test setup for the pullout and shear experiments. A variety of grout types including conventional concrete, Latex Concrete, UHPC, Polyester Concrete, 1428 HP, and EucoSpeed were also examined as the filler material in the pockets. Another variable that was looked into was the group effect of anchors. Shrestha et al. concluded that neither the type of the grout nor the group affected shear and axial capacity of anchors. In terms of the required time and effort for the grout removal, Latex Concrete was the most promising grout type. Overall, all of the grout types but Polyester Concrete and UHPC were recommended for future deck replacement. Another finding of the study was that by using the proposed detail, 70% of a full composite action was achieved.

2.5.3. Joints between Adjacent Deck Panels

Transverse shear keys (joints) between precast panels have to be designed such that they prevent relative vertical displacement between the adjacent panels and provide adequate path for the transfer of the positive moment and vertical shear due to the traffic load (Badie and Tadros, 2008).

There are two main types of transverse shear keys: male to female and female to female shear keys (Figure 2-5). Male-to-female shear keys have been implemented in combination with the longitudinal posttensioning in a few bridges. However, due to the tight tolerances in panel construction, leakage has always been a common challenge in such joints. Grouted female to female joints are most often used. Vertical shear forces applied at the joint are resisted by bearing and bond between the grout and the panel. Inclined surfaces increase the vertical shear strength of the joint (Badie and Tadros, 2008). Roughening the surface of the shear key has been found to enhance the bond between the grout and the shear key surface (Issa et al. 2000).

Longitudinal posttensioning has been used with majority of deck panel systems as a technique to eliminate the joint tensile stresses resulting from traffic load, and hence to prevent cracking and leakage. However, field posttensioning increases the construction time and cost, and complicates the deck placement process.

In the absence of the longitudinal post-tensioning, a wide closure joint is required to provide adequate lap splice length for deck reinforcement. Several researchers have investigated the structural performance of field-cast UHPC connections for bridge deck components. UHPC is a cementitious material with water-to-cementitious material ratio of less than 25%, and a high percentage of steel fibers. Two main reasons that made UHPC a perfect candidate for panel joints were the exceptional bond when cast against previously cast concrete and the ability to shorten the required development length of embedded steel reinforcement significantly (Perry and Royce, 2010). Large cyclic and static flexural and shear loading tests on full-scale field-cast UHPC connections demonstrated that they not only facilitate construction, but also the resulting deck system

meets or exceeds the performance requirements of conventional cast-in-place bridges by demonstrating favorable cracking behavior with no sign of interface debonding under cyclic loads (Graybeal 2010, 2014). Furthermore, under the ultimate static loading, the concrete cracking was followed by bar yielding and eventual compressive failure of the conventional concrete. This behavior is similar to monolithically-cast deck panels.

Deck panel joints over the pier in multi-span bridges with continuity for traffic loads are more critical than the joints along the spans, due to the relatively high strains that they could undergo. The deck-to-deck connection are more crucial in integral bridges, as deck bars need to provide an adequate load path for the transfer of the negative moment resulting from seismic lateral loading in addition to that of the service loads. AASHTO (2012) allows for splicing the deck reinforcement over the cap beam. However, Caltrans Memo to Designers 20-9 (2016) prohibits splices inside the critical zones of superstructure capacity-protected components. Critical zones are defined as locations where the moment demand is greater than 75% of the maximum moment. That being said, the common practice has been either to hook the deck bars into the cap beam or to mechanically splice them. Both approaches complicate the construction process and are time-consuming.

Figures

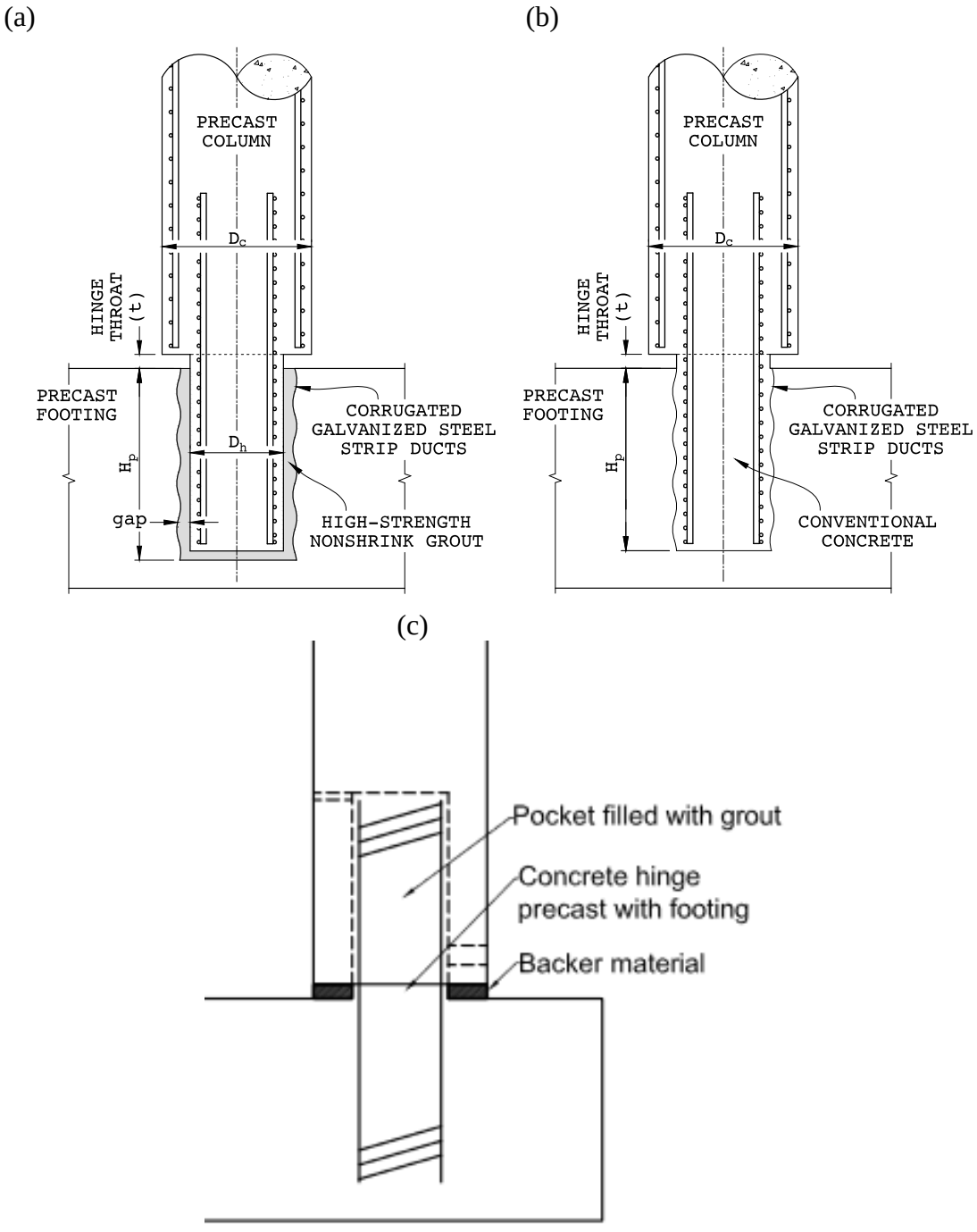

Figure 2.1 column to footing (a) rebar hinge pocket connection, (b) rebar hinge socket connection, (c) rebar hinge pocket connection with pocket left in column

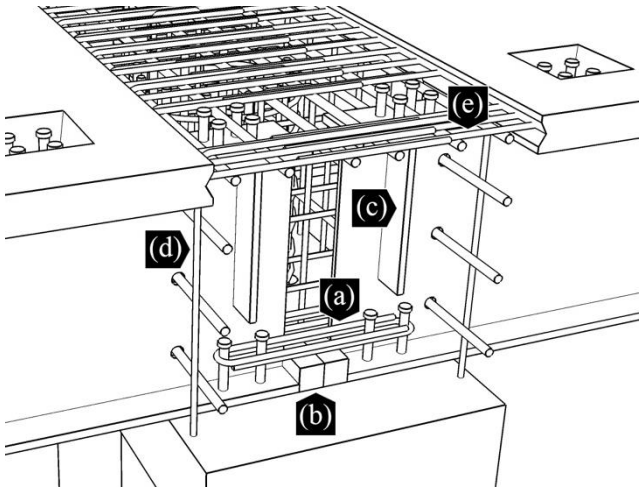

Figure 2.2 Details of the SDCL connection: (a) tie bar, (b) steel block, (c) stiffener, (d) cap beam stirrups (dowel bars), (e) deck longitudinal bars

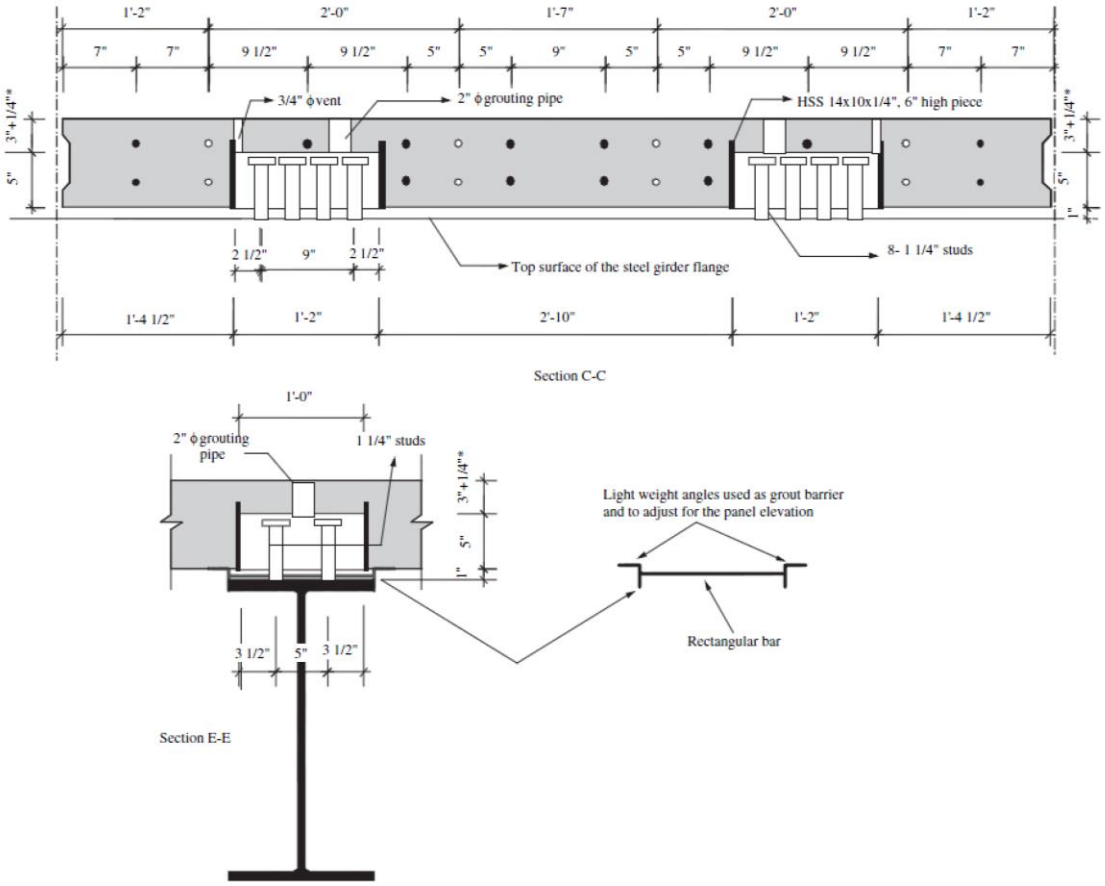

Figure 2.3 Connection between full-depth deck panels and steel plate girder (Badie and Tadros, 2008)

(a) (b)

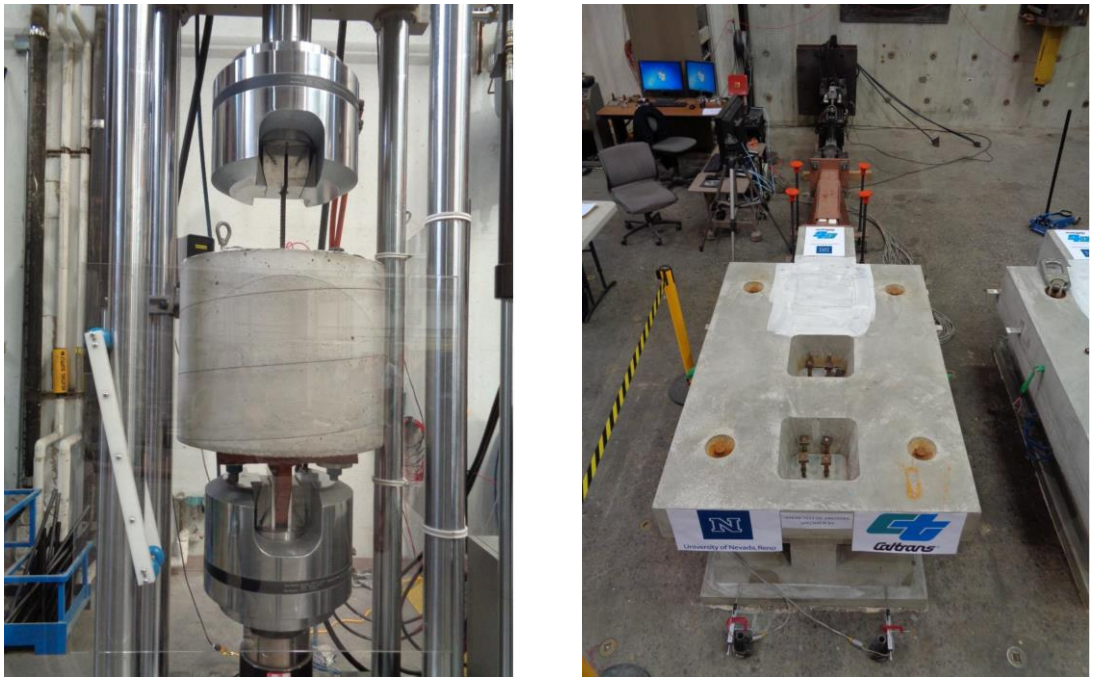

Figure 2.4 Test setup for (a) pullout and (b) shear tests (Shrestha et al. 2017)

(a) (b)

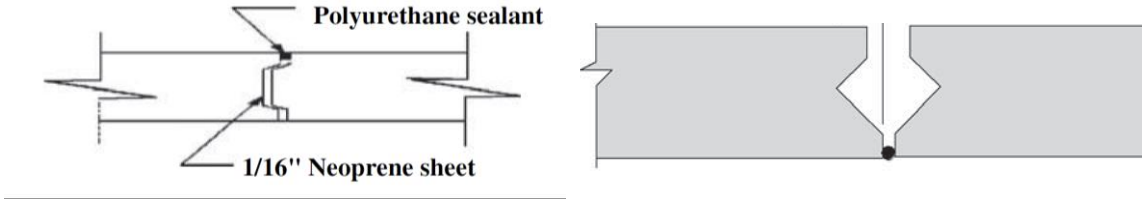

Figure 2.5 Typical detail for (a) male-to-female and (b) female-to-female joints between full-depth panels (Badie and Tadros, 2008)

2.6. References

Azizinamini, A., Yakel, A., & Farimani, M. (2005). Development of a Steel Bridge System-Simple for Dead Load and Continuous for Live Load: Volume 1-Analysis and Recommendations (No. NDOR Research Project Number P542).

Badie, S. S., & Tadros, M. K. (2008). Full-depth Precast Concrete Bridge Deck Panel Systems: Sameh S. Badie and Maher K. Tadros (Vol. 584). Transportation Research Board.

Caltrans, Splices in bar reinforcing steel, Memo to Designers 20-9 (2016), Caltrans, California Department of Transportation, Sacramento, CA

Cheng, Z. Y., Saiidi, M. S., & Sanders, D. (2010). "Seismic Design Method for Reinforced Concrete Two-Way Column Hinges". ACI Structural Journal, 107(5).

Culmo, M. P., Marsh, L., Stanton, J., & Mertz, D. (2017). "Recommended AASHTO Guide Specifications for ABC Design and Construction" (No. NCHRP Project 12-102).

Haraldsson, O. S., Janes, T. M., Eberhard, M. O., and Stanton, J. F. (2013). "Seismic resistance of socket connection between footing and precast column." Journal of Bridge Engineering, 18(9), 910-919.

Haroun, M., Pardoen, G., & Shepherd, R. (1993). Shear strength of pinned columns. Proceedings of the 2nd Annual Seismic Research Workshop.

Issa, M. A., Yousif, A. A., & Issa, M. A. (2000). Experimental behavior of full-depth precast concrete panels for bridge rehabilitation. *Structural Journal*, *97*(3), 397-407.

Kavianpour, F., & Saiidi, M. (2013). Experimental and Analytical Seismic Studies of a Four-Span Bridge System with Composite Piers. University of Nevada, Reno, Department of Civil and Environmental Engineering. Center for Civil Engineering Earthquake Research.

Lim, K. Y., and Mclean, D. I. (1991). "Scale model studies of moment-reducing hinge details in bridge columns." ACI Structural Journal, 88(4), 465-474.

Marsh, L.M., Wernli, M., B.E.Garrett, J.F.Stanton, M.O.Eberhard, and M.D.Weinert. (2011). NCHRP Report 698 "Application of Accelerated Bridge Construction Connections in Moderate-to-High Seismic Regions". Washington, D.C.: National Cooperative Highway Research Program, Transportation Research Board.

Matsumoto, E. E., Mark, C., Waggoner, M. E. K., Vogel, J., & Wolf, L. (2008). "Development of a precast concrete bent-cap system". PCI journal.

Matsumoto, E. E., Waggoner, M. C., Sumen, G., Kreger, M. E., Wood, S. L., & Breen, J. E. (2001). "Development of a Precast Bent Cap System" (No. Report no. RR-1748-2). University of Texas at Austin. Center for Transportation Research.

Mehrsoroush, A., Saiidi, M., & Ryan, K. (2017). "Development of Earthquake-Resistant Precast Pier Systems for Accelerated Bridge Construction in Nevada". (No. 555-14-803).

Mohebbi, A., Saiidi, M. S., & Itani, A. M. (2018a). Shake Table Studies and Analysis of a PT-UHPC Bridge Column with Pocket Connection. Journal of Structural Engineering, 144(4), 04018021.

Mohebbi, A., Saiidi, M. S., & Itani, A. M. (2018b). "Shake Table Studies and Analysis of a Precast Two-Column Bent with Advanced Materials and Pocket Connections". Journal of Bridge Engineering, 23(7), 04018046.

Mortensen, J., and M. Saiidi, "A Performance-Based Design Method for Confinement in Circular Columns," Civil Engineering Department, University of Nevada, Reno, Report No. CCEER 02-07, November 2002.

Motaref, S., Saiidi, M. S., & Sanders, D. (2013). Shake table studies of energy-dissipating segmental bridge columns. Journal of Bridge Engineering, 19(2), 186-199.

Pang, J., K.P.Steuck, L.Cohagen, Stanton, J., and Eberhard, M. (2008). "Rapidly Constructible Large-Bar Precast Bridge-Bent Seismic Connection'. Olympia, WA: Washington State Department of Transportation. WA-RD 684.2

PCI Design Handbook, (2004), Precast and Prestressed Concrete, 6th edition, MNL 120-04

Perry, V. H., & Mathew Royce, P. E. (2010). Innovative field-cast UHPC joints for precast bridge decks (side-by-side deck bulb-tees), Village of Lyons, New York: Design, prototyping, testing and construction. In Proc., 3rd Int. fib Congress Incorporating the PCI Annual Convention and Bridge Conf (Vol. 1, pp. 1054-1066).

Raynor, D. J., Lehman, D. E., & Stanton, J. F. (2002). Bond-slip response of reinforcing bars grouted in ducts. Structural Journal, 99(5), 568-576.

Restrepo, J. I., M. J. Tobolski, and E. E. Matsumoto, (2011). "Development of a precast bent cap system for seismic regions." NCHRP Rep. 681. Washington, DC: National Cooperative Highway Research Program.

Sadeghnejad, A., Azizinamini, A., (2017), "Extending the Application of Simple for Dead and Continuous for Live Load Steel Bridge System to ABC Applications in Seismic Regions. Phase II-Experimental" Web-based quarterly Research Seminar, ABC-UTC research center, Florida International University.

Shrestha, G. (2018). Seismic Studies of Superstructure and Substructure Connections for Accelerated Bridge Construction (Doctoral dissertation).

Steuck, K., Stanton, J., and Eberhard, M. (2009). "Anchorage of Large-Diameter Reinforcing Bars in Ducts". ACI Structural Journal, Volume 106, No. 4, pp. 506-513.

Taghinezhadbilondy, R. (2016). Extending Use of Simple for Dead Load and Continuous for Live Load (SDCL) Steel Bridge System to Seismic Areas.

Tazarv, M. and Saiidi, M.S. (2014). "Next Generation of Bridge Columns for Accelerated Bridge Construction in High Seismic Zones." Center For Civil Engineering Earthquake Research, Department of Civil and Environmental Engineering, University of Nevada, Reno, Nevada, Report No. CCEER-14-06, 400 pp.

Wassef, W. G., & Davis, D. (2004). NCHRP REPORT 527. Integral Steel Box-Beam Pier Caps. Transportation Research Board of the National Academies.

CHAPTER 3: DESIGN, CONSTRUCTION, AND SHAKE TABLE TESTING OF A STEEL GIRDER BRIDGE SYSTEM WITH ABC CONNECTIONS

This chapter is a stand-alone paper that is accepted for publication in ASCE Journal of Bridge Engineering

Abstract

Shake table experiment of a large-scale two-span ABC bridge model with steel superstructure incorporating six of the more promising ABC connections was conducted on shake tables at the University of Nevada, Reno. The objective was to investigate the seismic performance of the ABC connections integrated into a bridge system and to determine if ABC bridges can demonstrate adequate load path, integrity, and constructability. The bridge model was subjected to successive bi-directional motions simulating a modified version of the Northridge 1994 earthquake record. Test results showed that the ABC bridge emulated the behavior of cast-in-place bridge columns by undergoing large inelastic deformations in a ductile manner, by forming plastic hinges and extensive yielding of the longitudinal bars in the columns. Structural integrity was maintained in all connections through various earthquake levels. Construction procedure of the bridge model ensured the feasibility of handling and connecting different prefabricated members.

3.1. Introduction

Accelerated bridge construction (ABC) is becoming of great interest to bridge owners due to the several advantages it offers over traditional cast-in-place (CIP) methods. By reducing the onsite construction time, ABC costs the traveling public less time and money and enhances the work-zone safety. Connections between prefabricated elements play a vital role in the survival of ABC bridges under strong earthquakes. When ABC technology is used for connecting columns (where an inelastic response is expected) to the adjoining members, the connections must allow for the energy dissipation of the yielding element while maintaining their capacity and the integrity of the structural system. Another challenge for ABC is to develop connections that are practical and constructible efficiently. To date, various types of ABC connections have been studied at the component level, many with satisfactory results (Matsumoto et al. 2001; Restrepo et al. 2011; Tazarv and Saiidi 2014; Motaref et al. 2011; Mehrsoroush, et al. 2016; Mehraein and Saiidi 2016). The focus of this article is on six types of ABC connections that were integrated in a two-span bridge model: (1) rebar hinge pocket connection, (2) grouted duct connection, (3) Simple for dead continuous for live (SDCL) girder-to-cap beam connection, (4) girder-to-deck grouted pocket connection, (5) ultra-high performance concrete (UHPC)-filled joints between the deck panels, and (6) deck panel UHPC-filled connection above the (CIP) portion of the cap beam.

ABC column connections may be categorized as rigid or pinned, with the majority of past research being on the former. "Pin" or hinge connections are desirable for connecting the column to the footing as they result in smaller and more cost-effective foundations. Rebar hinge connection is a type of two-way hinge comprising a central reinforcement cage with a smaller diameter compared to that of the column. Saiidi et. al (2009),

performed a series of shake table tests on five single columns incorporating rebar hinges. From the test data, it was concluded that neither conventional shear friction nor diagonal shear methods were valid in predicting the shear capacity of two-way concrete bridge column hinges. The issue with the former method is that column lateral forces can cause significant flexural cracking and rotation at the hinge throat making the conventional shear friction assumption questionable. The issue with the latter is due to the extremely small aspect ratio of the hinge that prevents the formation of a 45^{o} diagonal tension crack across the hinge section. Mohebbi et al. (2017), conducted a shake table test on a two-column bent in which precast square columns were connected to the footing using circular rebar hinge pocket connections. The design and the detailing of rebar hinge was found to be successful. However, there has not been any application of the two-way hinge detail with pocket connection in the field, nor it has been tested under bi-directional loading.

A precast bent system intended for integral connections with prestressed girders was developed by Washington State Department of Transportation (Marsh, M. et al. 2010). The detail included a lower precast cap beam installed first to support the girders and a cast-in-place upper portion to integrate the pier and superstructure. The column bars were partially anchored in the lower cap beam in grouted ducts. The authors reported satisfactory performance of the connection under cyclic lateral loading. A similar detail, with UHPC rather than grout used in the ducts, was incorporated in one bridge in Northern California in early 2018 for the first time. A second bridge with this detail is under construction in S. California. Grouted duct connections (not hybrid) have been studied in the past, but only under in-plane loading. Combined effect of out-of-plane loading and in-plane rotation of the superstructure was unknown prior to the current research.

A seismic detail for cap beam to girder connection in integral steel bridges was developed by Taghinezhadbilondy et al. (2016) in which the steel girders were simply supported for the dead load and continuous for the live load (SDCL). A finite element model of the connection was evaluated under monotonic and cyclic loading, and the results were promising. Seismic performance of this connection was also experimentally tested at Florida International University (FIU) under cyclic lateral loading, confirming that the connection is suitable for high seismic regions (Sadeghnejad and Azizinamini, 2017). The model did not include precast elements and also was tested only in one direction. Moreover, the combined effect of out-plane loading and in-plane rotation of the superstructure was not included in the study.

Full-depth precast deck panels are known to expedite construction. Composite action between steel girders and precast deck panels can be obtained by pockets left in the deck panels over the girders to accommodate a cluster of shear studs (Badie and Tadros, 2008). Shrestha et al. (2017) showed that the used type of grout in the deck pockets has a negligible effect in the connection capacity. Longitudinal post-tensioning increases the construction time and cost and complicates the deck placement process (Badie and Tadros, 2008). Graybeal (2010, 2014a) showed that using the Ultra-high performance concrete (UHPC) in the joints between deck panels would improve the bond and reduce the required lap splice length for deck longitudinal reinforcement, thereby enabling the

use of narrower joints. This finding was utilized in the current study in the precast deck panel connections at the deck level over the cap beam and in the other precast deck-to-deck joints. Over the pier, longitudinal bars of the deck panels can be hooked in the cap beam, which adds to reinforcement congestion and requires extra time. The alternative practice is to use mechanical splices, which is also time consuming. It was decided to simplify the connection by using lap spliced bars combined with UHPC even though the deck-panel cap beam connection zone is critical.

Component tests have provided invaluable information about the local behavior of ABC connections under unidirectional loading. However, only one component extracted from a structural system is included in these tests with other elements of the system excluded. Two important questions are raised as a result: (1) How do these ABC components perform under real earthquakes that impose loading in different directions? and (2) What is the effect of interaction among the components. To answer these questions complex test models and loading programs requiring elaborate facilities and substantial budget are required. It is for these reasons that failure testing of structural systems is rare, even though, for new components to be accepted by the profession, system studies are sought. The study presented in this article was aimed at addressing these issues.

The primary objective of this study was to investigate the seismic performance of six ABC connections when integrated into a bridge system with steel superstructure under combined gravity and bidirectional simulated seismic excitations. Moreover, the adequacy of the emerging design methods for these connections was evaluated. Another objective of the study was to evaluate the feasibility of the construction methods and to identify construction issues in handling and connecting various prefabricated elements. This paper presents a summary of the design, construction, shake table testing, and observed damage of the test model.

3.2. Objectives of this Article

Detailed presentation and discussion of the measured data, analytical studies, and design implications of the study are beyond the space limits of this paper and hence are provided elsewhere (Shoushtari et al. “Pretest Analysis of Shake Table Response of a Two-Span Steel Girder Bridge incorporating ABC Connections”, submitted, UNR, Reno, Nevada; Shoushtari et al. “Seismic Performance of a Two-Span Steel Girder Bridge with ABC Connections Under Earthquake Loading”, working paper, UNR, Reno, Nevada; Shoushtari et al. “Numerical Modeling and Seismic Design of Steel Girder Bridge System with ABC Connections”, working paper, UNR, Reno, Nevada). Presenting the three primary components of this article (design, construction, and observed damage) is of significant benefit to designers and researchers. With respect to the design, it should be noted that there are currently no formal design codes or guidelines available for seismic design of ABC connections. The design methods utilized in the current study are emerging methods that are yet to be adopted by bridge code officials. Yet, designers are faced with the drive to adopt ABC in moderate and high seismic areas. The material in the paper provides an insight as to how the emerging methods are incorporated in the bridge design. Another unique aspect of the paper is the construction of the model that integrated different connections types for precast members. ABC is substantially

different than conventional construction. Several details of the bridge model have not been incorporated in the field or tested under realistic loading. Description of the construction sequence of the bridge model can provide a general roadmap relative to what is expected in the field, although there are some differences between the construction of a model bridge and an actual bridge. Finally, by providing an overview of the observed damage, the paper demonstrates whether the primary global objectives of the design were met.

3.3. Prototype Bridge

An assumed prototype bridge was scaled down by a scale factor of 0.35 to accommodate the capacity of shake tables. The configuration of the prototype is shown in Fig. 1. The prototype bridge comprised two equal spans of 30.5 m (100 ft). The width of the prototype superstructure section was 9.5 m (31 ft), allowing for two 3.6-m (12-ft) wide lanes and a shoulder. The diameter and clear height of the columns were 1.2 m (4 ft) and 6.1 m (20 ft), respectively. The prototype geometry, including the barrier rails, and the wearing surface resulted in approximately 3560 kN (800 kips) of dead load over the bent. Axial load index ($ALI = \frac{P_{dead}}{f'_c \times A_g}$) for the columns, defined as the dead load (Pdead) divided by the product of the nominal concrete compressive strength (f'c) and the gross cross-sectional area of each column (A_g), was 0.057.

3.4. Bridge Model Description

The geometric configuration of the 0.35-scale two-span bridge model and the 3-dimensional rendering are shown in Fig. 2 and Fig. 3, respectively. The bridge model was 3.4 m (11 ft) wide with two equal spans of 10.6 m (34'-8"). The superstructure including steel plate girders and full depth precast deck panels was supported on seat type abutments and a two-column precast bent. Columns were detailed to have moment connections at the top and pin connections at the bottom. The seismic weight of the bridge, the weight of all the bridge components excluding half of the columns and the footing, was 636 kN (143 kips). The axial load due to gravity loads was 205 kN (46 kip) for each column. The column clear height and spacing were 2.1 m (84 in.) and 1,981.2 mm (78 in.), respectively. Girders were simply supported for the gravity load and were made continuous afterwards.

3.5. Design

There are no codes for the seismic design of ABC bridges. Hence, the overall design of the bridge model was based on the AASHTO LRFD Bridge Design Specifications (2012) and the AASHTO Guide Specifications for LRFD Seismic Bridge Design (2014), while the ABC connection design was based on the published emerging methods (Saiidi et al. 2009; Marsh et al. 2010; Taghinezhadbilondy et al. 2016; Badie and Tadros, 2008; Graybeal 2010; Graybeal 2014a&b). It was assumed that the bridge was located at Lake Wood in the Los Angeles area, with the latitude and longitude of 3.84926 N, and 118.09252 W, respectively. Seismic design parameter values of the location are: A_S (acceleration coefficient) =0.473g, S_{DS} (design spectral acceleration coefficient at 0.2-sec period) = 1.155g, S_{D1} (design spectral acceleration coefficient at 1-sec period) = 0.637g,

T_S (SD1/ SDS) = 0.552 sec, T_0 (0.2 T_S) = 0.11 sec, and Site Class D. Seismic design category D (SDC D) was selected based on S_{D1} value.

The design strategy was to design a ductile substructure with an essentially elastic superstructure. Accordingly, the bridge components were designed such that the inelastic deformations occur in columns and the superstructure and footing remain essentially elastic with no significant yielding or damage during the shake table testing. The columns, girders, bent cap, deck to girder connection, and column to footing connections were designed for both the prototype and the scaled bridge. The footing, elastomeric bearings, and deck panels were only designed for the bridge model. The abutment back walls were assumed to be sacrificial, meaning that they fail under relatively small earthquakes and hence there is not passive resistance of the soil affecting the longitudinal response of the bridge. The transverse abutment shear keys were also assumed to be sacrificial. Both of these assumptions are conservative and consistent with the current practice of seismic design of the bridges (AASHTO Guide Spec., 2014).

3.5.1. Bent

Fig. 4 illustrates the two-column bent details. The nominal 28-day compressive strength of concrete in the bent was 27.6 MPa (4.0 ksi) with a maximum aggregate size of 10 mm (3/8 in.). The columns had a circular section, longitudinal steel ratio of 1.86%, and volumetric transverse steel ratio of 1.25%. The columns were designed based on the force-based approach according to the AASHTO LRFD (2012), and the design was checked using the displacement-based approach in accordance to the AASHTO Guide Specs (2014). The plastic moment capacities of the columns were determined using a fiber-discretized cross-sectional analysis based on the strain compatibility using XTRACT software (Chadwell and Imbsen, 2002). Nonlinear static (pushover) analysis was performed on a FE model in OpenSees (2000) to obtain the capacity of the pier in the transverse and longitudinal directions.

The column connections to the footing were through two-way hinges embedded in pockets the left in the footing. The hinge connections were designed based on the procedure developed by Saiidi et al. (2009). According to this procedure, the shear capacity of the hinge section is determined based on the friction in the compression zone with a shear friction coefficient of 0.45, which is lower than the value specified in design codes to account for the cyclic effects and the grinding of the hinge aggregate. The lateral pressure of the hinge confined concrete was calculated assuming the section is doubly confined by both the hinge and column spirals as recommended by Saiidi et al (2009). A 38.1mm (1.5in) gap was provided between the columns and the footing to allow for the column rotation at its base. Number 3 [Dia. = 9.525 mm (3/8 in.)] spiral at 70 mm (2.75 in.) pitch was obtained for the hinge transverse reinforcement using Mortensen and Saiidi's performance-based design method, for a target curvature ductility of 10. However, it was decided to use a spiral pitch of 38 mm (1.5 in.) to avoid the hinge failure under very strong earthquakes that were going to be applied to the bridge model.

The footing incorporated two corrugated steel pipes with nominal diameter of 305 mm (12 in.) to form circular pockets for the hinge elements. The footing needed to resist the bending moments and shear forces transferred from the columns, as well as the clamping

forces between the footing and the shake table. The embedment length of the column in the footing was 483 mm (19 in) corresponding to 1.25 times the required tension development length of the column longitudinal bars. This embedment length allowed for the bars to reach near the bottom of the footing (Fig. 1) to help form a strut and tie mechanism.

The cap beam was constructed in two stages, a lower and an upper part, with the former being precast and the latter being CIP. The girders, deck panels and the first stage of the superimposed mass that represented gravity were put in place before the CIP portion of the cap beam was cast. Accordingly, the design of the cap beam included two steps. The lower cap beam was designed for the construction loads including self-weight of the deck panels, girders, cap beam, and the stage I superimposed mass. Four longitudinal bars in the top layer of the lower cap beam were to resist the negative moment due to the dead loads during the construction. Although both spans were put in place almost simultaneously, torsional loading induced in case of placing one span at a time was taken into consideration in the design of the precast cap beam. The depth of the precast cap beam was determined such that sufficient length was available for the column bars to develop the required strength for the construction loading, with the anchorage in the precast part of the cap beam being through the grouted ducts. The width and depth of the precast cap beam were 609.6 mm (24 in.), and 190.5 mm (7.5 in.), respectively. The lower cap beam incorporated 24, 51-mm (2 in.) diameter corrugated galvanized metal ducts conforming to the ASTM A653 which were later filled with high-strength grout. The required anchorage length for column longitudinal bars developed in the grouted ducts of the precast cap beam (Restrepo et al. 2011), assuming 48.3 MPa (7 ksi) for grout compressive strength was 272 mm (10.7 in). However, the available length can develop 290 MPa (42 ksi) strength in the column bars, which was sufficient to resist the construction loads. The embedment length of the bars exceeded that required to develop the bars. However, it was necessary to extend the bars to near the top of the cap beam to help form a strut and tie mechanism in the column-cap beam joint.

The entire cap beam (the combined precast and CIP parts) was designed for the seismic loading with the total height available to develop the column bars. The longitudinal bars of the columns passed through the ducts and extended into the CIP part of the cap beam (Fig. 4). Spirals similar to the column spirals were installed around the ducts. The load transfer strength at the column-cap beam interface was evaluated using the AASHTO LRFD shear-friction design procedure. To account for the cyclic loading effects and the potential for significant cracking, the cohesion factor, c, was ignored completely. The friction factor, μ, and K1 and K2 were 0.6, 1.4 MPa (0.2 ksi), and 5.5 MPa (0.8 ksi) respectively (Marsh et al. 2010). The column-cap beam joint reinforcement was checked to ensure the joint region is adequately sized and reinforced. The authors believe that the full depth of the combined lower and upper parts of the cap beam participate in resisting the joint forces in both the longitudinal and transverse directions. Nonetheless, another load path for longitudinal force transfer was considered that assumes only the upper cap beam where the superstructure frames into the cap beam participates in the longitudinal force transfer. This meant that the joint forces are resisted by a reduced cap beam depth

but an increased effective width (along the length of the cap beam). The joint reinforcement and dimensions satisfied both cases.

3.5.2. Superstructure

Fig. 5 shows details of the girders. Girders being simply supported for the dead load and continuous for the live load, allowed the use of a uniform cross section for the girders throughout the bridge length. To use the same cross section for the interior and exterior girders, the dimensions of the girders were determined based on the interior girder because it carried the largest loads. The girders were designed for Strength I, and Service I load combination in accordance to chapter 6 of AASHTO LRFD (2012). The location of crossbeams between the girders was specified such that adequate lateral torsional buckling resistance was provided for both the negative and positive moment regions.

Details of a typical deck panel are shown in Fig. 6. The design of the prototype deck followed the AASHTO LRFD (2012) considering HL93 loading as the live load, and 50 PSF as the wearing surface. The required reinforcement area was then scaled down for the scaled deck panels. Because of the limited thickness of the deck panels [70 mm (2 3/4")], only one layer of reinforcement was used in each direction. Note that due to the girders being simply supported for the dead load, no negative moment is developed in the superstructure during construction. Therefore, the total negative moment at the pier (due to the gravity and seismic loading) is reduced, leading to a declined potential of cracking in the bridge deck. The bridge model included 22 precast deck panels joined with transverse UHPC-filled female-to-female joints. Utilizing UHPC in the joints, the required lap splice length for deck reinforcement was reduced. Graybeal (2014b) conducted an experimental study on the bond strength of #4 to #8 deformed bars embedded in UHPC and suggested a minimum embedment length of $10d_b$ and splice length of 75% of the embedment length ($7.5d_b$) for #4 to #8 bars. However, since Graybeal's study did not include #3 bars, it was decided to use the splice length of $10d_b$ [equivalent to 95 mm (3¾ in.)] for #3 deck longitudinal bars. Accordingly, 101.6 mm (4 in.) wide joints were used in between the deck panels.

With respect to the deck bar development length over the cap beam, the AASHTO (2012) allows for splicing the reinforcement, however the Caltrans Memo to Designers 20-9 (2016) does not allow splices inside the critical zones of superstructure capacity-protected components. Critical zones are locations where the moment demand is greater than 75% of the maximum moment. Therefore, although lap splice length was sufficient for the deck reinforcement over the pier using normal strength grouts, UHPC was used in the upper 70 mm (2 ¾ in.) of the cap beam to match the deck thickness.

It was important to ensure the deck panels are not overloaded and damaged during handling. The lift locations in the deck panels were designed according to chapter 5, PCI Design Handbook (2004).

Connection of the deck panels to the girders was through clusters of four 19-mm (¾-in) studs with a spacing of 63.5 mm (2 ½ in.), welded to the girder top flange and embedded in deck pockets left in the panels. The spacing of the center of pockets in the longitudinal direction was 457 mm (18 in.). The deck pockets were filled with high strength, non-shrink grout afterwards. Shear studs were designed for Strength and Fatigue limit states

based on Chapter 6, AASHTO LRFD (2012). The shear capacity of the studs was calculated using the specified compressive strength and modulus of elasticity of the grout. It was necessary to make sure no slippage occurs between the deck and the girders, thereby to ensure the full-composite action. Due to a lack of data for steel bridges, a bilinear model for precast girder to panel connectors was utilized (Shreshta et al. 2017). Due to the different diameter and length of the studs in the bridge model, the stiffnesses were scaled accordingly. The estimated maximum slippage between the deck and the girders was 0.03 mm (0.015 in.) under the loading during the last earthquake run.

Five components of the SDCL connection are illustrated in Fig. 7. The design of the connection followed a procedure developed by Taghinezhadbilondy et al. (2016). Tie bars (two U-shaped #3 bars on each side of each girder) were tied around the shear studs welded to the girders bottom flanges. The required area for these tie bars depends on the vertical acceleration of the earthquake and was determined based on the positive moment induced by 25% of weight of the structure acting upward. Steel blocks of size 51 mm by 51 mm by 152 mm (2 in. by 2 in. by 6 in.) were welded to the end of girder bottom flanges to prevent concrete crushing under negative moment. The steel blocks were as wide as the bottom flange. The end stiffeners were intended to help passing the compression force from the girder top flange to the concrete. The height of the end stiffeners was designed to allow for sufficient space for the placement of the tie bars on the girders bottom flanges. Cap beam stirrups (also known as dowel bars) were designed for the torsion and shear under longitudinal seismic excitations (along traffic). Dowel bars are the main load-carrying mechanism under reversed loading. As recommended by Taghinezhadbilondy, 2016, the design of the dowel bars could be based on established Caltrans (Caltrans, 2013) design provisions for capacity protected elements. Live load continuity was provided by the deck longitudinal reinforcement over the pier. In the proposed detail by Taghinezhadbilondy et al. (2016), the end of the deck longitudinal bars was hooked in the cap beam with 90° hook. However, to simplify construction and handling and placement of precast deck panels, it was decided to splice the deck reinforcement over the pier with long lengths embedded in UHPC.

The abutment seats (Fig. 8) were designed for the tributary weight of the superstructure. The maximum displacement of the bridge model under 200% of the target design earthquake was obtained from pretest response history analysis and was utilized in calculating the minimum required support length.

To duplicate the column axial load index and stresses of the prototype bridge, superimposed mass was assumed on the superstructure. The superimposed mass was provided by 280 KN (63 kips) of lead pallets and 325 KN (37 kips) of concrete blocks. Lead pallets represented additional dead load of the structural components (labeled as DC1) and were placed while the girders were simply supported. Concrete blocks represented dead load due to non-structural attachments, including curb, railings, sidewalks or barriers (labeled as DC2), as well as future wearing surface (labeled as DW). Concrete blocks were added after the spans were continuously supported.

3.6. Pretest Analysis

Detailed analytical studies of the preliminary test model were conducted to (a) ensure the feasibility of the shake table tests, (b) estimate design forces for the preliminary design of the components, (c) select suitable ground motions, (d) develop the shake table testing protocol, and (e) identify proper location and distribution of instrumentation. The seismic response of the bridge model was investigated under a large number of near-fault and far-field earthquake records. Two- and three-dimensional finite element models of the bridge model for both the prototype and scaled bridge were developed in OpenSees (2000), and SAP2000 (2015) finite element packages. Linear analysis under service dead and live loads, nonlinear static analysis, and nonlinear response history analysis were conducted. Details of the pretest analytical studies are provided elsewhere (Shoushtari et al. "Pretest Analysis of Shake Table Response of a Two-Span Steel Girder Bridge incorporating ABC Connections", submitted, UNR, Reno, Nevada).

3.7. Construction

Fig. 9(a) to Fig. 9(c) show the precast footing, precast cap beam, and the columns; respectively. The surface of the rebar hinge was roughened to increase bonding with grout. Fig. 10 shows the construction sequence of the bent. The top surface of the precast cap beam was roughened to provide a better bonding with the concrete in the upper cap beam. The columns were inserted in the footing pockets [Fig. 10(a)], while 38.1 mm (1.5 in.) spacers provided the vertical gap between the footing and the column. The columns were temporarily secured before high strength non-shrink grout was cast and cured in the gap between the columns and the footing [Fig. 10(b), Fig. 10(c)]. The precast cap beam was placed over the columns and the ducts were grouted [Fig. 10(d), Fig. 10(e)]. The entire bent was then moved over the central shake table [Fig. 10(f)]. Four 152×610 mm, 19 mm thick (6×24 in., 3/4 in. thick), 70A Durometer Neoprene Rubber Sheets were used on the precast cap beam and underneath girders.

Fig. 11 shows the construction sequence of the superstructure [Fig. 11(a)]. Four masonry plates were installed at the top of the abutment blocks with the top surface flushed with that of the blocks. They were then covered with Teflon plates. Girders and cross frames were fabricated by a local contractor. Stainless-steel plates, connected to the bottom of the girders through sole plates, were mirror finished to reduce the coefficient of friction with the abutment Teflon plates. Girders and cross frames were assembled using high strength A325X bolts tightened by turn-of-the-nut method with 1/3 turn [Fig. 11(b)]. A steel block [50×50×152 mm (2×2×6 in.)] was welded to the bottom end of each girder over the pier to transfer the reaction forces. Square pockets were left in the deck panels using wooden formworks, located at the location of each cluster of studs in the girders. PVC ducts were left at the specified locations of deck panels for passing the threaded rods that connect the superimposed masses to the superstructure [Fig. 11(c)]. The deck panels were placed over the girders at the specified locations while girders were simply supported on temporary supports [Fig. 11(d)]. The deck pockets were filled with grout [Fig. 11(e)]. The deck transverse joints were filled with UHPC [Fig. 11(f)]. Two concrete blocks were anchored to the two shake tables at each end of the bridge model to support the abutment seats. Upon curing of the UHPC in the deck joints, each complete

superstructure span was placed over temporary supports on a steel frame near the bent at one end and the abutment seats at the other end [Fig. 11(g)]. The spans were slowly lowered onto the cap beam, one girder at a time, with the girders alternating between the spans to avoid a large unbalanced moment in the columns of the pier. The first set of superimposed masses consisted of the lead pallets that were placed at the specified locations over the deck. Conventional concrete was cast in the upper cap beam up to the bottom of deck level after the reinforcement was put in place. UHPC was cast in the top layer [Fig. 11(h)]. After concrete and UHPC were cured, the second set of superimposed mass, which consisted of concrete blocks, was placed on top of the deck. The lead pallets and concrete blocks were then anchored to the panels. Stress checks were done for all the precast components to determine the size of the member and the configuration of the lifting points and to avoid cracking during erection and transportation.

3.8. Material Properties

Different materials were used in the construction of the bridge model: (1) steel (reinforcing steel bars, structural steel for the plate girders, studs, and cross frames, and high-strength threaded rods); (2) conventional concrete; (3) cementitious grout; (4) UHPC; and (5) Teflon sheets. Three different steel materials were used: ASTM A709 Grade 50 for the plate girders, ASTM A709 Grade 36 for the cross frames and stiffeners, and ASTM A108 for the shear studs. Welding electrode for the plate girders was E70XX. ASTM A706 Grade 60 #5 bars and ASTM A615 Grade 60 #3 bars were used as the reinforcing steel.

Table 1 summarizes the average test-day compressive strength data for the concrete, UHPC, and grout used in the bridge model. The compressive strength was determined by testing 150×300 mm (6×12 in.) cylinders for concrete and 75×150 mm (3×6 in.) cylinders for UHPC. UHPC mix design, and testing procedure to determine the compressive strength of the samples were conducted according to the Ductal product data sheet (Lafarge, 2009). Note that cylinder end preparation comprises two steps: saw cutting and grinding of the ends; however, the latter was not performed due to the limitations of the grinding machine. Because the ends were not ground the measured compressive strength were underestimated. Static and dynamic flow tests were also conducted based on the ASTM C 230 for the quality control of the UHPC mix.

A non-shrinkage, high-strength grout with commercial name of SEALTIGHT 1428 HP was used for grouting ducts of the lower cap beam, deck pockets, and the footing pockets for the column base hinges. The 1428 HP is a hydraulic-cement-based, precision grout that is typically used for grouting precast columns and segmental bridges. The compressive strength of the grout was determined by testing 50×50 mm (2×2 in.) cubes in accordance with the ASTM C109 standard.

3.9. Instrumentation

"To monitor the response of the bridge model, 280 channels of data were collected. In addition, 42 data acquisition channels recorded shake table data, such as displacement, velocity, acceleration, and hydraulic fluid pressure. Twenty-two displacement transducers and six tri-axial accelerometers were utilized to measure displacements and

accelerations of the bridge at the abutments, pier, and mid-spans in three directions. To measure strains in the column longitudinal bars and the spirals in the top plastic hinge regions, 28 strain gauges were installed at different heights in each column (Fig. 12 (a) and (b)). Strains in the two-way hinge regions were measured using 20 strain gauges at three levels of the longitudinal bars and two levels of the spirals. Twenty-four linear variable differential transformers (LVDT) displacement transducers were installed at six levels of each column to measure curvatures at the top and bottom of the columns as well as the relative displacement between the columns and the footing in the longitudinal and transverse directions (Fig. 13 (a) and (b)). Sixteen LVDTs were utilized to determine any relative displacements or rotations between the bent cap and the superstructure, and to measure relative displacements between the deck and the girders (Fig. 14 (a) and (b)). To determine if the cap beam and deck strains were indeed small and below the yield strain, 30 strain gauges were installed on the longitudinal and lateral reinforcement in several locations of the cap beam. Printed markers were attached on the bridge as targets, and digital image correlation (DIC) target-tracking method was utilized to obtain the displacement, velocity, and acceleration histories of each target on the structure."

3.10. Test Setup and Loading Protocol

Fig. 15 shows the test setup. Also shown in the figure are several steel frames that served as a safety system in case of the collapse of the model, as well as the lead pallets and concrete blocks that served as the superimposed mass. Two horizontal components of the 1994 Northridge earthquake acceleration history recorded at the Sylmar station, RSN1084_SCS052 and RSN1084 _SCS142, were simulated in the test using the central shake table. The former was applied in the transverse direction, and the latter in the longitudinal direction. The target shake table motions were the same as those used in shake table testing of the two similar two-span ABC bridge models (Calt Bridge-1, Calt-Bridge-2) with prestressed concrete girders, with the former tested prior and the latter tested after the current bridge model ["Bridge System Seismic Research", 2018]. Using the same ground motions facilitated future comparison of the seismic response of two common bridge types. The tables supporting the abutments were stationary as the bridge did not include a shear key or an abutment backwall. To account for the similitude requirements, the time axis of the acceleration record was compressed by a factor of 0.592, which corresponds to the square root of the dimensional scale length factor. Fig. 16 shows the time-scaled acceleration, velocity, and displacement histories of the input motions with unscaled amplitudes. The amplitude of the design earthquake was determined so that the peak resultant displacements obtained from the nonlinear dynamic analysis and that obtained from the orthogonal combination of the design displacement demands were approximately the same. As a result, the acceleration records for each component were further scaled by a factor of 0.6 to build the target design earthquake (TDE). The response spectra for the two components of the TDE and their square root of sum of the squares (SRSS) resultant under 5% damping is shown in Fig. 17.

The loading protocol was determined such that the maximum displacement in each run helps construct the pushover curve from pre-yield state to failure based on the envelope of the hysteresis force-displacement curve in each direction. Accordingly, the loading protocol started with 0.3×TDE to capture the elastic response and followed by 0.65×TDE

and 1.0×TDE, continued to 2.25× TDE with 0.25×TDE increments to capture different damage states. The corresponding acceleration scale factors were 0.18, 0.39, 0.6, 0.75, 0.9, 1.05, 1.2, and 1.35. The earthquake amplitudes were not increased beyond 2.25xDE because extensive damage in the concrete core in the column top plastic hinges had occurred and the longitudinal bars had buckled. Before applying each earthquake run and after the last run, the bridge was subjected to random white noise motions in the longitudinal and transverse directions to determine the natural frequencies and damping ratios as the extent of damage in the bridge increased. The target biaxial shake table motions are presented in Table 2.

3.11. Observed Damage

Before starting the test and after each run, the bridge model was monitored for any apparent damage. Cracks were marked and labeled according to the run number, and the crack widths were measured. Table 3 shows the maximum crack widths in the columns in different runs in the top and bottom of the columns. Note that the residual crack widths were measured after each run and are not a measure of the maximum crack widths during the earthquake runs. It should also be noted that after Run 4, concrete spalled and monitoring the width of the remaining cracks was not continued.

3.11.1. Column plastic hinges

Fig. 18 and 19 show the progression of damage in the top moment connections for the north and south columns, respectively. Damage in both columns started with hairline flexural cracks in the first Run. During Run 2, flexural cracking increased in both columns, and thin inclined shear cracks with a maximum width of 0.13 mm (0.01 in.) began to form. Also, spalling of the cover concrete on the northwest side of the south column began in Run 2 and propagated in Runs 3 and 4. Spalling of the cover concrete in the north column started in Run 3 and in the southeast face and extended in the next two runs (Run 4 and 5). The spirals of the south column were visible after Run 5. The spirals and longitudinal bars of the north column were partially exposed after Run 6. At the end of Run 7, damage began to penetrate into the core concrete in the north column. During the last run, longitudinal bars of the north column buckled, and the core damage turned into a large loss of core concrete immediately under the cap beam. Minor in-plane rotations were observed in Run 4 and the subsequent runs. It is believed that in-plane rotations were because of unsymmetrical damages in the columns.

3.11.2. Column-cap beam connection

The column bars were anchored in the corrugated ducts filled with high-strength grout over 191 mm (7.5 in.), which was the depth of the precast portion of the cap beam (Fig. 4). The remaining part of the bars [483 mm (19 in.)] was anchored in the CIP portion of the cap beam with the total embedment length, bar diameter ratio of 30. This might be considered as a hybrid ABC-CIP connection. No studies of this type of connections subjected to biaxial seismic loading had been conducted in the past. Potential failure in this type of connection is pull out of column longitudinal bars or damage to the cap beam in the joint zone. No sign of the duct pullout or bar pullout was apparent, which indicates that embedment length of the column longitudinal bars was sufficient, and the bar force transfer mechanism was appropriate. Minor spalling of the grout in the ducts at the

column-cap beam interface was noticed. This allowed for the spread of yielding in the column longitudinal bars. Examination of the joint zone in the cap beam indicated no spalling or diagonal cracks despite the fact that the connection was subjected to biaxial loading (Fig. 20).

3.11.3. Rebar hinge pocket connections

Fig. 21 shows the damage state of rebar hinge pocket connections after Run 8. No sign of flexural or shear cracks were detected on the face of the columns near the hinge, except for the initial shrinkage cracks. Damage was limited to the spalling of the cover concrete in the hinge throat and did not penetrate into the surrounding grout in pockets nor the footing. Spalling of the concrete in the hinge throat began during small-amplitude earthquake runs. At the end of Run 8, the transverse reinforcement in the hinge throat was partially visible in both hinges. Moreover, yielding of the rebar hinge longitudinal bars was spread adequately without debonding the bars at the column-footing interface, and none of the bars fractured even after core failure at the column top plastic hinges. The hinge gap was not closed during the tests, which indicated that the 38.1-mm (1.5-in.) was sufficient to allow for the column rotation even under very strong earthquakes. No slippage of the rebar hinge relative to the footing was observed throughout testing.

3.11.4. Cap beam

Fig. 22 shows the cap beam after Run 8. Except for the hairline flexural and shear cracks developed in the precast portion of the cap beam during construction (Run 0), no other damage was detected on the cap beam faces during the testing. Fig. 23 shows the condition of the cap beam-girder connection after the last Run. Few hairline cracks were noticed on the west side of the cast-in-place portion of the cap beam between the two northern girders, but these cracks had been formed during small-amplitude motions and did not propagate or widen in the subsequent runs.

3.11.5. Superstructure joints

Of the six connection types that were integrated in the bridge model, three were in the superstructure: grouted pocket connections between the girders and the deck panels, joints between the deck panels, and the deck panel connection above the CIP portion of the cap beam, with the latter two utilizing UHPC. Fig. 24 shows the damage state in all the three connections after Run 8. No crack was visible in the grouted pocket connections except for the initial shrinkage cracks. Furthermore, no crack was noticed in UHPC/concrete interface of the panel joints which indicates sufficient bond between the two materials. Deck panel connection above the CIP portion of the cap beam remained capacity protected as damage was limited to a few hairline cracks in the bottom of two deck panels adjacent to the pier. No damage was noted in the deck panels except for the hairline cracks in the bottom, adjacent to the UHPC joint over the pier. These cracks can be observed in Fig. 23.

3.12. Comparison of Damage with Conventional Bridges

Vosooghi and Saiidi (2012) developed fragility curves based on the shake table or cyclic load test data from 32 standard CIP bridge columns for six response parameters (RS) at

five repairable damage states (DS). No similar studies have been conducted for ABC columns. To explore the applicability of the CIP fragility curves to the precast columns in the two-span bridge test model, the probability of damage for these columns was determined using the CIP fragility curves. Table 4 lists the damage states and the associated extent of the apparent damages. The maximum drift ratio (MDR) is the key indicator of the probability of column damage being at a given DS. The resultant displacement and drift histories of the pier for select earthquake runs are shown in Fig. 25. Table 5 shows the maximum resultant drift ratio and the observed column DS for each run. The probability of occurrence (PO) for each damage state were obtained using the developed fragility curves and are shown in the last column of Table 5. For instance, minor spalling observed in both columns after Run 3 indicates that columns were in DS-2. The maximum resultant drift ratio for Run 3 (TDE) was 3.6%. Using MDR fragility curves, there is a 99% chance that the columns have passed DS-1, and there are 85% and 30% probability that columns are in DS-2 and DS-3, respectively. DS-2 is the first DS in Run 3, for which the PO is greater than 50%. Similarly, the drift ratio of 6.0% in Run 5 corresponds to the 90%, 48%, 23%, and 8% probability of occurrence for DS-3, DS-4, DS-5, and failure, respectively. Visibility of the column spirals in Run 5 means that columns are in DS-4, which is again in a good agreement with the data obtained from the fragility curves. Comparison of the observed damage states for the columns in the bridge model with damage states estimated from the fragility curves shows that the apparent damage in the ABC columns was similar to that of the CIP bridge columns for most of the runs.

3.13. Summery and Conclusions

This paper presented the design, construction, and testing of a 0.35 scale, two-span steel girder bridge model incorporating precast elements and six connection types (referred to as ABC connections) intended for accelerated bridge construction (ABC). The model was tested to failure on shake tables at the University of Nevada, Reno. The objectives of the study were (1) to determine the adequacy of some of the emerging design methods for critical ABC connections, (2) to evaluate feasibility of the construction methods and identify construction issues as various prefabricated components are handled and connected, and (3) to determine the seismic performance of the integrated bridge model under various levels of bidirectional earthquakes including motions that simulated 225% of the design earthquake. The present paper addresses the first two objectives and the apparent damage observed in the shake table tests. Detailed measured and analytical results are described elsewhere. The following are the main findings from this study.

1. Design procedures for the ABC connections ensured that the performance of the ABC bridge system was emulative of conventional bridges, as the model underwent large deformations in a ductile manner by forming plastic hinges at predefined locations. The structural integrity was maintained even during extreme seismic loading.
2. Damage states of the columns in most earthquake runs was similar to that in cast-in-place bridge columns.
3. Visible damage in the cap beam, superstructure, and all ABC connections incorporated in the superstructure was limited to a few hairline cracks in the

cap beam and on the bottom side of the deck panels adjacent to the pier; which is acceptable in capacity protected design.

4. Minor spalling of the grout in the column-cap beam interface allowed the spread of yielding in the column longitudinal bars. Moreover, yielding of the rebar hinge longitudinal bars was spread adequately without the need to debond the bars at the column-footing interface, and none of the hinge longitudinal bars fractured even after confined concrete core failure in the top column plastic hinges.
5. The embedment length of the rebar hinge section in the footing (1.25 times the required tension development length of the column longitudinal bars) was sufficient to develop the hinge plastic moment. No slippage of rebar hinge connection relative to the footing was observed.
6. Although the bridge had no skew, minor in-plane rotations were observed during the design run. The in-plane rotation increased in subsequent runs, which is believed to be due to unequal damage in the columns.

3.14. Acknowledgement

The study presented in this article was supported by the Accelerated Bridge Construction University Transportation Center (ABC-UTC) at the Florida International University (FIU). This study would not have been possible without the assistance and advice of the UNR Earthquake Engineering Laboratory staff Dr. Patrick Laplace, Chad Lyttle, Todd Lyttle, and Mark Lattin. The support and advice of ABC-UTC director, Dr. Atorod Azizinamini, is greatly appreciated. Thanks are due to Mojtaba Alian, Jose Benjumea Royero, Jared Jones, Amir Sadeghnezhad, Dr. Alireza Mohebbi, and Dr. Ali Mehrsoroush. The authors would like to thank Lafarge North America Inc. for donating UHPC material, C&K Johnson Industries for donating corrugated metal ducts, Reno Iron Works for fabrication of steel girders at a reduced cost, and NSBA for donating steel material for the girders, cross frames, and other accessories.

3.15. References

American Association of State Highway and Transportation Officials (AASHTO). (2014). “Guide Specifications for LRFD Seismic Bridge Design”, Washington, D.C.

American Association of State Highway and Transportation Officials (AASHTO), (2012). AASHTO LRFD Bridge Design Specifications, 6th edition.

ASTM A653/A653M-11. “Standard specification for steel sheet, zinc-coated (galvanized) or zinc-iron alloy-coated (galvannealed) by the hot-dip process”, West Conshohocken, PA; (2011). 14pp

Badie, S. S, and Tadros, M. K, (2008). “Full-Depth Precast Concrete Bridge Deck Panel Systems”, Report 584 by National Cooperative Highway Research Program.

Bridge System Seismic Research for Accelerated Bridge Construction (ABC), https://wolfweb.unr.edu/homepage/saiidi/caltrans/abc-systems.html, 2018, [accessed 10 October 2018]

Caltrans. Seismic Design Criteria (SDC). (2013). version 1.7. California Department of Transportation, Sacramento, CA

Caltrans, Splices in bar reinforcing steel, Memo to Designers 20-9 (2016), Caltrans, California Department of Transportation, Sacramento, CA

Chadwell, C. B., & Imbsen, R. A. (2002). XTRACT-cross section analysis software for structural and earthquake engineering. *TRC, Rancho Cordova, CA,⟨http://www. imbsen. com/xtract. htm⟩(Aug. 30, 2011)*.

Graybeal, B. (2010). "Behavior of Field-Cast Ultra-High Performance Concrete Bridge Deck Connections under Cyclic and Static Structural Loading," Federal Highway Administration, Report No. FHWA-HRT-11-023.

Graybeal, B., (2014a), "Design and Construction of Field-Cast UHPC Connections", Federal Highway Administration Publication No. FHWA-HRT-14-084. Pp. 1-36.

Graybeal, B., (2014b), "Bond Behavior of Reinforcing Steel in Ultra-High Performance Concrete", Federal Highway Administration. Publication No. FHWA-HRT-14-090.

Lafarge, Product Data Sheet: Ductal® JS1000, www.imagineductal.com, (2009).

Marsh, M. L., Stanton, J. F., Eberhard, M. O., Haraldsson, O., & Khaleghi, B. (2010). A precast bridge bent system for seismic regions.

Matsumoto, E. E., M. C. Waggoner, G. Sumen, and M. E. Kreger, (2001). "Development of a precast bent cap system". FHWA Rep. No. FHWA/ TX-0-1748-2. Austin, TX: Center for Transportation Research, Univ. of Texas.

McKenna, F., Fenves, G., and Scott, M., (2000). "Open System for Earthquake Engineering Simulation (OpenSees)", Berkeley, California: Pacific Earthquake Engineering Research Center.

Mehraein, M., and M. S. Saiidi. (2016). "Seismic performance of bridge column-pile-shaft pin connections for application in accelerated bridge construction". Rep. No. CCEER-16-01. Reno, NV: Univ. of Nevada.

Mehrsoroush, A., and Saiidi, M. (2014). "Experimental and analytical seismic studies of bridge piers with innovative pipe pin column-footing connections and precast cap beams." Rep. No. CCEER-14-07, Center for Civil Engineering Earthquake Research, Dept. of Civil and Environmental Engineering, Univ. of Nevada, Reno, NV.

Mehrsoroush, A., and M. S. Saiidi. (2016). "Cyclic response of precast bridge piers with novel column-base pipe pins and pocket cap beam connections". J. Bridge Eng. 04015080.

Mohebbi, A., M. Saiidi, and A. Itani. (2017). "Development and seismic evaluation of pier systems w/pocket connections, CFRP Tendons, and ECC/ UHPC columns". Rep. No. CCEER-17-02. Reno, NV: Dept. of Civil and Environmental Engineering, Univ. of Nevada.

Mortensen, J., and M. Saiidi, "A Performance-Based Design Method for Confinement in Circular Columns," Civil Engineering Department, University of Nevada, Reno, Report No. CCEER 02-07, November 2002.

Motaref, S., M. Saiidi, and D. Sanders, (2011). “Seismic response of precast bridge columns with energy dissipating joints”. Rep. No. CCEER-11-01. Reno, NV: Dept. of Civil and Environmental Engineering, Univ. of Nevada.

PCI Design Handbook, (2004), Precast and Prestressed Concrete, 6th edition, MNL 120-04

Restrepo, J. I., M. J. Tobolski, and E. E. Matsumoto, (2011). “Development of a precast bent cap system for seismic regions.” NCHRP Rep. 681. Washington, DC: National Cooperative Highway Research Program.

Sadeghnejad, A., Azizinamini, A., (2017), “Extending the Application of Simple for Dead and Continuous for Live Load Steel Bridge System to ABC Applications in Seismic Regions. Phase II-Experimental” Web-based quarterly Research Seminar, ABC-UTC research center, Florida International University.

Saiidi, M. S., Cheng, Z. Y., & Sanders, D. (2009). “Experimental Study of Two-Way Reinforced Concrete Column Hinges under Seismic Loads”. ACI Structural Journal, 106(3), 340.

Shrestha, G., Itani, A., and Saiidi, M. (2017) “Seismic Performance of Precast Full-Depth Decks in Accelerated Bridge Construction” Center for Civil Engineering Earthquake Research, Department of Civil and Environmental Engineering, University of Nevada, Reno, Report No. CCEER-17-05.

Taghinezhadbilondy, R., Yakel, A., and Azizinamini, A., (2016), “Extending Use of Simple for Dead Load and Continuous for Live Load (SDCL) Steel Bridge System to Seismic Areas”. Dept. of Civil and Environmental Engineering, Florida International University, Miami, FL.

Tazarv, M., and Saiidi, M. S., (2014). “Next generation of bridge columns for accelerated bridge construction in high seismic zones”. Rep. No. CCEER-14-06. Reno, NV: Dept. of Civil and Environmental Engineering, Univ. of Nevada.

Vosooghi, A., and Saiidi, M. S., (2012). “Experimental fragility curves for seismic response of reinforced concrete bridge columns.” ACI Struct. J. 109 (6), 825–834.

Table 3.1 Measured compressive strength of conventional concrete, grout, and UHPC

Material	Element	Test-day compressive strength, MPa (ksi)
Conventional concrete	Precast bent	64.0 (9.3)
	CIP cap beam	52.6 (7.6)
	Deck - east span	58.9 (8.6)
	Deck - west span	43.5 (6.3)
Grout	Deck pocket - east Span	80.8 (11.7)
	Deck pocket - west Span	75.3 (10.9)
	Column-to-footing	64.8 (9.4)
	Column-to-cap beam	85.2 (12.3)
UHPC	Deck joints	126.3 (18.3)
	Deck joint over the pier	151.1 (21.9)

Table 3.2 Target testing protocol

Run #	Factor	PGA (g, long.)	PGA (g, trans.)	%DE
1	0.18	0.17	0.11	30%
2	0.39	0.36	0.24	65%
3	0.60	0.56	0.37	100%
4	0.75	0.70	0.47	125%
5	0.90	0.83	0.56	150%
6	1.05	0.97	0.66	175%
7	1.20	1.11	0.75	200%
8	1.35	1.23	0.83	225%

Table 3.3 Crack width

Run #	Crack width							
	North column				South column			
	Top		Bottom		Top		Bottom	
	in.	mm	in.	mm	in.	mm	in.	mm
1	0.003	0.076	0.002	0.051	0.003	0.076	0.000	0.000
2	0.025	0.635	0.002	0.051	0.016	0.406	0.000	0.000
3	0.040	1.016	0.002	0.051	0.030	0.762	0.002	0.051
4	0.045	1.143	0.002	0.051	0.040	1.016	0.002	0.051
5	Major spalling		0.002	0.051	Major spalling		0.002	0.051
6	Major spalling		0.002	0.051	Major spalling		0.002	0.051
7	Major spalling		0.002	0.051	Major spalling		0.002	0.051
8	Major spalling		0.002	0.051	Major spalling		0.002	0.051

Table 3.4 Apparent damage associated for each damage state

DS No.	Apparent damage
DS-1	Flexural cracks
DS-2	Minor spalling and possible shear cracks
DS-3	Extensive cracks and spalling
DS-4	Visible lateral and/or longitudinal reinforcing bar
DS-5	Compressive failure of the concrete core edge (imminent failure)

Table 3.5 Probability of occurrence for each damage state for all runs

Run No.	% TDE	MDR (resultant)	Observed DS	PO for each DS			
1	30%	1.0%	DS-1	10%DS-1[1]			
2	65%	2.4%	DS-2	**85%DS-1[2]**	4%DS-2		
3	100%	3.6%	DS-2	98%DS-1	**85%DS-2**	30%DS-3	
4	125%	5.1%	DS-3	99%DS-2	**80%DS-3**	32%DS-4	14%DS-5
5	150%	6.0%	DS-4	90%DS-3	**48%DS-4**	23%DS-5	8%Failure
6	175%	6.2%	DS-4	95%DS-3	**55%DS-4**	30%DS-5	12%Failure
7	200%	6.0%	DS-5	90%DS-3	**50%DS-4**	25%DS-5	10%Failure
8	225%	6.9%	Failure	**65%DS-4**	40%DS-5	20%Failure	

[1] PO for the damage states that are not shown are either 0% or 100%.

[2] Bold DS for each run shows the first DS in that run for which the probability of occurrence is more than 50% (For run 5, it is less than, but very close to 50%).

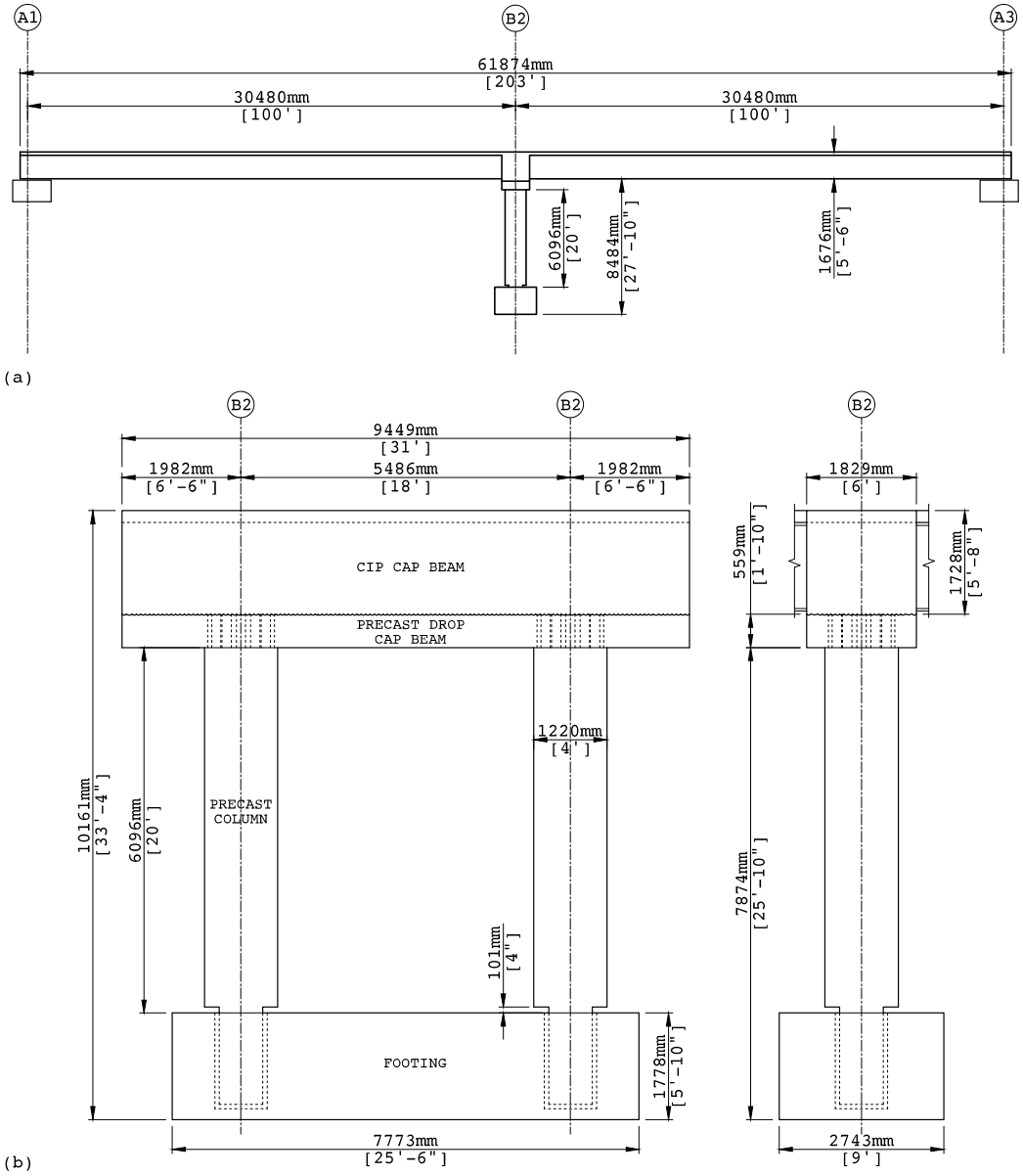

Figure 3.1 Configuration of the prototype bridge, (a) general details, (b) bent details

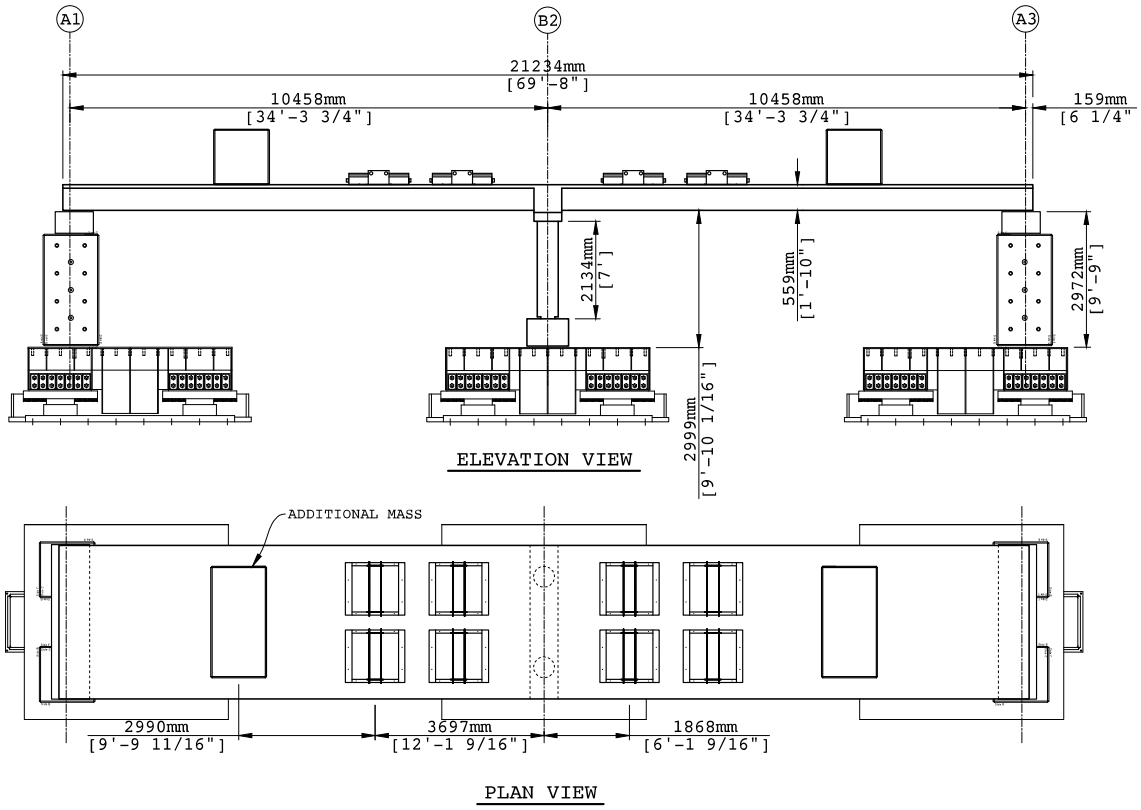

Figure 3.2 Geometric details of the bridge model

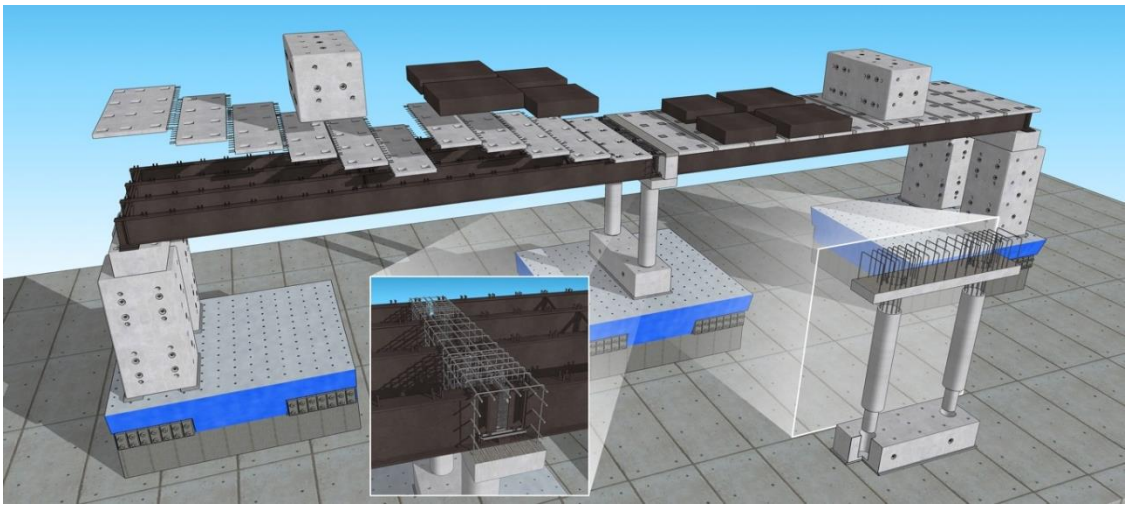

Figure 3.3 3D rendering of the bridge model

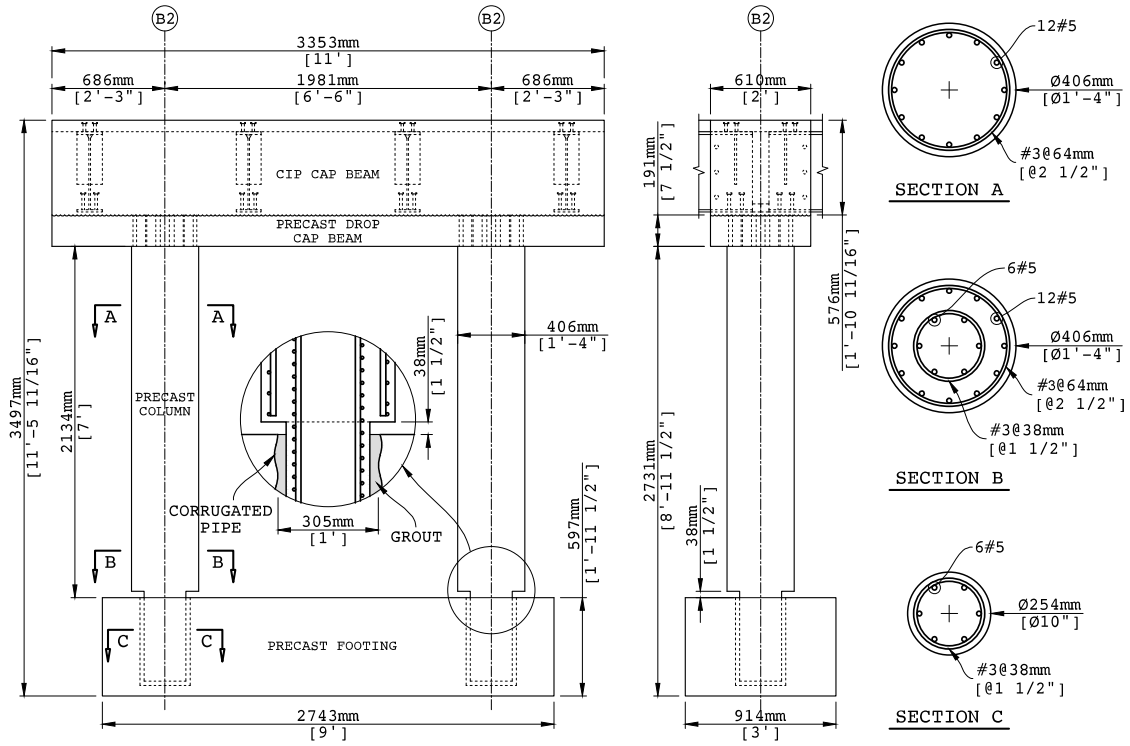

Figure 3.4 Two-column bent details

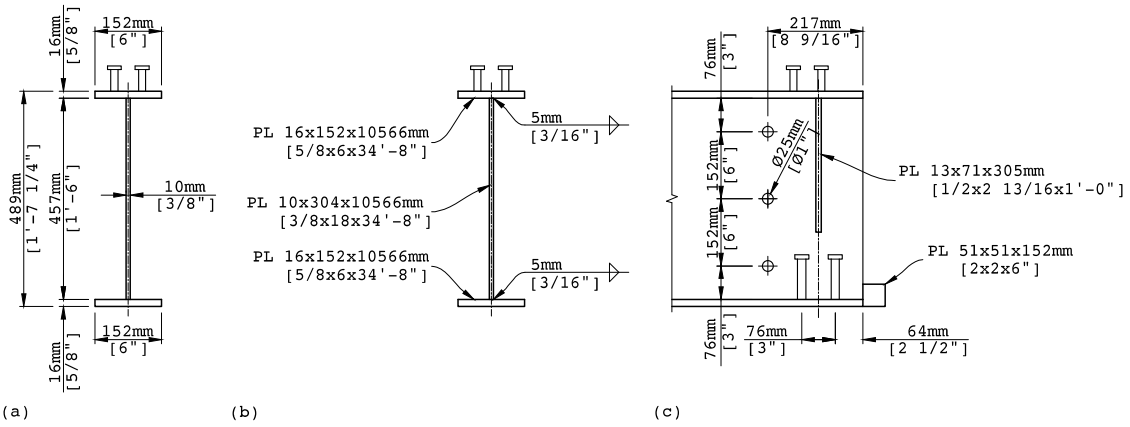

Figure 3.5 Details of the girder: (a) girder cross section dimensions, (b) girder details, (c) girder details over the pier

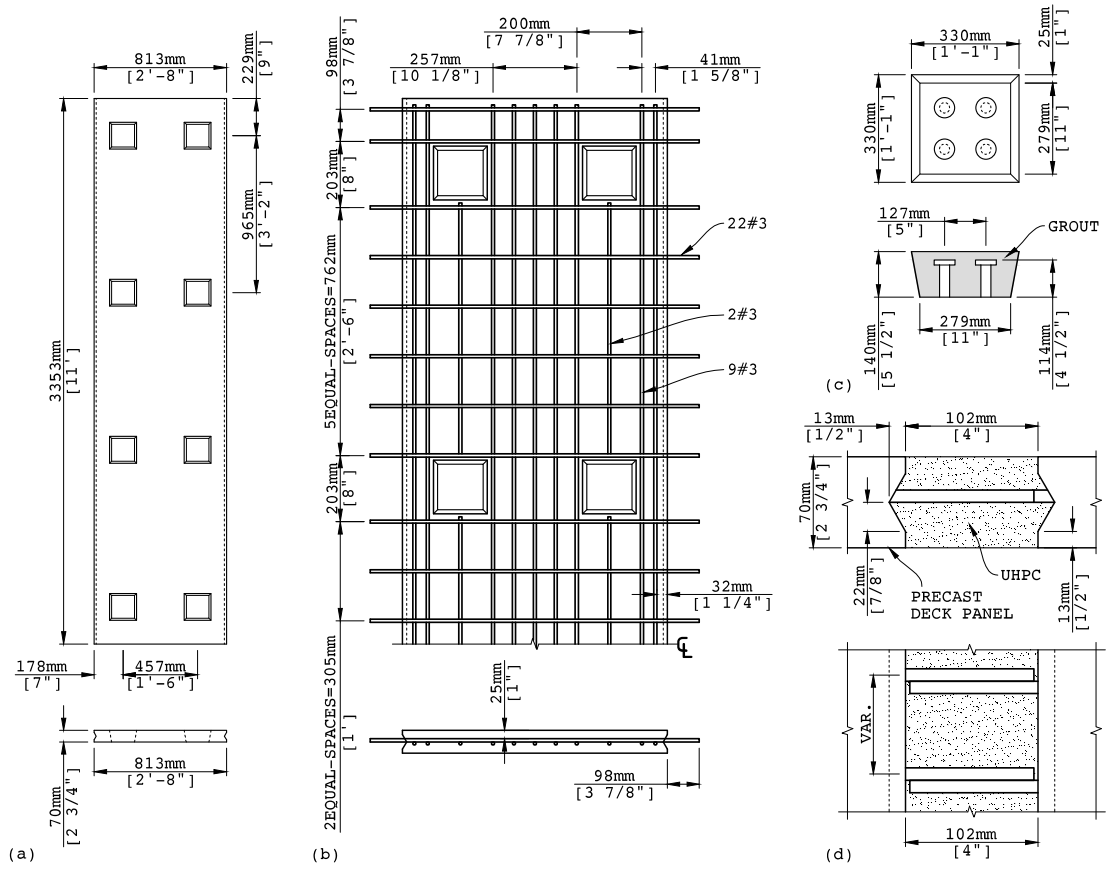

Figure 3.6 Details of a typical deck panel: (a) general dimensions, (b) details of reinforcement, (c) deck pocket details, (d) details of deck panel joints

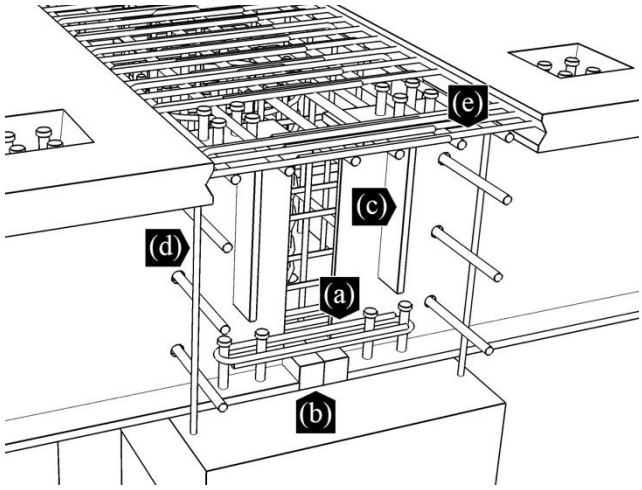

Figure 3.7 Details of the SDCL connection: (a) tie bar, (b) steel block, (c) stiffener, (d) cap beam stirrups (dowel bars), (e) deck longitudinal bars

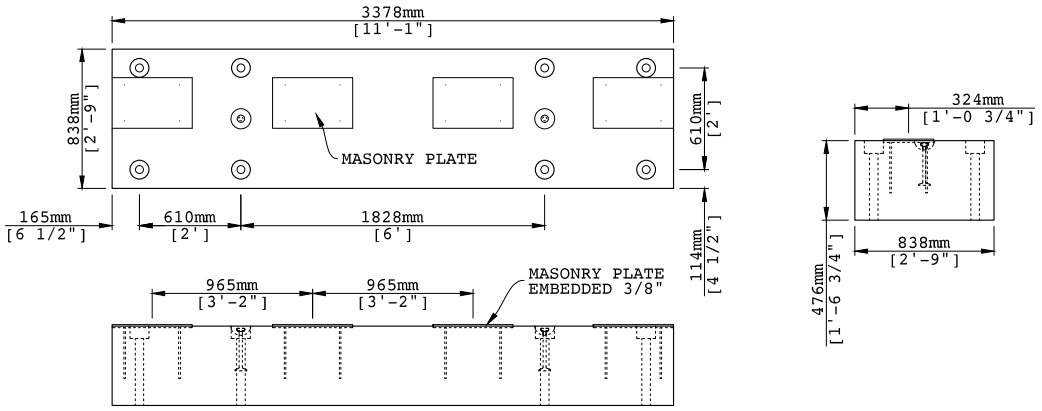

Figure 3.8 Details of the abutment seat

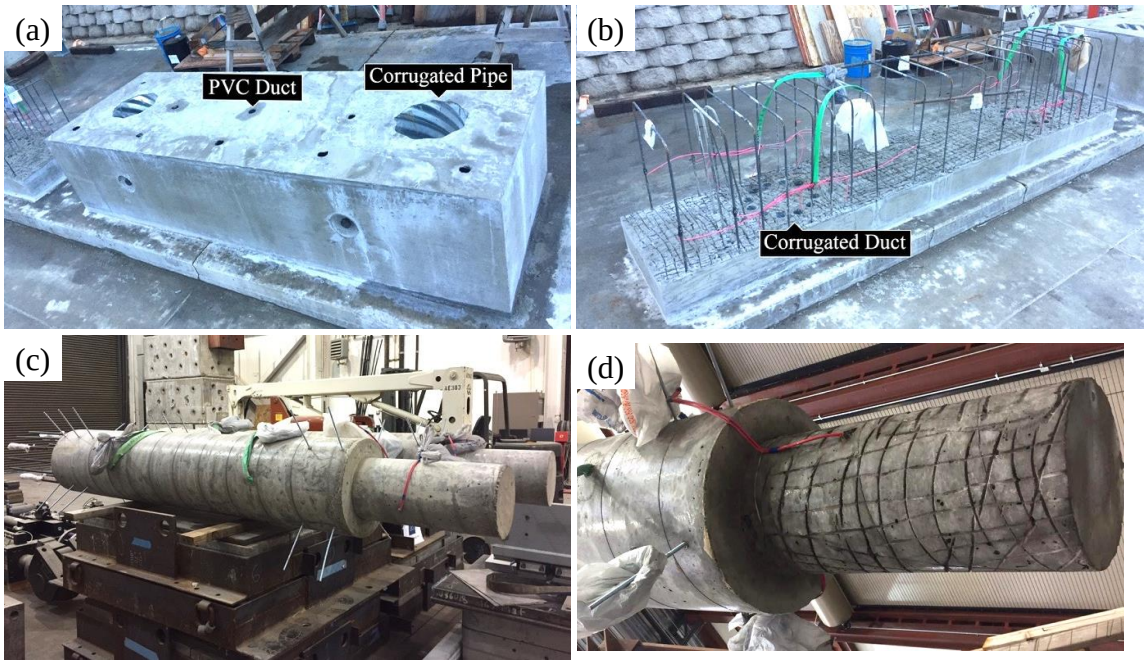

Figure 3.9 Prefabricated elements of the bent (a) Precast footing with two circular pockets, (b) Precast cap beam with corrugated ducts, (c) Column, (d) Roughened surface of rebar hinge (Images by Elmira Shoushtari)

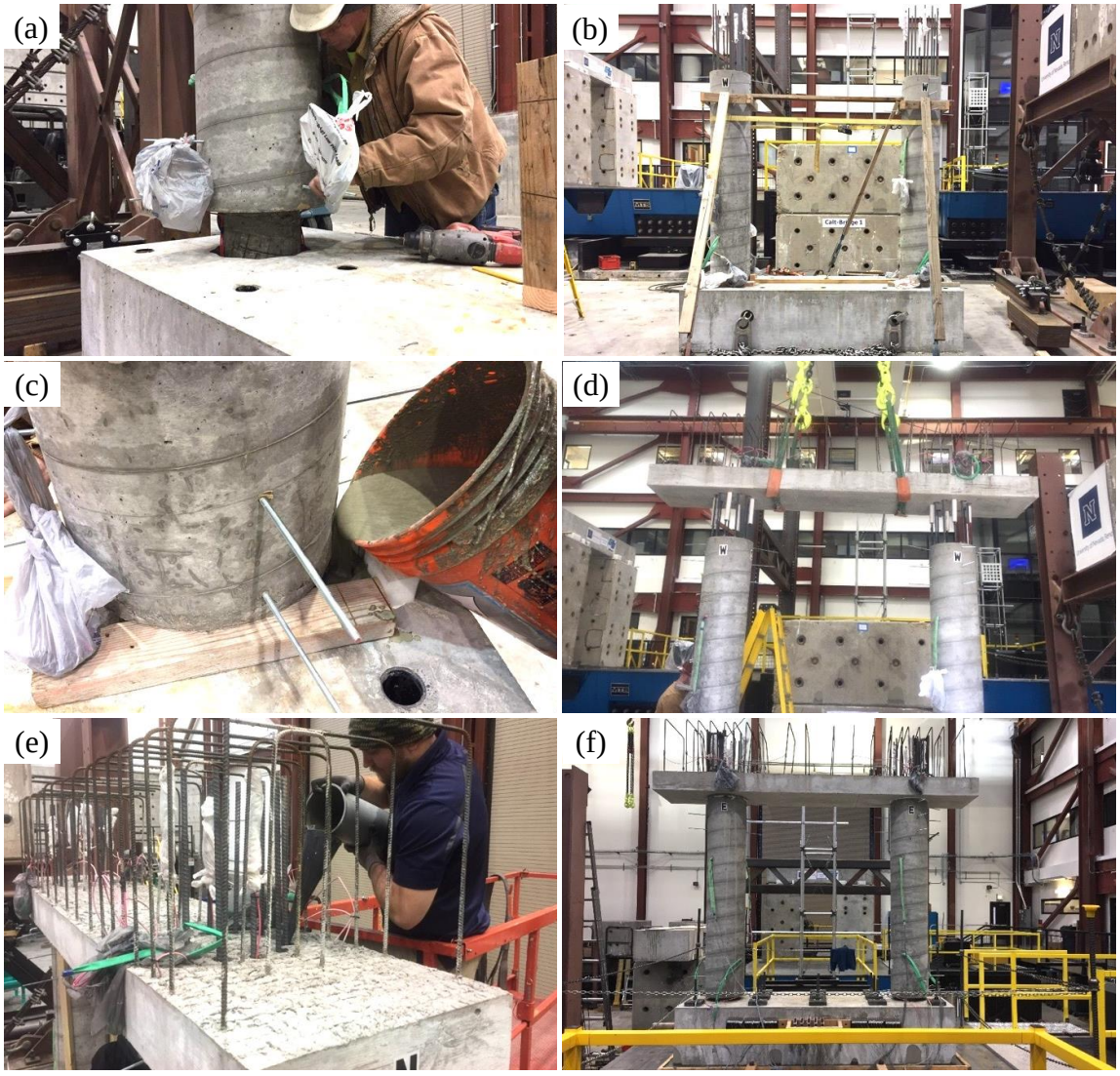

Figure 3.10 (a) Inserting column into the footing, (b) Securing columns temporarily, (c) Grouting the spacing between the column and the footing, (d) placing precast cap beam on the columns, (e) Grouting cap beam ducts, (f) Precast bent on the shake table (Images by Elmira Shoushtari)

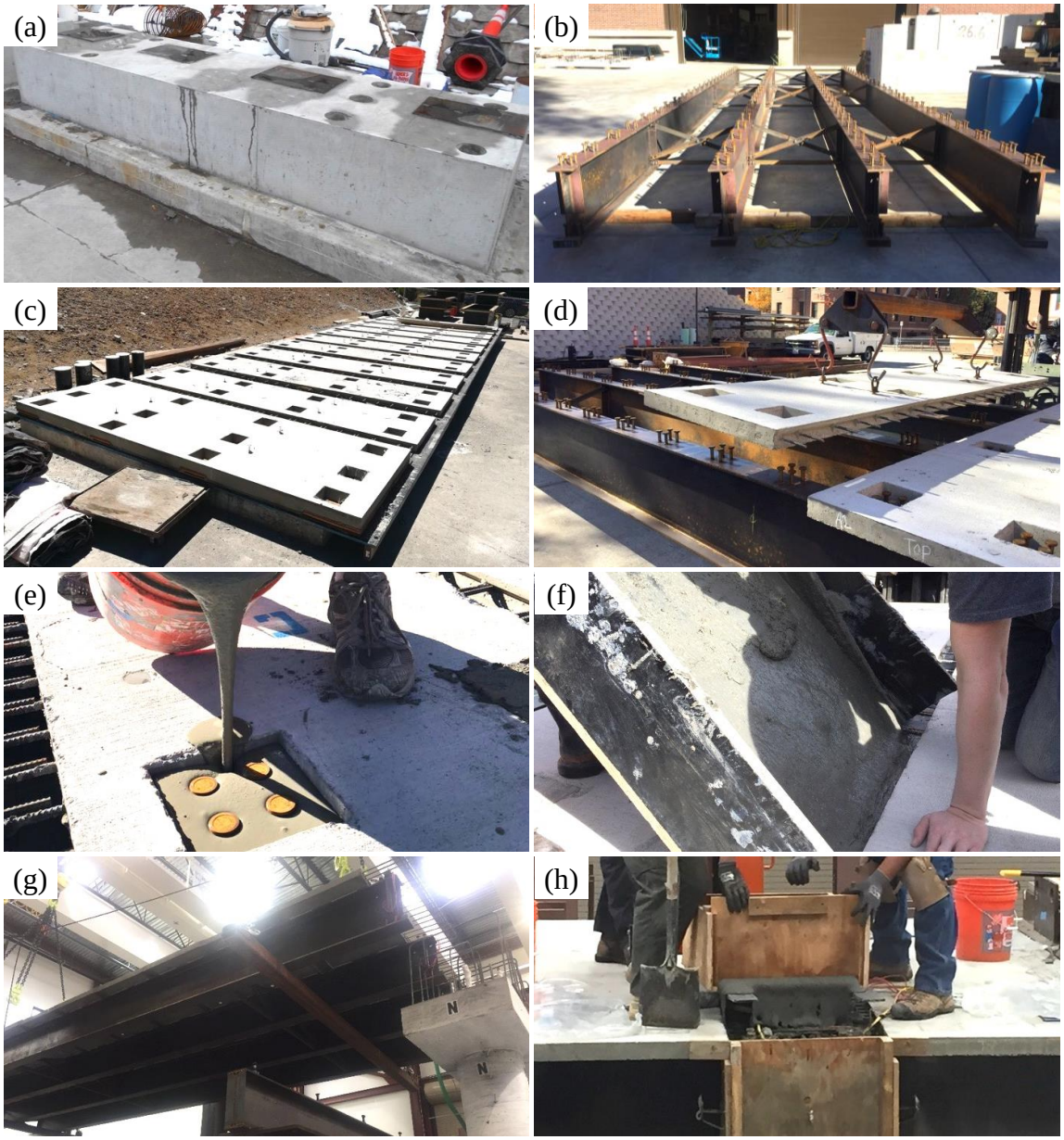

Figure 3.11 (a) Abutment seat, (b) Steel girders, (c) Deck panels, (d) Placement of deck panels over the girders, (e) Grouting deck pockets, (f) Casting UHPC in the joints, (g) Placement of east span over the abutment seat and precast cap beam, (h) Casting UHPC in the top layer of cap beam (Images by Elmira Shoushtari)

Figure 3.12 Test setup (Image by Elmira Shoushtari)

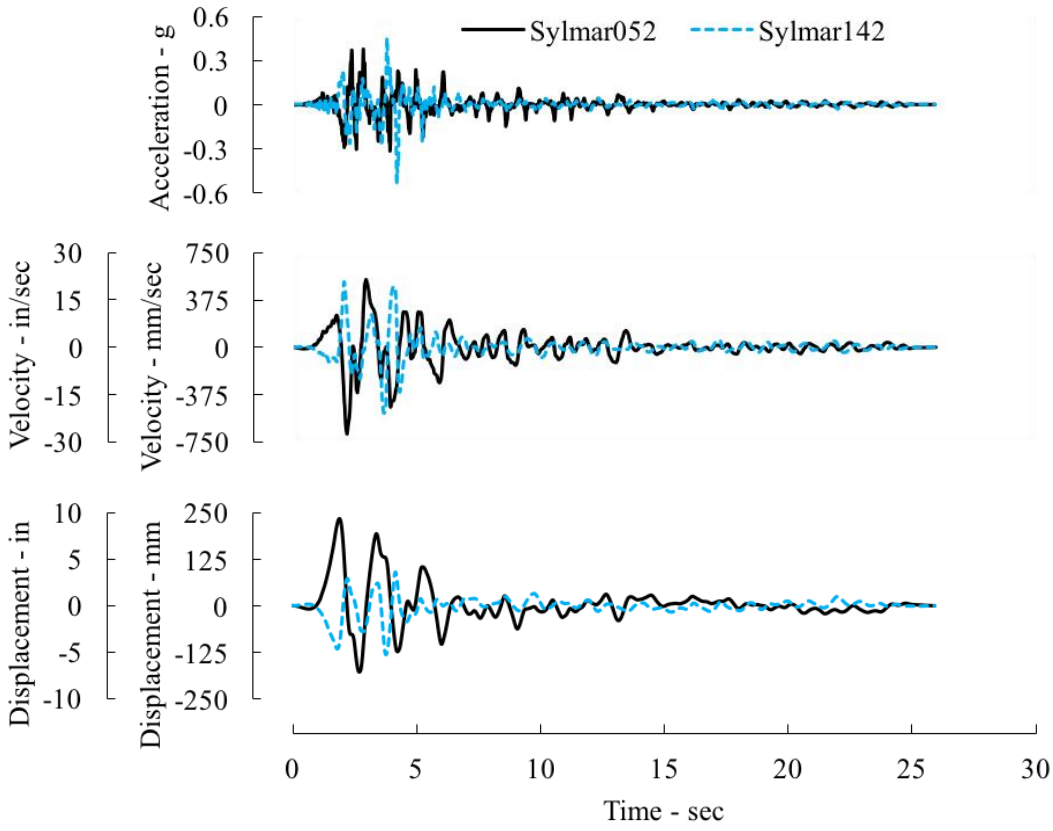

Figure 3.13 Time-scaled acceleration histories of the input motions with unscaled amplitudes

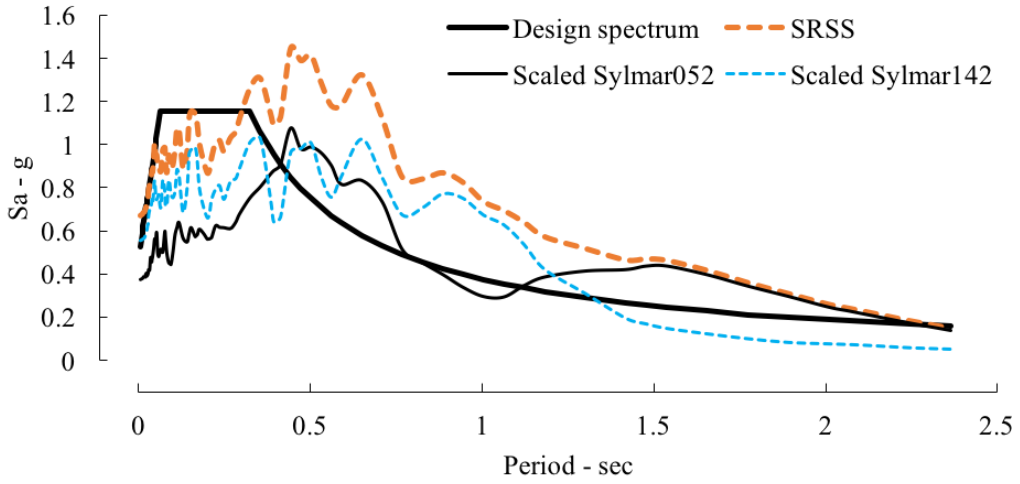

Figure 3.14 Design response spectrum and scaled response spectrum of the ground motion components and their SRSS resultant.

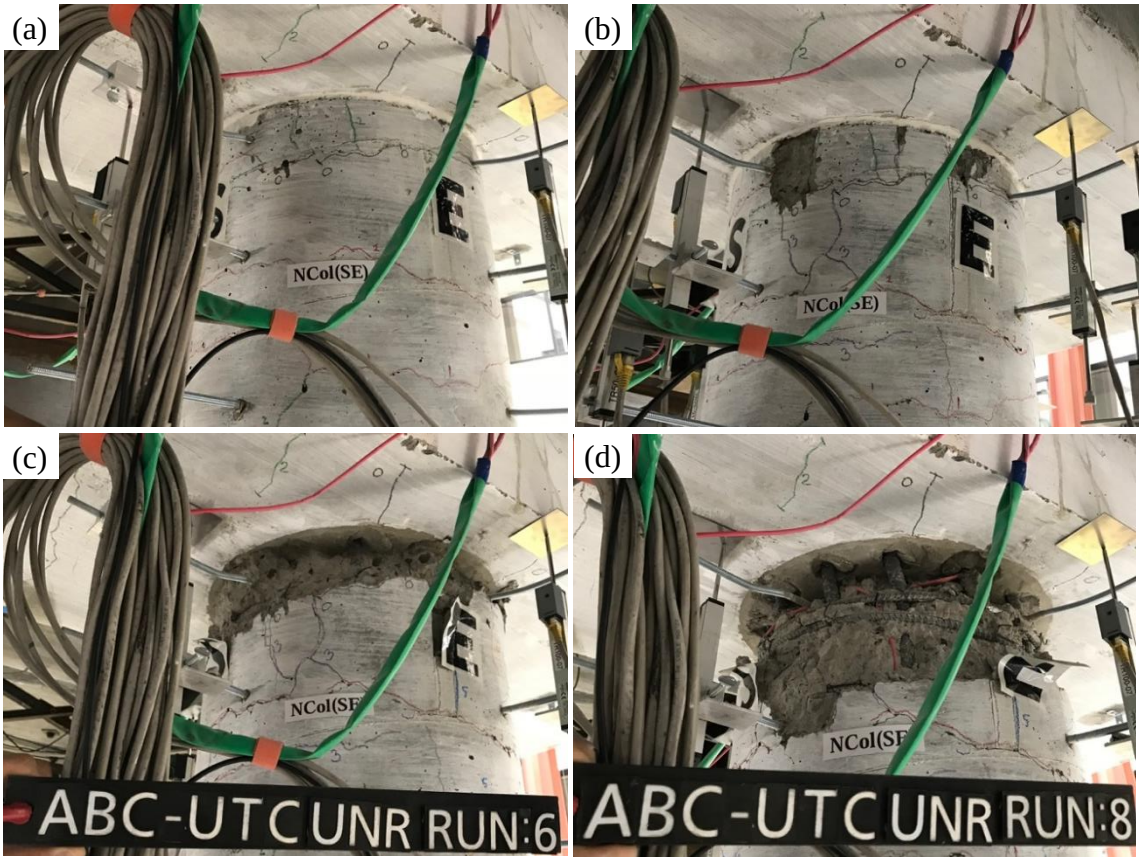

Figure 3.15 Damage progression in the north column, southeast side: (a) Run 2, (b) Run 4, (c) Run 6, (d) Run 8 (Images by Elmira Shoushtari)

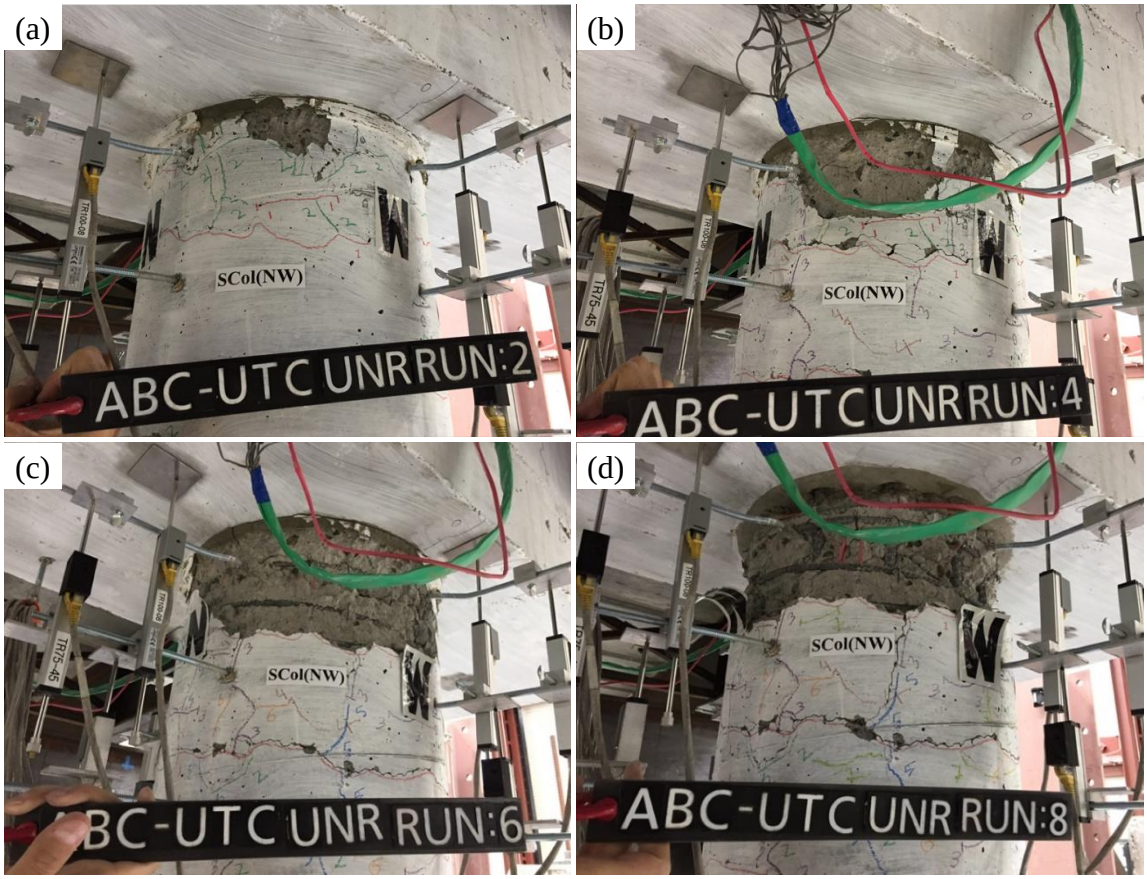

Figure 3.16 Fig. 16 Damage progression in the south column, northwest side: (a) Run 2, (b) Run 4, (c) Run 6, (d) Run 8 (Images by Elmira Shoushtari)

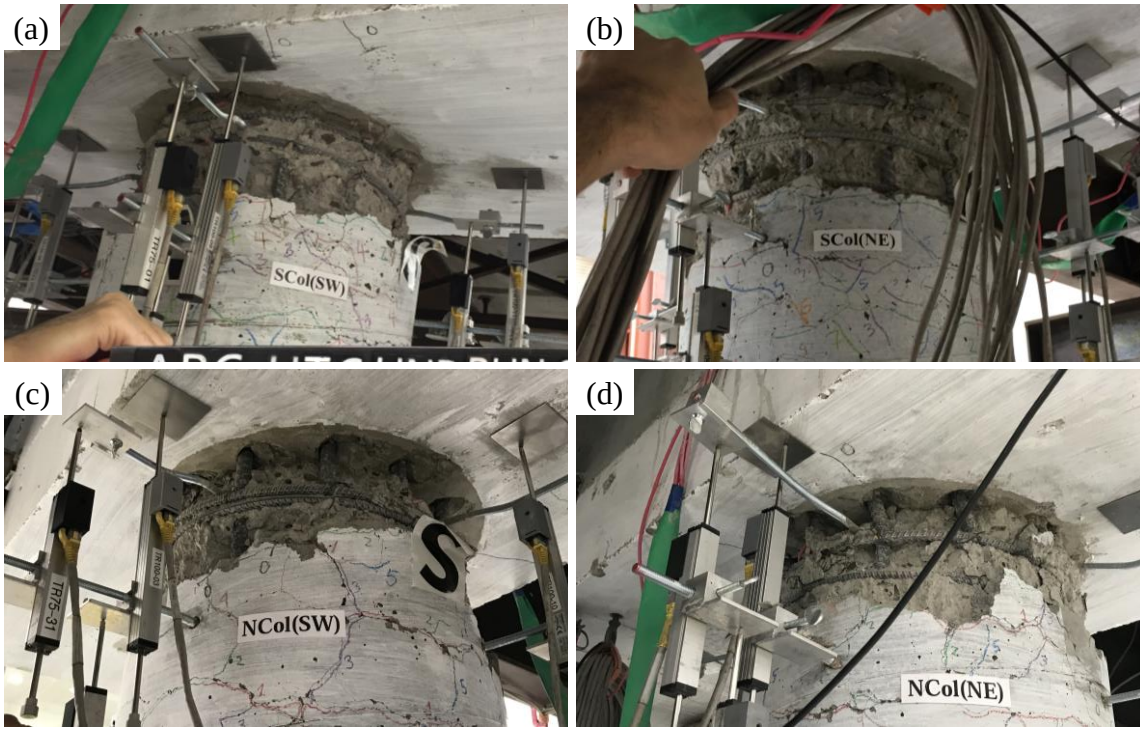

Figure 3.17 Damage states of the column-cap beam connection after Run 8: (a) North column - Southwest view, (b) North column - Northeast view, (c) South column - Southwest view, (d) South column - Northeast view (Images by Elmira Shoushtari)

Figure 3.18 Damage states of the rebar hinge after Run 8: (a) North column - Northwest view, (b) North column - Southeast view, (c) South column - Northwest view, (d) South column - Southeast view (Images by Elmira Shoushtari)

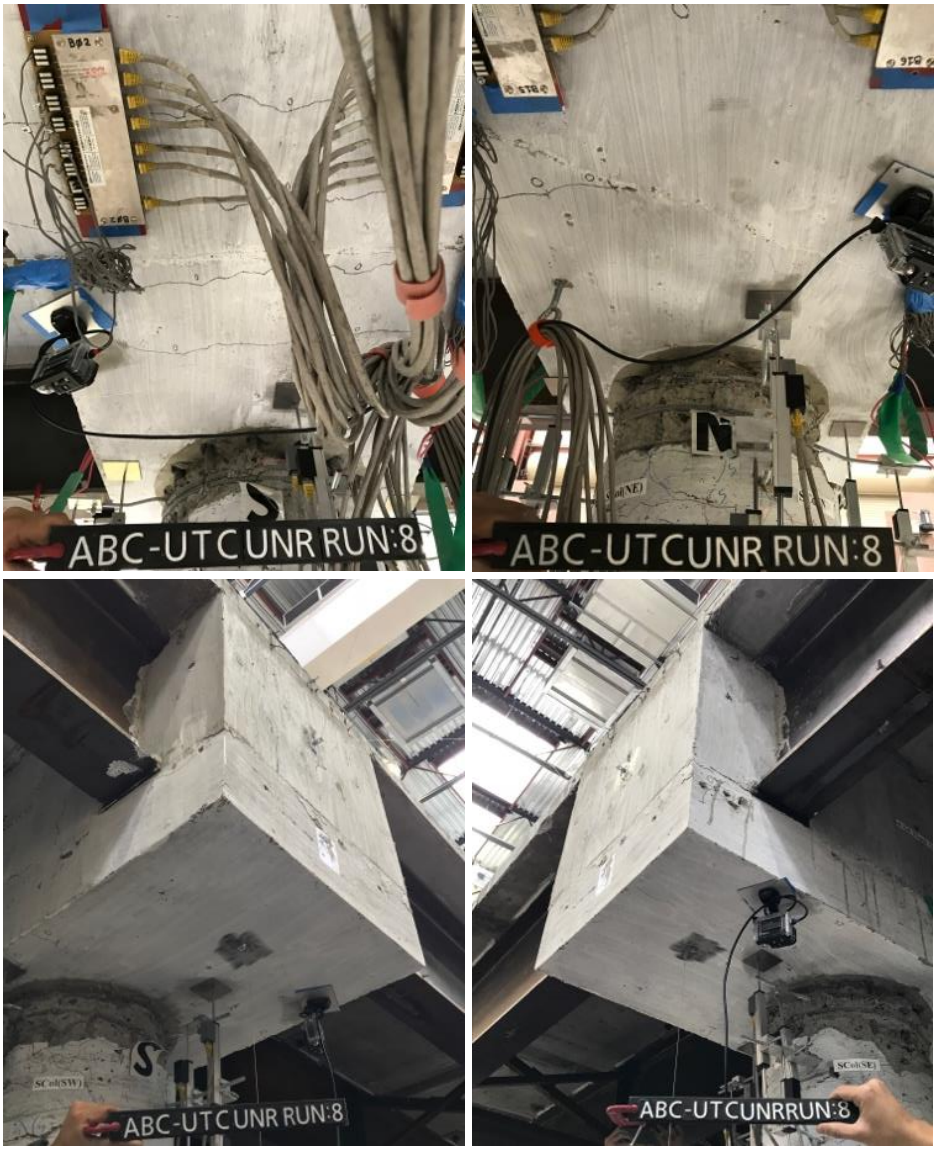

Figure 3.19 Damage states of the precast cap beam after the last run (Images by Elmira Shoushtari)

Figure 3.20 Cap beam to girder connection damage state (Images by Elmira Shoushtari)

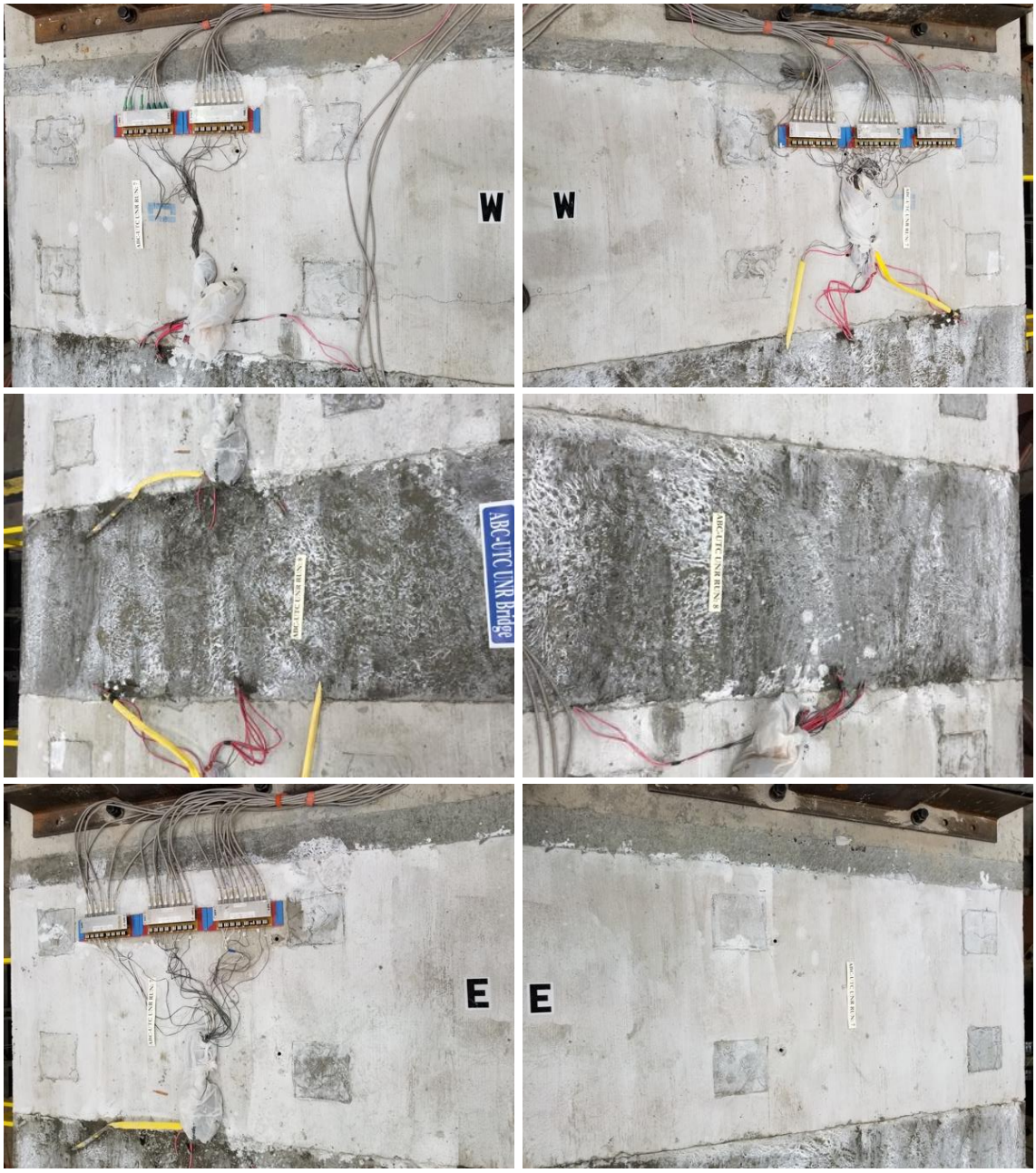

Figure 3.21 Damage states of the superstructure joints (Images by Elmira Shoushtari)

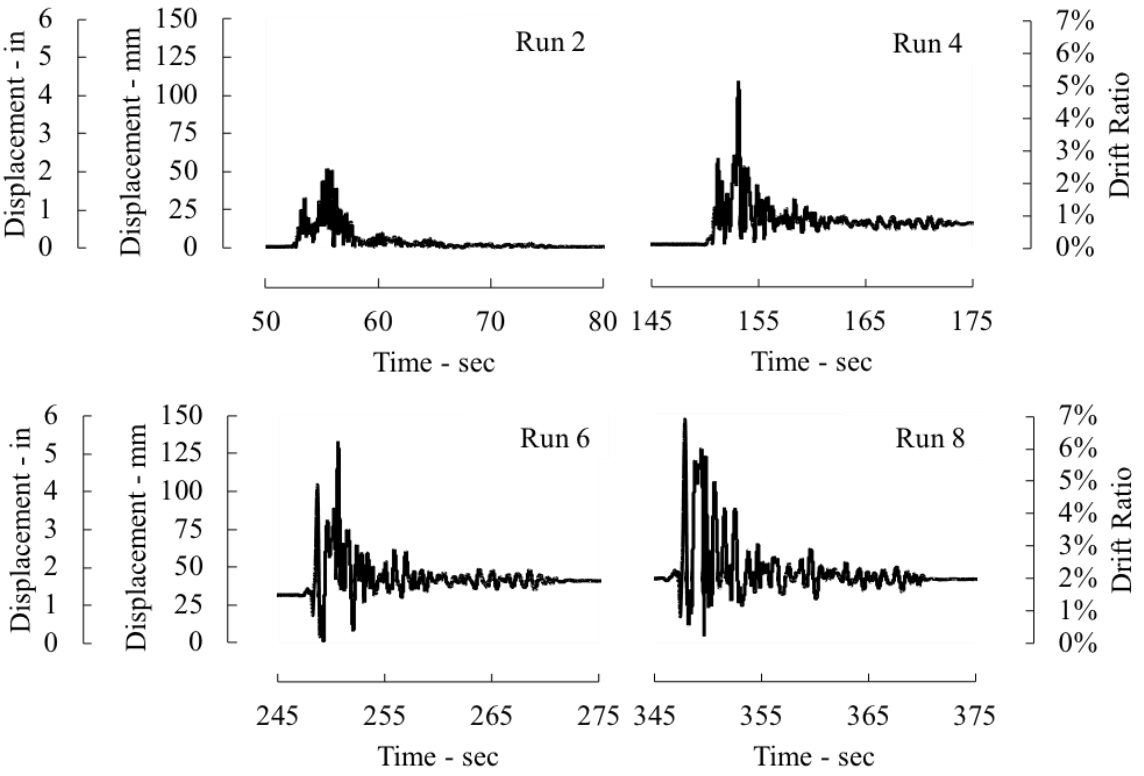

Figure 3.22 Displacement (and drift ratio) history of the bridge model during Run 2, Run 4, Run 6, Run 8

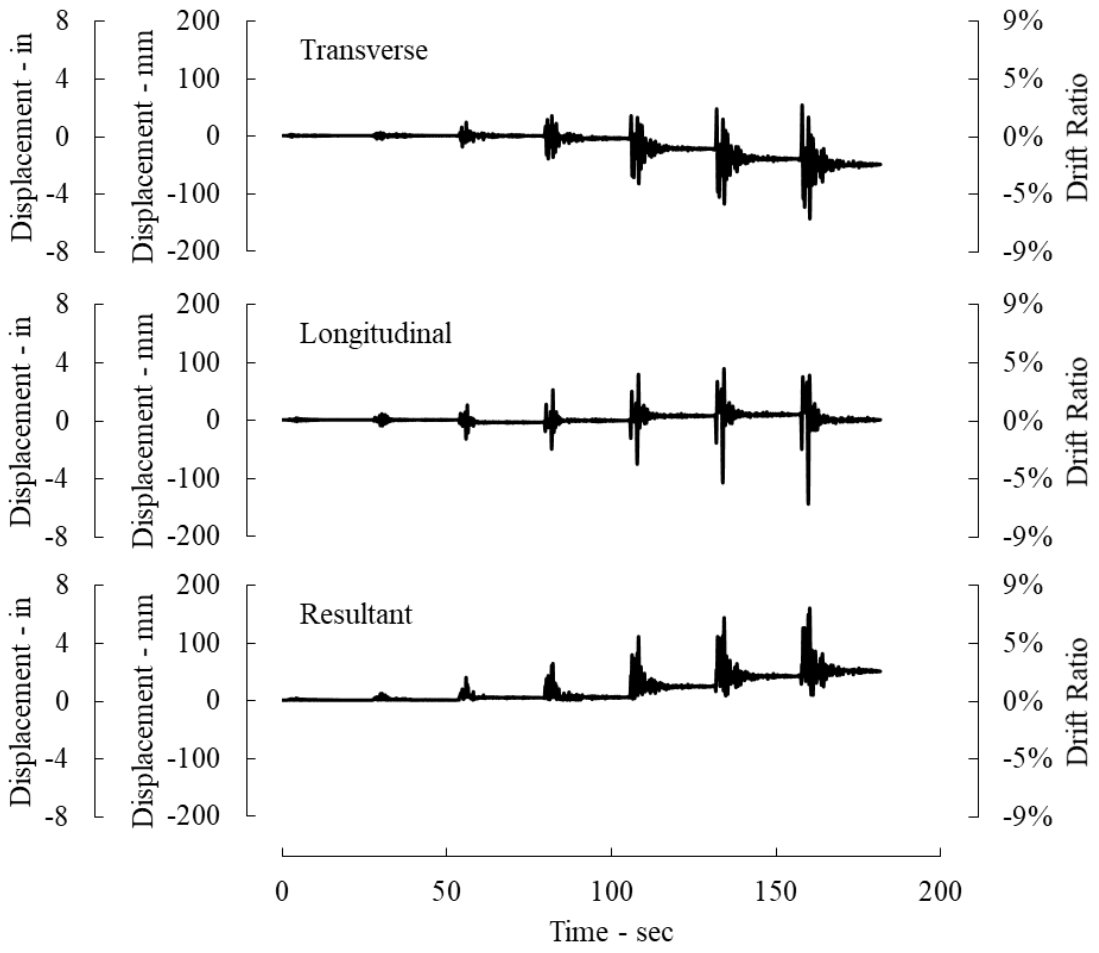

Figure 3.23 Predicted bent displacement response in the transverse (top) and longitudinal (middle) directions and bent resultant displacement (bottom)

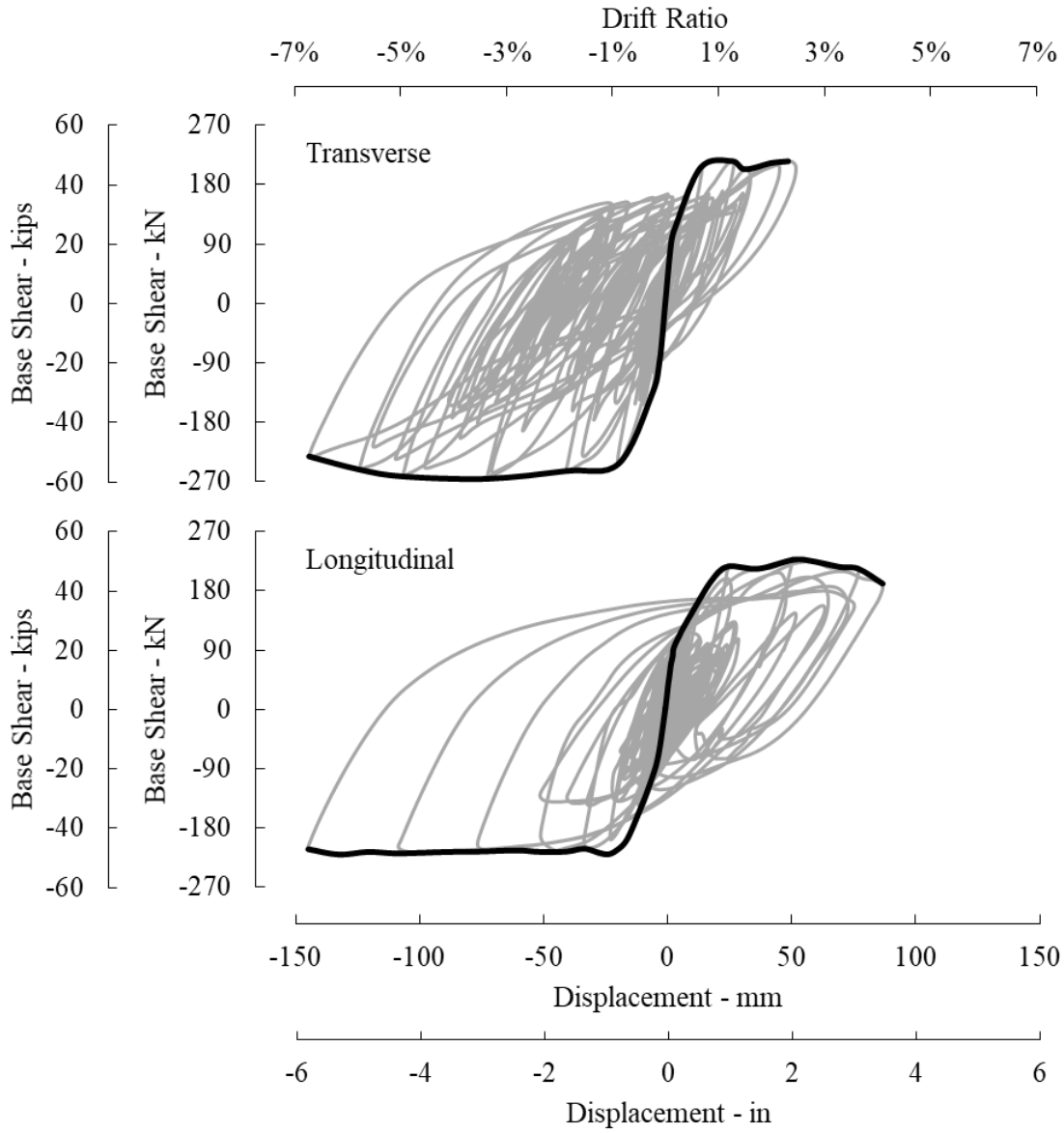

Figure 3.24 Bent hysteresis curves in the longitudinal and transverse directions and associated backbone curves

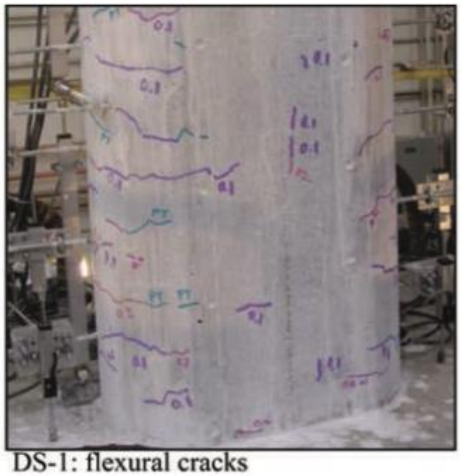

DS-1: flexural cracks

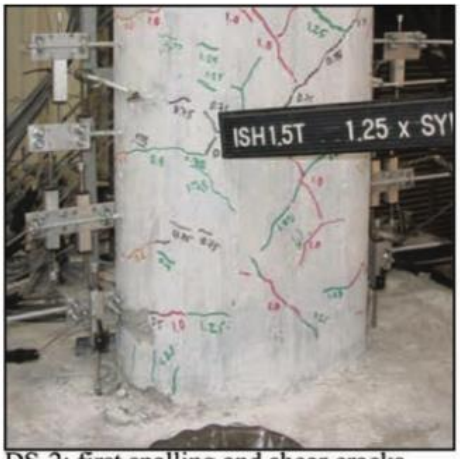

DS-2: first spalling and shear cracks

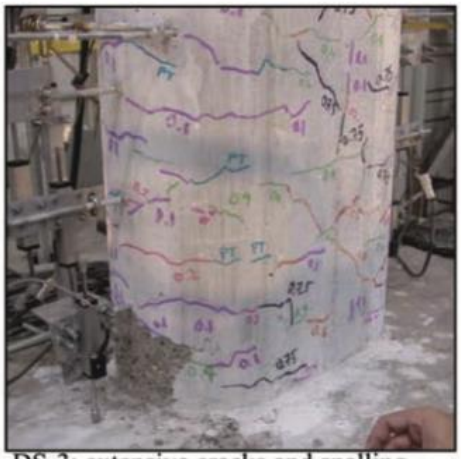

DS-3: extensive cracks and spalling

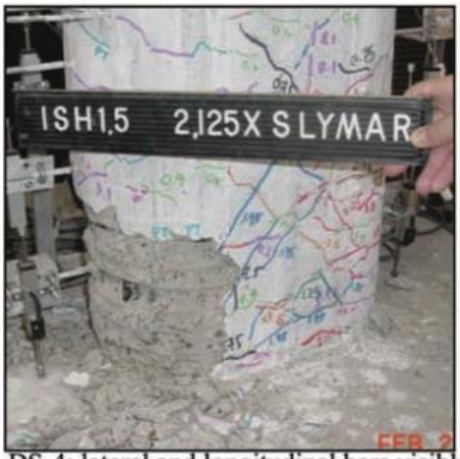

DS-4: lateral and longitudinal bars visible

DS-5: imminent failure

Figure 3.25 Five distinct damage states in the RC bridge columns (Vosooghi and Saiidi, 2012)

CHAPTER 4: SEISMIC PERFORMANCE OF A TWO-SPAN STEEL GIRDER BRIDGE WITH ABC CONNECTIONS

This chapter is a stand-alone paper that is submitted for possible publication in Earthquake Spectra Journal

Abstract

The first shake table test of a steel girder bridge system constructed using accelerated bridge construction (ABC) techniques was conducted at the University of Nevada, Reno. The objective of this study was to determine the adequacy of the seismic performance of a bridge system with six types of ABC connections under strong bidirectional earthquake shaking. The test model was a 0.35-scale, two-span steel plate-girder bridge with seat type abutments and two-column bent. The six incorporated promising ABC connections were only tested under unidirectional loading and yet to be verified holistically. The model was subjected to eight earthquake motions adopted from the 1994 Northridge-Sylmar ground motion and applied with increasing amplitudes. This paper presents the global and local response of the bridge model, and demonstrates that the bridge performance was satisfactory and emulative of conventional bridges. The columns experienced up to 6.9% drifts while ABC connections, among capacity-protected elements, remained elastic.

4.1. Introduction

With the extensive population growth and economic development over the past few decades, there has been an increasing demand to replace decaying highway bridges or to build new ones. Conventional bridge construction often causes traffic delays and compromises the safety of highway workers and the traveling public. Accelerated bridge construction (ABC), using prefabricated elements, makes bridge construction faster, safer, and potentially more economical, while maintaining or even improving the quality and durability of bridges. An important challenge for ABC is to develop connections that assure proper energy dissipation of the yielding element as well as the integrity of the structural system under strong earthquakes. Another challenge is that ABC connections and prefabricated components should be constructible and easy to transport.

Various ABC connections have been developed and investigated in the past few years under seismic loading with the primary intent of building a solid understanding of the local behavior of the connections, and as such the experimental studies were mostly limited either to the component level or bridge subassembly. These studies have been beneficial in formulating preliminary design guidelines and building a certain level of confidence in utilizing ABC techniques [Matsumoto et al. (2001); Restrepo et al. (2011); Tazarv and Saiidi (2014); Mehrsoroush, et al. (2014); Mehraein and Saiidi (2016)]. However, bridge system studies are essential to fully understand the performance of ABC connections and their interaction with prefabricated components as would be experienced in realistic bridges and to build confidence in holistic bridge performance. The primary objective of this study was to address this issue through comprehensive analytical and experimental investigation of a large-scale two-span steel girder bridge model incorporating six ABC connections subjected to bi-directional horizontal earthquake motions. Other objectives were to determine the adequacy of the emerging design

guidelines and modeling procedures as well as the feasibility of the construction methods. The aforementioned ABC connections were: (1) rebar hinge pocket connection (connecting columns to the footing); (2) grouted duct connection (connecting columns to a hybrid cap beam); (3) simple for dead, continuous for live (SDCL) connection (connecting superstructure to the bent); (4) panel-to-girder grouted pocket connection; (5) short-spliced deck panel rebars in the transverse panel-to-panel joints filled with ultra-high performance concrete (UHPC); and (6) spliced deck panel rebars in UHPC-filled panel-to-panel joint over the pier.

Rebar hinge pocket connection is a two-way hinge, comprising a cluster of bars located in a pattern with a diameter that is smaller than that of the column, embedded in the pockets left in the footing or cap beam. Although shake table tests of the two-column bents incorporating rebar hinge pocket connection have led to satisfactory results under unidirectional loading [Mehrsoroush, et al. (2016) and Mohebbi et al. (2017)], there has not been any reported experiments at the system level or under bi-directional loading.

With respect to column-cap beam connection, a precast bent system that was developed for integral connections with prestressed girders was tested under cyclic lateral loading [Marsh, M. L. et al. (2010)]. The bent incorporated a two-stage hybrid cap beam consisting of a lower precast and upper cast-in-place segment. Column bars were partially anchored in the grout-filled ducts embedded in the precast cap beam. Test results were promising; however, the combined effect of the out-of-plane and in-plane loading on the connection was not investigated.

For steel girder bridges, SDCL bent-to-superstructure integral connections subject to seismic loads was developed [Taghinezhadbilondy et al. (2016)] and successfully tested under uni-directional cyclic lateral loading [Sadeghnejad and Azizinamini (2017)]. In this detail, girders are simply supported for the dead load but are made continuous afterwards for live and seismic loads. The seismic performance of the SDCL connection under biaxial seismic loading when integrated with a hybrid cap beam and column grouted duct connection is not yet investigated.

Full continuity of full-depth precast deck panels to steel girders can be accomplished by embedded studs in grout-filled deck pockets (Badie and Tadros, 2008). This detail was further investigated by Shrestha, et al. (2017). These studies were also conducted on components only. Given the superior bond strength of UHPC, it can significantly reduce the required splice length of prefabricated deck bars in the joints and accordingly reduce the joint width [Graybeal (2010, 2014a)]. Another important ABC connection is the deck panel joint over the pier, which is critical due to high strains. As a result, the common practice is either to hook deck bars into the cap beam or mechanically splice the bars. Both approaches are time-consuming and add to reinforcement congestion. In the current study, it was decided to use long lap-spliced bars combined with UHPC to simplify construction.

Detailed discussion of the test model bridge design, construction, testing program, and apparent damage were presented by Shoushtari et al. (2019a). Furthermore, pretest analytical studies of the test model were conducted to ensure the feasibility of the shake table tests, determine the suitable input ground motions and loading protocol, and

investigate the seismic response of the bridge model under a large number of near-fault and far-field earthquake records [Shoushtari et al. (2019b)]. This paper focuses on the measured global and local response of the test model. The global parameters included in the paper are the displacement response, force-displacement relationship of the pier, superstructure in-plane rotation, and variation of the bridge dynamic properties. The local response parameters consist of the performance of all connection types in terms of apparent damage, strain, curvature, rotation, slippage, etc.

4.2. Bridge Model Description

Figure 1 shows the elevation, plan view, and the superstructure cross section of the two-span bridge model that was designed, constructed, and tested at the shake table laboratory of the University of Nevada, Reno. The bridge was a symmetric non-skewed, 0.35 scale of an assumed typical prototype. The bridge model had two equal spans of 10.6 m (34'-8"). Also, shown in Figure 1 is a cross section of the superstructure, which included four steel plate girders and full depth precast deck panels. The superstructure was supported through bearings on seat type abutments and a two-column precast bent. To simplify construction, shear keys and abutment back-walls were assumed to be sacrificial and were not included in the model. Columns were designed to be "pinned" at the footing and integral with the superstructure. The seismic weight of the bridge, the weight of all the bridge components excluding one-half of the columns and the entire footing, was 623 kN (140 kips). The girders were simply supported for gravity loads but were made continuous afterwards. Extra mass was placed over the superstructure (Figure 1) to simulate realistic stresses in all elements. The axial load index of the columns (defined as the column axial load due to the gravity loads divided by the gross cross-sectional area and the specified concrete compressive strength) was 5.7%.

The cap beam was constructed in two stages, a lower precast and an upper CIP segment. Figure 2 shows schematics of column connections to the footing and cap beam. The column bases were rebar hinges that were connected to the footing through pocket connections. At the top, the columns were connected to the precast portion of the cap beam through grouted ducts with the column longitudinal bars extended beyond the ducts into the CIP segment. This detail is referred to as "hybrid" because it combines anchorage of the column longitudinal bars in grouted ducts and CIP. The connection between the superstructure and the bent was an integral type simulating SDCL as shown in Figure 3. Also shown in the figure are the four main elements of the SDCL connection, the dowel bars, tie bars, steel blocks, and partial depth stiffeners. After the girders were supported on the precast cap beam, the rest of the cap beam was cast, making the girders continuous over the pier. Figure 4 shows the details of the deck panel connection to the girders and adjacent deck panels. Four studs were used in grouted deck pocket connections (Fig. 4b). Straight deck bars extended in the deck transverse joints, which were filled with UHPC to decrease the required lap splice length (Fig. 4c). Although lap splice length was sufficient for the deck reinforcement development over the pier using normal strength grouts, UHPC was used in the upper 70 mm (2 ¾ in.) of the cap beam (to match the deck thickness) because lap splices are not normally allowed in critical zones.

There are no official seismic codes for ABC bridges, so the overall design of the bridge model was according to the AASHTO LRFD Bridge Design Specifications (2012) and the AASHTO Guide Specifications for LRFD Seismic Bridge Design (2014), but the design of the connections was based on emerging ABC designed methods in the literature (Saiidi et al. 2009; Marsh et al. 2010; Taghinezhadbilondy et al. 2016; Badie and Tadros, 2008; Shrestha et al. 2018; Graybeal 2010; Graybeal 2014a&b). The strategy was to design a ductile substructure with an essentially elastic superstructure and connections. The bridge model was assumed to be located in Los Angeles area, Lake Wood, with a latitude and longitude of 33.84926 N, and 118.0952 W, respectively, and site class D. Table 1 summarizes the design properties of the bridge components. Table 2 lists the measured properties of steel reinforcement and test-day properties of cementitious materials. Pretest modal analysis was conducted on the bridge model assuming cracked section properties for the columns to determine the natural periods of vibration [Shoushtari, et al. 2019(a)]. The first three modes were superstructure in-plane rotation, longitudinal (along traffic), and transverse with periods of 2.57, 0.58, and 0.48 s, respectively.

Table 4.1 Properties of the bridge model

Scale factor	0.35
Span length	10.6 m (34 ft-8 in.)
Width of the bridge	3.4 m (11 ft)
Column diameter	406 mm (16 in.)
Column height[1]	2.13 m (84 in.)
Aspect ratio	5.25
Spacing Between Columns	2.0 m (6 ft - 6 in.)
Rebar hinge diameter	254 mm (10 in.)
Rebar hinge gap	38.1 mm (1.5 in.)
Axial load index[2] (dead load)	5.7% [axial load= 205 kN (46 kips)
Column longitudinal bar	12#5 [dia.= 16 mm (0.625 in.)], ρl =1.83%
Column transverse steel	#3 [dia.= 9.5 mm (0.375 in.)] @ 63 mm (2.5 in.), ρs=1.25%
Rebar hinge longitudinal bar	6#5 [dia.= 16 mm (0.625 in.)], ρl =2.40%
Rebar hinge transverse steel	#3 [dia.= 9.5 mm (0.375 in.)] @ 38 mm (1.5 in.)

[1] As-built height of the columns was 2.15 m (84.75 in.)

[2] Based on concrete nominal strength of f'c=28 MPa (4.0 ksi)

Table 4.2 Measured compressive strength of conventional concrete, grout, and UHPC

Material	Element	Test-day compressive strength, MPa (ksi)
Conventional concrete	Columns, precast cap beam, footing	64.0 (9.3)
	CIP cap beam	52.6 (7.6)
	Deck - east span	58.9 (8.6)
	Deck - west span	43.5 (6.3)
Grout	Deck pocket - east Span	80.8 (11.7)
	Deck pocket - west Span	75.3 (10.9)
	Column-to-footing	64.8 (9.4)
	Column-to-cap beam	85.2 (12.3)
UHPC	Deck joints	126.3 (18.3)
	Deck joint over the pier	151.1 (21.9)

4.3. Shake Table Tests

Figure 5 shows the test setup. Also shown in the figure are the safety frames and the superimposed mass in the form of lead pallets and concrete blocks. Two horizontal components of the 1994 Northridge-Sylmar earthquake record with increasing amplitudes were simulated in the test using the central shake table, while the other two shake tables were stationary. The design level earthquake (DE) was defined such that the peak resultant displacement obtained from the nonlinear dynamic analysis was approximately the same as that obtained from the orthogonal combination of the design displacement demands. As a result, the acceleration values for each component were multiplied by a factor of 0.6 to build the design earthquake. The target and achieved PGA of shake table motions are listed in Table 3.

The loading protocol included eight bi-directional shake table motions varying from 30% of DE to 225% of DE to capture different damage states. The component with higher PGA was applied in the longitudinal direction to impose a large demand on superstructure connection to the substructure. White noise tests were conducted before each earthquake run and after the last run to measure the variations in the test model dynamic properties during the test. The white noise motions were randomly-generated with frequency content from 0 – 30Hz and PGA of 0.15g. Figure 6 shows the response spectra of all earthquake runs in addition to the AASHTO design spectrum. The time axis of the acceleration record was compressed by a factor of 0.592, corresponding to the square root of the dimensional scale factor of the bridge model (λ=0.35). Marked in the figures are also the calculated fundamental longitudinal and transverse periods of the bridge model determined based on the column cracked section properties.

Table 4.3 Target and achieved shake table motions

		PGA, (g)							
		Run 1	Run 2	Run 3	Run 4	Run 5	Run 6	Run 7	Run 8
% of the DE		30%	65%	100%	125%	150%	175%	200%	225%
Longitudinal	Target	0.17	0.36	0.56	0.70	0.83	0.97	1.11	1.23
	Achieved	0.14	0.29	0.39	0.45	0.56	0.67	0.83	0.89
Transverse	Target	0.11	0.24	0.37	0.47	0.56	0.66	0.75	0.83
	Achieved	0.13	0.20	0.32	0.40	0.55	0.63	0.74	0.83

4.4. Global Measured Results

4.4.1. Displacement Response

The absolute transverse displacements of the superstructure were recorded at five locations: the top of the bent, the top of the abutment seats, and mid-spans. The absolute longitudinal displacements were measured at four locations at the four corners of the superstructure at the abutments. The relative displacements in each direction were determined by subtracting the corresponding shake table displacements from the absolute displacements. The longitudinal displacement of the bridge model was determined as the average of the four displacement measurements. Resultant displacement was defined as the square root of the sum of the squares of displacement measurements in the transverse and longitudinal directions. Figure 7 presents pier longitudinal, transverse, and resultant relative displacement histories during runs 3 (the design run) and 8 (the final run: 225% design run). Figure 8 shows the maximum and residual drift ratios in each run. It is clear that the peak and residual displacements in the longitudinal direction were always higher than those in the transverse direction. This is attributed to the higher intensity of the component which was applied in the longitudinal direction (Figure 6). The peak resultant drift ratio during the design earthquake (DE) was 3.0%. At the end of the DE run, extensive flexural cracks and minor spalling of the cover concrete were observed in the columns (Figure 9(a)). At the end of the run 6 (causing a resultant drift ratio of 6.0%, twice that of DE), the spirals of the south column and the spirals and longitudinal bars of the north column were partially exposed (Figure 9(b)). During the last run and in the north column, the extensive core damage (which was initiated in the previous run) coincided with the buckling of the longitudinal bars. Figure 9(c) shows the final damage states of the column top plastic hinges. Extensive presentation and discussion of damage states at different locations of the model are presented in Shoushtari et al. (2019a).

The bent residual displacements in the transverse direction were insignificant until the last run. In the longitudinal direction, residual displacement was not significant until the end of DE, but noticeably increased from run 4 to 6 and stabilized until the end of the test. It is worth noting that although there is no limitation for the residual displacements of the bridge columns in the U.S. bridge design codes, the Japanese seismic design specifications for highway bridges (Japan Road Association, 2002) limits the residual

drift to 1%. As shown in figure 8, the bent longitudinal and resultant residual drift ratios exceeded this limit starting in run 5, which was associated with 150% DE.

As indicted in the introduction, one of the objectives of the study was to determine the effect of bi-directional earthquake motions. Therefore, it was important to examine if the displacement response was indeed bi-axial rather than uncoupled uniaxial transverse and longitudinal displacements. To assess the extent of bi-directional response, the bent horizontal cumulative particle movement relative to the shake table was plotted for all the runs (Figure 10). Positive transverse and longitudinal displacements indicate southward and westward movements, respectively. It can be seen that there were simultaneous displacements in both orthogonal directions. Moreover, the maximum longitudinal displacements toward the west and the east were comparable indicating a symmetric response in this direction. In the transverse direction, however, northward movement was dominant. To determine the degree of coupling between the two orthogonal directions of the bridge model, a "coupling index" (CI) was defined (Saiidi et al. (2013)) as OA/OB (Figure 10) for each quadrant. The coupling index for a circulate motion is 0.71 and is regarded as a highly coupled movement. The distribution of the average coupling index (CI_{ave}), defined as the average of the indices in all four quadrants, and individual coupling indices are shown in Figure 11. The figure shows that the average coupling index ranged from 0.3 to 0.5, indicating a relatively high coupling degree. The average CI did not change significantly as the earthquake amplitude increased. The data also shows that the movement of the bridge was dominant in the NW-SE direction up to the run 4 but toward the north afterwards.

4.4.2. Force-Displacement Response

Since incorporating load cells in the columns was not feasible, the bent base shear was determined indirectly using the method described by Johnson et al. (2008). In this method, lateral forces calculated from the hydraulic fluid pressure in the shake table actuators were modified by subtracting the shake table friction and the inertial force due to the shake table mass. The inertial force was calculated based on the measured shake table acceleration multiplied by the shake table mass plus the rigidly-attached footing and safety frames. Note that the superstructure was supported on abutment seats with minimal friction. Therefore, the total shake table lateral force was resisted essentially by the bent.

To assess the overall lateral force-displacement relationship of the bridge model, the hysteresis relationship between the bent base shear and horizontal displacement of the bent was studied (Figure 12). The hysteresis curves were relatively wide, indicating good energy dissipation. Furthermore, the strength degradation was minimal. The relatively sharp downward slope in the positive zone of the transverse response was mainly due to the fact stiffness had already degraded but displacements were relatively small.

The envelopes of the hysteresis curves were idealized by elasto-plastic curves such that the elastic branch passes through the first column longitudinal bar yielding associated with each direction of the motion. The plastic branch was then adjusted to preserve energy. Because of the symmetry in the bridge response in the longitudinal direction and asymmetry in the transverse direction; displacement ductility and effective period

calculations were conducted using the average of the idealized longitudinal force-displacement relationship in the positive and negative directions. However, only the idealized curve for the dominant direction of the transverse response was used. To obtain displacement ductilities, peak measured displacement was divided the by the effective yield displacement. The first slope of the idealized elasto-plastic curves were regarded as the effective stiffness of the bent in the associated direction resulting in 7.7 kN/mm (44.2 kip/in) and 6.5 kN/mm (37.2 kip/in) in the longitudinal and transverse directions, respectively. These values were further used to determine the effective measured periods and resulted in 0.57 second in the longitudinal and 0.62 second in the transverse direction.

4.4.3. Superstructure In-plan Rotation

Assuming a rigid superstructure, the in-plane rotation was determined as the difference between the transverse displacements at the east and west abutments, divided by the distance between the sensors, which was 19.6 m (64'-3 ½"). Figure 13 shows the peak rotations versus the transverse spectral acceleration at the fundamental period (Sa(T1)). As shown, no appreciable rotation was noted until run 3 (DE). However, starting from run 4 some rotations were observed ranging from 0.002 to 0.004 rad, which were not significant. The rotations did not necessarily increase as the PGA increased. Since the bridge model was symmetric and with zero skew angle, in-plane rotation could be attributed to the fundamental mode shape of the bridge which was rotational. Furthermore, unsymmetrical damage in the columns that started from run 4 could have contributed to relocating the bridge center of stiffness and hence causing superstructure in-plane rotation.

4.4.4. Variation of the Dynamic Properties

The amplitude of the white noise motions was kept intentionally small to avoid introducing any damage. As a result, the white noise test data could not be used to determine representative effective stiffness properties of the bridge model. Therefore, the effective stiffness, K_{secant}, as affected by different earthquake runs was determined by estimating the slope of the associated measured force-displacement relationship plots. The variation of the bridge model stiffnesses in the two orthogonal directions and the associated periods as a function of earthquake spectral acceleration at the fundamental period are shown in Figure 14 and are discussed in 4-2. As shown in the Figure, the periods increased 73% in the longitudinal and 118% in transverse directions throughout the seismic tests, indicating the softening of the bent. In the longitudinal direction, the bent stiffness reduction and the period elongation were negligible after run 4 during which the resultant drift ratio was 5%.

4.5. Local Measured Results

4.5.1. Rebar Hinge Pocket Connection

The apparent damage in the rebar hinge connections was limited to spalling of the cover concrete in the hinge throat. None of the bars fractured even during the last run when the confined core was damaged in the top plastic hinges of the columns. The hinge gap was not closed during the tests, which indicated that the 38.1-mm (1.5-in.) was sufficient to

allow for the column rotation. Hinge gap closure is undesirable because it increases the plastic moment at the base, which leads to higher plastic shear in the column and potential shear failure. Figure 15 shows the peak measured tensile strains of the steel in and the vicinity of the base hinges. As shown, the peak strain in the rebar hinge longitudinal bars was 22.3 times the measured yield strain. In contrast, the hinge spirals did not yield even in the last run during which the peak strain was 81% of the yield strain in the south column. The spiral of the south rebar hinge became partially visible during this run.

Figure 16 shows the maximum strain profile over the height for the hinge longitudinal bars. The peak strain occurred in the south column and was associated with the loading in the longitudinal direction of the bridge model. As shown, yielding of the bar was spread over a height of 152.4 mm (6 in.) into the footing and the columns. The strain profile indicates that the pocket connection at the hinge was effective because the maximum strain occurred at the footing-column interface where the hinge throat was.

The peak horizontal slippage of the rebar hinges relative to the footing was 6.6 mm (0.26 in.) in the transverse direction and 4.6 mm (0.18 in.) in the longitudinal direction corresponding to 0.3% and 0.22% drift ratios, respectively. It is evident that the horizontal slippage is negligible compared to the maximum drift ratios of the bent. Furthermore, the relatively small slippage is a direct indication that the rebar hinges did not fail in shear.

To measure the curvatures and rotations over the gage lengths at the top plastic hinge zones and at the base hinges, pairs of displacement transducers were used around the columns at three levels of the columns top connections and two levels of the hinge connections. Figure 17 shows the base hinge rotations. As expected the main rotation happened at the hinge throat due to its smaller section. The hinge twist angle (rotation in the horizontal plane) was measured using the same transducers that measured hinge horizontal slippage. The relationship between the hinge maximum longitudinal bar strain and hinge twist angle for each column is shown in Figure 18. Note that the south hinge twist angles were not reliable for runs 6 and 7 due to the malfunction of transducers, and hence are not shown in the figure. Figure 18 shows that yielding of the hinge longitudinal bars alone did not lead to large twist angles. The angles increased significantly only after there was significant damage in the concrete at the hinge throat in run 5 and after.

4.5.2. Grouted Duct Connection

Figure 19(a) shows that the peak tensile strain in the longitudinal bars of the columns reached about 20 times the yield strain during the last run. Figure 19(b) shows that the north column spiral yielded in the last run, which allowed for buckling of the longitudinal bars seen in the plastic hinge. Figure 20 shows the measured curvature profiles of the north column in each direction and for different runs. Curvatures at each level were the ratio of the calculated rotations of that level to the gage lengths of the transducers. The maximum measured curvature was 1.02e-4 rad/mm (0.0026 rad/in) and in the north column which is consistent with the observations during the test in which spalling of the north column plastic hinge was more significant than that of the south column. The peak curvatures occurred at the top level due to the yielding and bond slip effects. Curvatures

(and rotations) associated with longitudinal loading were generally larger than those of the transverse direction, which is attributable to higher spectral acceleration of the longitudinal component (Figure 6). Furthermore, the graphs show that curvatures were spread over the plastic hinge length, and effect that is normally seen in CIP columns with rigid connections.

Figure 21 shows the strain profile of the extreme column longitudinal bar in the top moment connections. It can be seen that the strains were well distributed in the plastic hinge zone. The maximum strains occurred at the bottom of the cap beam (elevation zero) indicating that the cap-beam connection detail provided full fixity. The peak strain within the cap beam was slightly larger than the yield strain. This further demonstrates that the column-cap beam connection detail was effective in mimicking CIP moment connection. The strain data are consistent with the fact that the connection exhibited no sign of the duct or bar pullout or cap beam damage in the hinge even under 6.9% resultant drift ratio. Only minor spalling of the grout just above the column-cap beam interface was noticed during the last runs. Spalling of this nature is not expected in CIP construction, but appeared to have insignificant effect of the connection behavior. Overall, the grouted duct connection combined with the hybrid cap beam successfully transferred the column plastic moment to the superstructure.

4.5.3. SDCL Superstructure-to-Bent Connection

Figure 22 shows the maximum tensile strain in the cap beam longitudinal bars, deck longitudinal bars (Fig. 4c), cap beam stirrups, and ties around the studs welded to the girders bottom flanges (Fig. 3). The cap beam, deck, and the girders are designed as capacity-protected members (meaning that they should remain elastic or nearly elastic with maximum strains that are either less than or equal the yield strain or exceed the yield strain only slightly).

As shown in Figure 22, strains in the deck longitudinal bars remained well below the yield strain. Also, no apparent damage was observed in the vicinity of the deck panel joint over the pier except for a few hairline cracks parallel to the cap beam and at the bottom of the two deck panels adjacent to the pier [Shoushtari et al. 2019(a)]. The relatively small peak strains and the lack of damage indicate that the joint provided adequate load path and longitudinal continuity even under strong motions.

The cap beam was designed with an overstrength factor of 1.2 (AASHTO, 2014);. However, even under 2.25 times the design earthquake, the peak measured strains in the cap beam longitudinal bars and stirrups were less than 20%, and 45% of the yield strain, respectively. Therefore, the design objective of capacity-protected cap beam was met. Note that the initial strains for cap beam reinforcement are due to the construction loading. Tie bars are designed for the vertical component of the earthquake; however, a minimum value is required even under horizontal component of motions [Taghinezhadbilondy et al. 2016]. This design objective was confirmed as peak strains were substantially less than the yield strain (below 10% of the yield strain) and remained almost the same during all the earthquake runs.

To examine if full rigidity was provided by the SDCL connection, displacement of the girders relative to the cap beam in the longitudinal direction was measured using

displacement transducers. The maximum relative displacement was 0.2 mm [0.0067 in.], which is negligible. This indicates that girders were essentially fixed to the cap beam and did not slip even under strong motions. The maximum vertical movement of the girder relative to the cap beam was 0.5 mm [0.0197 in.], which is considered insignificant. The close-to-zero slippages confirm that the connection of the superstructure to the cap beam was indeed a rigid connection as intended.

Overall, SDCL connection performed as envisioned in the design: The column overstrength moment was transferred from substructure to the superstructure, while the cap beam and SDCL connection remained essentially elastic.

4.5.4. Deck Panel Connections

Three types of connections were used to provide continuity between the deck panels and between the deck panels and other components of the superstructure: (a) Grouted deck panel pocket connections, (b) connections between the deck panels within each span, and (c) connections between deck panels from one span to the next. The performance of these connections was evaluated to determine if, similar to other superstructure components, these connections remain undamaged and provide full connectivity during seismic loading.

4.5.4.1. Grouted Deck Panel Connections

The grouted pocket connections between the deck panels and the girders are shown in Figure 4b. Relative displacements between the deck panels and the girders were measured in one interior and one exterior girder in the west span at 1.8 m [6 ft] from the pier centerline. This location was identified as the most critical location undergoing the maximum shear based on the pretest analytical studies (Shoushtari et al. 2019b). The maximum displacements in the longitudinal and transverse directions were 0.09 mm (0.0036 in.) and 0.04 mm (0.0014 in.), and occurred in the exterior and interior girders, respectively. The apparent damage at the grouted pocket connections was limited to the hairline shrinkage cracks in the grout or around the pockets that were visible before the shake table tests (Figure 9d). It is evident that the grouted pocket connections remained damage free.

4.5.4.2. UHPC-Filled Joints between Adjacent Deck Panels

Strains of the deck bars in the joint near the pier were measured. The peak strain was only 9.3% of the yield strain. No sign of damage was observed except for the initial shrinkage cracks (Figure 9d). Small strains and lack of the cracks parallel to the joints indicate that sufficient bond was provided at the concrete-UHPC interface and between the deck panels.

4.5.4.3. Deck Panel UHPC-Filled Connection above the Cap Beam

No damage was observed in the connection (Figure 9f) except for a few hairline cracks parallel to the joint (section 5-3). As shown in Figure 22, the peak strain in the deck panel was only 14% of the yield strain. These indicate that splicing deck longitudinal bars in UHPC over the pier not only provided full longitudinal connectivity between the spans, but also was successful in forming the strut and tie mechanism between the column and

deck longitudinal bars and hence providing the integrity between the superstructure and substructure under earthquake loading. The conventional practice to anchor the deck panel bars over the cap beam is hooked deck reinforcement or to use mechanical splices. Both of these were avoided in the bridge test model to prevent steel reinforcement congestion. To ensure sufficient splice behavior, however, UHPC was used at the deck level. This technique reduces reinforcement congestion and simplifies construction compared to the other alternatives. The lack of apparent damage and relative low strain indicate that the lap splice in combination with UHPC is a viable connection over the pier in ABC bridges in high-seismic areas.

4.6. Conclusions

Much confidence remains to materialize in the seismic performance of bridges that combine prefabricated substructure and superstructure elements (intended for accelerated bridge construction, ABC) because connections of these structures can be critical. The study presented in this article was aimed to address this issue. The following conclusions were drawn based on the data presented in the article:

- The ABC bridge test model performed as envisioned in the design and was emulative of CIP bridges: (1) damage was limited to column plastic hinges; (2) cap beam, deck panels, and the four connections incorporated in the superstructure remained damage free; (3) column failure was in a ductile flexural mode after undergoing a 6.9% resultant drift ratio under simultaneous action of two horizontal simulated earthquake components; and (4) the sufficient load path was provided for the transfer of the seismic forces. The relatively high coupling index between the two loading directions shows that motions were indeed bidirectional.
- The displacement ductility capacity and drift capacity of the bent were comparable to those observed in conventional bridges.
- The performance of the rebar hinge pocket connection was satisfactory as the maximum strain occurred at the footing-column interface, yielding of the hinge longitudinal bars was spread well into the adjoining members, and gap closure was prevented with no bar fracture or damage to the pocket connection.
- The grouted duct connection combined with the hybrid cap beam successfully transferred the column plastic moment to the superstructure under bidirectional motions. Previous research was limited to only grouted duct connections tested under unidirectional loading of connection components. The maximum longitudinal bar strain occurred just below the cap beam with some yielding penetrating into the precast cap beam. No sign of duct or bar pullout was noticed even under 6.9% resultant drift ratio. Furthermore, the superstructure-to-bent slippage and rotation were negligible, which means that the joint performs as a monolithic joint. The deck-to-girder slippage was also nearly zero indicating full composite action between the deck and the girders.

Despite the zero skew angle of the bridge and symmetric geometry, small in-plane rotations were noticed after run 4 and continued afterwards. These rotations are attributed

to the fundamental mode being the in-plane rotation and the un-symmetric damages in the columns that relocated the pier center of stiffness.

4.7. Acknowledgement

The Accelerated Bridge Construction University Transportation Center (ABC-UTC) based at the Florida International University (FIU) supported this study. Thanks to the UNR Earthquake Engineering Laboratory staff: Dr. Patrick Laplace, Chad Lyttle, Todd Lyttle, Mark Lattin; and the ABC-UTC Director, Dr. Atorod Azizinamini. The authors would like to thank Lafarge North America Inc., C&K Johnson Industries, National Steel Bridge Alliance (NSBA), Reno Iron Works and Utah Pacific Steel for their support.

4.8. References

American Association of State Highway and Transportation Officials (AASHTO), (2012). AASHTO LRFD Bridge Design Specifications, 6th edition.

American Association of State Highway and Transportation Officials (AASHTO). (2014). "Guide Specifications for LRFD Seismic Bridge Design", Washington, D.C.

Badie, S. S, and Tadros, M. K, (2008). "Full-Depth Precast Concrete Bridge Deck Panel Systems", Report 584 by National Cooperative Highway Research Program.

Graybeal, B. (2010). "Behavior of Field-Cast Ultra-High Performance Concrete Bridge Deck Connections under Cyclic and Static Structural Loading," Federal Highway Administration, Report No. FHWA-HRT-11-023.

Graybeal, B., (2014a), "Design and Construction of Field-Cast UHPC Connections", Federal Highway Administration Publication No. FHWA-HRT-14-084. Pp. 1-36.

Graybeal, B., (2014b), "Bond Behavior of Reinforcing Steel in Ultra-High Performance Concrete", Federal Highway Administration. Publication No. FHWA-HRT-14-090.

Japan Road Association (2000), Design Specifications for Highway Bridges, Part Seismic Design (English edition).

Lafarge, Product Data Sheet: Ductal® JS1000, www.imagineductal.com, (2009).

Marsh, M. L., Stanton, J. F., Eberhard, M. O., Haraldsson, O., & Khaleghi, B. (2010). A precast bridge bent system for seismic regions.

Matsumoto, E. E., M. C. Waggoner, G. Sumen, and M. E. Kreger, (2001). "Development of a precast bent cap system". FHWA Rep. No. FHWA/ TX-0-1748-2. Austin, TX: Center for Transportation Research, Univ. of Texas.

Mehraein, M., and M. S. Saiidi. (2016). "Seismic performance of bridge column-pile-shaft pin connections for application in accelerated bridge construction". Rep. No. CCEER-16-01. Reno, NV: Univ. of Nevada.

Mehrsoroush, A., and Saiidi, M., "Seismic Performance of Two-Column Bridge Piers with Innovative Precast Members and Pipe Pin Connections, "Special Session, Extreme Load Performance and Design of Bridges for Accelerated Bridge Construction," 7th International Conference on Bridge Maintenance, Safety, and Management, Shanghai, China, July 2014, Paper No. CH199, pp.1472-1479.

Mehrsoroush, A., and M. S. Saiidi. (2016). “Cyclic response of precast bridge piers with novel column-base pipe pins and pocket cap beam connections”. J. Bridge Eng. 04015080.

Mohebbi, A., Saiidi, M. S., & Itani, A. M. (2018). Shake Table Studies and Analysis of a PT-UHPC Bridge Column with Pocket Connection. Journal of Structural Engineering, 144(4), 04018021.

Mohebbi, A., Saiidi, M. S., & Itani, A. M. (2017). Seismic design of precast piers with pocket connections, CFRP tendons, and ECC/UHPC columns. *Int J Bridge Eng Spec*, (2017), 99-123.

Restrepo, J. I., M. J. Tobolski, and E. E. Matsumoto, (2011). “Development of a precast bent cap system for seismic regions.” NCHRP Rep. 681. Washington, DC: National Cooperative Highway Research Program.

Sadeghnejad, A., Azizinamini, A., (2017), “Extending the Application of Simple for Dead and Continuous for Live Load Steel Bridge System to ABC Applications in Seismic Regions. Phase II-Experimental” Web-based quarterly Research Seminar, ABC-UTC research center, Florida International University.

Shrestha, G., Itani, A., and Saiidi, M. (2017) “Seismic Performance of Precast Full-Depth Decks in Accelerated Bridge Construction” Center for Civil Engineering Earthquake Research, Department of Civil and Environmental Engineering, University of Nevada, Reno, Report No. CCEER-17-05.

Shrestha, G. (2018). Seismic Studies of Superstructure and Substructure Connections for Accelerated Bridge Construction (Doctoral dissertation).

Shoushtari, E., Saiidi, M., and Itani, A., Moustafa, M. (2019a) “Design, construction, and Shake Table Testing of a Steel Girder Bridge System with ABC Connections”, ASCE Journal of Bridge Engineering, Manuscript submitted for publication

Shoushtari, E., Saiidi, M., and Itani, A., Moustafa, M. (2019b) “Pretest Analysis of Shake Table Response of a Two-Span Steel Girder Bridge Incorporating ABC Connections”, Manuscript in preparation.

Taghinezhadbilondy, R., Yakel, A., and Azizinamini, A., (2016), “Extending Use of Simple for Dead Load and Continuous for Live Load (SDCL) Steel Bridge System to Seismic Areas”. Dept. of Civil and Environmental Engineering, Florida International University, Miami, FL.

Tazarv, M., and Saiidi, M. S., (2014). “Next generation of bridge columns for accelerated bridge construction in high seismic zones”. Rep. No. CCEER-14-06. Reno, NV: Dept. of Civil and Environmental Engineering, Univ. of Nevada.

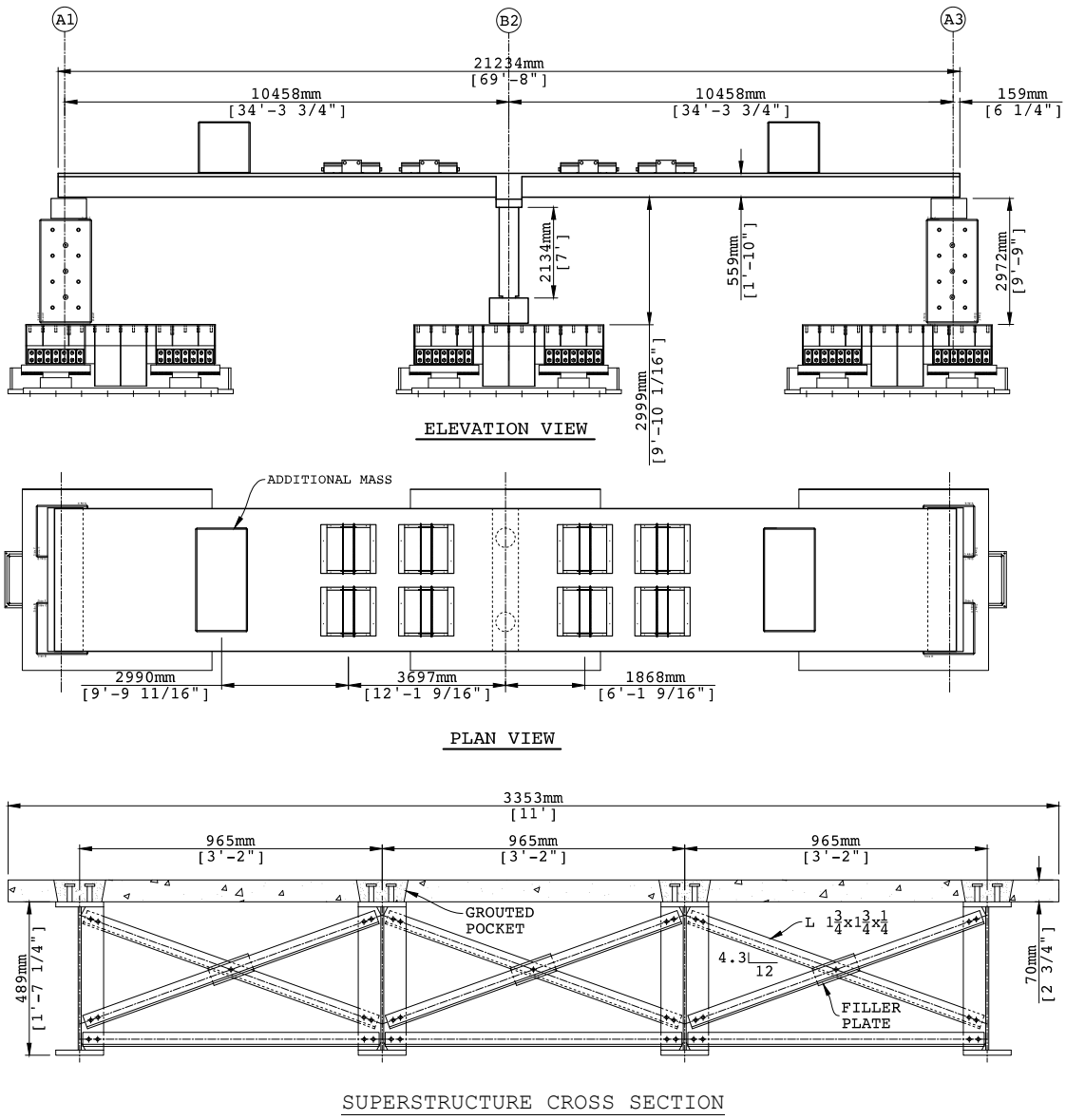

Figure 4.1 Geometric configuration of the bridge model

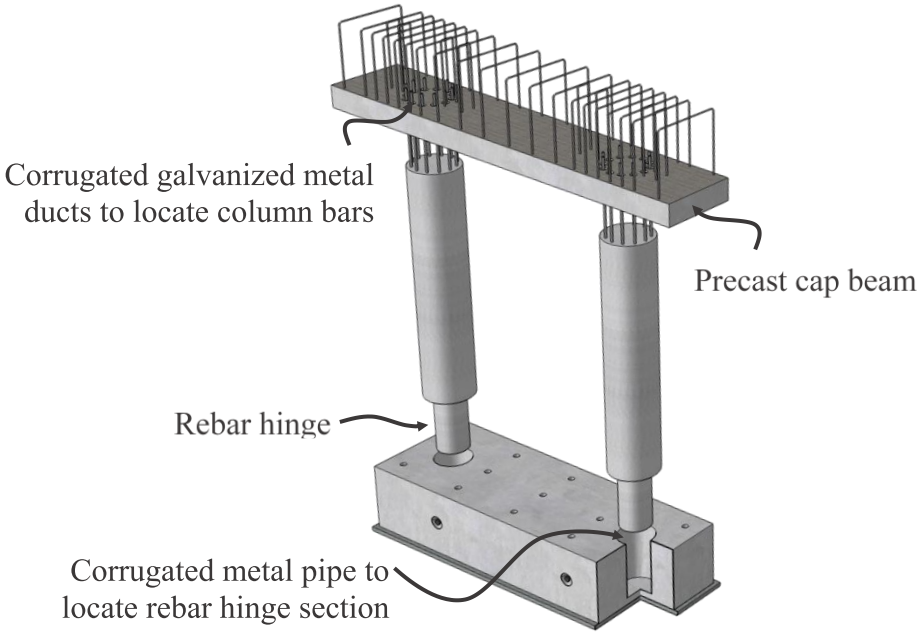

Figure 4.2 Column-to-footing and column-to-cap beam connections

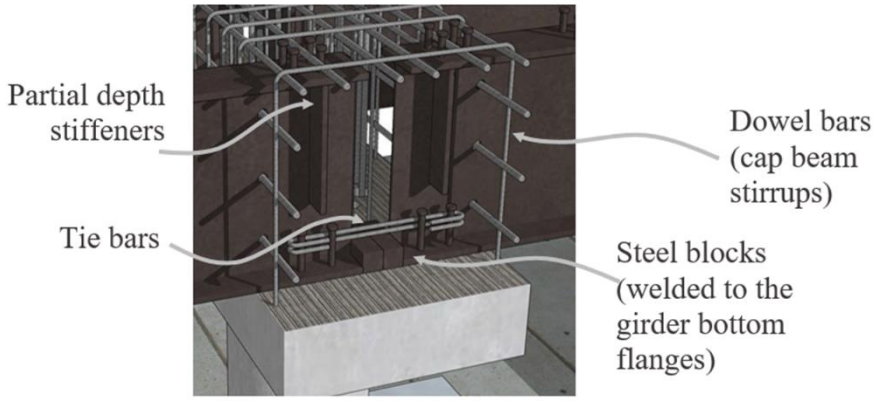

Figure 4.3 SDCL connection (before the placement of deck panels)

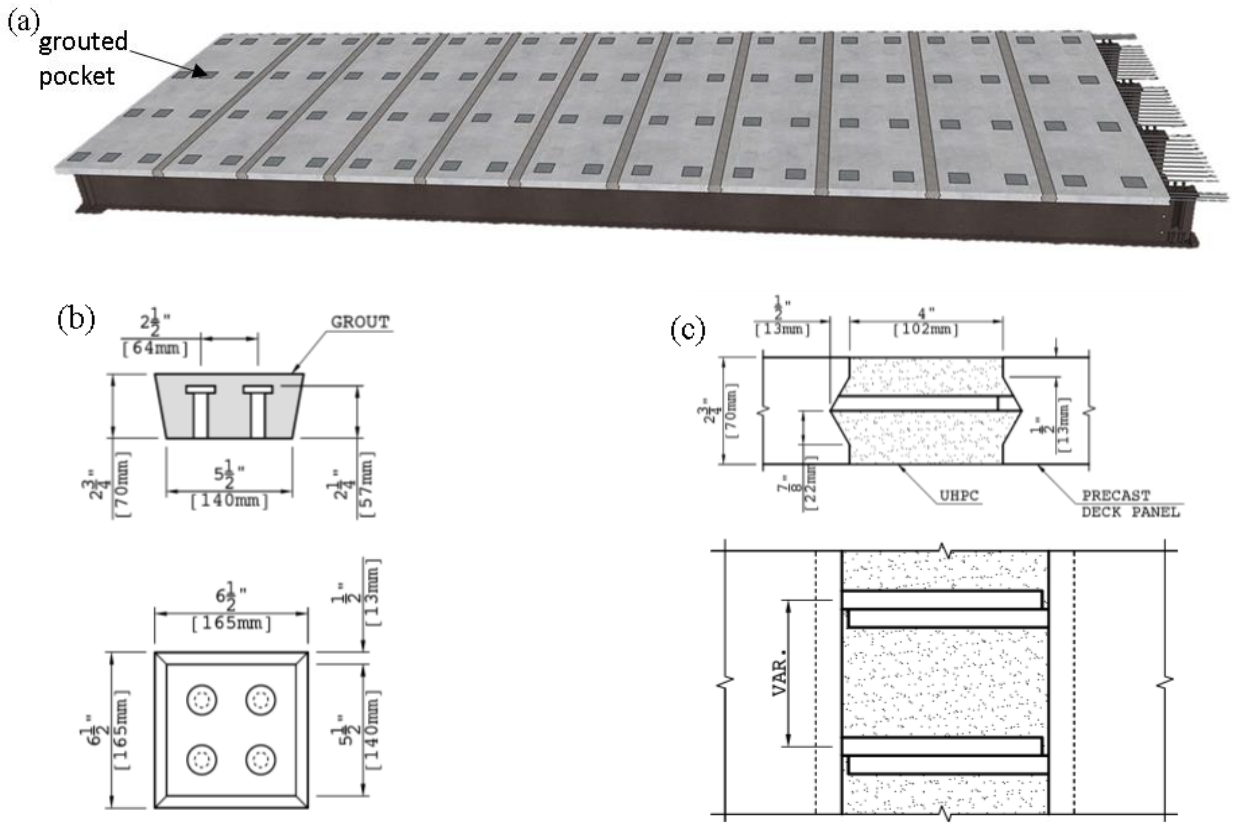

Figure 4.4 (a) The schematics of the superstructure of one span, (b) Details of the deck-to-girder connection, (c) Details of the deck transverse joints

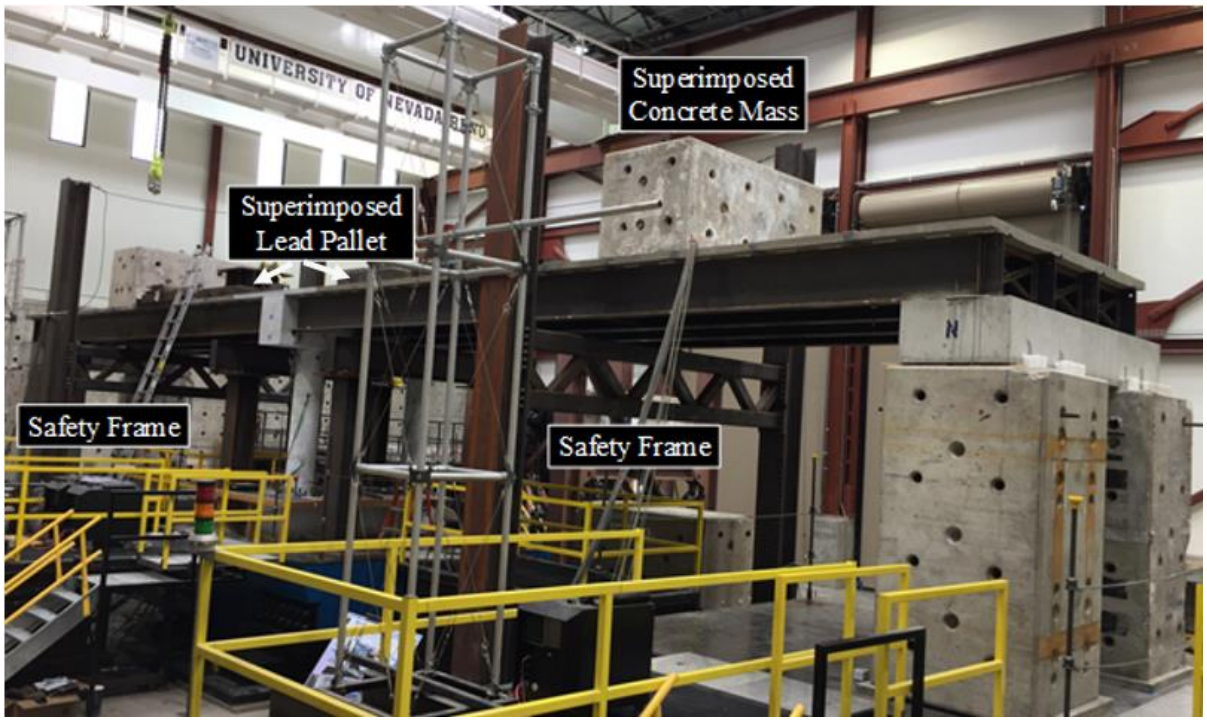

Figure 4.5 Test setup

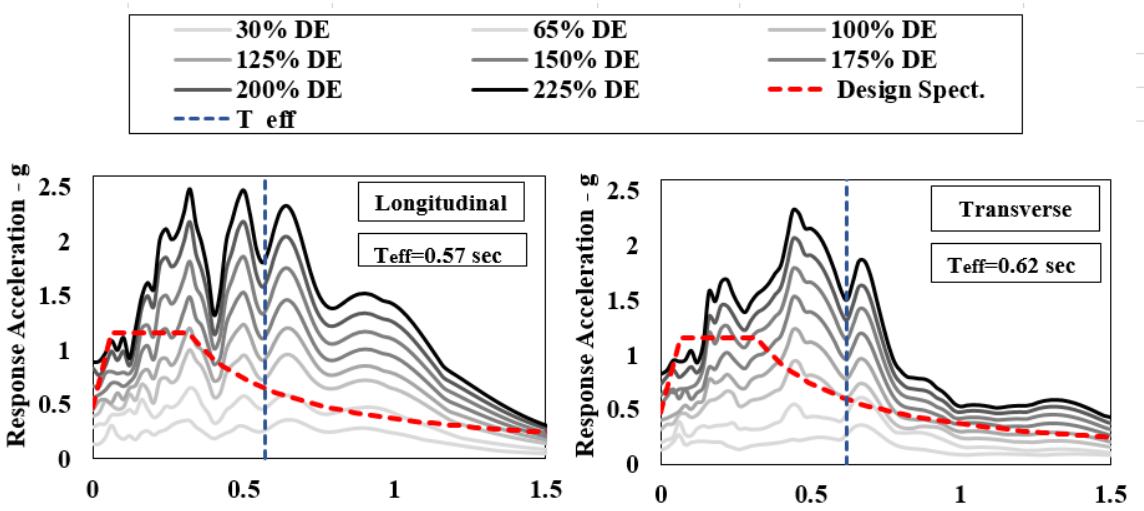

Figure 4.6 Response spectra for each earthquake run, the design spectrum, and the effective periods

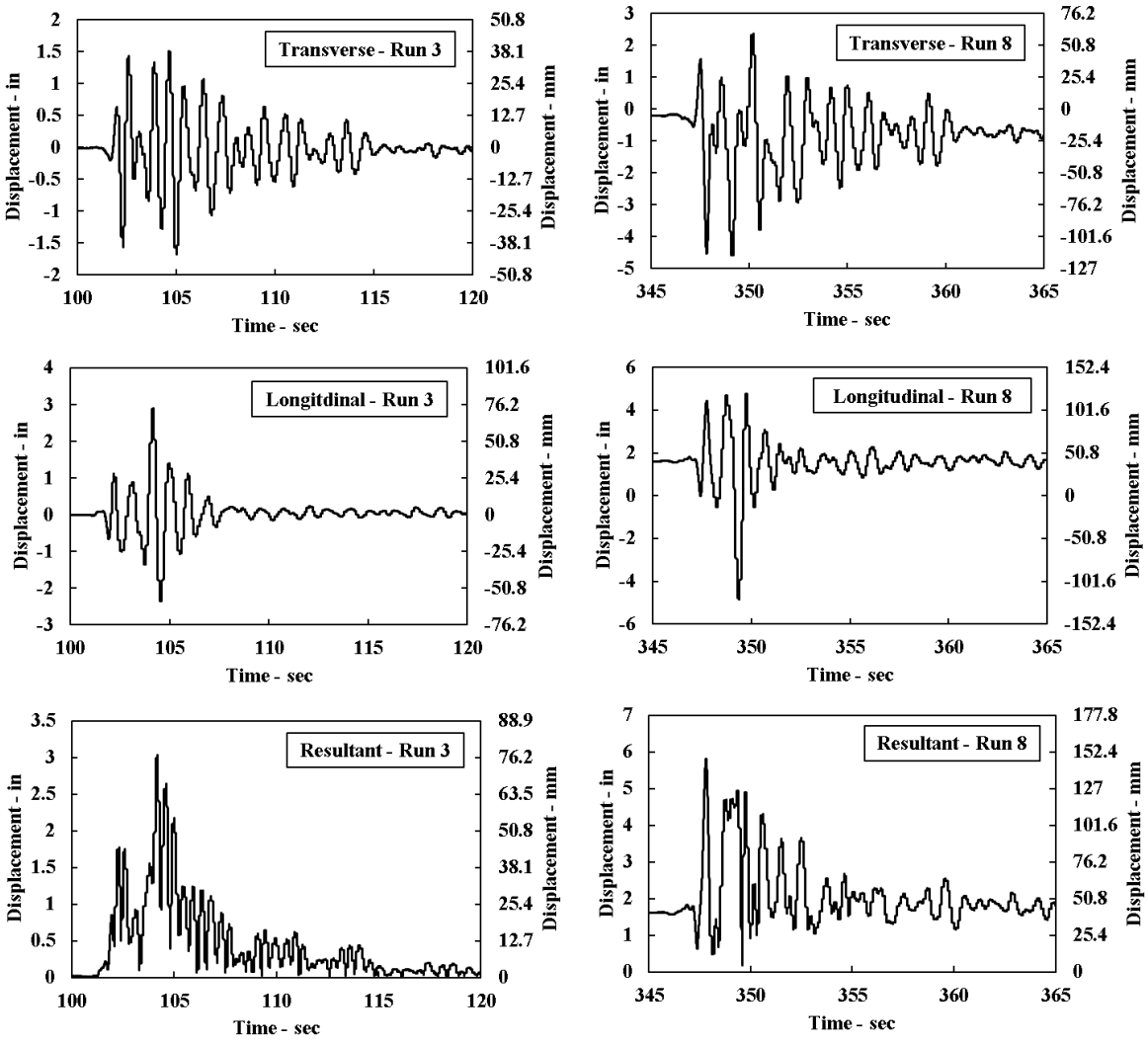

Figure 4.7 Measured displacement histories for runs 3 and 8 (For clarity, only 20 seconds of each run are shown)

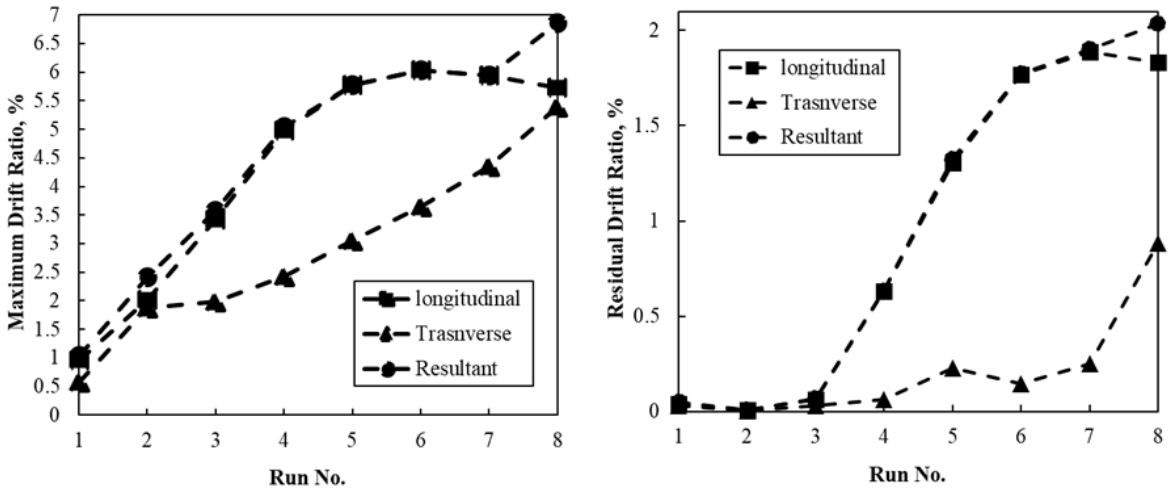

Figure 4.8 Bent peak and residual drift ratios

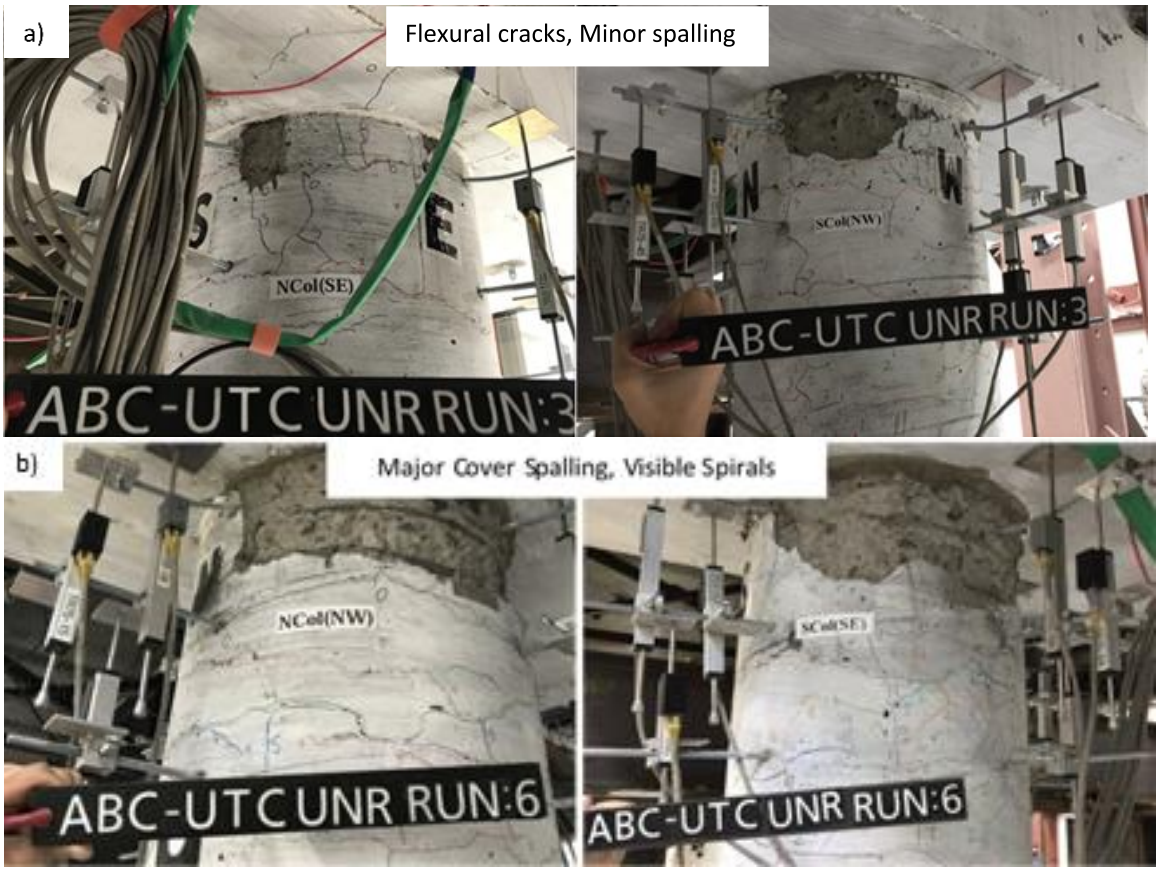

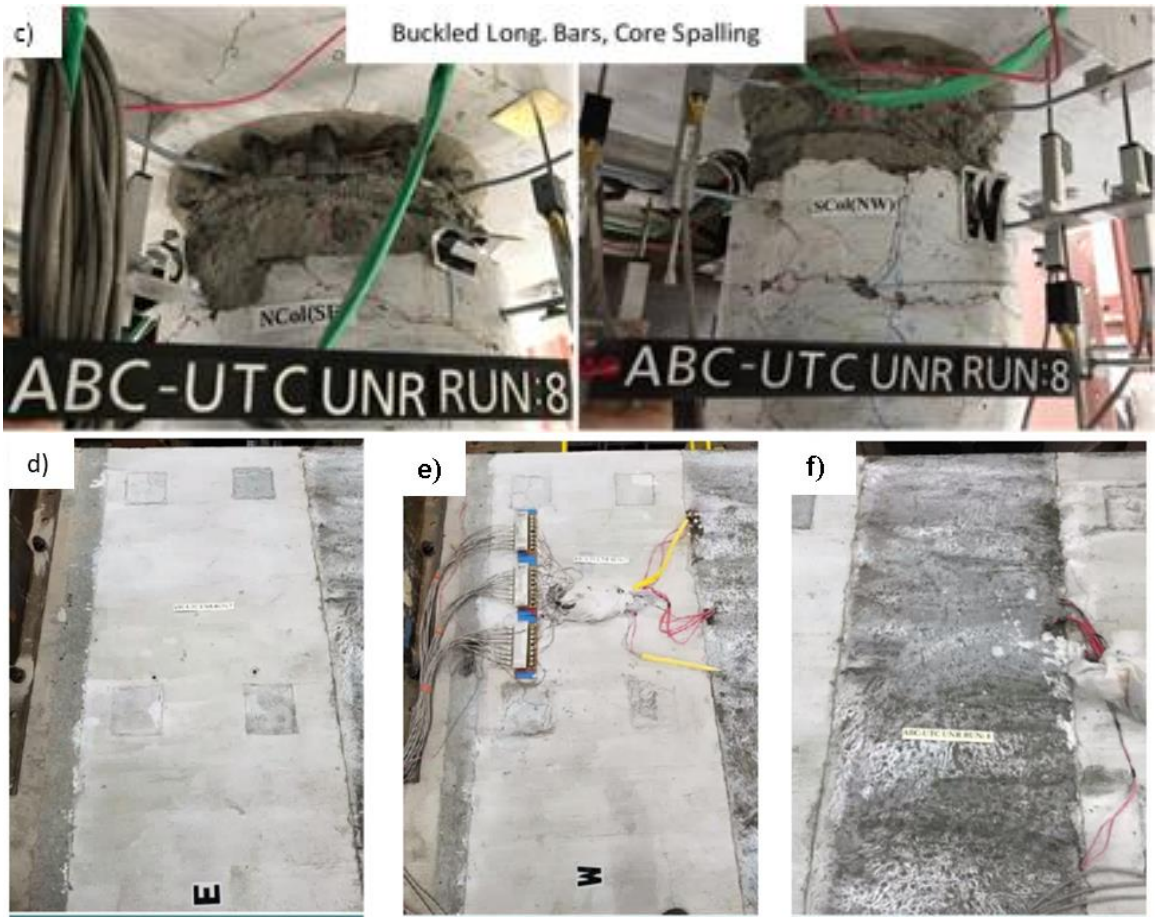

Figure 4.9 Damage states of the column top moment connections at the end of a) run 3, b) run 6, c) run 8; and damage states of the d) girder-to-deck grout-filled pocket connection, e) Panel-to-panel UHPC joint (middle), f) UHPC joint over the pier

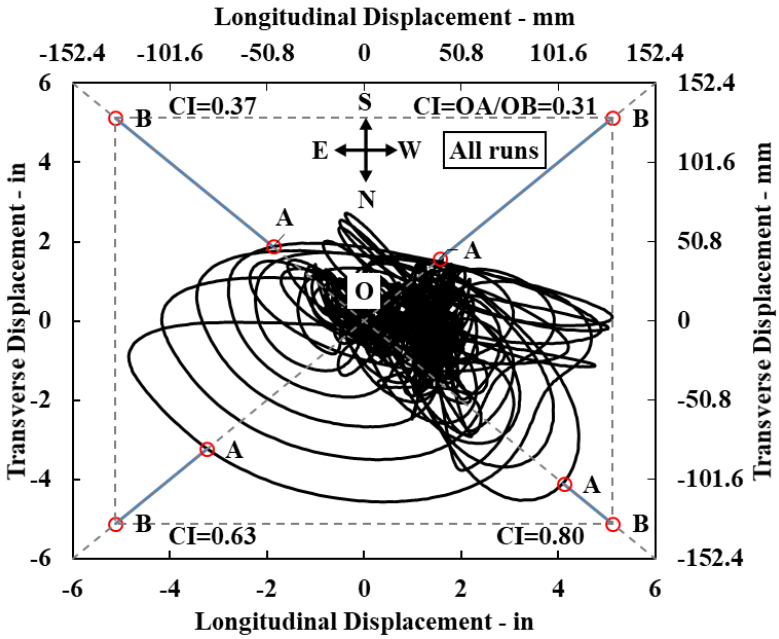

Figure 4.10 Bent top particle movement in the horizontal plane relative to the shake table

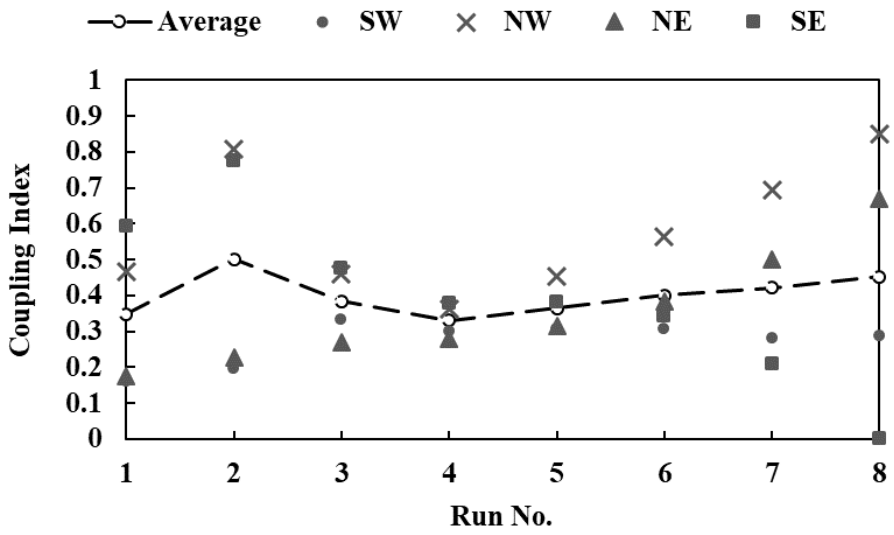

Figure 4.11 Distribution of the coupling indices for each quadrant and the average coupling index

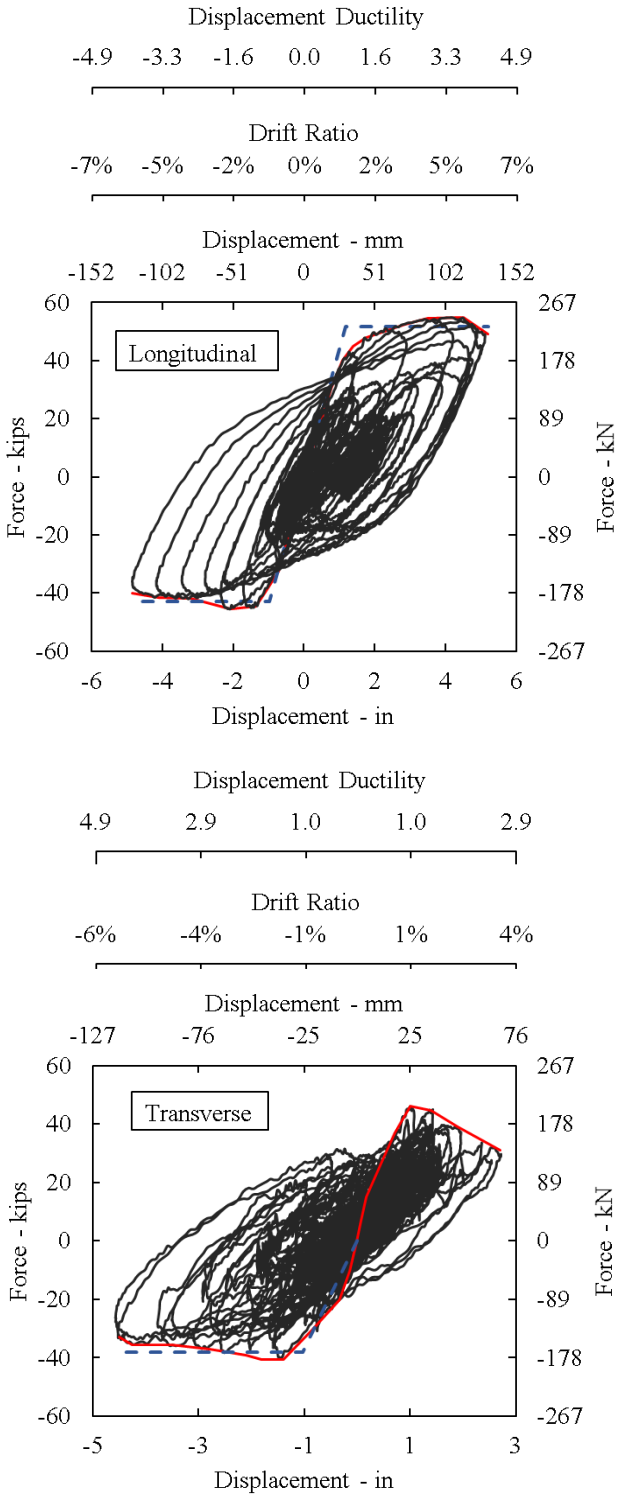

Figure 4.12 Cumulative measured force vs. displacement, envelopes (red), and idealized (blue dashed line) curves

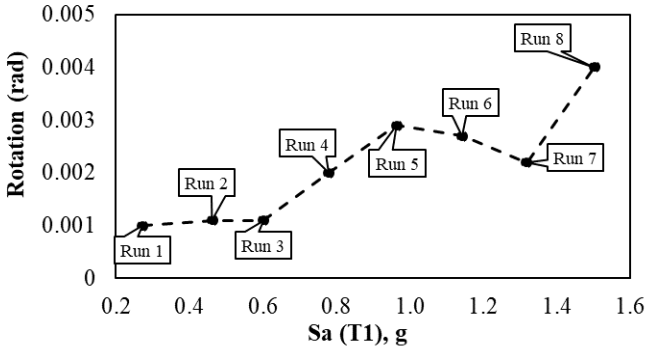

Figure 4.13 Superstructure peak in-plane rotation

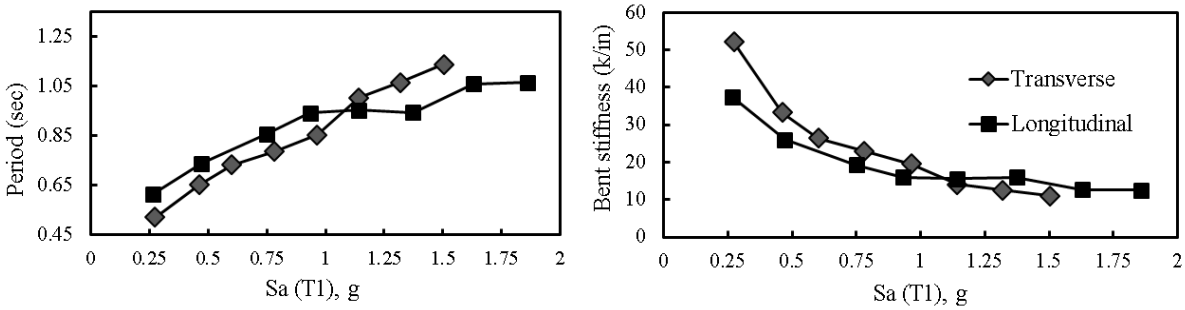

Figure 4.14 Variation of the bent secant stiffnesses and periods throughout seismic tests

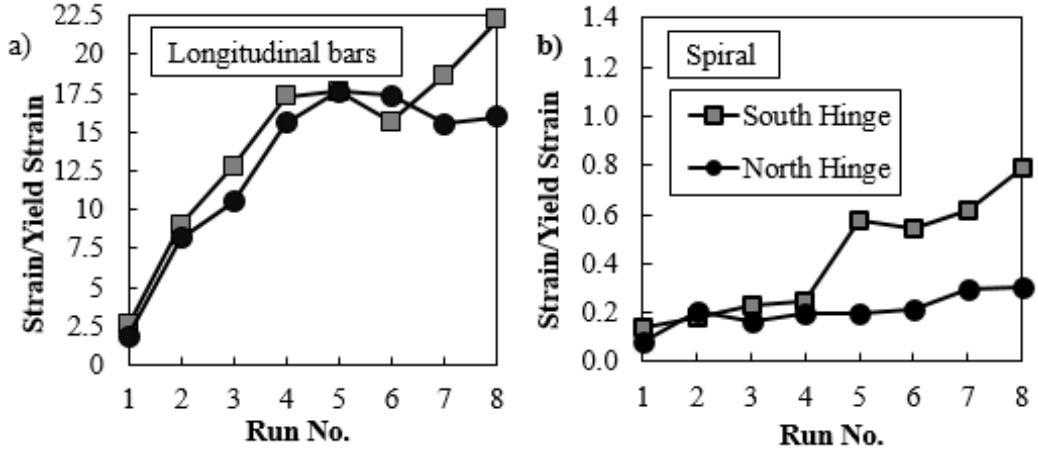

Figure 4.15 Peak tensile strains in rebar hinge a) longitudinal bars, b) spiral

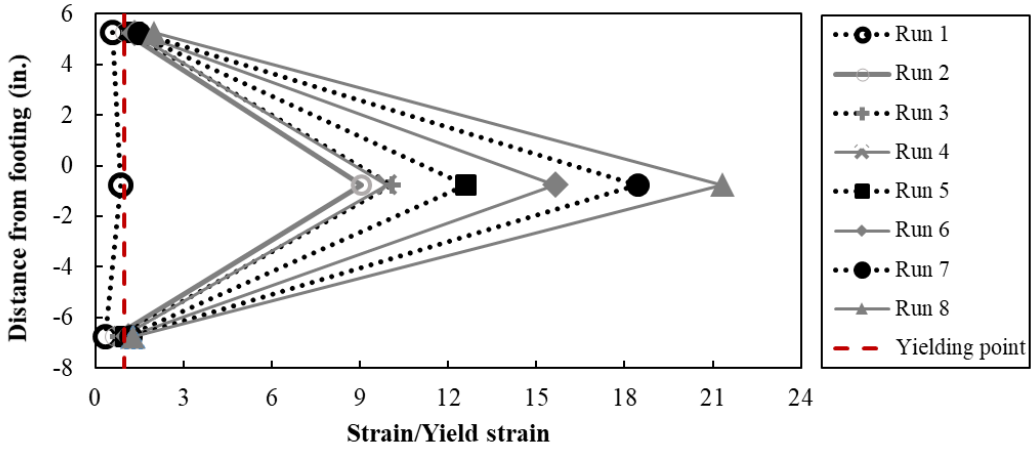

Figure 4.16 Strain profile for the extreme rebar hinge longitudinal bar (South column, west bar)

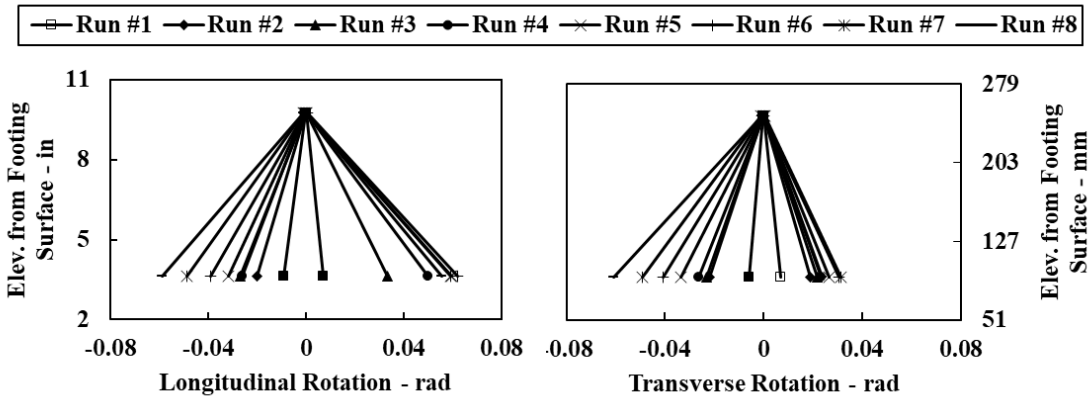

Figure 4.17 Rotation profile along the height for north base hinge

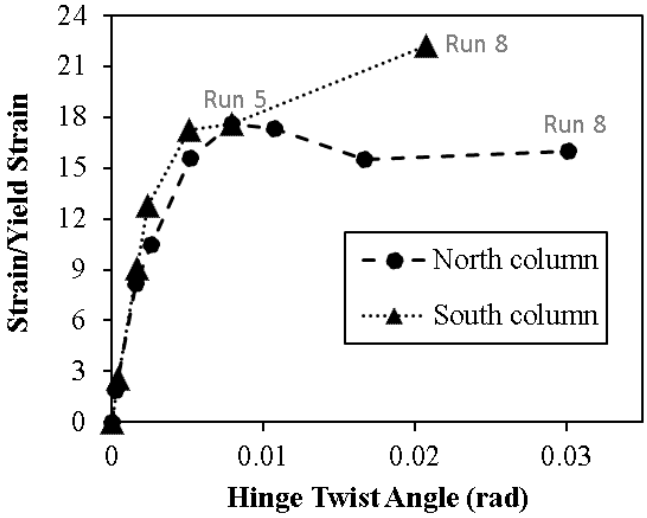

Figure 4.18 Maximum hinge longitudinal bar strain versus hinge in-plane rotation

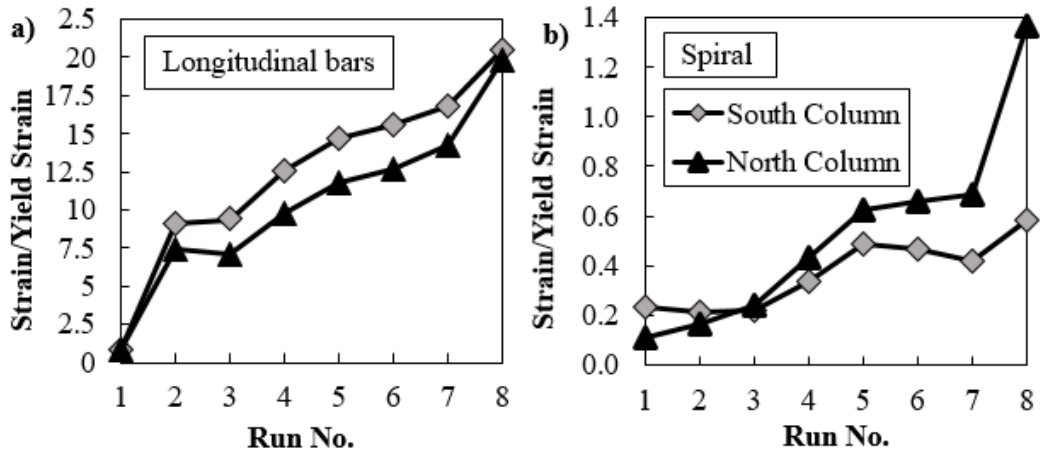

Figure 4.19 Peak tensile strains in column plastic hinge a) longitudinal bars, b) spiral

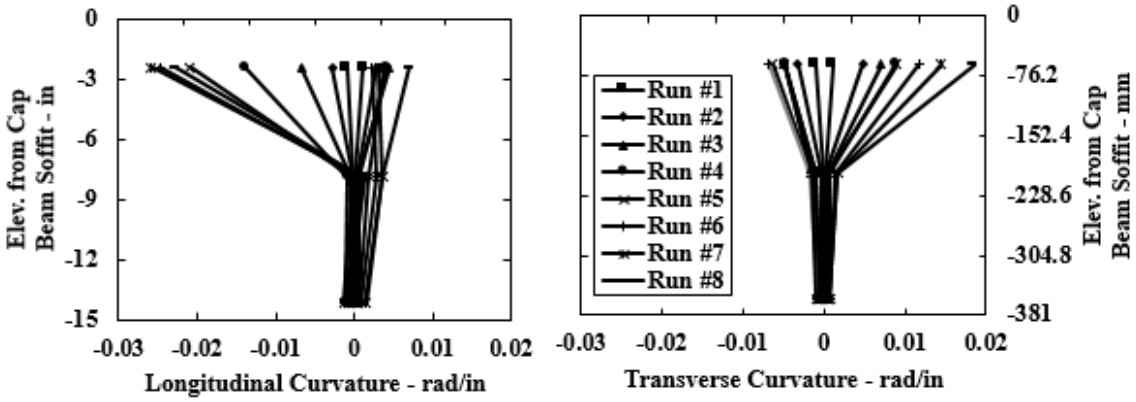

Figure 4.20 Rotation (top figures) and curvature (bottom figures) profiles along the height, for north column top moment connection

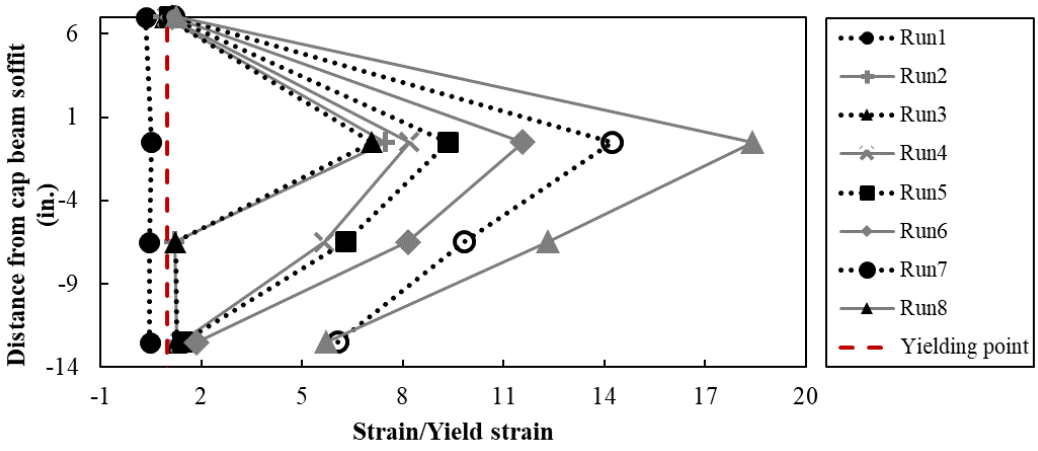

Figure 4.21 Strain profile for the extreme column longitudinal bar (North column, north bar)

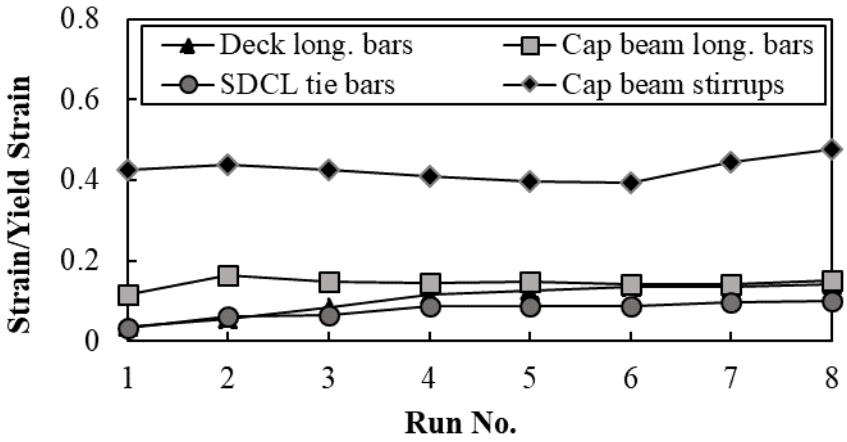

Figure 4.22 Peak tensile strains in cap beam long. bars, stirrups, and tie bars, and deck long. bars

CHAPTER 5: SUMMARY AND CONCLUSIONS

5.1. Summary

Many connections intended for use in accelerated bridge construction (ABC) have been developed and investigated in terms of their local behavior in the past few years. However, to facilitate the use of ABC in routine bridge design and construction in moderate and high seismic zones, information on the holistic seismic performance of the bridge systems integrating various ABC column and superstructure connections is of great interest and highly desired. The lack of sufficient experimental facilities has been, in part, the reason for the scarcity of bridge system seismic testing. The study presented in this document was aimed to address this knowledge gap.

This report presents the design, construction, experimental studies, and analytical investigation of a 0.35 scale, two-span steel girder bridge model incorporating prefabricated elements and six ABC connection types under different levels of earthquake intensity. The ABC connections incorporated in the bridge model were: 1) rebar hinge pocket connection (connecting columns to the footing); (2) column to hybrid cap beam grouted duct connection; (3) SDCL (simple for dead, continuous for live) seismic detail for superstructure to bent cap connection; (4) panel-to-girder grouted pocket connection; (5) short-spliced deck panel rebars in the transverse panel-to-panel joints filled with ultra-high performance concrete (UHPC); and (6) spliced deck panel rebars in UHPC-filled panel-to-panel joint over the pier. The bridge model was subjected to eight biaxial earthquake motions with increasing amplitudes simulating a modified version of the 1994 Northridge-Sylmar earthquake record.

The main objective of the study was to evaluate the performance of ABC bridges combining multiple connection types under various levels of bi-directional earthquakes including motions that simulated 225% of the design level earthquake. Other objectives were to assess the adequacy of some of the emerging design methods for critical ABC connections, the constructability of the prefabricated elements and ABC constructions, the applicability of the current analytical modeling methods for ABC bridges, and the effect of key parameters that were not included in the experimental phase of the study.

A comprehensive state-of-the-art literature review was conducted on the ABC connections that were selected for incorporation in the test model and was presented in Ch. 2. Given that the design and construction procedures for ABC connections are not yet adopted in bridge codes as of this writing, detailed discussion of the design, construction, and shake table testing of the bridge model were included in Chapter 3 and Appendix A. Following the shake table test, the observed and measured performance of the model were evaluated in terms of the extent of the apparent damage, local responses, and global response parameters as discussed in Chapter 4 and Appendix B.

5.2. Observations of Experimental Studies

The key observations from the experimental phase of the project were as follows:

1) The performance of the ABC bridge model was satisfactory and emulative of cast-in-place bridges. The column connections underwent large inelastic deformations in a ductile flexural mode while the four other ABC connections and

the capacity-protected components remained elastic and damage free. The structural integrity was maintained even during extreme seismic loading.

2) Columns failure occurred after undergoing a 6.9% resultant drift ratio. During the last run, the longitudinal bars in the north column buckled, and the core damage turned into a large loss of core concrete immediately under the cap beam.
3) Visible damage in the cap beam, superstructure, and all ABC connections incorporated in the superstructure was limited to a few hairline cracks in the cap beam and on the bottom of the deck panels adjacent to the pier; which is an acceptable in capacity protected design.
4) No duct or bar pullout was noticed in the grouted duct connection. Damage was limited to minor spalling of the grout in the ducts at the column-cap beam interface, which allowed for the spread of yielding in the column longitudinal bars. Buckling of the longitudinal bars in the column plastic hinges showed that the column-cap beam connection was effective in forcing plastic hinging of the columns. Although the connection was subjected to bi-axial loading, no spalling or diagonal cracks was observed in the cap beam. These indicate that embedment length of the column longitudinal bars was sufficient, and the bar force transfer mechanism was appropriate.
5) The embedment length of the rebar hinge section in the footing (1.25 times the required tension development length of the column longitudinal bars) was sufficient to develop the hinge plastic moment.
6) The maximum strain in the rebar hinge pocket connection occurred at the footing-column interface, yielding of the hinge longitudinal bars was spreading well into the adjoining members, and gap closure was prevented with no bar fracture or damage to the pocket connection.
7) The peak horizontal slippage of the rebar hinges relative to the footing was negligible compared to the bent displacements. The rebar hinge sections resisted the column plastic shear and did not fail in shear.
8) The peak relative deformation between the deck panels and the girders was negligible even under the 2.25 times design level earthquake.
9) No damage was visible in the field-cast UHPC joints over the pier and between the adjacent deck panels except for a few hairline cracks parallel to the joint on the bottom of the deck panels adjacent to the pier.
10) Despite the fact that the bridge model had no skew angle, minor superstructure in-plane rotations were observed in Run 4 (corresponding to 125% of the design level earthquake) and the subsequent runs. These rotations are attributed to the fundamental mode being the in-plane rotation, the asymmetric damages in the columns, and asymmetric friction forces that relocated the bridge center of stiffness, which was at the bent in the intact bridge.

5.3. Conclusions

The key conclusions drawn from the experimental studies conducted in this investigation are highlighted as follows.

1) Steel girder bridges that incorporate prefabricated elements and ABC connections can offer excellent seismic performance and constructability under bi-axial horizontal seismic loading.
2) The seismic performance of column-cap beam connections in which the column longitudinal bars are partially anchored in a lower precast cap beam in grouted ducts and extended further into the cast-in-place portion of the cap beam is similar to cast-in-place construction, where columns and cap beam are cast monolithically.
3) Rebar hinge pocket connections performed well under combined strong biaxial horizontal earthquake loading by developing nonlinearity in the rebar hinge longitudinal bars and spalling of the hinge throat cover with no shear failure.
4) Steel superstructure to cap beam connection that relies on the deck longitudinal bars and cap beam stirrups for the transfer of the negative and positive moments, respectively can perform as a rigid joint and is similar to cast-in-place construction under strong horizontal biaxial seismic loading.
5) Grout-filled deck pocket connections and field cast UHPC joints between adjacent deck panels provide sufficient structural integrity under severe earthquake loading.
6) Field cast UHPC joints over the pier provide sufficient structural integrity under severe earthquake loading. This method is an excellent alternative to using mechanical splices or utilizing hooked bars over the piers, both of which complicate construction.

APPENDIX A: DESIGN, CONSTRUCTION, AND TESTING

This appendix contains complete documentation of the design, construction, and testing of the two-span bridge model. General discussion of the material presented in this appendix was included in various chapters of the main report. The documents are presented in the following order:

A.1. Test model drawings

A.2. Construction photos

A.3. Material test data

A.3.1. Reinforcing steel

A.3.2. Concrete, grout, and UHPC

A.4. Instrumentation, test setup, and loading protocol

A.1. Test model drawings

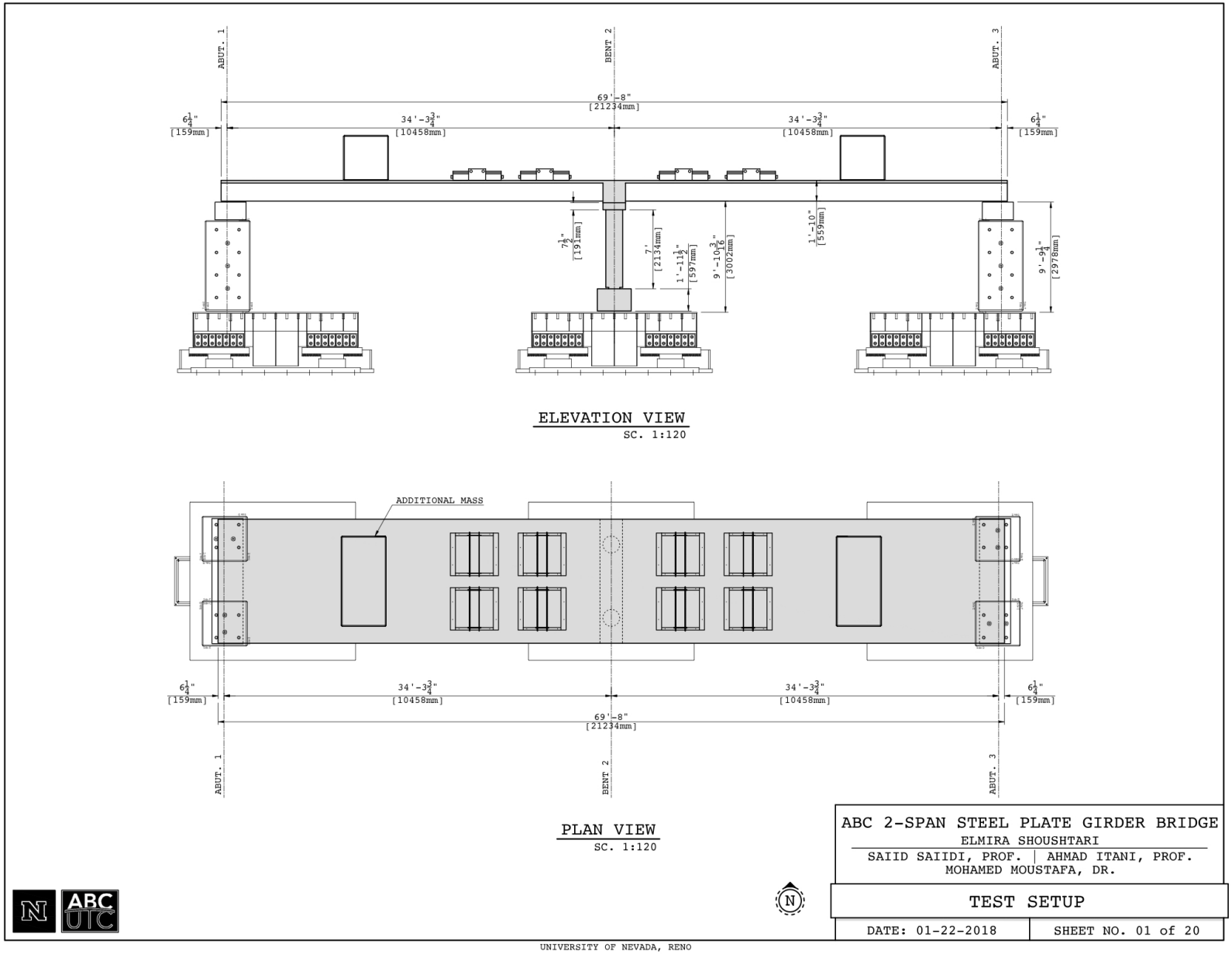

Figure A.1 Test setup

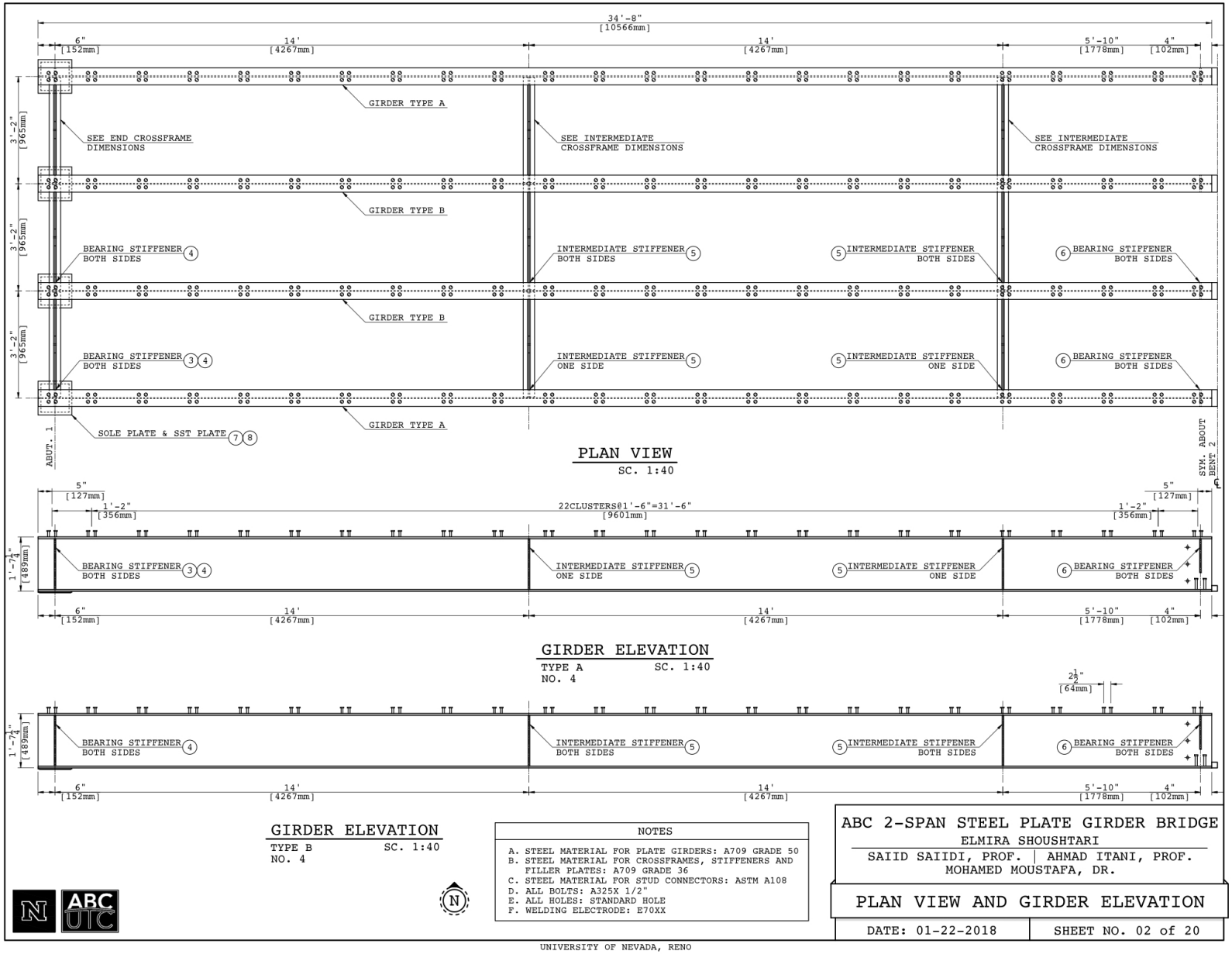

Figure A.2 Plan view and girder elevation

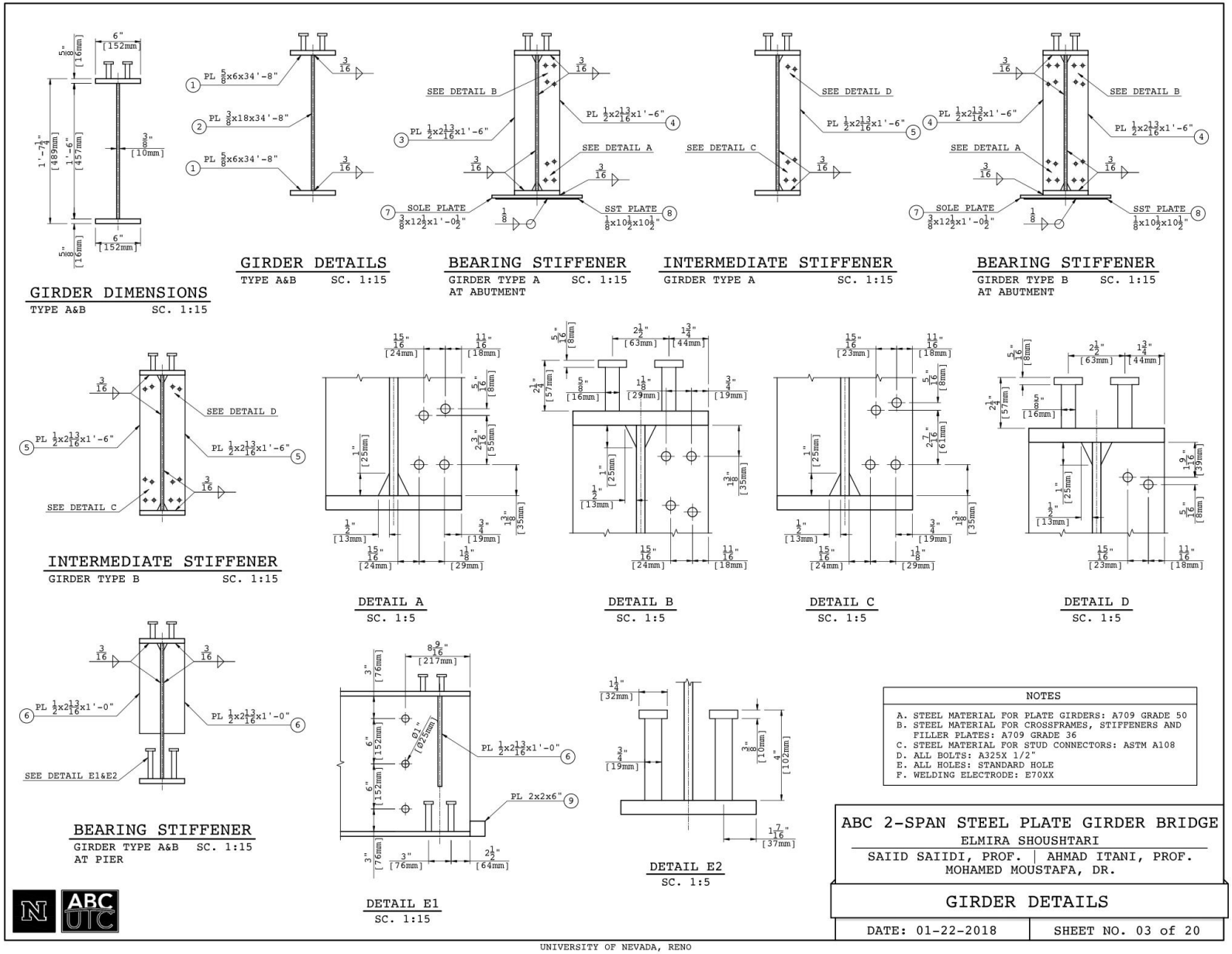

Figure A.3 Girder details

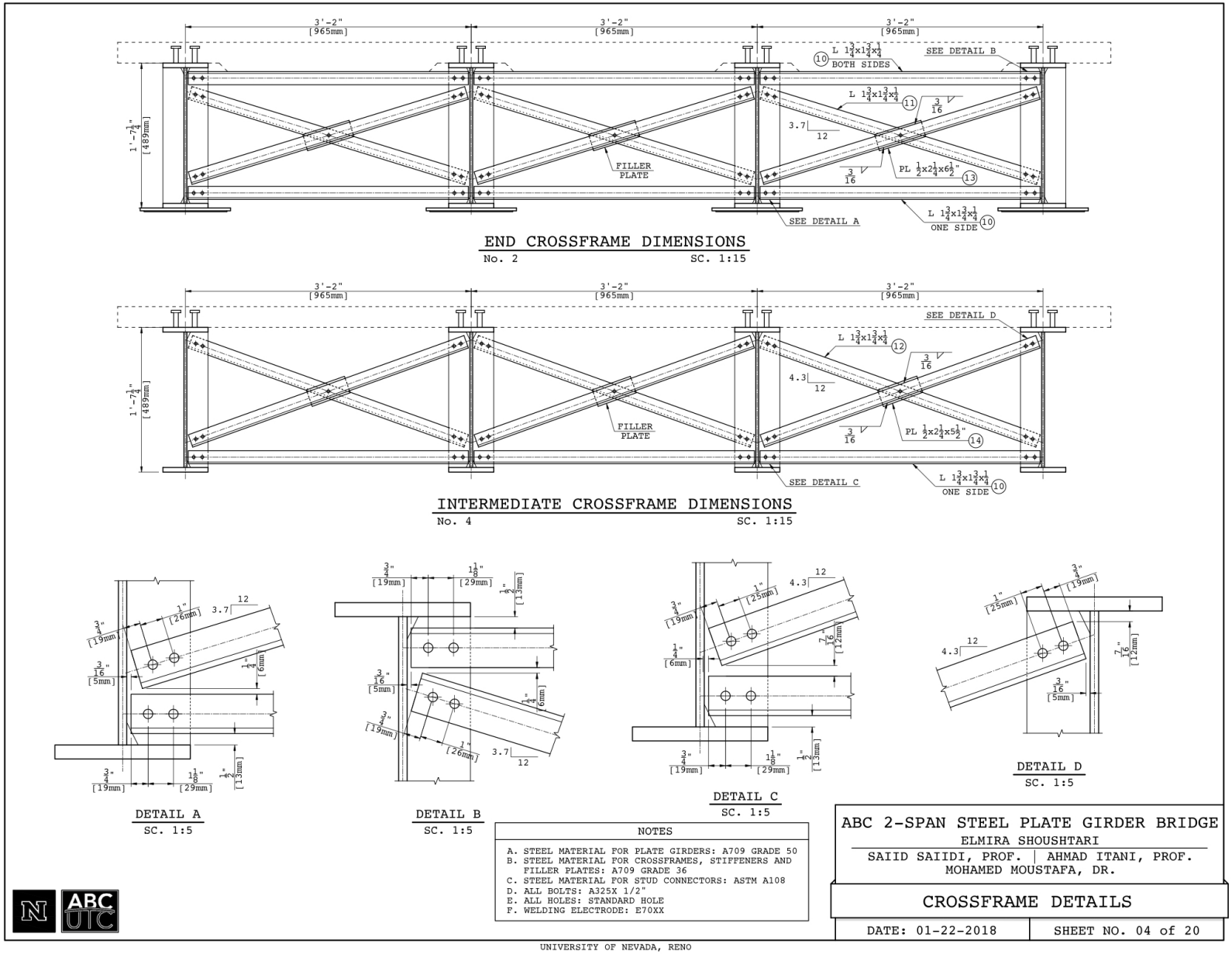

Figure A.4 Cross frame details

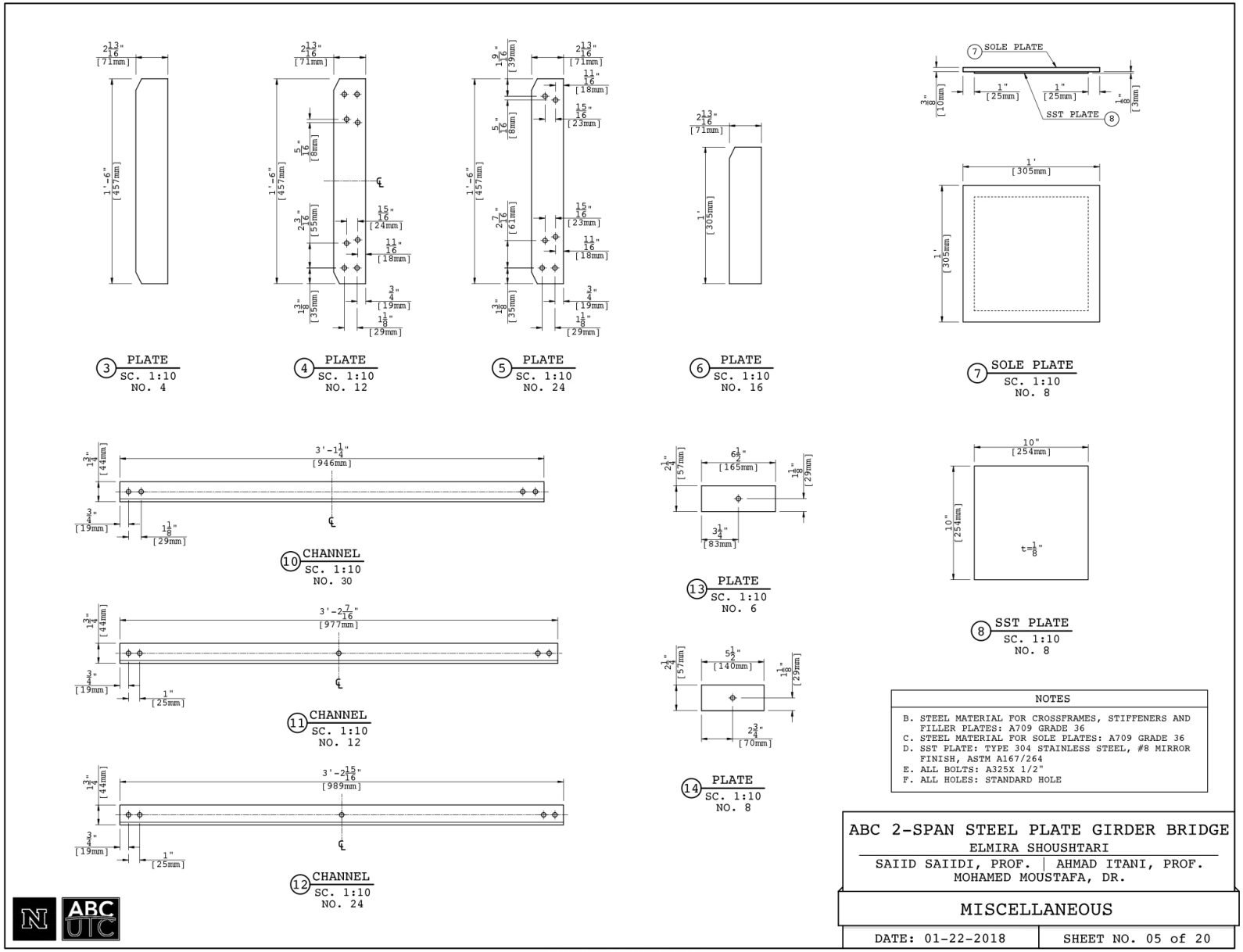

Figure A.5 Girder and cross frame details

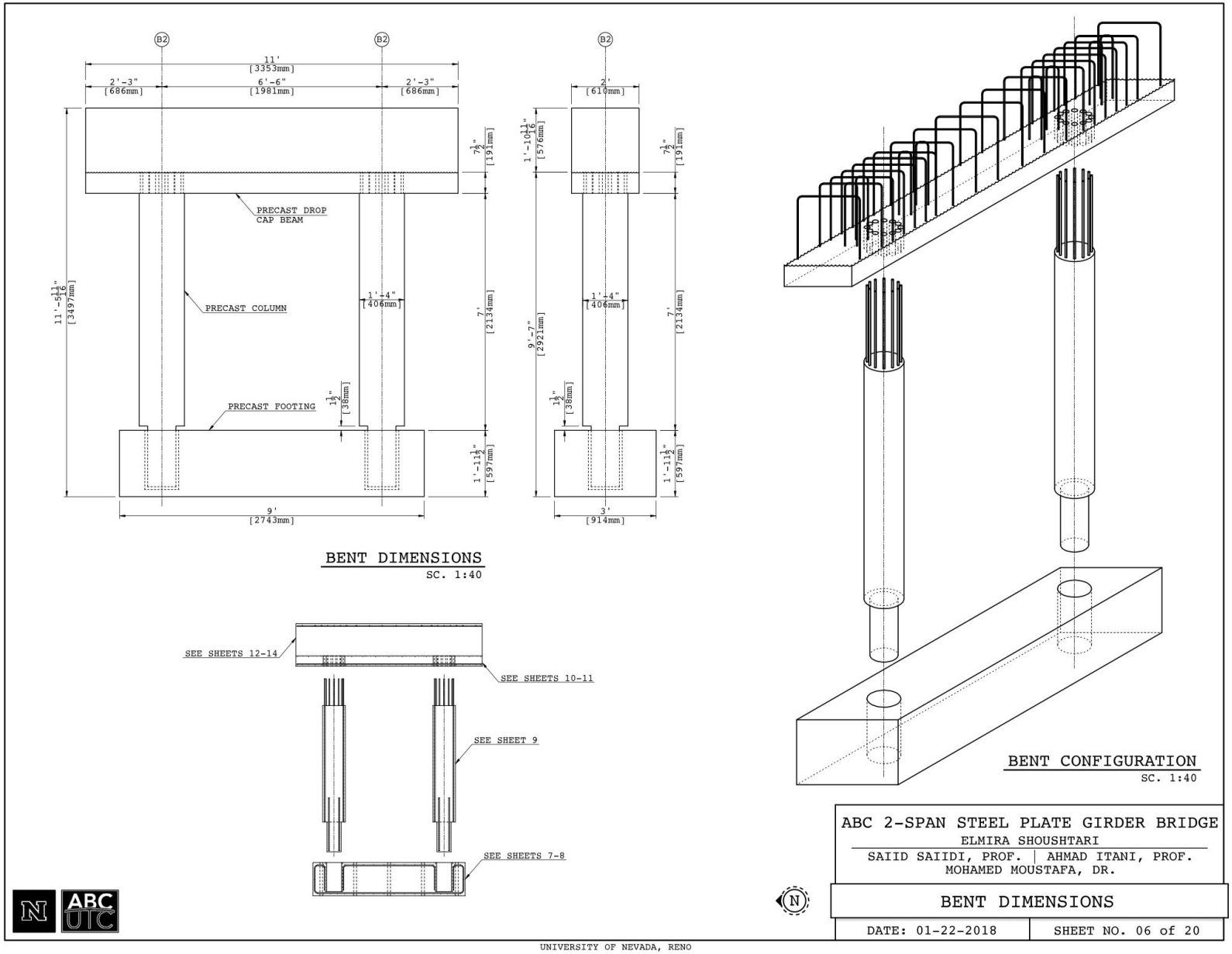

Figure A.6 Bent dimensions

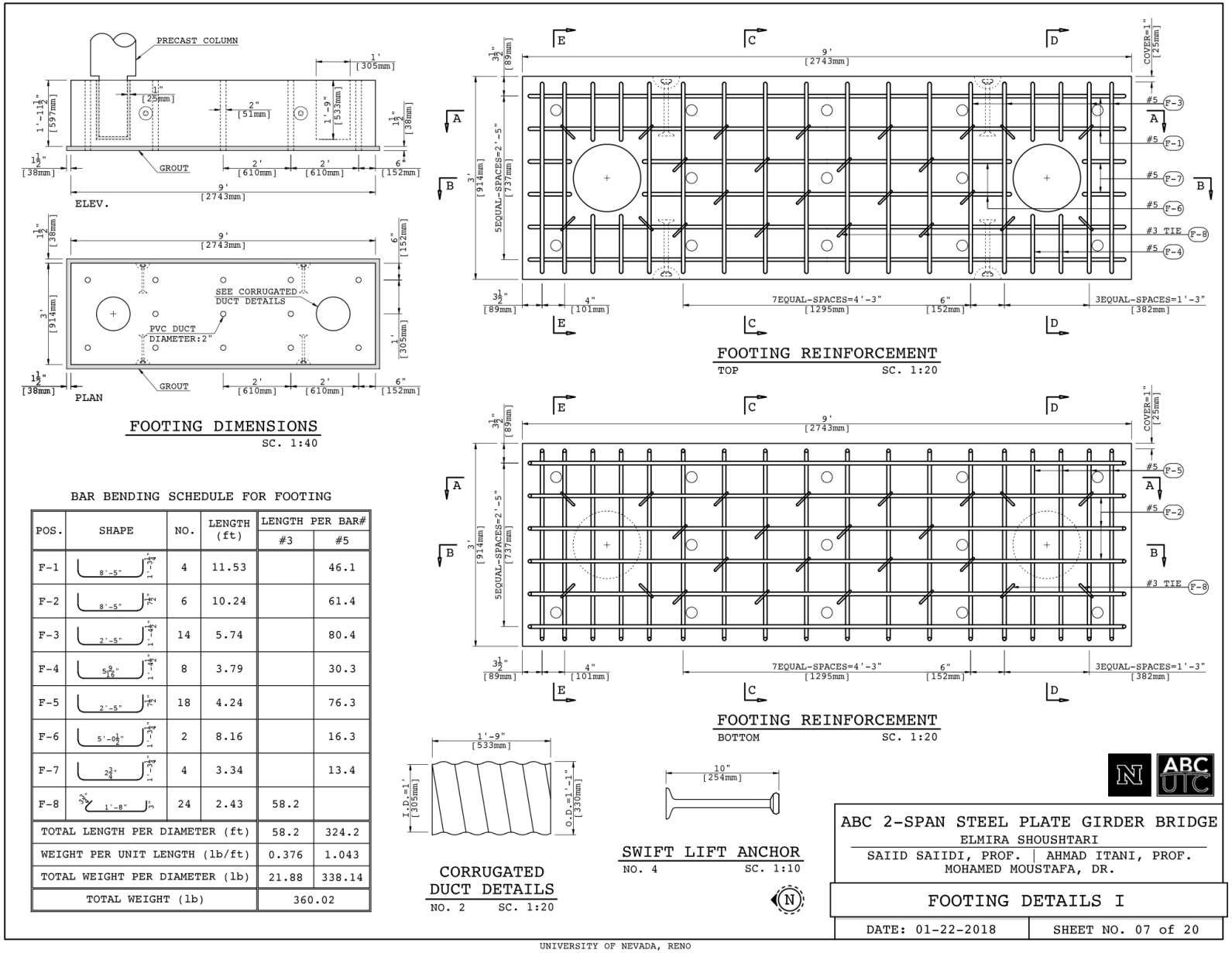

BAR BENDING SCHEDULE FOR FOOTING

POS.	SHAPE	NO.	LENGTH (ft)	LENGTH PER BAR#	
				#3	#5
F-1	8'-5"	4	11.53		46.1
F-2	8'-5"	6	10.24		61.4
F-3	2'-5"	14	5.74		80.4
F-4	5 9/16"	8	3.79		30.3
F-5	2'-5"	18	4.24		76.3
F-6	5'-0 1/2"	2	8.16		16.3
F-7	2 3/4"	4	3.34		13.4
F-8	1'-8"	24	2.43	58.2	
TOTAL LENGTH PER DIAMETER (ft)				58.2	324.2
WEIGHT PER UNIT LENGTH (lb/ft)				0.376	1.043
TOTAL WEIGHT PER DIAMETER (lb)				21.88	338.14
TOTAL WEIGHT (lb)				360.02	

Figure A.7 Reinforcement and details of the footing (I)

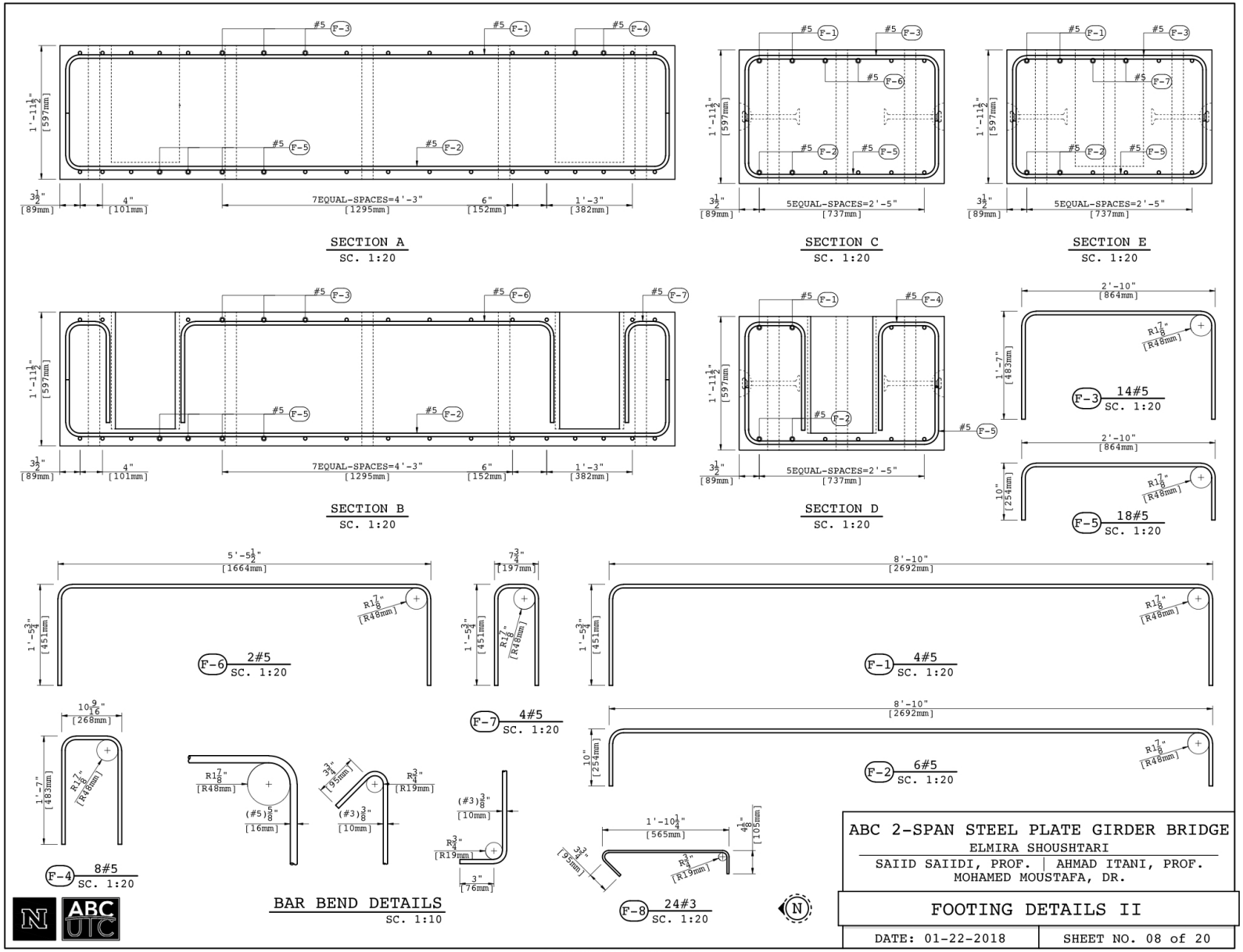

Figure A.8 Reinforcement and details of the footing (II)

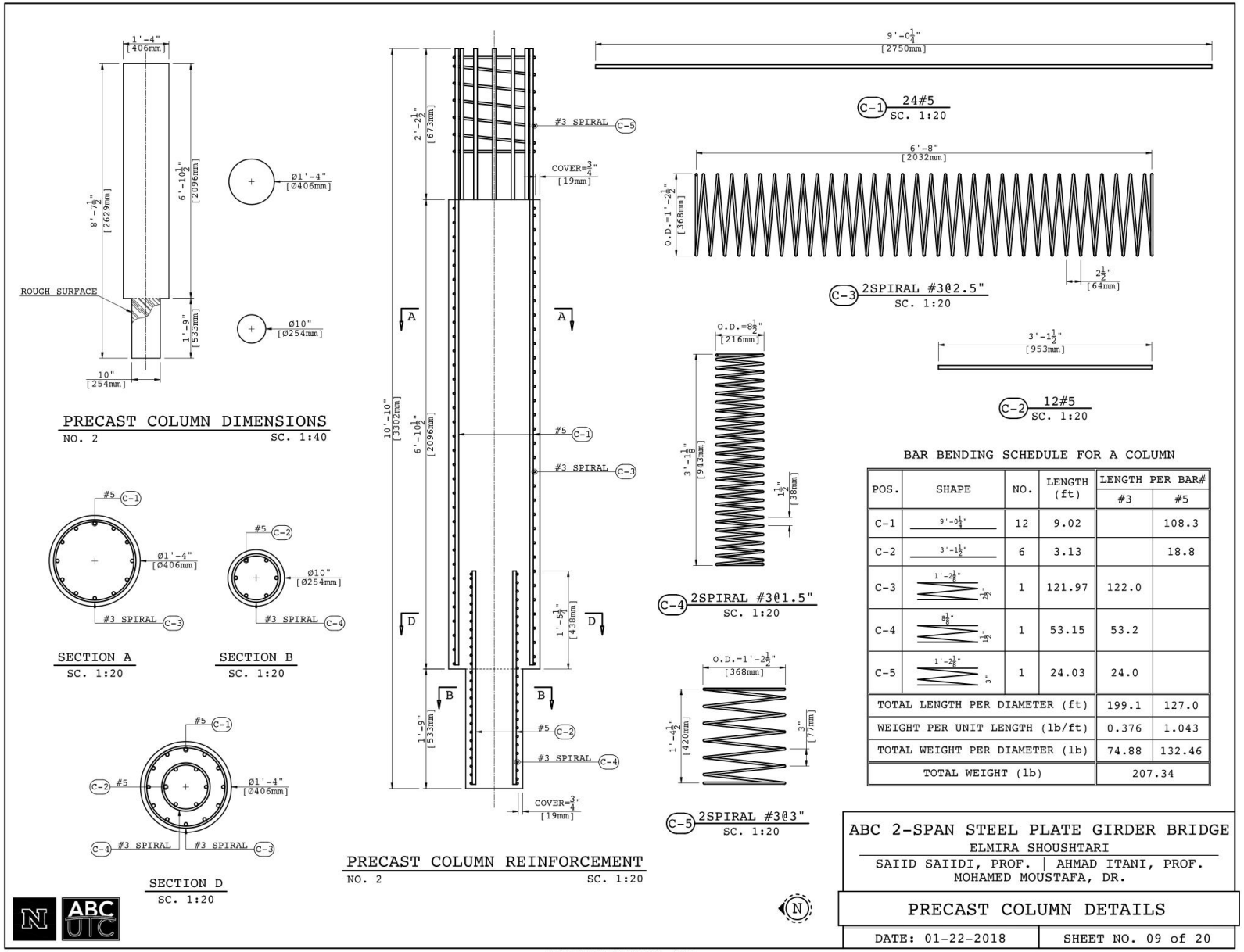

Figure A.9 Reinforcement and details of the column

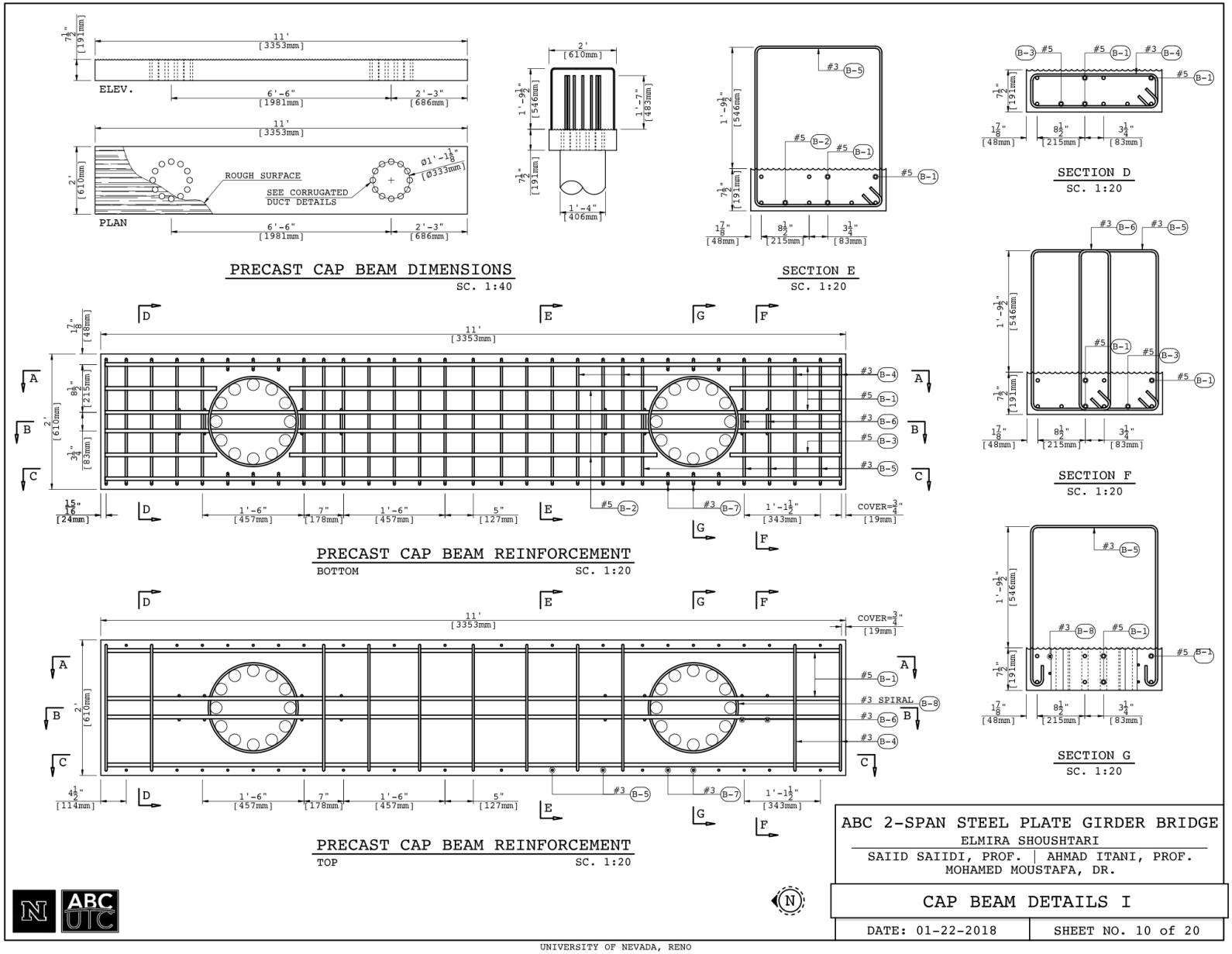

Figure A.10 Reinforcement and details of the cap beam (I)

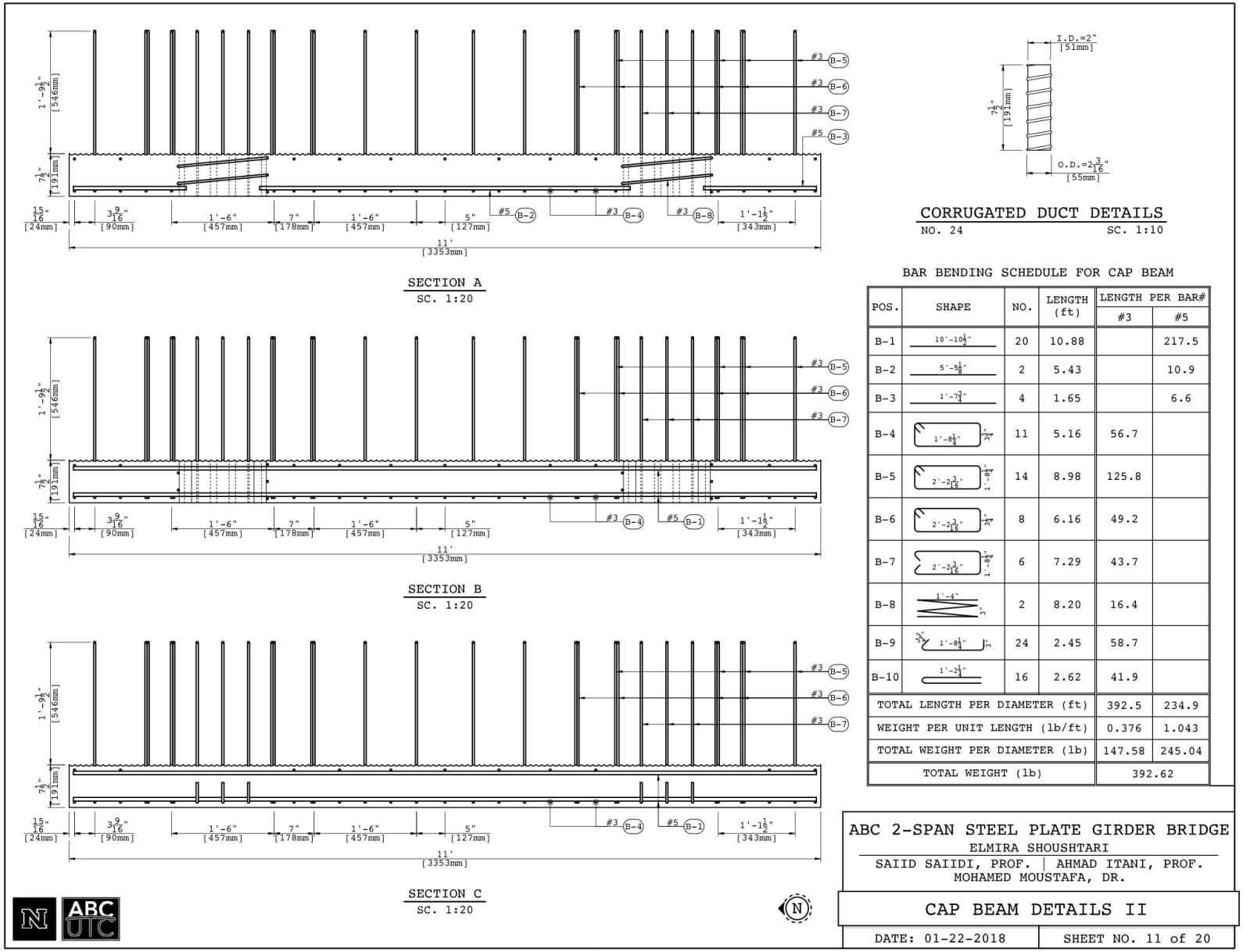

POS.	SHAPE	NO.	LENGTH (ft)	LENGTH PER BAR#	
				#3	#5
B-1	10'-10¼"	20	10.88		217.5
B-2	5'-5⅛"	2	5.43		10.9
B-3	1'-7¾"	4	1.65		6.6
B-4	1'-8¼"	11	5.16	56.7	
B-5	2'-2 3/16"	14	8.98	125.8	
B-6	2'-2 3/16"	8	6.16	49.2	
B-7	2'-2 3/16"	6	7.29	43.7	
B-8	1'-4"	2	8.20	16.4	
B-9	1'-8¼"	24	2.45	58.7	
B-10	1'-2¼"	16	2.62	41.9	
TOTAL LENGTH PER DIAMETER (ft)				392.5	234.9
WEIGHT PER UNIT LENGTH (lb/ft)				0.376	1.043
TOTAL WEIGHT PER DIAMETER (lb)				147.58	245.04
TOTAL WEIGHT (lb)				392.62	

Figure A.11 Reinforcement and details of the cap beam (II)

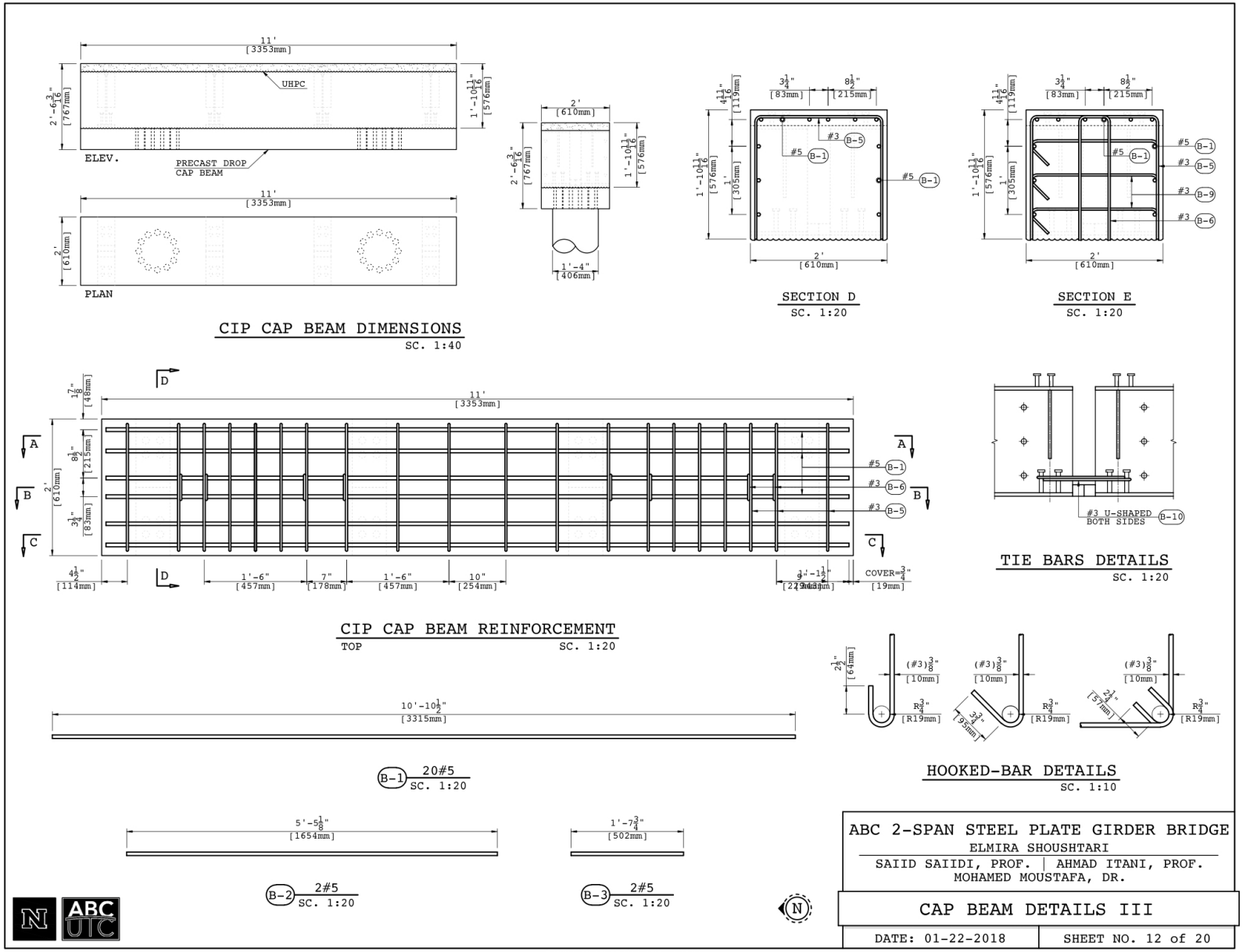

Figure A.12 Reinforcement and details of the cap beam (III)

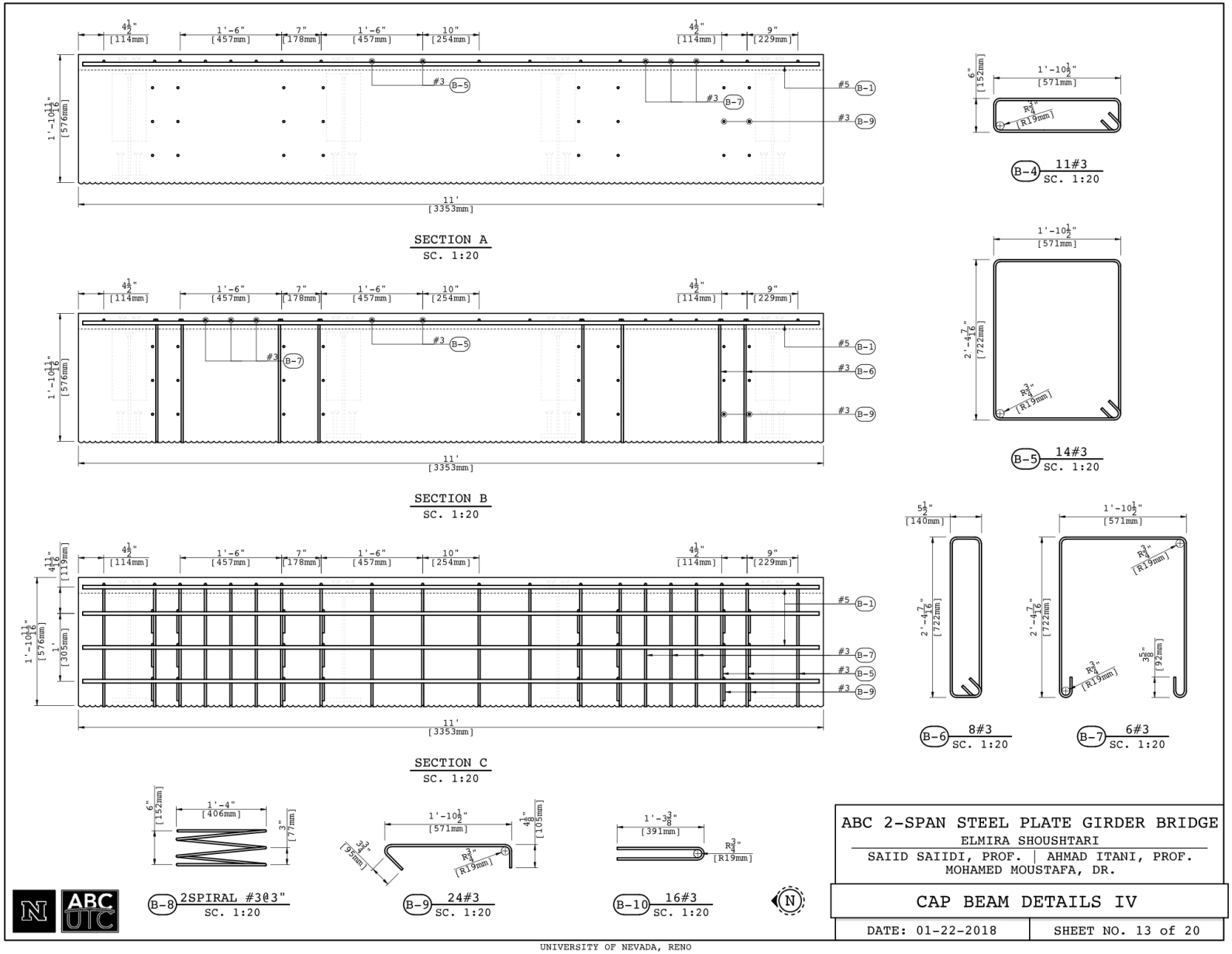

Figure A.13 Reinforcement and details of the cap beam (IV)

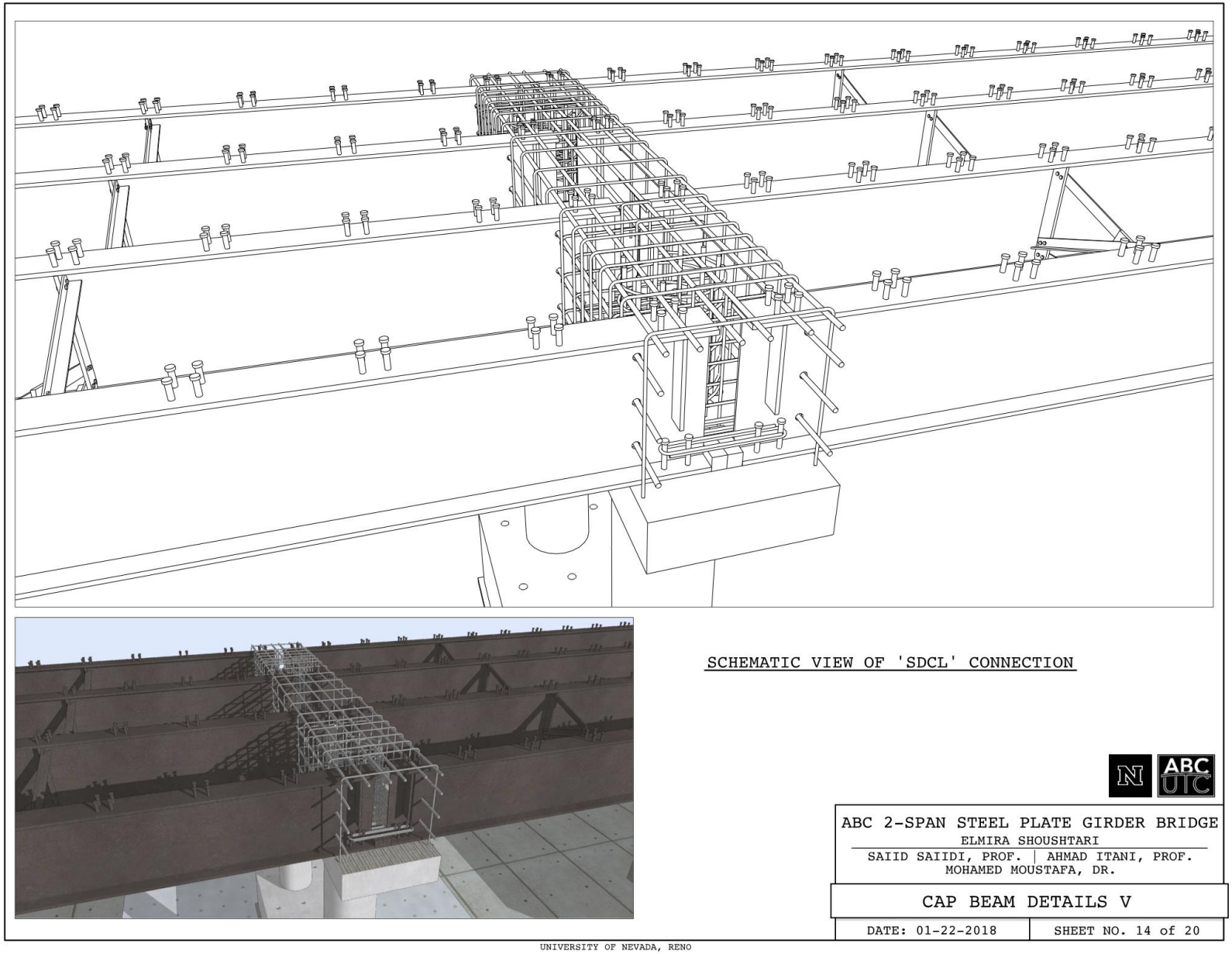

Figure A.14 Reinforcement and details of the cap beam (V)

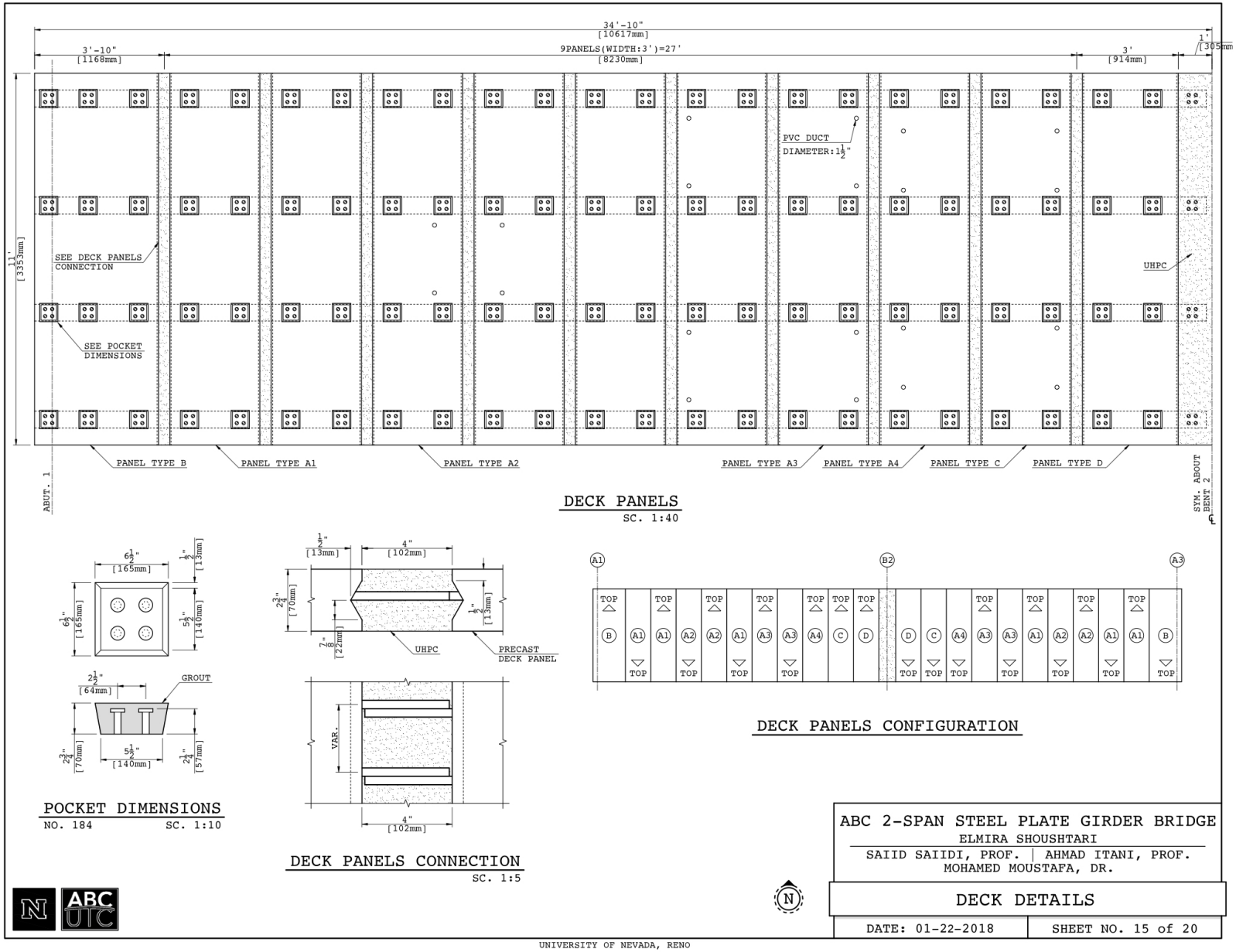

Figure A.15 Details of deck panels (I)

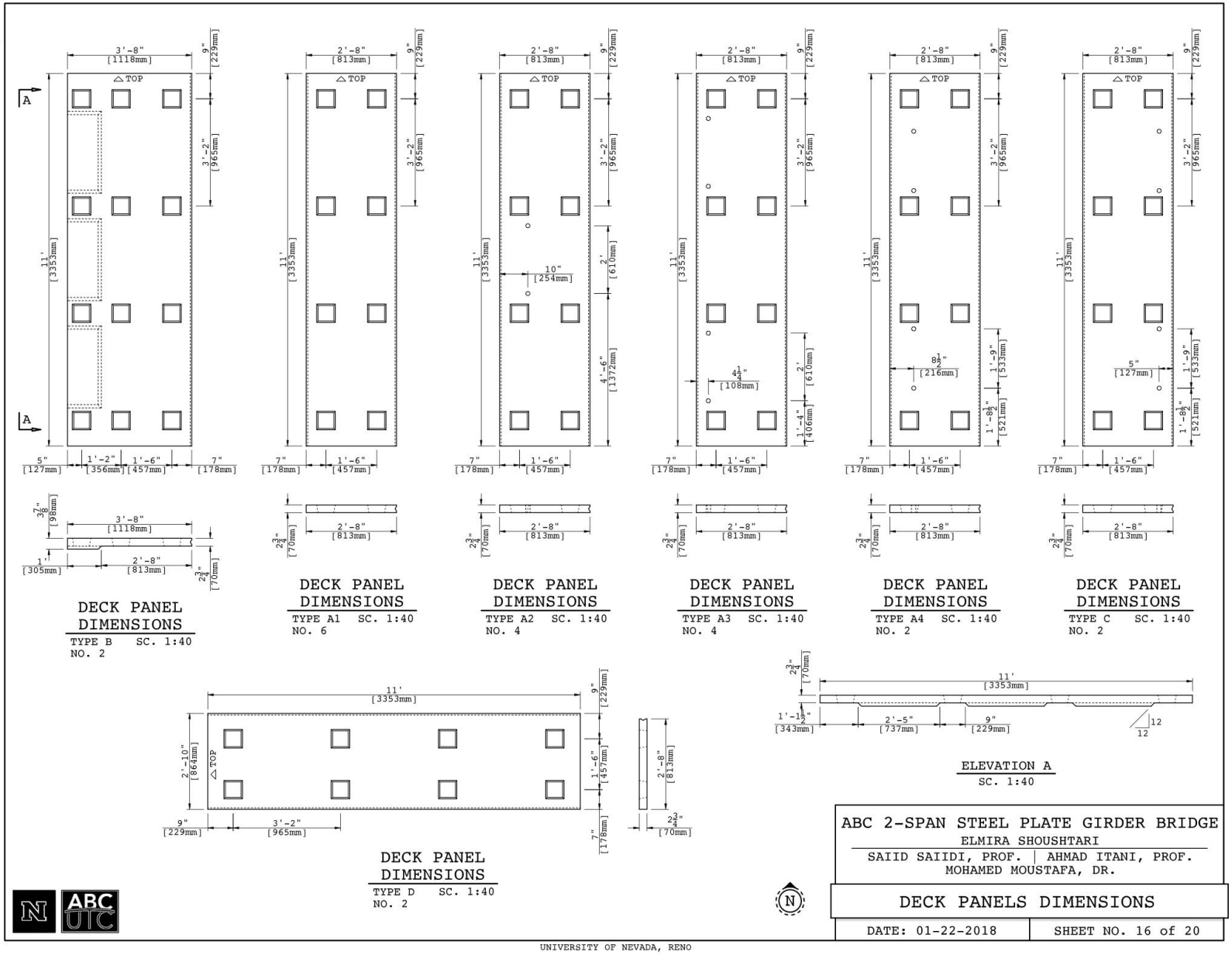

Figure A.16 Details of deck panels (II)

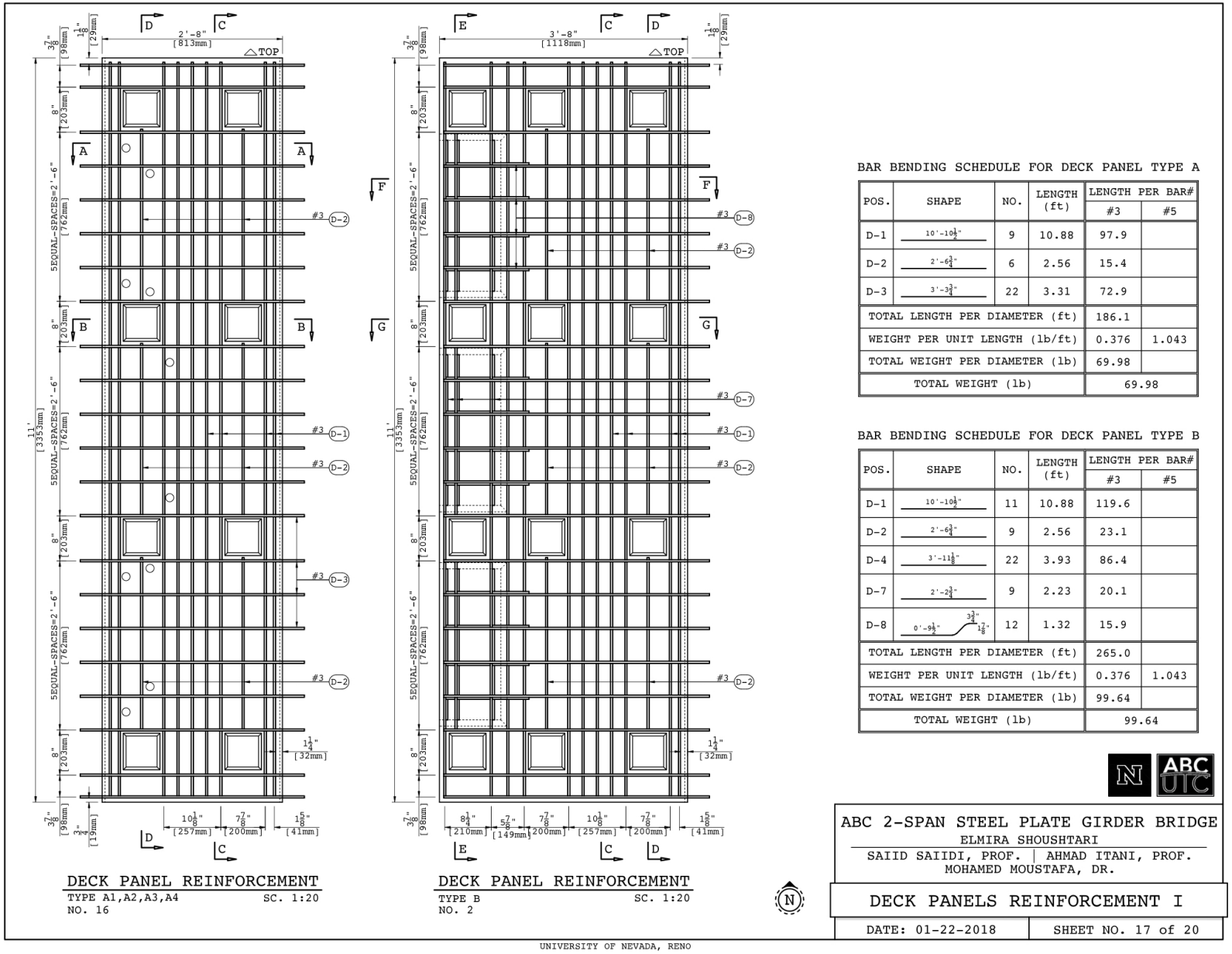

POS.	SHAPE	NO.	LENGTH (ft)	LENGTH PER BAR#	
				#3	#5
D-1	10'-10½"	9	10.88	97.9	
D-2	2'-6¾"	6	2.56	15.4	
D-3	3'-3¾"	22	3.31	72.9	
TOTAL LENGTH PER DIAMETER (ft)				186.1	
WEIGHT PER UNIT LENGTH (lb/ft)				0.376	1.043
TOTAL WEIGHT PER DIAMETER (lb)				69.98	
TOTAL WEIGHT (lb)				69.98	

POS.	SHAPE	NO.	LENGTH (ft)	LENGTH PER BAR#	
				#3	#5
D-1	10'-10½"	11	10.88	119.6	
D-2	2'-6¾"	9	2.56	23.1	
D-4	3'-11⅛"	22	3.93	86.4	
D-7	2'-2¾"	9	2.23	20.1	
D-8	0'-9½" 3¾" 1⅞"	12	1.32	15.9	
TOTAL LENGTH PER DIAMETER (ft)				265.0	
WEIGHT PER UNIT LENGTH (lb/ft)				0.376	1.043
TOTAL WEIGHT PER DIAMETER (lb)				99.64	
TOTAL WEIGHT (lb)				99.64	

Figure A.17 Reinforcement of deck panels (I)

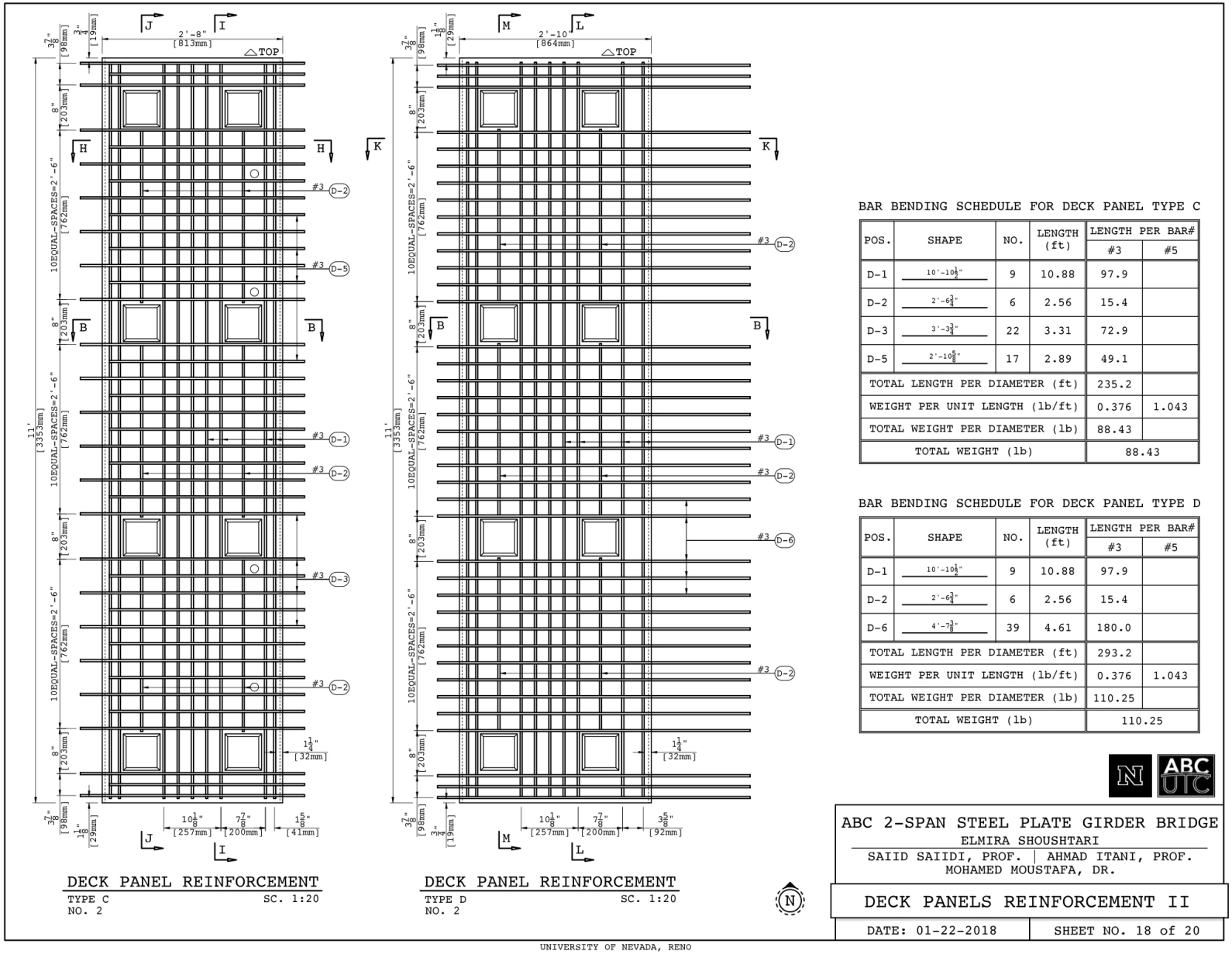

BAR BENDING SCHEDULE FOR DECK PANEL TYPE C

POS.	SHAPE	NO.	LENGTH (ft)	LENGTH PER BAR#	
				#3	#5
D-1	10'-10 1/2"	9	10.88	97.9	
D-2	2'-6 3/4"	6	2.56	15.4	
D-3	3'-3 3/4"	22	3.31	72.9	
D-5	2'-10 5/8"	17	2.89	49.1	
TOTAL LENGTH PER DIAMETER (ft)				235.2	
WEIGHT PER UNIT LENGTH (lb/ft)				0.376	1.043
TOTAL WEIGHT PER DIAMETER (lb)				88.43	
TOTAL WEIGHT (lb)				88.43	

BAR BENDING SCHEDULE FOR DECK PANEL TYPE D

POS.	SHAPE	NO.	LENGTH (ft)	LENGTH PER BAR#	
				#3	#5
D-1	10'-10 1/2"	9	10.88	97.9	
D-2	2'-6 3/4"	6	2.56	15.4	
D-6	4'-7 3/8"	39	4.61	180.0	
TOTAL LENGTH PER DIAMETER (ft)				293.2	
WEIGHT PER UNIT LENGTH (lb/ft)				0.376	1.043
TOTAL WEIGHT PER DIAMETER (lb)				110.25	
TOTAL WEIGHT (lb)				110.25	

ABC 2-SPAN STEEL PLATE GIRDER BRIDGE

ELMIRA SHOUSHTARI

SAIID SAIIDI, PROF. | AHMAD ITANI, PROF.
MOHAMED MOUSTAFA, DR.

DECK PANELS REINFORCEMENT II

DATE: 01-22-2018 | SHEET NO. 18 of 20

Figure A.18 Reinforcement of deck panels (II)

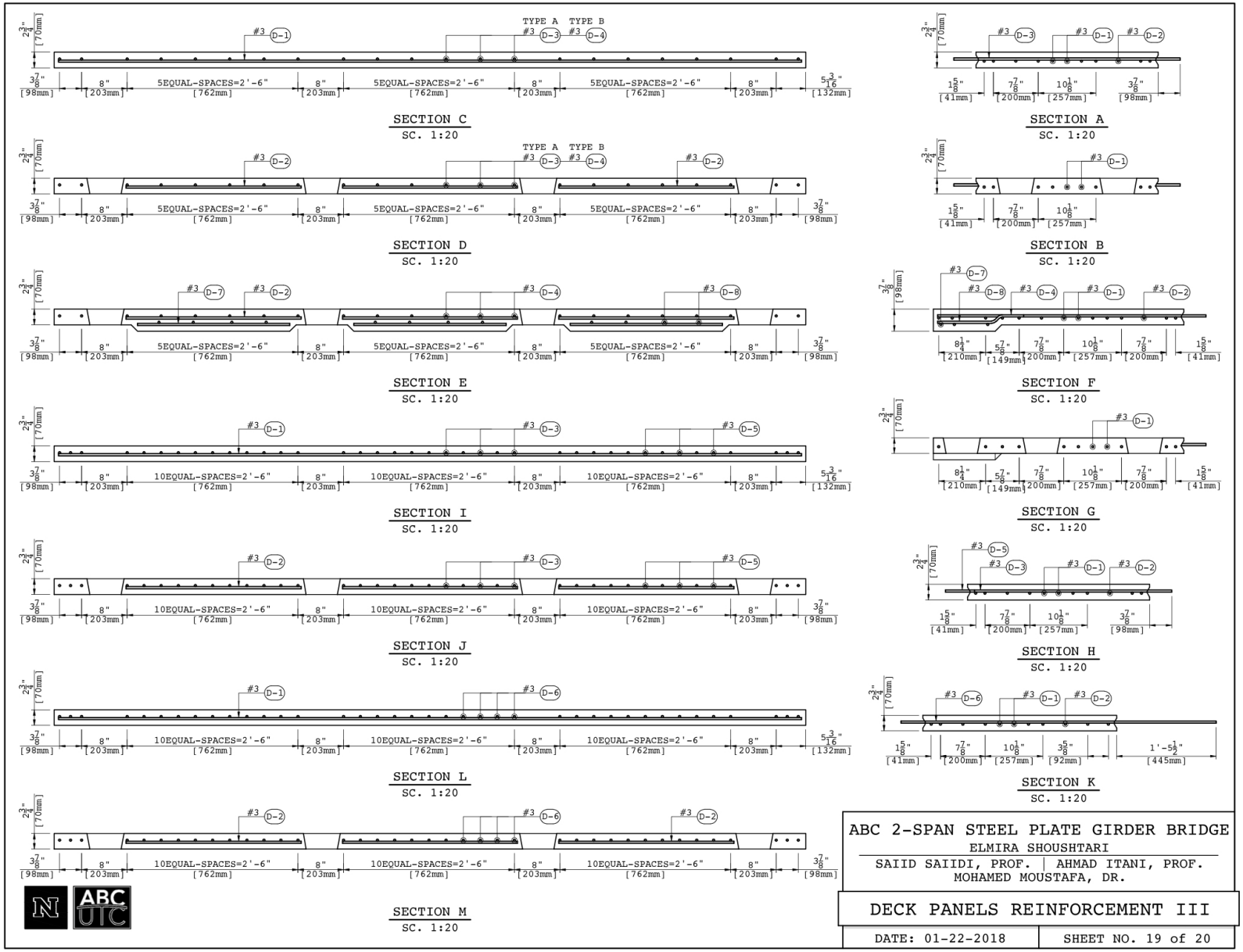

Figure A.19 Reinforcement of deck panels (III)

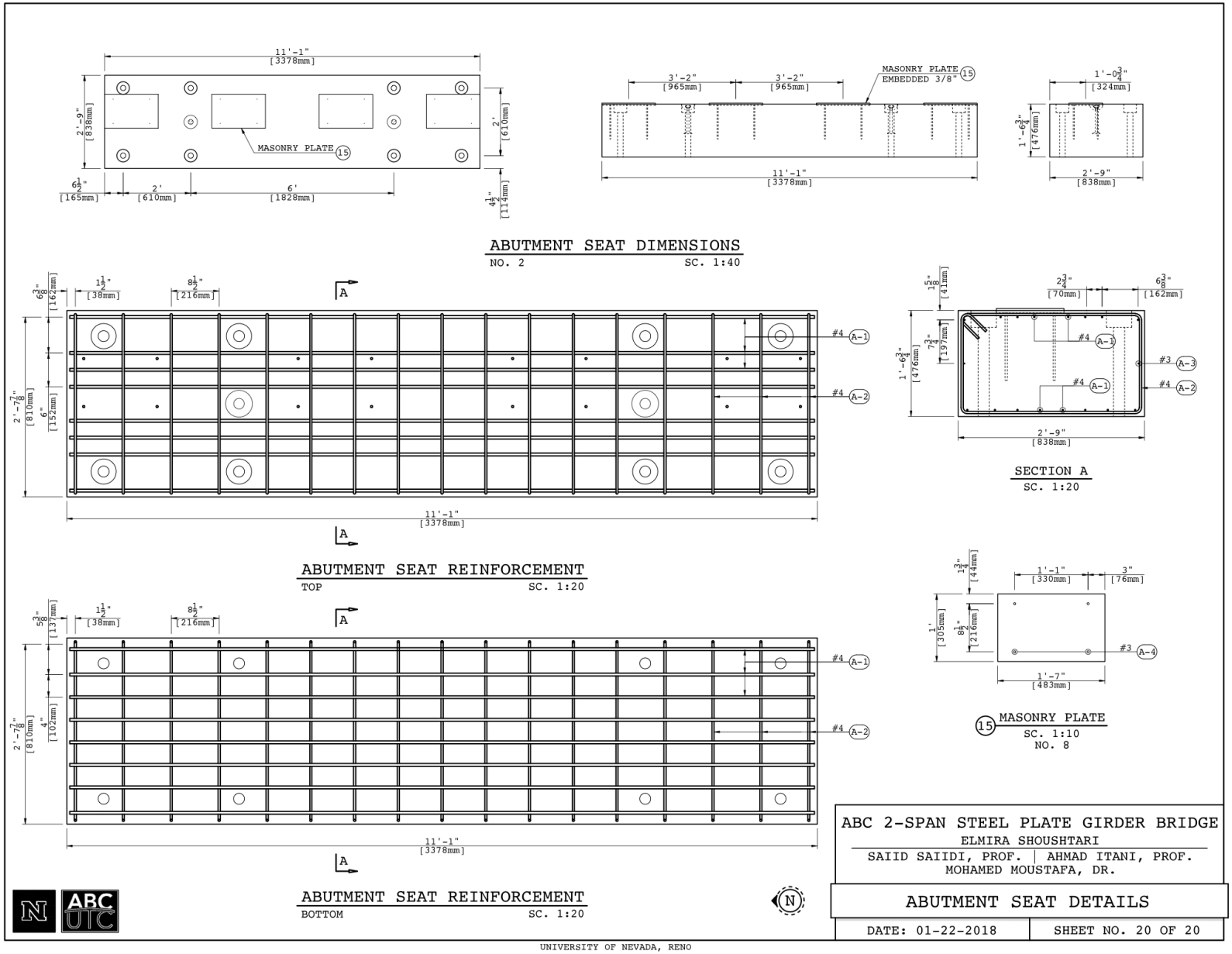

Figure A.20 Reinforcement and details of the abutment seat

A.2. Construction photos

Figure A.21 Fillet welding of girder flanges to the web

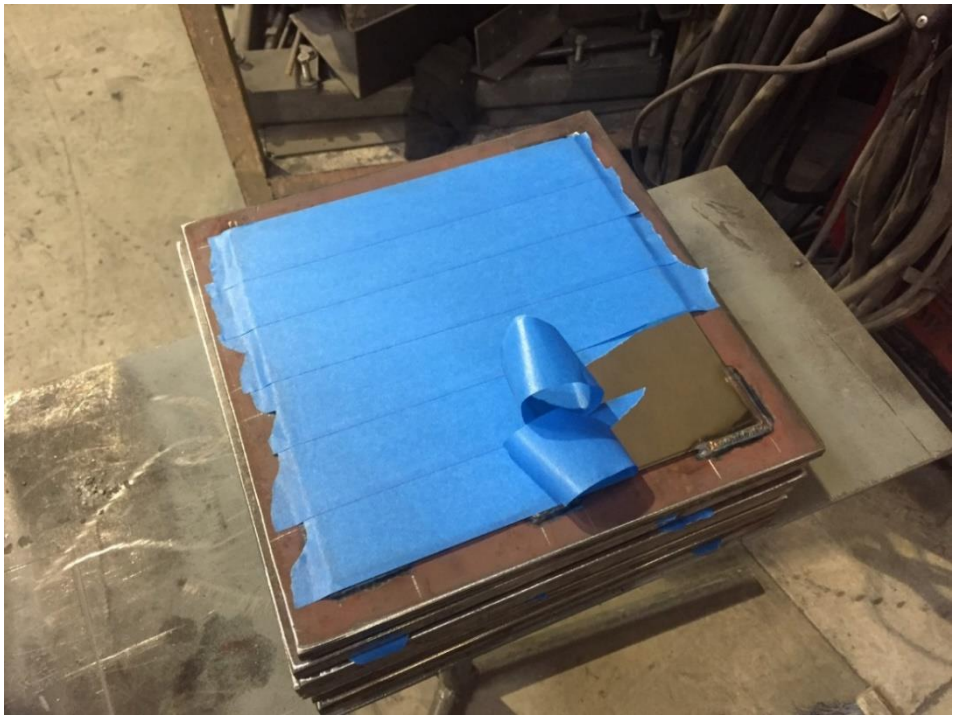

Figure A.22 SSN plate with mirror finish welded to the sole plate

Figure A.23 Shooting the studs

Figure A.24 Plate girder detail over pier

Figure A.25

Figure A.26 Assembled girders and cross frames (east span)

Figure A.27 Footing reinforcement, formwork, PVC ducts, and corrugated pipes

Figure A.28 Casting and vibration of footing concrete

Figure A.29 Finishing the footing concrete surface

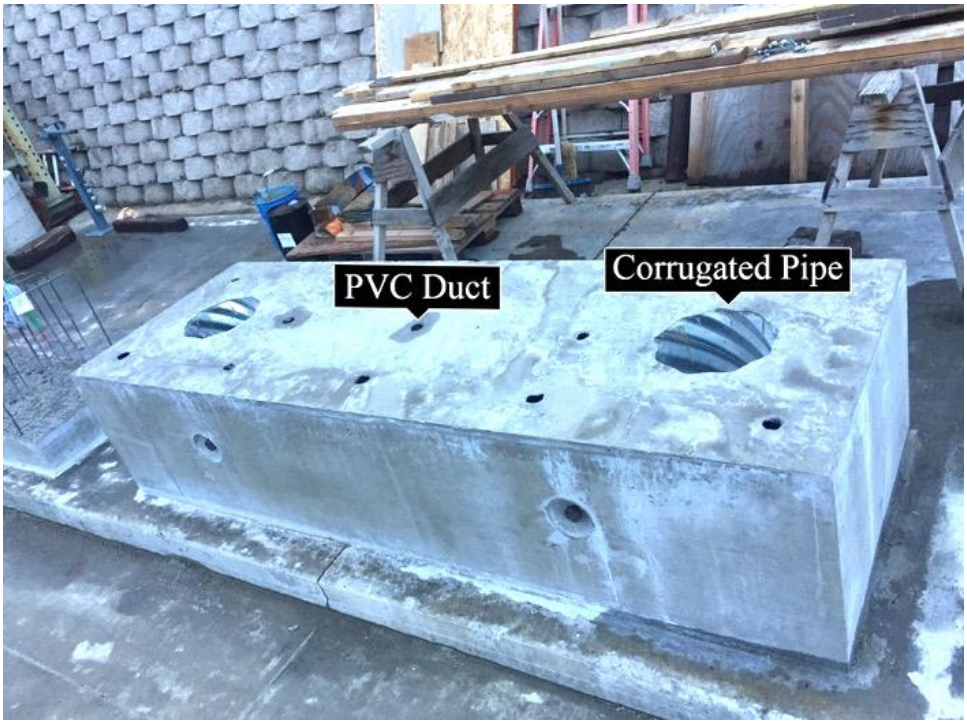

Figure A.30 Precast footing with two circular pockets

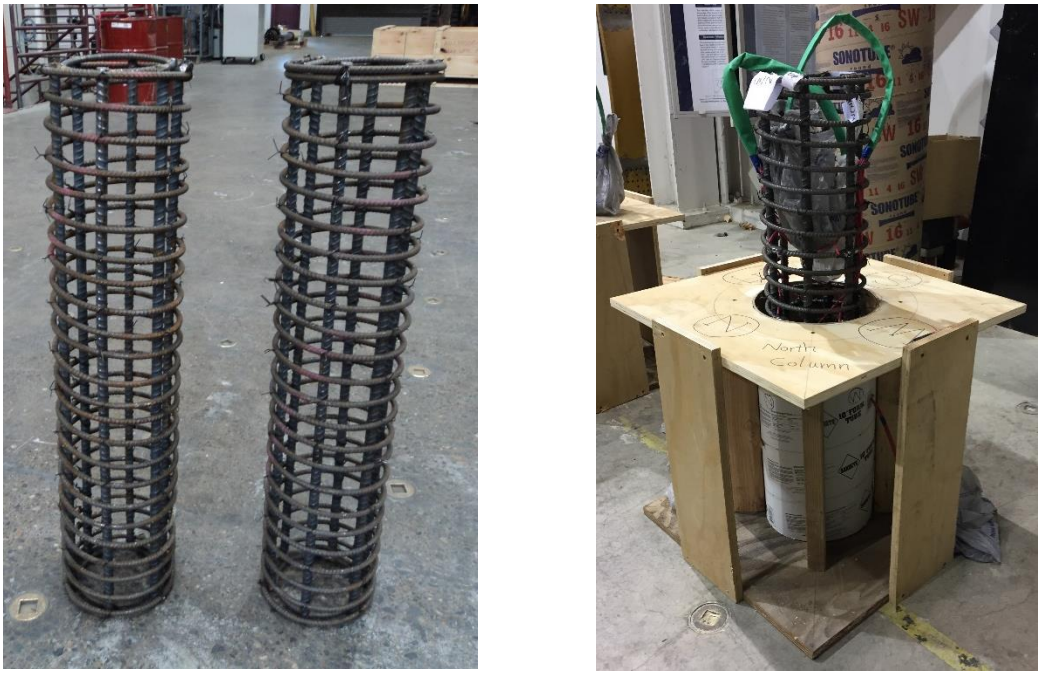

(a) (b)

Figure A.31 Rebar hinge (a) reinforcement cage (b) sonotube and formwork

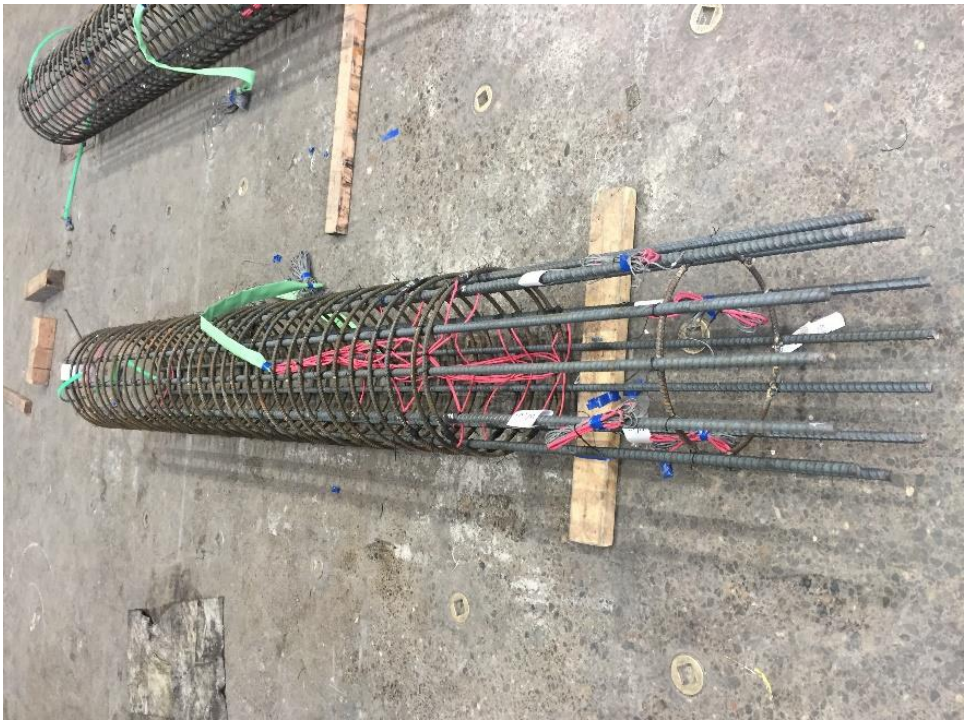

Figure A.32 Column reinforcement cage

(a) (b)

Figure A.33 The placement of (a) column reinforcement cage (b) column sonotube

Figure A.34 Casting the column concrete

Figure A.35 Columns after casting the concrete

Figure A.36 Precast cap beam reinforcement cage

Figure A.37 Precast cap beam reinforcement cage

(a) (b)

Figure A.38 Precast cap beam formwork (a) before (b) after the placement of corrugated ducts and reinforcement cage

Figure A.39 Cap beam after casting and removing the formwork

Figure A.40 Formwork and reinforcement of deck panels

Figure A.41 Deck panels after removing the formwork

Figure A.42 Placing deck panels on the girders

Figure A.43 Pouring grout in pockets of deck panels

Figure A.44 Casting UHPC in the deck panels joints

Figure A.45 Superstructure after casting grout and UHPC in deck pockets

Figure A.46 Superstructure after casting grout and UHPC in deck pockets

Figure A.47 Superstructure after casting grout and UHPC in deck pockets

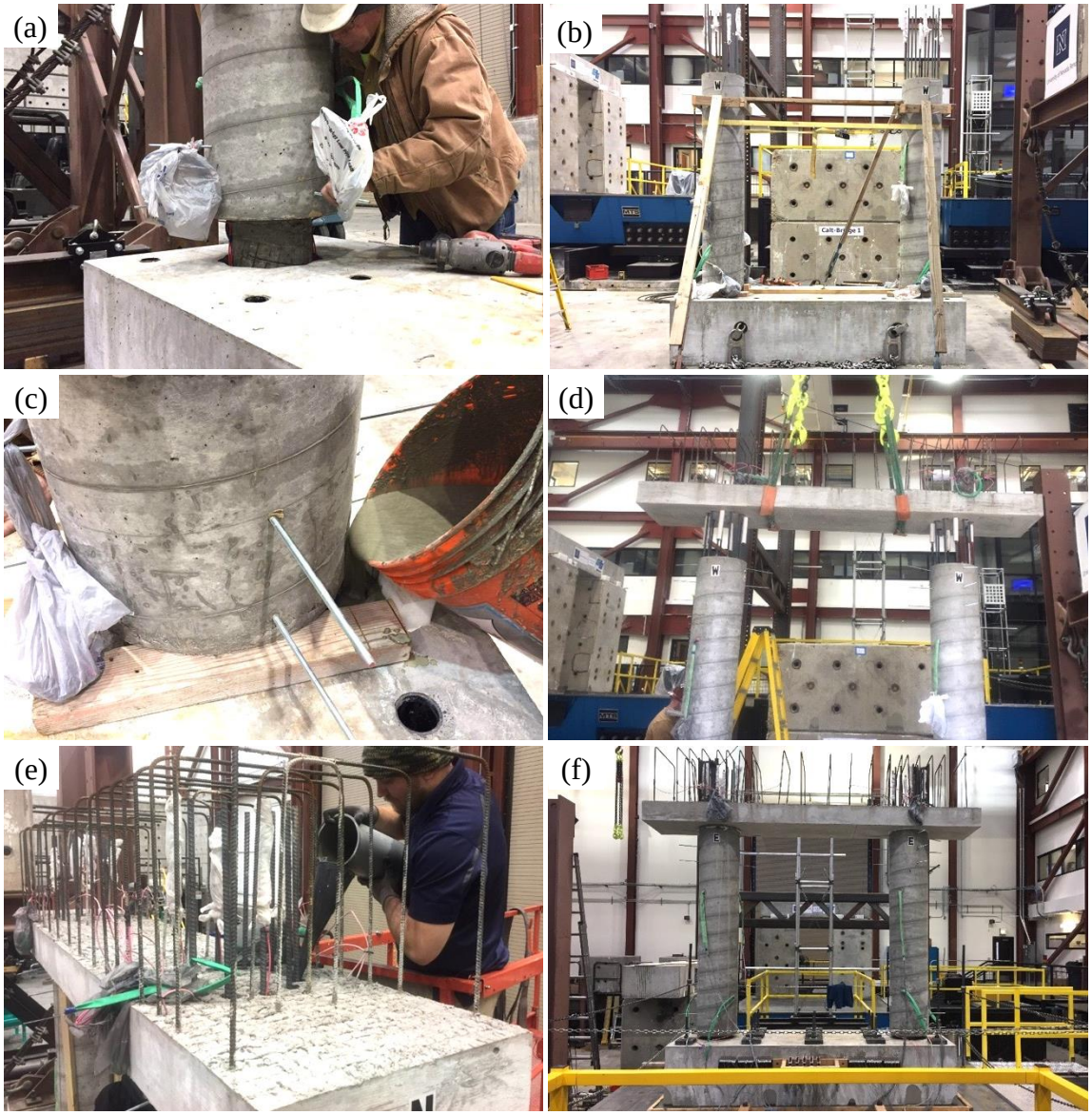

Figure A.48 (a) Inserting column into the footing, (b) Securing columns temporarily, (c) Grouting the spacing between the column and the footing, (d) placing precast cap beam on the columns, (e) Grouting cap beam ducts, (f) Precast bent on the shake table (Images by Elmira Shoushtari)

Figure A.49 Placement of east span over the abutment seat and precast cap beam

Figure A.50 Casting UHPC in the top layer of cap beam

A.3. Material test data

Table A.1 Compressive concrete strength used in the bridge model

		7-day strength (psi)	28-day strength (psi)
Bent	Concrete	4420	6190
	Grout (column-to-cap beam)	10034	11200
	Grout (column-to-footing)	6920	7750
Superstructure	Concrete east span panels	5003	6867
	Concrete west span panels	5507 (14-day)	7032
	Grout (pockets of east panel)	9450	9923
	Grout (pockets of west panel)	8734	9263
	UHPC (panel joints)	14900	19900 (33-day)
CIP cap-beam	Concrete (CIP cap)	5567	-
	UHPC (panel joints)	14800	-

Table A.2 Mechanical properties of reinforcing bars

	Fy (ksi)	Fu (ksi)	εu (%)
#5 (column)	76	101	10.8
#5 (footing & cap beam)	70	94	11.6
#3 (bent)	71	99	10.4

A.4. Test setup, instrumentation, and loading protocol

Figure A.51 Test setup

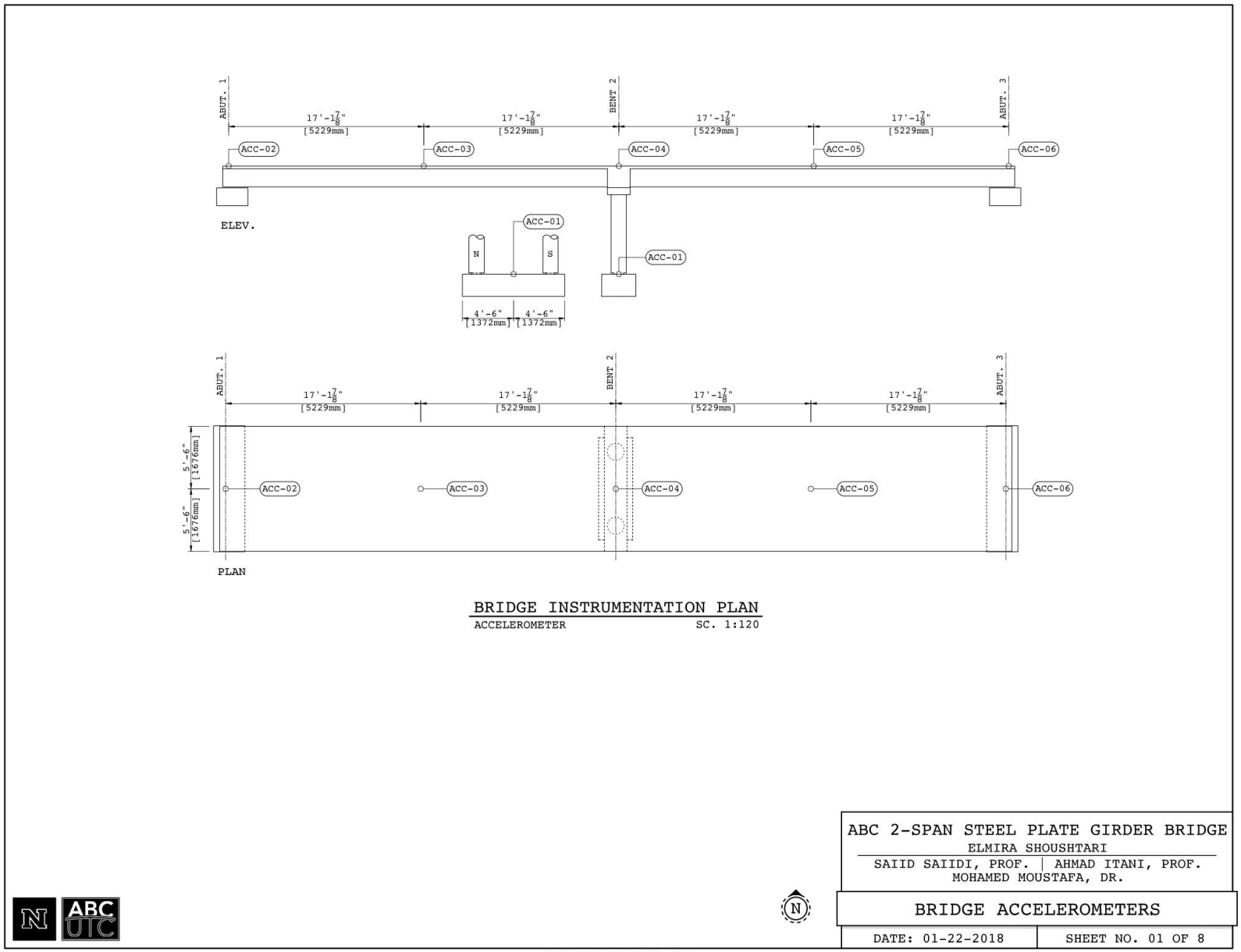

Figure A.52 Accelerometers

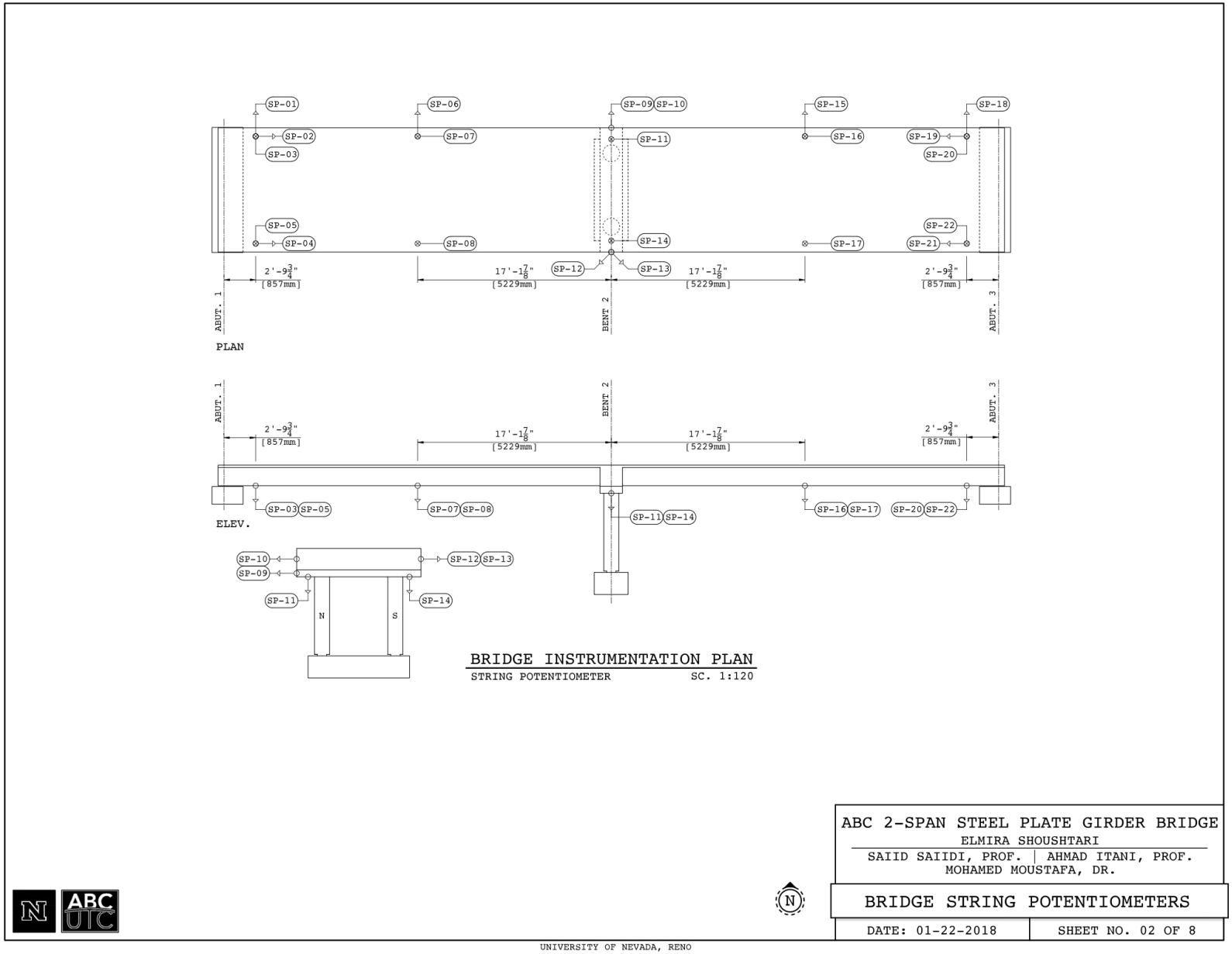

Figure A.53 Spring potentiometers

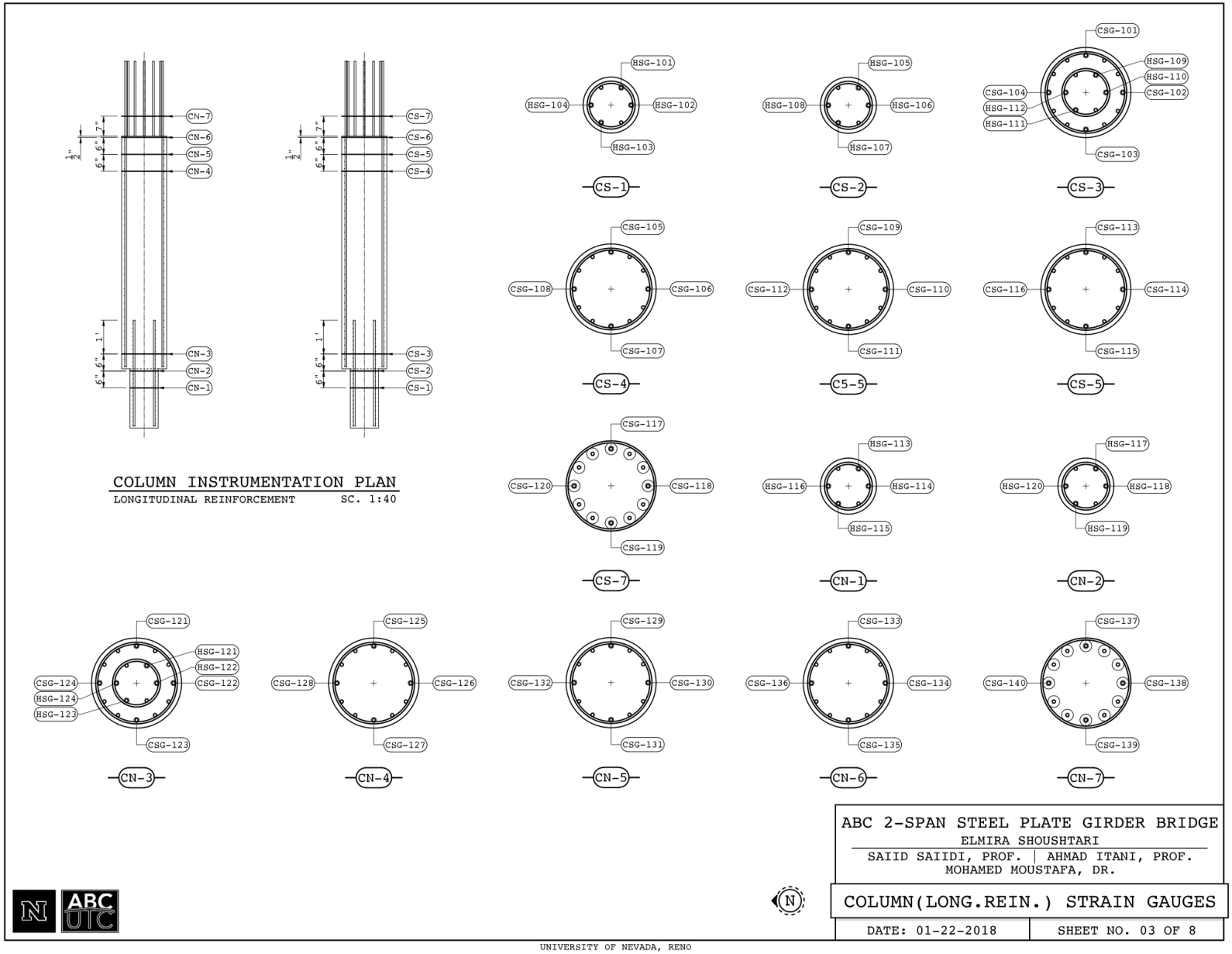

Figure A.54 Strain gauges of column longitudinal reinforcement

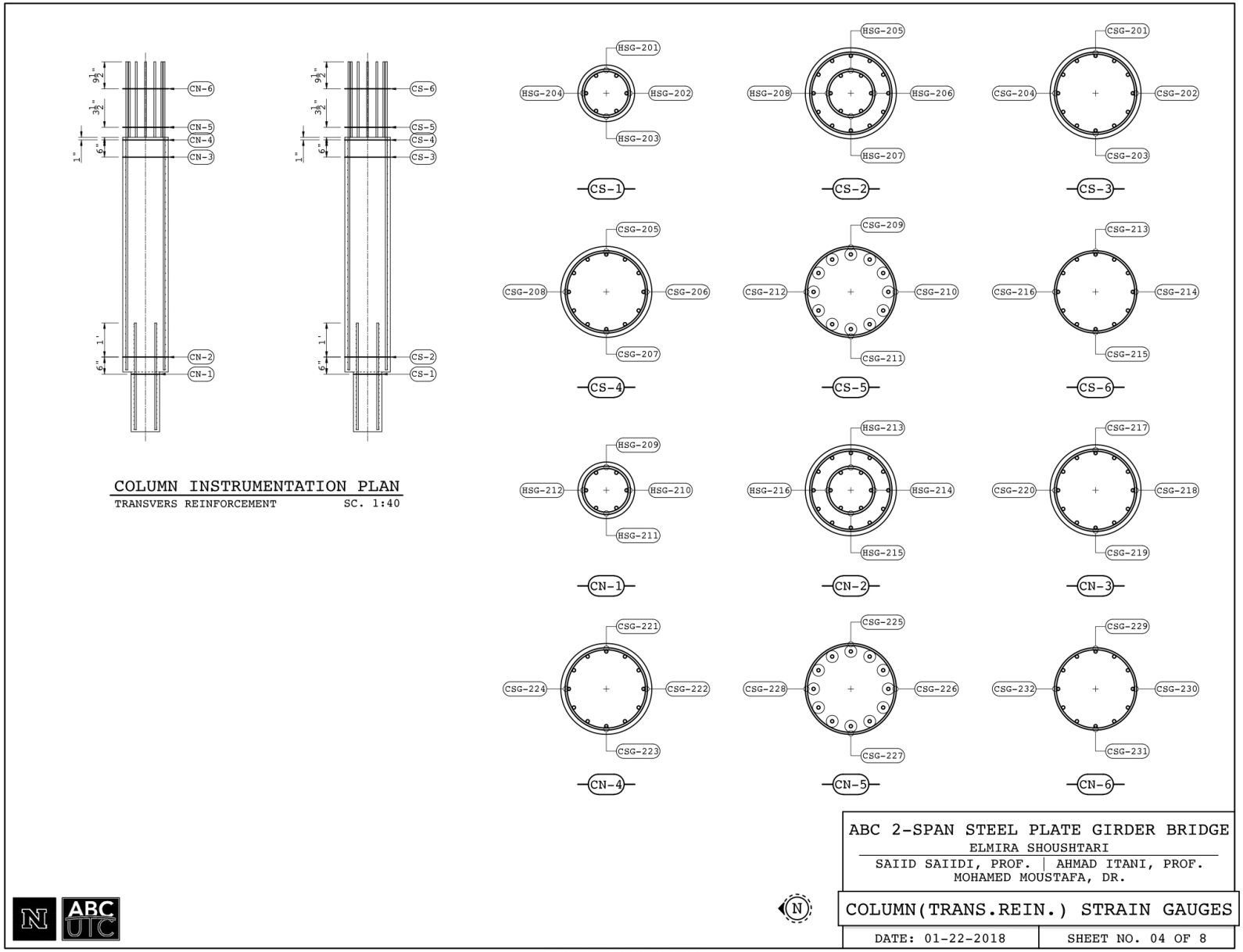

Figure A.55 Strain gauges of column transverse reinforcement

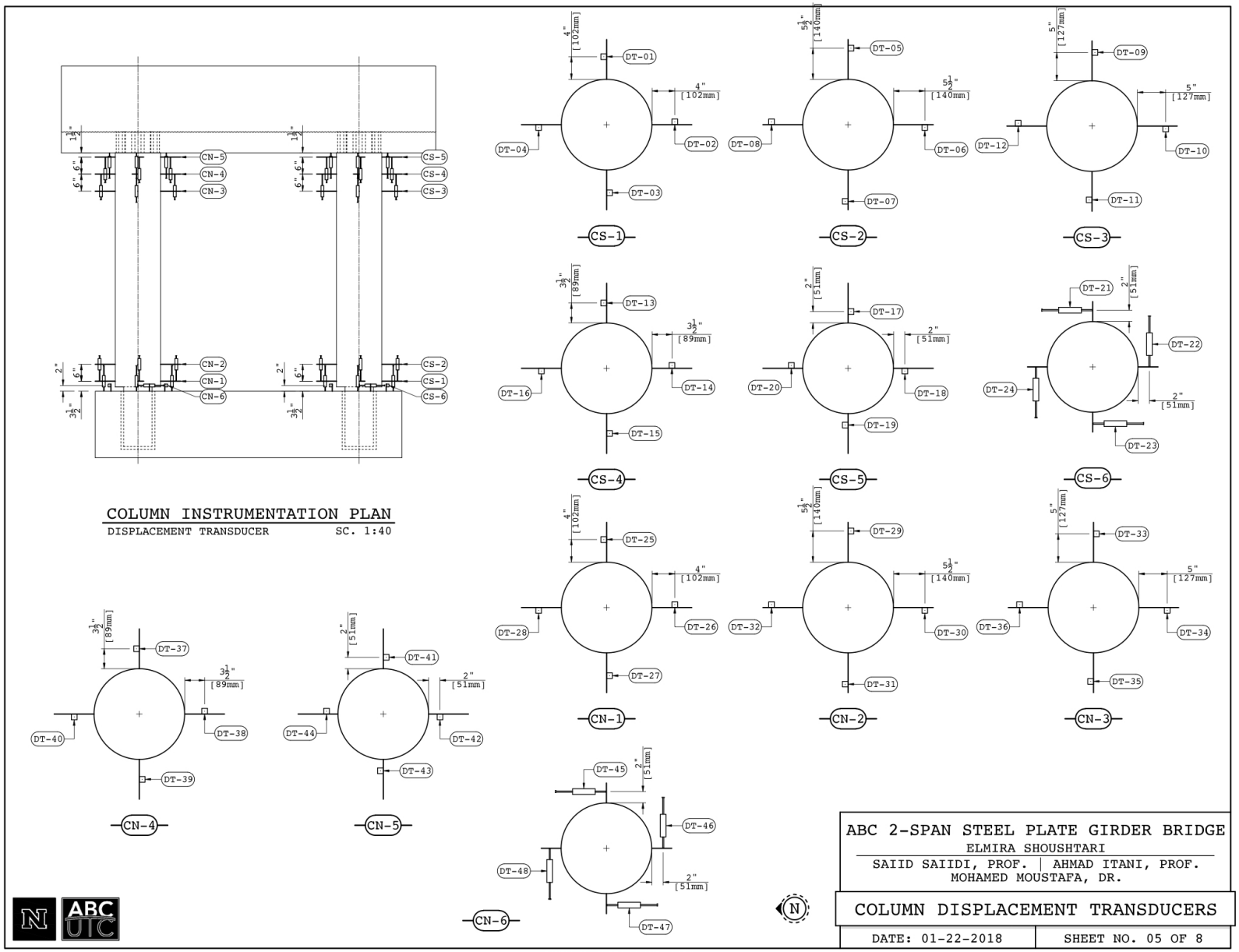

Figure A.56 Column displacement transducers

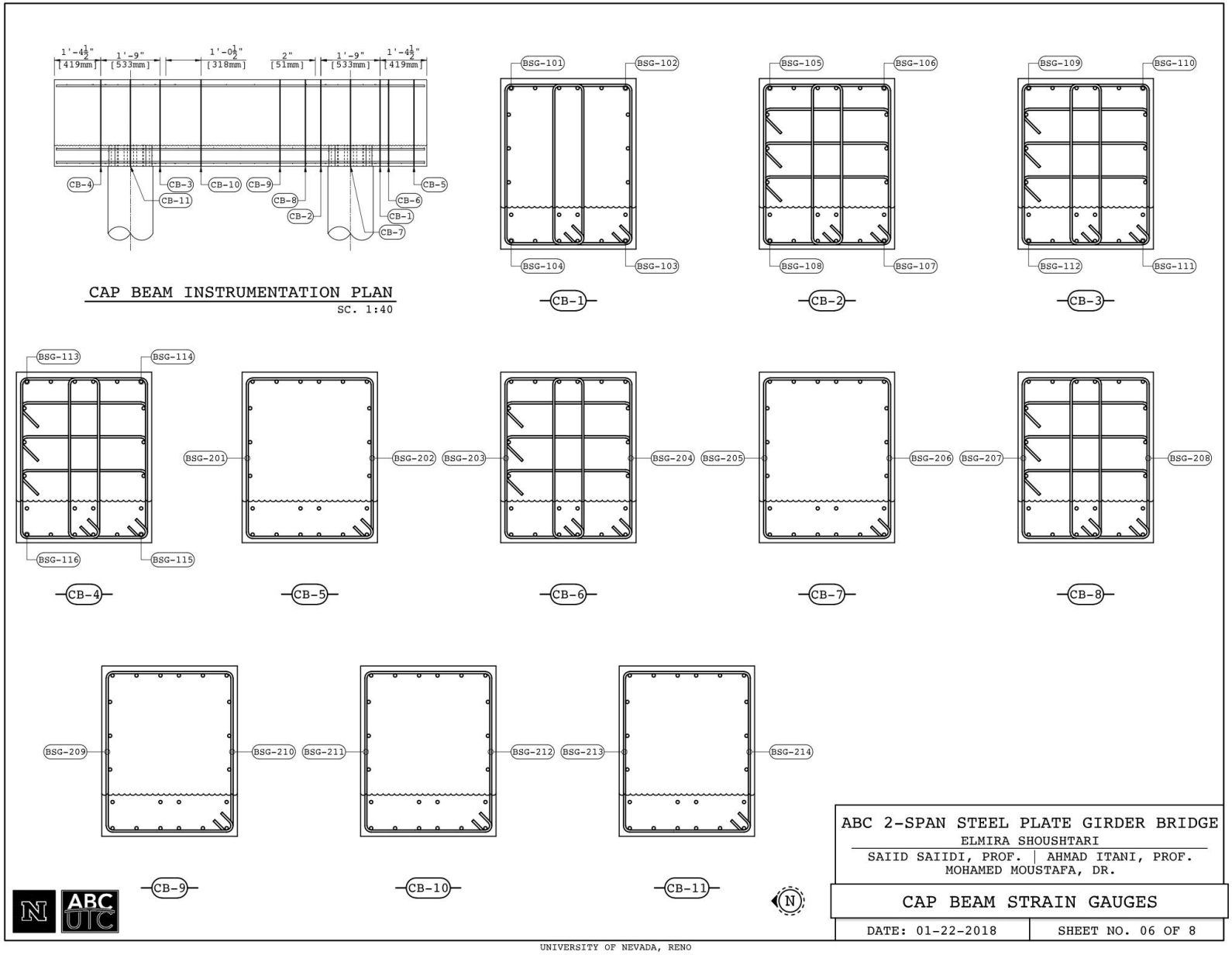

Figure A.57 Cap beam strain gauges

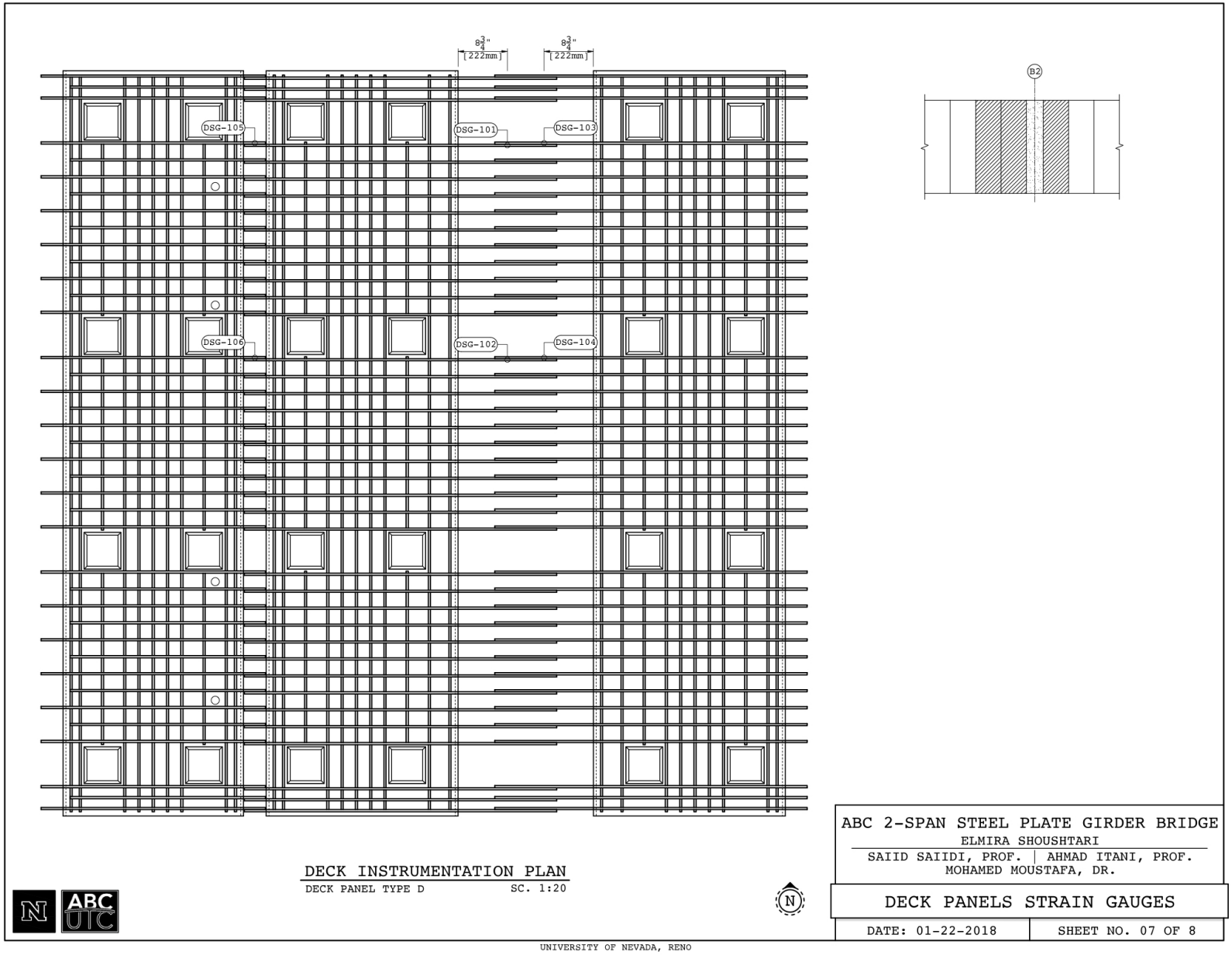

Figure A.58 Deck panels strain gauges

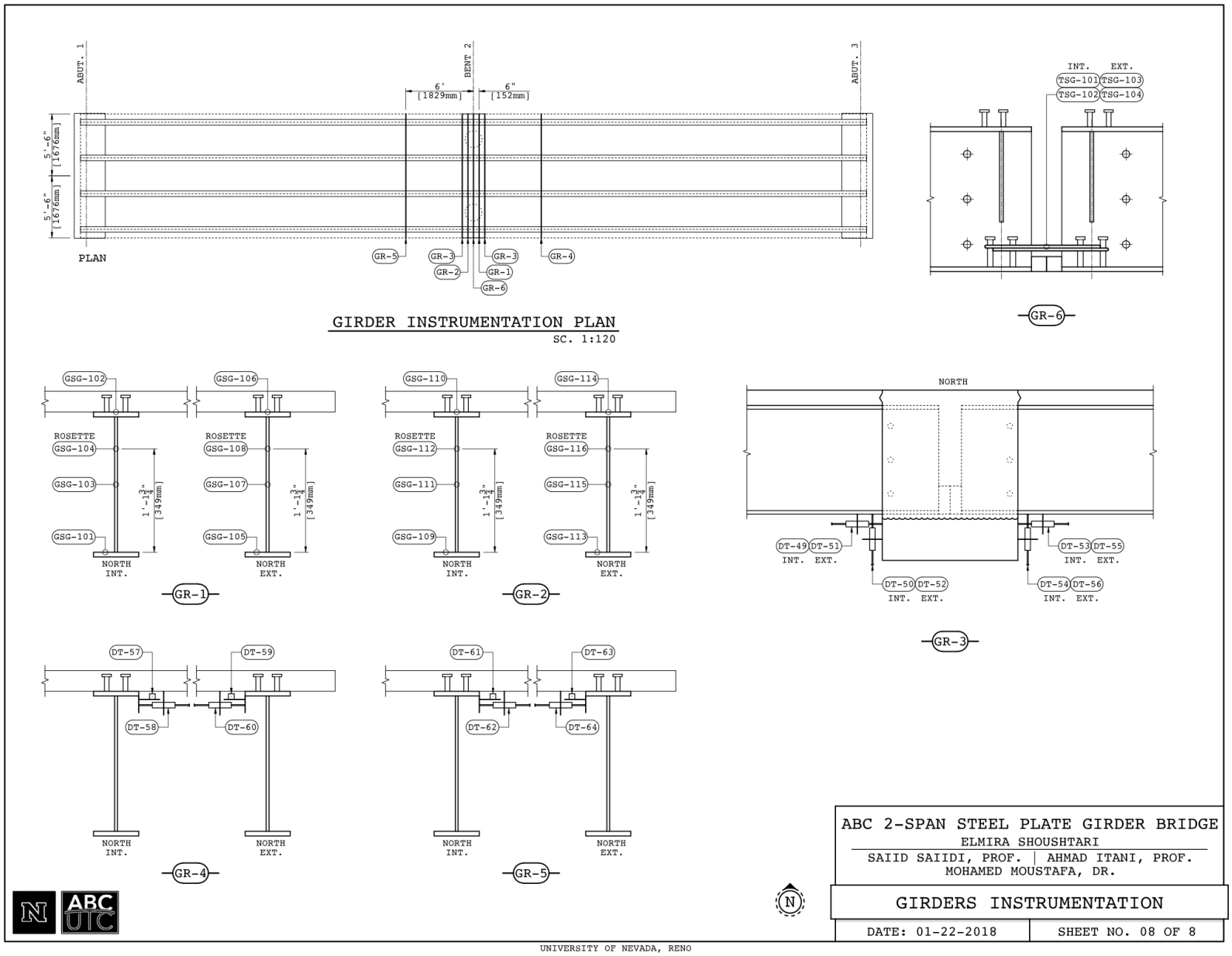

Figure A.59 Deck panels strain gauges

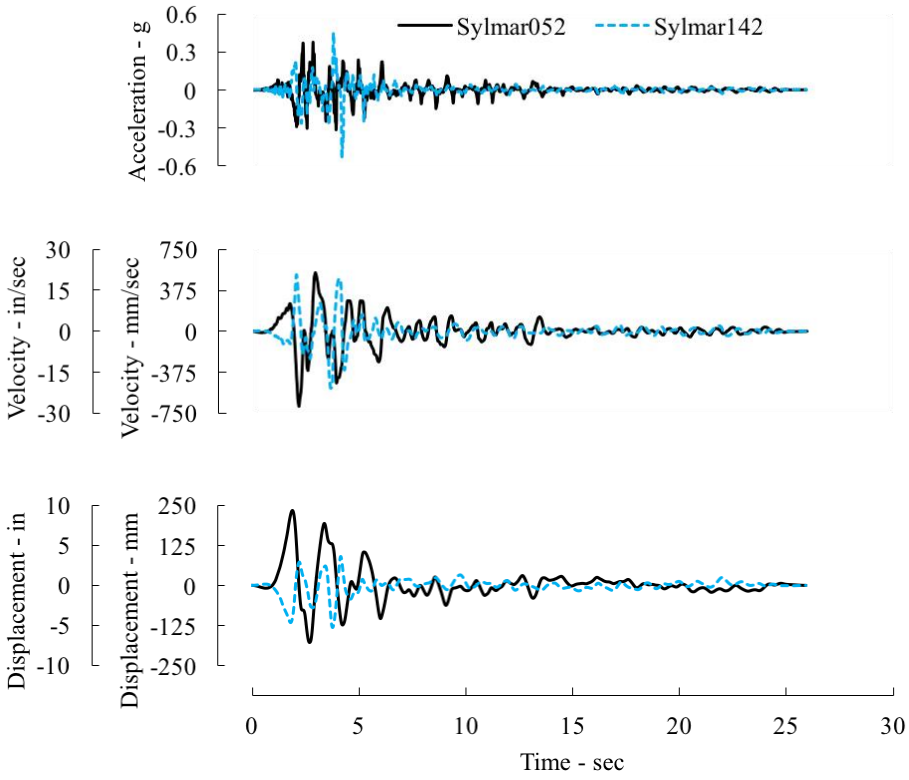

Figure A.60 Time-scaled acceleration histories of the input motions with unscaled amplitudes

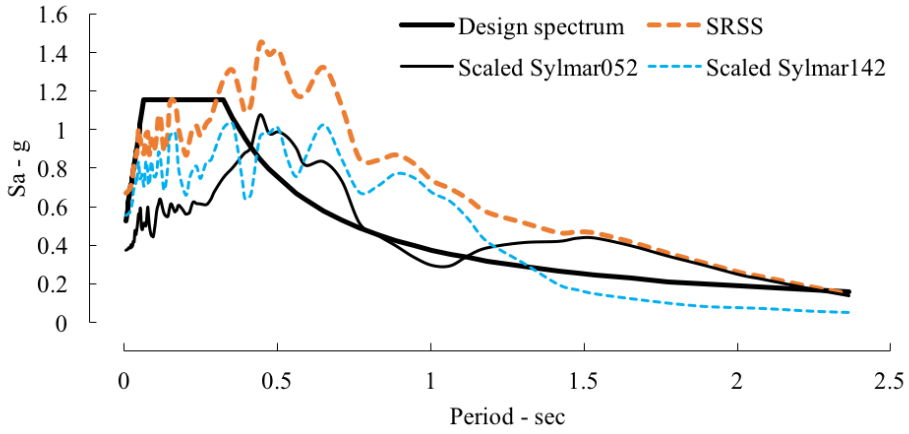

Figure A.61 Design response spectrum and scaled response spectrum of the ground motion components and their SRSS resultant.

APPENDIX B: SHAKE TABLE TEST RESULTS

This appendix contains complete documentation of the shake table test results. General discussion of the material presented in this appendix was included in various chapters of the main report and more specifically in chapter 4. The documents are presented in the following order:

B.1. Apparent damage

B.2. Measured results

B.1. Apparent damage

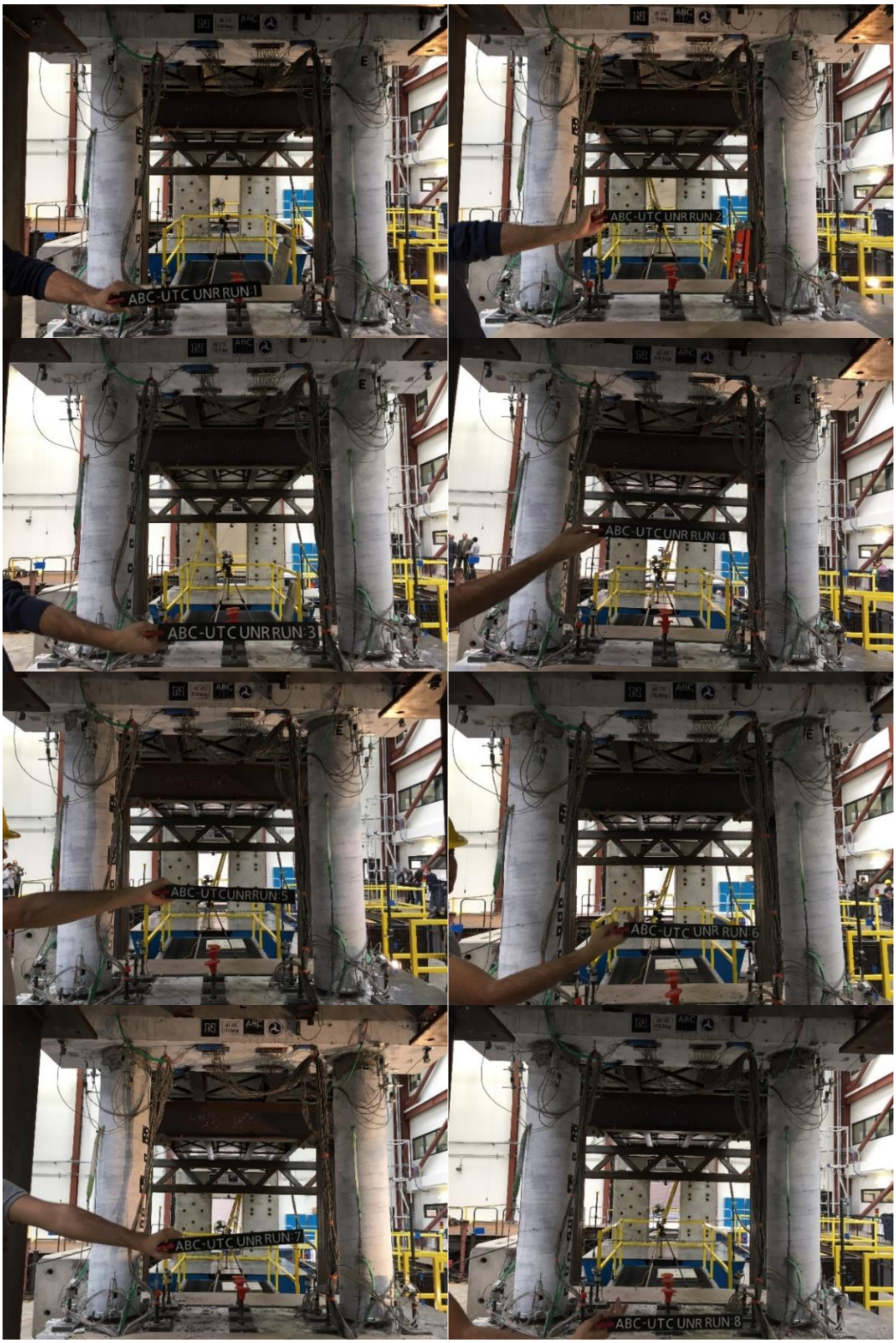

Figure B.1 Damage states of the bent after each run

Figure B.2 Damage states of the south column plastic hinges after Run 1

Figure B.3 Damage states of the south column plastic hinges after Run 2

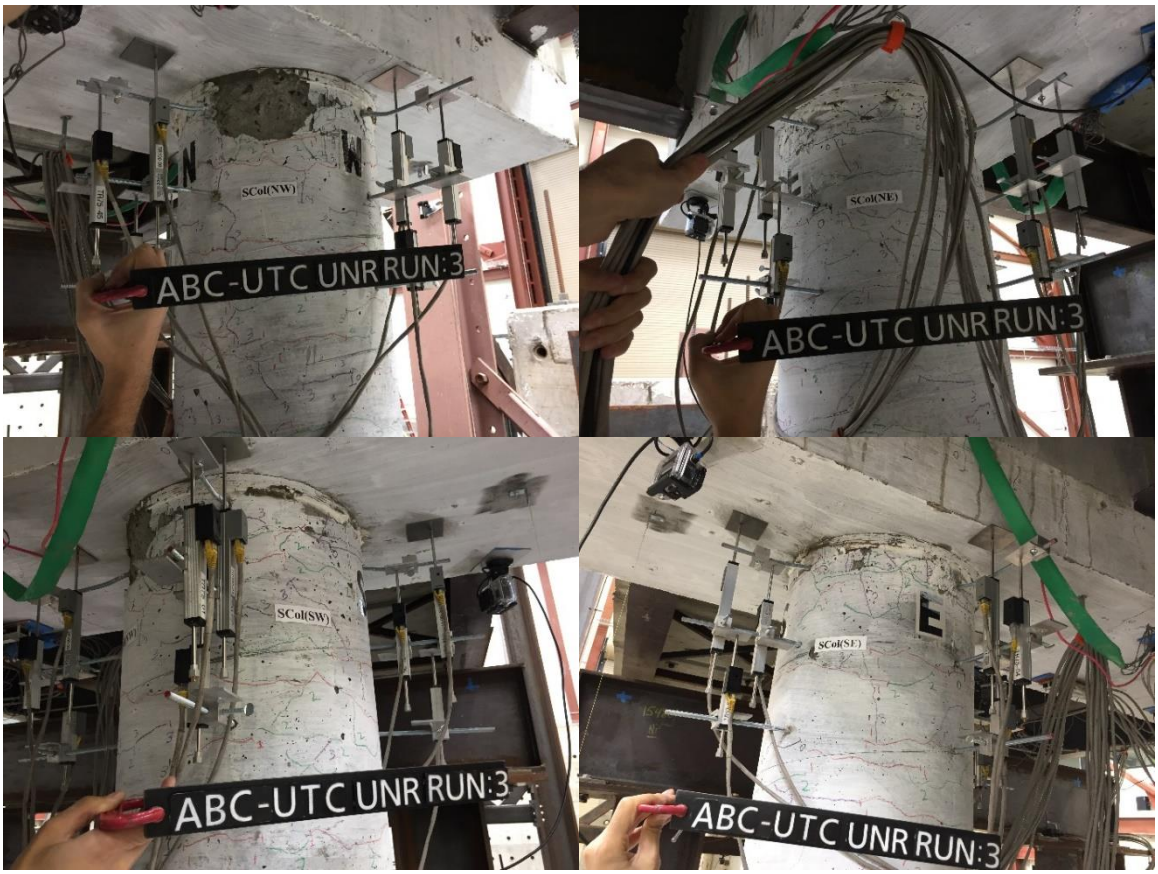

Figure B.4 Damage states of the south column plastic hinges after Run 3

Figure B.5 Damage states of the south column plastic hinges after Run 4

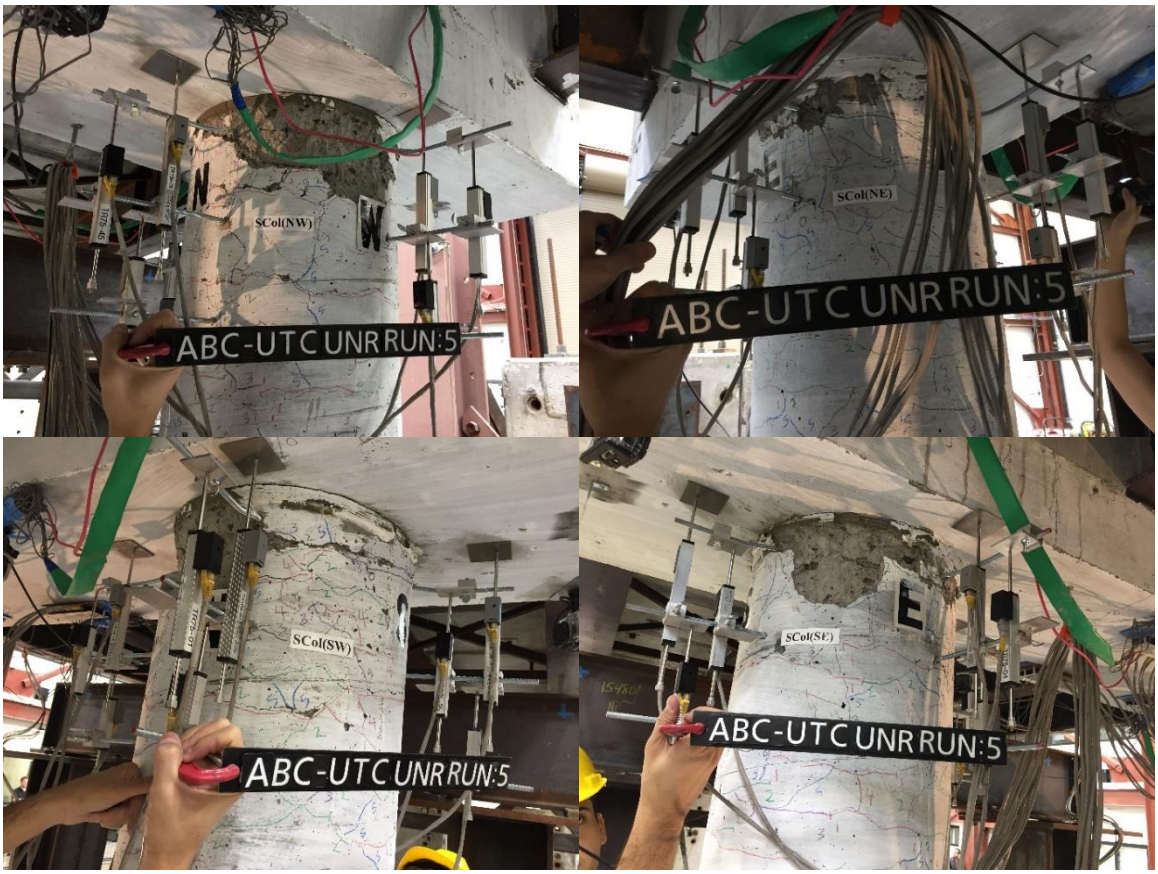

Figure B.6 Damage states of the south column plastic hinges after Run 5

Figure B.7 Damage states of the south column plastic hinges after Run 6

Figure B.8 Damage states of the south column plastic hinges after Run 7

Figure B.9 Damage states of the south column plastic hinges after Run 8

B.2. Measured results

Table B.1 Target and achieved shake table motions

		PGA, (g)							
		Run 1	Run 2	Run 3	Run 4	Run 5	Run 6	Run 7	Run 8
% of the DE		30%	65%	100%	125%	150%	175%	200%	225%
Longitudinal	Target	0.17	0.36	0.56	0.70	0.83	0.97	1.11	1.23
	Achieved	0.14	0.29	0.39	0.45	0.56	0.67	0.83	0.89
Transverse	Target	0.11	0.24	0.37	0.47	0.56	0.66	0.75	0.83
	Achieved	0.13	0.20	0.32	0.40	0.55	0.63	0.74	0.83

Table B.2 Maximum and minimum measured strains (με), column longitudinal bars (bold numbers indicate post-yield strains)

Run #	CSG101		CSG102		CSG103		CSG104		CSG105	
	Max.	Min.	Max.	Min.	Max.	Min.	Max.	Min.	Max.	Min.
Run 1	323	-179	310	-179	193	-89	138	-241	946	-1680
Run 2	131	-454	316	-475	151	-296	96	-399	1490	**-3090**
Run 3	0	-523	165	-523	172	-378	-14	-461	2290	**-3200**
Run 4	-96	-585	48	-557	55	-475	-83	-502	2450	**-2990**
Run 5	-138	-599	-21	-571	-28	-543	-131	-550	2490	**-3340**
Run 6	-179	-592	-69	-585	-55	-571	-158	-557	**4750**	**-9110**
Run 7	-234	-619	-124	-592	-89	-598	-193	-571	**3960**	**-21300**
Run 8	-282	-633	-193	-619	-131	-626	-206	-564	**2830**	**-23100**

Run #	CSG106		CSG107		CSG108		CSG109		CSG110	
	Max.	Min.	Max.	Min.	Max.	Min.	Max.	Min.	Max.	Min.
Run 1	670	-1430	1000	-1790	1000	-1460	1070	-1780	670	-1480
Run 2	1400	**-3200**	1710	**-3280**	2080	**-4850**	2050	**-3640**	1650	**-3420**
Run 3	1480	**-3270**	2140	**-3610**	2160	**-5280**	**9000**	**-16700**	1760	**-3930**
Run 4	1610	**-3400**	2000	**-18400**	2050	**-6420**	**7020**	**-13900**	1990	**-5520**
Run 5	1600	**-3480**	1040	**-21400**	1130	**-13300**	**9220**	**-17100**	1840	**-19900**
Run 6	1610	**-4150**	435	**-22200**	-421	**-18500**	**10400**	**-23400**	**-3090**	**-21100**
Run 7	1700	**-5170**	124	**-22700**	-1610	**-21700**	**9790**	**-29200**	-2060	**-22500**
Run 8	1930	**-5540**	-228	**-23300**	**-3250**	**-25100**	**10400**	**-35300**	-1040	**-20900**

Table B.3 Maximum and minimum measured strains (με), column longitudinal bars (bold numbers indicate post-yield strains)

Run #	CSG111		CSG112		CSG113		CSG114		CSG115	
	Max.	Min.	Max.	Min.	Max.	Min.	Max.	Min.	Max.	Min.
Run 1	1320	-1990	1380	-1410	1050	-1960	347	-1670	1290	-2060
Run 2	2300	**-4440**	2420	**-17800**	1680	**-21700**	693	**-23900**	1090	**-17400**
Run 3	2580	**-22400**	**2960**	**-16900**	863	**-21400**	**-9730**	**-24500**	-76	**-23700**
Run 4	2350	**-29200**	1040	**-20400**	**4690**	**-18900**	**-7670**	**-23800**	627	**-32700**
Run 5	**3750**	**-34100**	-967	**-24600**	**8090**	**-24100**	**-8160**	**-25500**	1910	**-38300**
Run 6	**5140**	**-36000**	-483	**-31600**	**10400**	**-29500**	**-6570**	**-29000**	**3240**	**-40800**
Run 7	**7560**	**-35900**	-2010	**-38300**	**10600**	**-35200**	**-4020**	**-29700**	**3230**	**-41800**
Run 8	**10100**	**-36500**	**-6770**	**-46300**	**13400**	**-41400**	-1840	**-27800**	-2470	**-43400**

Run #	CSG116		CSG117		CSG118		CSG119		CSG120	
	Max.	Min.	Max.	Min.	Max.	Min.	Max.	Min.	Max.	Min.
Run 1	1210	-1350	353	-1260	235	-850	497	-1090	438	-883
Run 2	2280	**-23300**	837	-2320	988	-2200	1290	-2120	1720	-2410
Run 3	-276	**-20700**	1280	-2540	1410	-2410	1860	-2410	1780	**-2660**
Run 4	586	**-23200**	1620	**-2850**	1720	-2520	1910	**-2680**	1950	**-2860**
Run 5	1240	**-28800**	1790	**-3120**	1790	**-2640**	2160	**-2840**	2060	**-3150**
Run 6	**4220**	**-36000**	1860	**-3320**	1930	**-2750**	2270	**-3020**	2160	**-3410**
Run 7	**3240**	**-43800**	1870	**-3490**	2120	**-2910**	2300	**-3170**	2390	**-4070**
Run 8	359	**-53500**	1820	**-3600**	2260	**-2960**	2260	**-3370**	**2640**	**-5940**

Table B.4 Maximum and minimum measured strains (με), column longitudinal bars (bold numbers indicate post-yield strains)

Run #	CSG121		CSG122		CSG123		CSG124		CSG125	
	Max.	Min.	Max.	Min.	Max.	Min.	Max.	Min.	Max.	Min.
Run 1	262	-41	172	-41	275	-241	220	-261	911	-2240
Run 2	172	-172	69	-282	193	-372	234	-413	1490	**-3610**
Run 3	158	-262	-62	-358	76	-434	76	-488	1930	**-3730**
Run 4	97	-344	-151	-447	-7	-475	0	-523	2120	**-3670**
Run 5	41	-358	-199	-474	-76	-523	-41	-557	**2880**	**-7300**
Run 6	-14	-379	-220	-516	-124	-537	-83	-578	1890	**-15900**
Run 7	-62	-386	-241	-536	-151	-557	-138	-592	359	**-18500**
Run 8	-103	-413	-275	-557	-186	-585	-179	-612	-166	**-19600**

Run #	CSG126		CSG127		CSG128		CSG129		CSG130	
	Max.	Min.	Max.	Min.	Max.	Min.	Max.	Min.	Max.	Min.
Run 1	738	-1390	842	-1880	614	-1210	1080	-1810	807	-1250
Run 2	1590	**-3190**	1300	**-3330**	1180	**-3350**	2130	**-3050**	1740	**-3790**
Run 3	1740	**-3480**	1770	**-4050**	1290	**-3290**	**2710**	**-11200**	2020	**-12500**
Run 4	1790	**-4200**	1650	**-19700**	1370	**-3610**	**4730**	**-9970**	1430	**-12200**
Run 5	1770	**-13300**	-1040	**-20500**	1570	**-3820**	**4330**	**-13800**	442	**-15000**
Run 6	-421	**-15100**	-1530	**-20600**	1500	**-4880**	**3900**	**-17600**	1170	**-18800**
Run 7	-704	**-16600**	-2170	**-19400**	1280	**-15800**	**3390**	**-22700**	2240	**-18900**
Run 8	-1350	**-15300**	**-3480**	**-17300**	**-2920**	**-15000**	**3430**	**-27400**	**4690**	**-16600**

Table B.5 Maximum and minimum measured strains (με), column longitudinal bars (bold numbers indicate post-yield strains)

Run #	CSG131		CSG132		CSG133		CSG134		CSG135	
	Max.	Min.	Max.	Min.	Max.	Min.	Max.	Min.	Max.	Min.
Run 1	1150	-1810	856	-1160	1030	-2030	925	-1150	1190	-1440
Run 2	1950	**-3310**	1900	**-3170**	2070	**-15000**	1440	**-15900**	973	**-12700**
Run 3	1850	**-17800**	2000	**-3220**	**6250**	**-16100**	497	**-16500**	925	**-18600**
Run 4	1380	**-21100**	2230	**-14800**	**12700**	**-14100**	911	**-17400**	1370	**-25500**
Run 5	-919	**-3740**	-1570	**-16500**	**16800**	**-17700**	1520	**-21700**	76	**-30800**
Run 6	-477	**-3630**	**-3610**	**-21300**	**21400**	**-21100**	**7160**	**-25400**	**-4200**	**-33000**
Run 7	0	**-3340**	**-5230**	**-25700**	**28500**	**-22300**	**14200**	**-23800**	**-15400**	**-31000**
Run 8	83	**-2900**	**-7910**	**-32200**	**31300**	**-10500**	**15700**	**-14300**	**-24400**	**-51700**

Run #	CSG136		CSG137		CSG138		CSG139		CSG140	
	Max.	Min.	Max.	Min.	Max.	Min.	Max.	Min.	Max.	Min.
Run 1	856	-1330	111	-39	274	-1020	608	-1160	249	-883
Run 2	1520	**-19500**	144	-52	1220	-2590	1410	-2170	1210	-2280
Run 3	**-4110**	**-18500**	229	26	1410	**-2830**	1900	-2520	1450	-2410
Run 4	**-5470**	**-21400**	105	-118	1540	**-3020**	1860	**-2860**	1670	-2560
Run 5	**-8470**	**-24400**	33	-164	1600	**-3200**	2120	**-3060**	1820	**-2750**
Run 6	**-11200**	**-30200**	13	-183	1700	**-3790**	2320	**-3290**	1790	**-2940**
Run 7	**-15800**	**-37200**	-7	-164	1720	**-4350**	2420	**-3770**	1820	**-3120**
Run 8	**-23000**	**-48100**	-26	-190	1650	**-4660**	2210	**-4090**	1710	**-3300**

Table B.6 Maximum and minimum measured strains (με), column spiral

Run #	CSG201		CSG202		CSG203		CSG204		CSG205	
	Max.	Min.	Max.	Min.	Max.	Min.	Max.	Min.	Max.	Min.
Run 1	55	-124	131	0	48	-483	193	117	124	7
Run 2	-62	-186	48	-131	-110	-518	325	117	276	0
Run 3	-48	-338	-28	-221	-124	-539	414	21	276	69
Run 4	-97	-821	-55	-338	-90	-476	428	-90	193	-435
Run 5	-83	-1200	-14	-304	-145	-566	497	-83	104	-594
Run 6	-41	-1150	55	-393	-159	-746	546	-228	117	-545
Run 7	-7	-828	76	-531	-242	-946	573	-345	152	-490
Run 8	-7	-642	131	-669	-338	-1120	546	-546	359	-538

Run #	CSG206		CSG207		CSG208		CSG209		CSG210	
	Max.	Min.	Max.	Min.	Max.	Min.	Max.	Min.	Max.	Min.
Run 1	180	69	124	-172	152	48	200	131	-110	-573
Run 2	186	41	-48	-227	249	14	207	117	-117	-380
Run 3	255	35	-69	-289	269	-41	193	69	-145	-449
Run 4	228	62	-96	-310	269	-97	166	14	-214	-746
Run 5	200	0	-76	-406	283	-207	152	-14	-235	-1100
Run 6	159	-48	-96	-695	318	-104	131	-28	-249	-663
Run 7	207	-131	-158	-1020	345	-221	131	-48	-242	-1020
Run 8	435	-456	-248	-1430	387	-1290	117	-76	-249	-1070

Table B.7 Maximum and minimum measured strains (με), column spiral

Run #	CSG211		CSG212		CSG213		CSG214		CSG215	
	Max.	Min.	Max.	Min.	Max.	Min.	Max.	Min.	Max.	Min.
Run 1	352	283	41	-7	13	-46	-13	-72	7	-46
Run 2	345	249	41	-21	-7	-59	-33	-92	0	-79
Run 3	338	221	41	-41	-26	-85	-46	-124	-20	-105
Run 4	297	186	-28	-111	-124	-196	-92	-209	-59	-131
Run 5	276	166	-28	-124	-98	-157	-144	-236	-79	-144
Run 6	269	117	-7	-145	-105	-164	-150	-249	-92	-164
Run 7	249	90	7	-159	-118	-177	-164	-255	-105	-177
Run 8	235	62	-14	-159	-118	-183	-177	-262	-111	-203

Run #	CSG216		CSG217		CSG218		CSG219		CSG220	
	Max.	Min.	Max.	Min.	Max.	Min.	Max.	Min.	Max.	Min.
Run 1	-20	-72	83	-62	97	-269	138	-69	69	-14
Run 2	-33	-92	21	-324	-90	-407	41	-97	55	-69
Run 3	-52	-111	-173	-594	-248	-511	7	-124	104	-97
Run 4	-124	-190	-297	-794	-262	-600	-21	-228	186	-193
Run 5	-144	-196	-283	-856	-145	-704	-35	-290	304	-221
Run 6	-157	-216	-249	-877	14	-1010	-41	-324	331	-311
Run 7	-170	-236	-235	-870	131	-1130	-76	-414	331	-386
Run 8	-177	-242	-345	-1010	200	-1190	-110	-511	290	-504

Table B.8 Maximum and minimum measured strains (με), column spiral (bold numbers indicate post-yield strains)

Run #	CSG221		CSG222		CSG223		CSG224	
	Max.	Min.	Max.	Min.	Max.	Min.	Max.	Min.
Run 1	104	-200	117	14	117	-14	48	-28
Run 2	-21	-283	110	0	62	-62	180	-7
Run 3	-104	-462	173	28	124	-193	276	90
Run 4	-200	-1060	179	14	124	-304	304	90
Run 5	-228	-1530	145	-110	214	-421	332	-131
Run 6	-186	-1620	207	-393	228	-497	366	-138
Run 7	-193	-1680	311	-414	352	-704	428	-712
Run 8	138	-1620	476	-1090	428	-967	1970	**-3350**

Table B.9 Maximum and minimum measured strains (με), rebar hinge longitudinal bars (bold numbers indicate post-yield strains)

Run #	HSG101		HSG102		HSG103		HSG104		HSG105	
	Max.	Min.	Max.	Min.	Max.	Min.	Max.	Min.	Max.	Min.
Run 1	557	-1220	1130	-1800	503	-1380	771	-2040	956	-1380
Run 2	908	-2500	1600	-2600	812	-2450	1310	**-2650**	936	**-16700**
Run 3	1490	**-2900**	1940	**-2770**	1310	**-2810**	1580	**-2750**	**-4940**	**-21600**
Run 4	1790	**-3430**	2100	**-3090**	1580	**-3010**	1790	**-2740**	**-3710**	**-32400**
Run 5	2060	**-4470**	2430	**-3840**	1800	**-3110**	1900	**-2880**	**-6010**	**-34700**
Run 6	2240	**-5940**	**3140**	**-5760**	1990	**-3240**	2020	**-3030**	**-8550**	**-33600**
Run 7	2540	**-6620**	**3380**	**-7170**	2230	**-3520**	2150	**-3170**	**-9750**	**-30800**
Run 8	**2640**	**-6780**	**2940**	**-8740**	**2770**	**-4800**	2310	**-3450**	**-8350**	**-26200**

Table B.10 Maximum and minimum measured strains (με), rebar hinge longitudinal bars (bold numbers indicate strains more than εy)

Run #	HSG106		HSG107		HSG108		HSG109		HSG110	
	Max.	Min.	Max.	Min.	Max.	Min.	Max.	Min.	Max.	Min.
Run 1	**6180**	**-5020**	1010	-2050	1780	**-2880**	489	-943	1380	-1090
Run 2	**10300**	**-20300**	1160	**-21800**	1540	**-17100**	729	-2000	1680	-1910
Run 3	**12300**	**-30800**	**-3650**	**-24300**	**9130**	**-21800**	1110	-2460	1950	-2210
Run 4	**11700**	**-41600**	**-2680**	**-23900**	**18900**	**-17300**	1290	**-2770**	2120	-2470
Run 5	**12600**	**-42500**	1150	**-30400**	**28300**	**-22700**	1440	**-2860**	2150	**-2650**
Run 6	**11600**	**-30600**	**4160**	**-37700**	**37100**	**-24300**	1570	**-2880**	2220	**-2790**
Run 7	**15300**	**-16300**	**9720**	**-44400**	**45000**	**-22800**	1620	**-2840**	2270	**-2960**
Run 8	**13600**	**-6780**	**12300**	**-51400**	**53600**	**-17700**	1660	**-2750**	2350	**-3410**

Run #	HSG111		HSG112		HSG113		HSG114		HSG115	
	Max.	Min.	Max.	Min.	Max.	Min.	Max.	Min.	Max.	Min.
Run 1	730	-805	551	-1520	1360	-1460	929	-709	1260	-2310
Run 2	915	-1570	812	-1900	1540	-2520	1270	-2090	1840	**-3170**
Run 3	1480	-1910	1000	-2070	1910	**-2880**	1740	**-2890**	2220	**-4130**
Run 4	1660	-2180	1210	-2050	2070	**-3150**	1910	**-3220**	2410	**-4700**
Run 5	1760	-2480	1250	-2200	2150	**-3520**	2170	**-4170**	**2940**	**-5960**
Run 6	1840	**-2710**	1310	-2310	2360	**-4050**	**2730**	**-7700**	**3510**	**-7970**
Run 7	1890	**-2900**	1410	-2390	**2620**	**-4660**	**3720**	**-8990**	**3670**	**-9930**
Run 8	1930	**-3060**	1470	-2420	**2890**	**-5490**	**3660**	**-8870**	**3830**	**-12000**

Table B.11 Maximum and minimum measured strains (με), rebar hinge longitudinal bars (bold numbers indicate strains more than εy)

Run #	HSG116		HSG117		HSG118		HSG119		HSG120	
	Max.	Min.	Max.	Min.	Max.	Min.	Max.	Min.	Max.	Min.
Run 1	633	-1160	1910	-1930	1660	-1250	2000	-2530	1100	-1160
Run 2	991	-2460	**2970**	**-19700**	**3950**	**-6890**	**5300**	**-11700**	1160	**-11300**
Run 3	1290	**-2920**	**2970**	**-25300**	**10400**	**-18600**	**7490**	**-15500**	-2350	**-14500**
Run 4	1440	**-3230**	**6270**	**-37600**	**3060**	**-2660**	**7410**	**-12800**	-1760	**-13600**
Run 5	1570	**-3700**	**2690**	**-42500**	2040	-1680	**7930**	**-17500**	-558	**-16300**
Run 6	1800	**-4150**	**-2860**	**-41800**	**2790**	-1680	**8680**	**-21600**	-255	**-21500**
Run 7	2110	**-4870**	**-9150**	**-37400**	**4070**	-1360	**9900**	**-24000**	-1600	**-27800**
Run 8	2410	**-6460**	-	-	**15100**	-1620	**10000**	**-24900**	**-5830**	**-29500**

Run #	HSG121		HSG122		HSG123		HSG124	
	Max.	Min.	Max.	Min.	Max.	Min.	Max.	Min.
Run 1	867	-1230	399	-330	**4430**	2000	475	-1040
Run 2	1050	-2150	606	-1510	**4880**	1450	771	-2060
Run 3	1470	-2610	936	-2230	**5010**	1200	1090	-2350
Run 4	1810	**-3150**	1150	-2610	**5090**	1200	1290	-2470
Run 5	2060	**-3590**	1420	**-2840**	**5120**	1010	1400	**-2750**
Run 6	2230	**-3950**	1580	**-2990**	**5140**	840	1540	**-3020**
Run 7	2470	**-4250**	1680	**-2960**	**5210**	737	1670	**-3240**
Run 8	**2650**	**-4520**	1700	**-2890**	**5230**	399	1790	**-3500**

Table B.12 Maximum and minimum measured strains (με), rebar hinge spiral

Run #	HSG201		HSG202		HSG203		HSG204		HSG205	
	Max.	Min.	Max.	Min.	Max.	Min.	Max.	Min.	Max.	Min.
Run 1	337	0	165	28	124	-41	310	34	83	-14
Run 2	330	69	282	-131	303	-48	434	76	28	-62
Run 3	365	28	289	-165	324	-7	557	14	41	-62
Run 4	324	-193	-	-	344	-482	612	-145	14	-151
Run 5	365	-489	-	-	413	-1410	674	-103	7	-193
Run 6	358	-915	227	-516	365	-1320	612	-275	14	-206
Run 7	241	-1510	165	-922	434	-778	619	-943	21	-213
Run 8	186	-1940	385	-702	517	-351	-	-	14	-199

Run #	HSG206		HSG207		HSG208		HSG209		HSG210	
	Max.	Min.	Max.	Min.	Max.	Min.	Max.	Min.	Max.	Min.
Run 1	76	-28	62	7	131	41	165	28	193	14
Run 2	62	-145	62	-14	117	0	496	14	344	103
Run 3	90	-172	96	-7	165	14	943	14	365	207
Run 4	83	-213	83	-14	179	28	496	-200	385	172
Run 5	90	-227	117	-14	186	21	-	-	447	110
Run 6	90	-227	144	0	200	7	-	-	303	-117
Run 7	96	-227	172	0	179	7	-	-	289	-530
Run 8	90	-255	172	-7	179	-7	-	-	441	-743

Table B.13 Maximum and minimum measured strains (με), rebar hinge spiral

Run #	HSG211		HSG212		HSG213		HSG214		HSG215	
	Max.	Min.	Max.	Min.	Max.	Min.	Max.	Min.	Max.	Min.
Run 1	69	7	124	-55	165	-21	103	-1160	89	28
Run 2	48	-28	96	-158	289	-21	-172	-2120	76	0
Run 3	28	-41	110	-117	255	-124	-674	-2200	76	7
Run 4	-14	-96	76	-103	234	-145	-461	-1420	34	-34
Run 5	-21	-103	200	-193	213	-303	-544	-1590	48	-28
Run 6	-34	-117	358	-372	186	-502	-592	-1710	69	-28
Run 7	-34	-110	454	-427	200	-723	-619	-1890	83	-28
Run 8	-41	-110	626	-310	296	-743	-695	-2190	96	-14

Run #	HSG216	
	Max.	Min.
Run 1	62	-76
Run 2	7	-330
Run 3	-103	-399
Run 4	-172	-475
Run 5	-186	-488
Run 6	-193	-516
Run 7	-199	-530
Run 8	-206	-557

Table B.14 Maximum and minimum measured strains (με), cap beam longitudinal bars

Run #	BSG101		BSG102		BSG103		BSG104		BSG105	
	Max.	Min.	Max.	Min.	Max.	Min.	Max.	Min.	Max.	Min.
Run 1	-13	-65	-7	-72	242	179	-	-	7	-85
Run 2	-20	-85	-20	-92	269	173	-	-	26	-137
Run 3	-39	-105	-39	-118	276	179	-	-	0	-170
Run 4	-72	-137	-72	-150	228	138	-	-	-26	-196
Run 5	-85	-150	-85	-170	221	131	-	-	-33	-209
Run 6	-98	-164	-105	-183	214	124	-	-	-39	-222
Run 7	-105	-170	-118	-196	221	110	-	-	-46	-236
Run 8	-111	-177	-131	-209	214	97	-	-	-52	-255

Run #	BSG106		BSG107		BSG108		BSG109		BSG110	
	Max.	Min.	Max.	Min.	Max.	Min.	Max.	Min.	Max.	Min.
Run 1	-13	-118	193	28	255	138	13	-78	-7	-72
Run 2	-	-	283	-76	318	76	26	-157	7	-131
Run 3	-	-	311	-55	318	48	7	-170	-13	-164
Run 4	-700	-1780	276	-90	262	-48	-20	-196	-26	-183
Run 5	33	-177	269	-145	242	-90	-33	-209	-46	-203
Run 6	13	-190	242	-214	242	-152	-46	-229	-72	-229
Run 7	7	-196	242	-304	214	-262	-65	-248	-79	-249
Run 8	7	-203	228	-373	200	-359	-78	-248	-98	-262

Table B.15 Maximum and minimum measured strains (με), cap beam longitudinal bars

Run #	BSG111		BSG112		BSG113		BSG114		BSG115	
	Max.	Min.	Max.	Min.	Max.	Min.	Max.	Min.	Max.	Min.
Run 1	221	97	283	76	26	-59	-13	-72	165	83
Run 2	318	62	401	-48	0	-79	-20	-92	172	55
Run 3	304	-7	366	-117	-13	-105	-33	-105	206	55
Run 4	255	-90	352	-152	-39	-118	-46	-118	179	0
Run 5	262	-124	359	-200	-46	-131	-59	-144	165	-14
Run 6	249	-159	345	-235	-52	-150	-72	-150	151	-34
Run 7	255	-179	345	-249	-65	-157	-92	-157	144	-34
Run 8	242	-179	338	-269	-85	-157	-98	-170	124	-55

Run #	BSG116	
	Max.	Min.
Run 1	-145	-214
Run 2	-124	-235
Run 3	-90	-249
Run 4	-104	-290
Run 5	-111	-297
Run 6	-111	-304
Run 7	-111	-304
Run 8	-117	-311

Table B.16 Maximum and minimum measured strains (με), cap beam stirrups (bold numbers indicate post-yield strains)

Run #	BSG201		BSG202		BSG203		BSG204		BSG205	
	Max.	Min.	Max.	Min.	Max.	Min.	Max.	Min.	Max.	Min.
Run 1	643	587	808	739	-214	-277	1040	967	-649	-822
Run 2	636	574	794	697	-194	-283	1070	960	-580	-842
Run 3	629	560	780	677	-214	-304	1040	939	-594	-849
Run 4	622	546	766	663	-235	-353	1000	905	-635	-870
Run 5	608	532	739	649	-249	-366	974	884	-621	-898
Run 6	601	518	725	628	-263	-401	967	863	-628	-967
Run 7	601	518	725	621	-339	-477	967	856	-649	-1090
Run 8	587	511	718	621	-353	-505	960	843	-670	-1170

Run #	BSG206		BSG207		BSG208		BSG209		BSG210	
	Max.	Min.	Max.	Min.	Max.	Min.	Max.	Min.	Max.	Min.
Run 1	622	456	994	939	552	497	-	-	718	539
Run 2	663	387	980	911	545	476	-	-	711	380
Run 3	712	373	960	897	552	462	-	-	697	338
Run 4	739	339	953	870	525	442	-	-	663	-41
Run 5	746	332	932	863	518	442	-	-	649	-159
Run 6	739	311	918	835	497	435	-	-	-	-
Run 7	705	276	890	821	490	428	-	-	-	-
Run 8	684	256	884	808	483	414	-	-	-	-

Table B.17 Maximum and minimum measured strains (με), cap beam stirrups (bold numbers indicate post-yield strains)

Run #	BSG211		BSG212		BSG213		BSG214	
	Max.	Min.	Max.	Min.	Max.	Min.	Max.	Min.
Run 1	-311	-366	539	483	711	532	628	449
Run 2	-324	-393	552	490	787	490	697	421
Run 3	-331	-407	546	463	787	463	767	442
Run 4	-359	-435	525	442	815	428	746	407
Run 5	-373	-456	518	442	822	394	739	394
Run 6	-387	-462	518	435	822	373	691	373
Run 7	-387	-462	511	435	828	352	656	352
Run 8	-393	-469	497	435	822	338	622	338

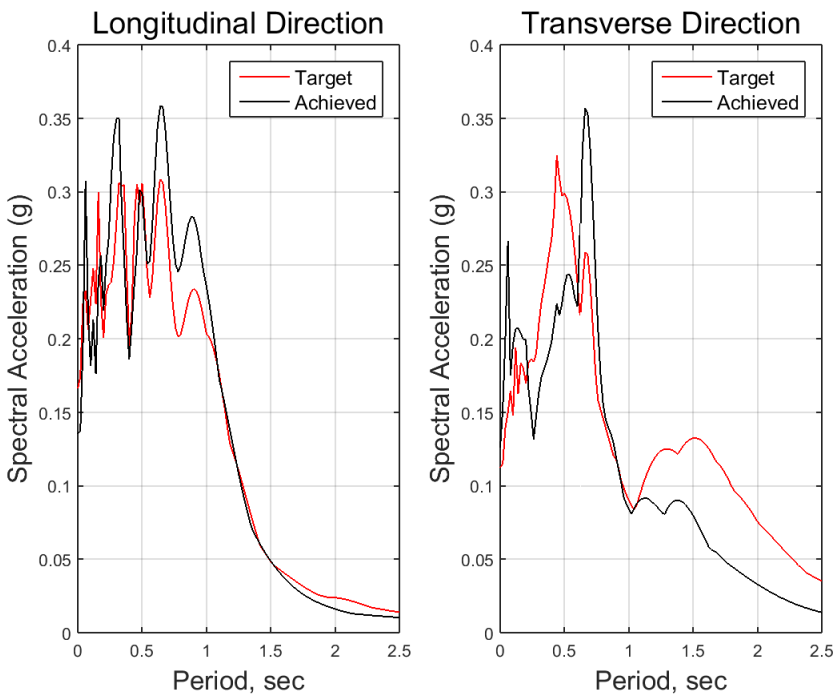

Figure B.10 Achieved vs. Target response spectra – Run1

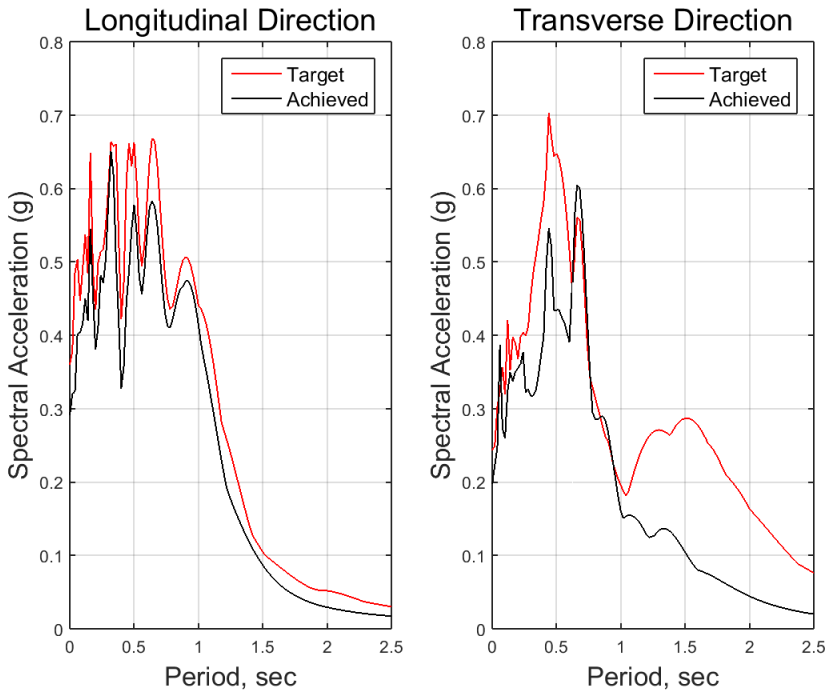

Figure B.11 Achieved vs. Target response spectra – Run2

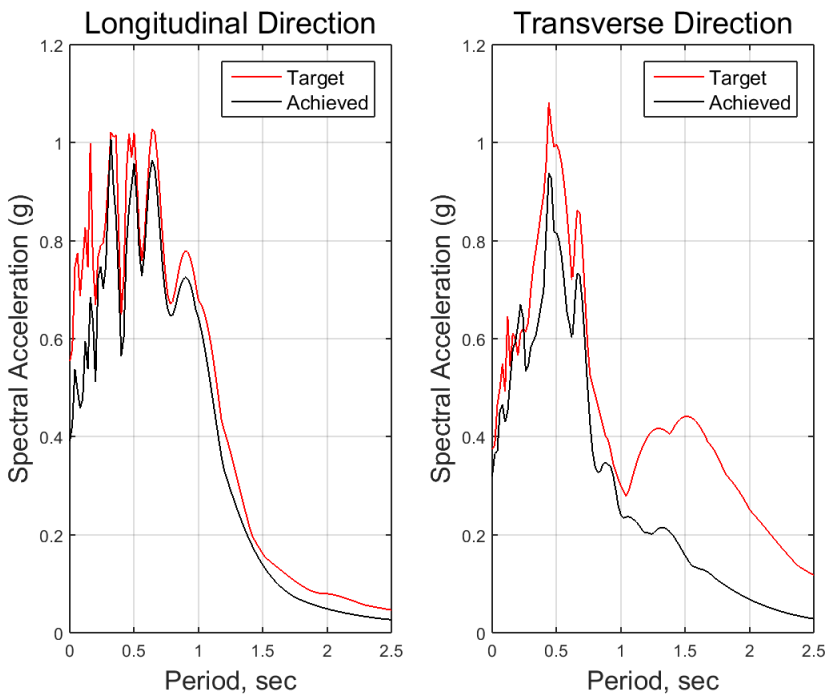

Figure B.12 Achieved vs. Target response spectra – Run3

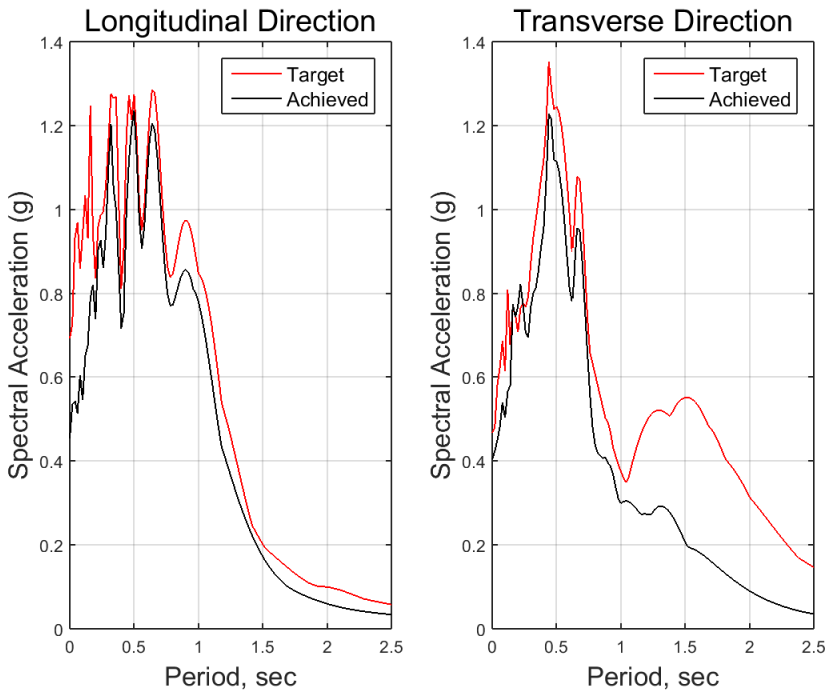

Figure B.13 Achieved vs. Target response spectra – Run4

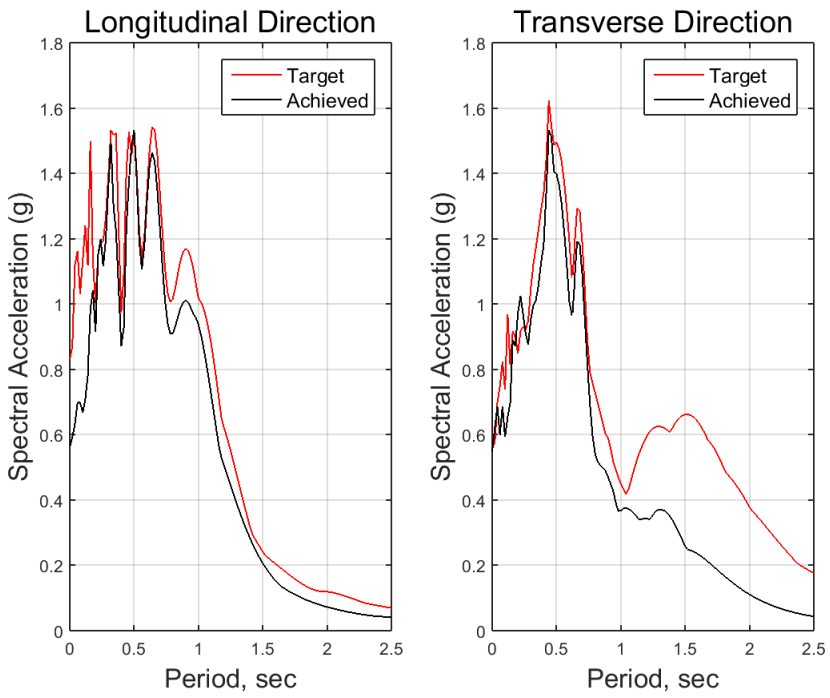

Figure B.14 Achieved vs. Target response spectra – Run5

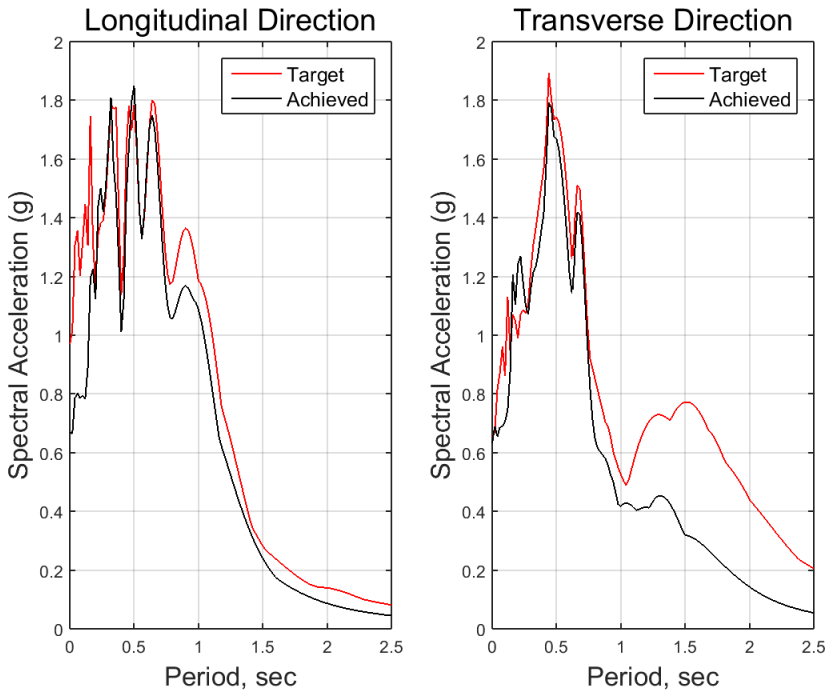

Figure B.15 Achieved vs. Target response spectra – Run6

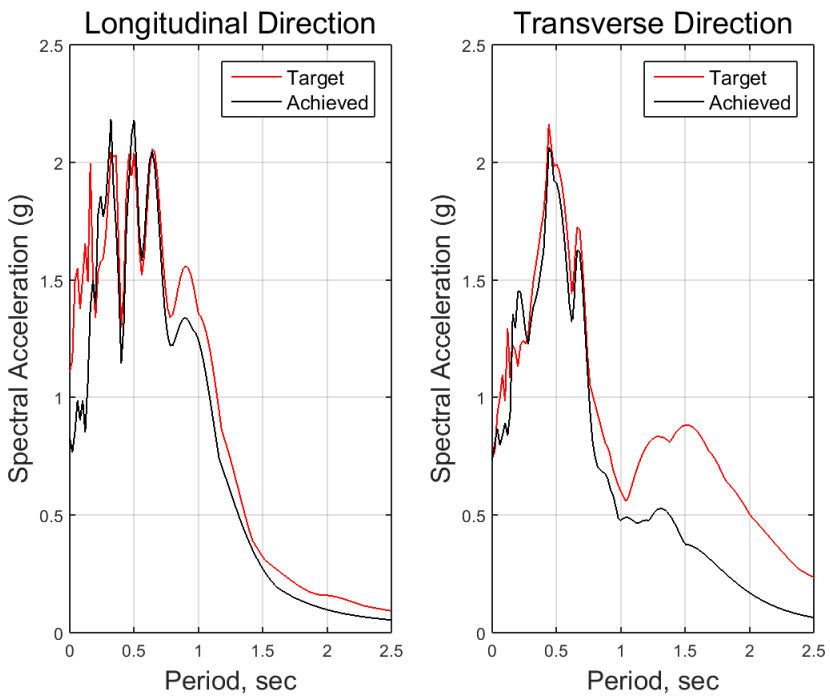

Figure B.16 Achieved vs. Target response spectra – Run7

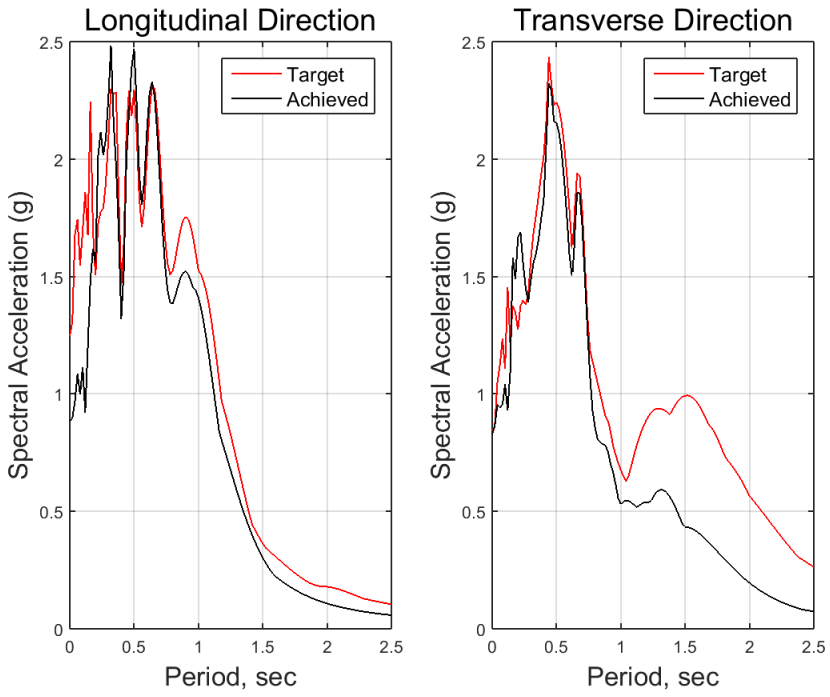

Figure B.17 Achieved vs. Target response spectra – Run8

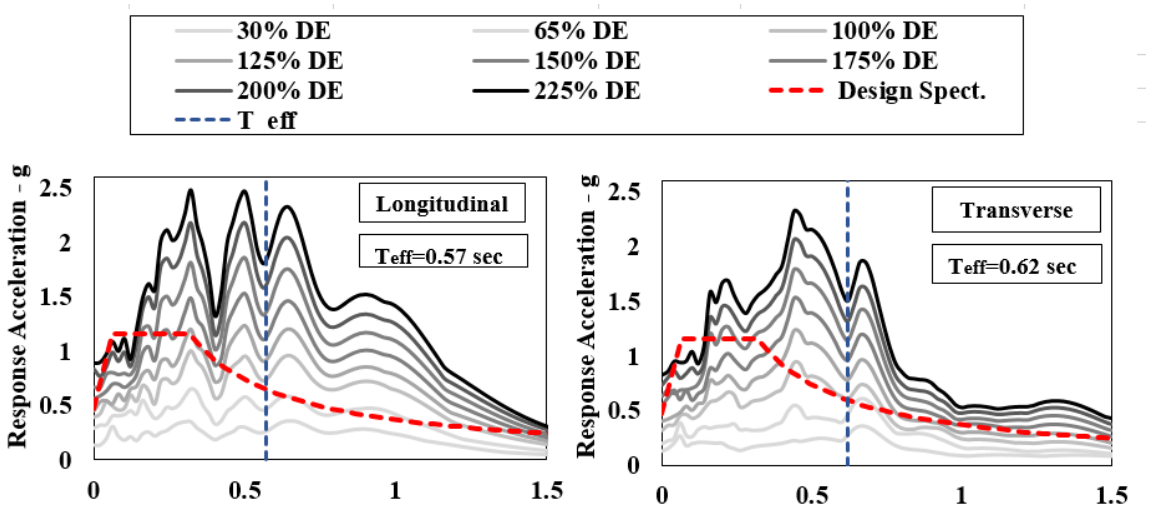

Figure B.18 Response spectra for each earthquake run, the design spectrum, and the effective periods

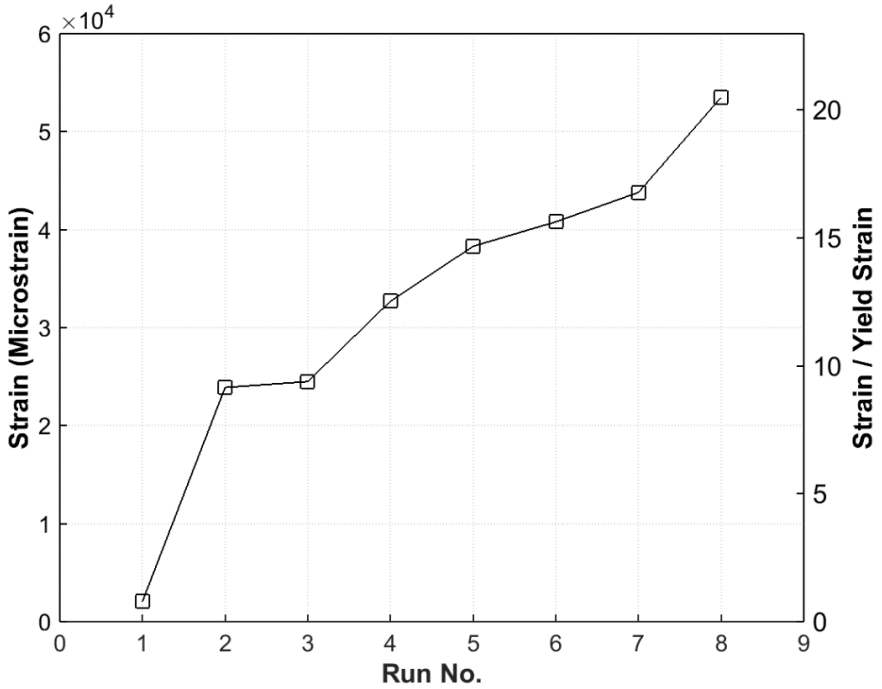

Figure B.19 Maximum strain in south column longitudinal bars at each run (plastic hinge zone: CS4, CS5, CS6)

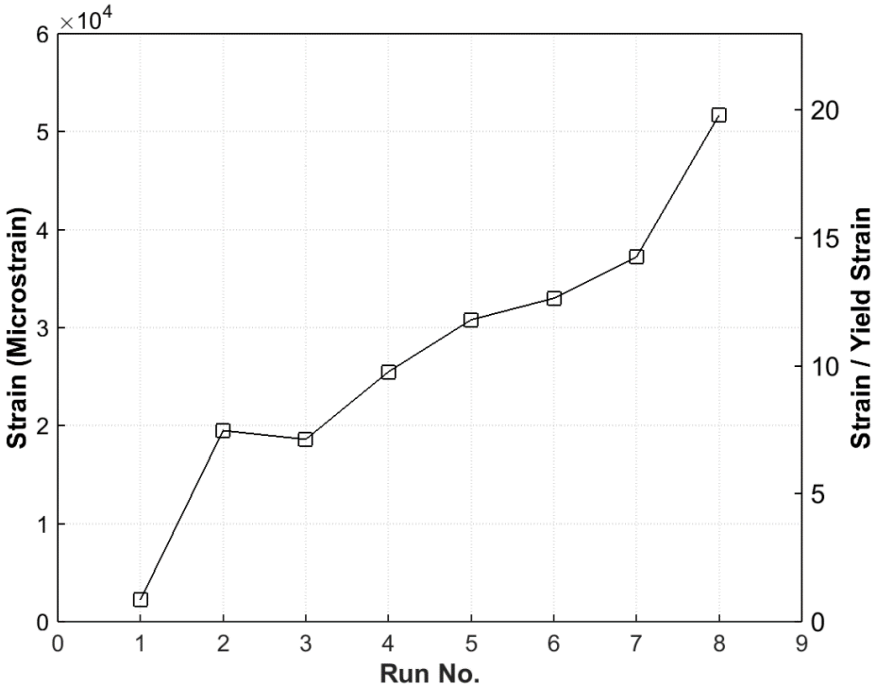

Figure B.20 Maximum strain in north column longitudinal bars at each run (plastic hinge zone: CN4, CN5, CN6)

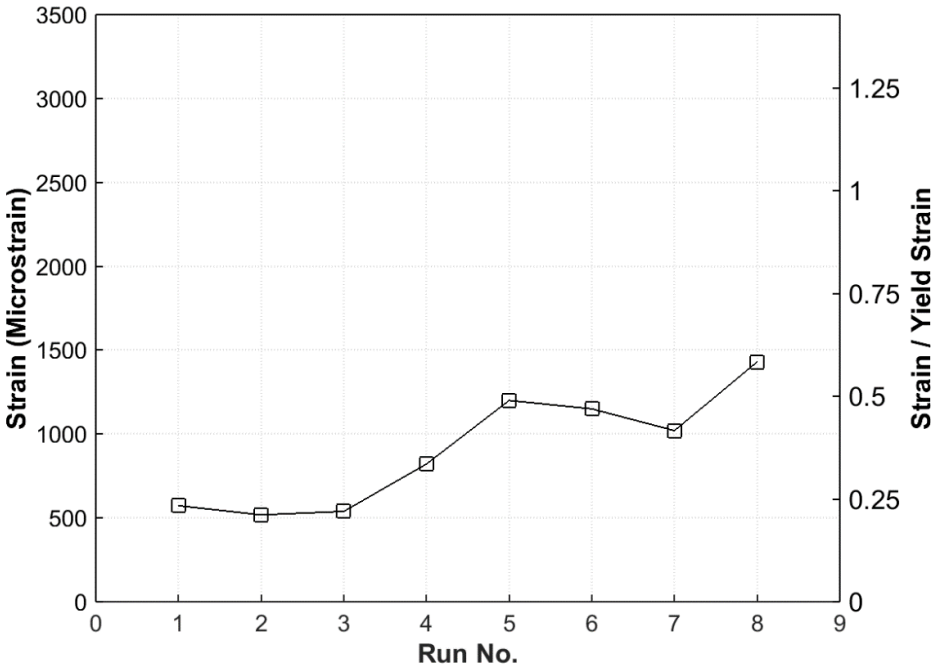

Figure B.21 Maximum strain in south column spirals at each run (plastic hinge zone: CS3, CS4, CS5)

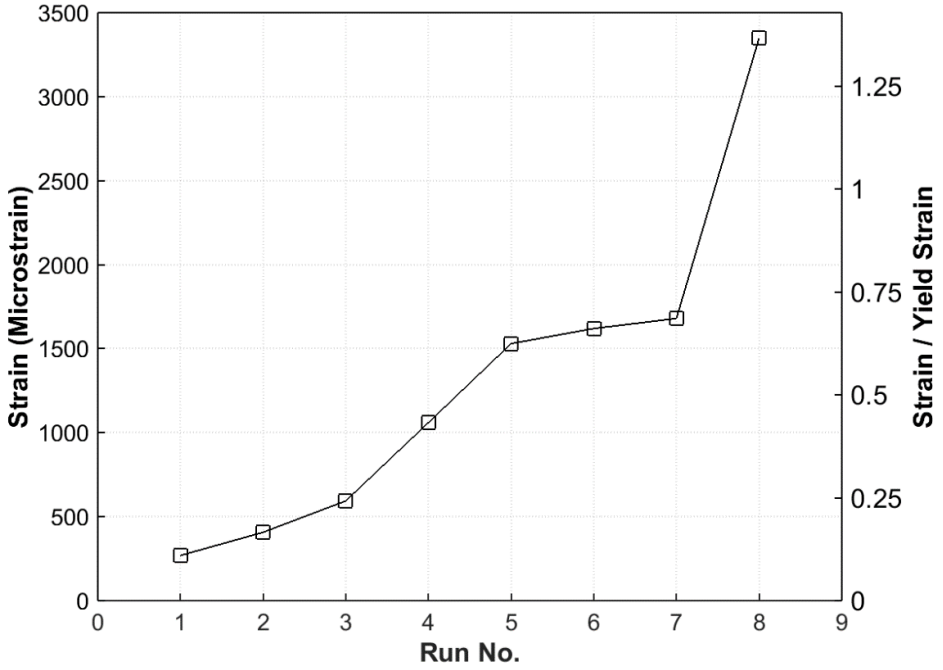

Figure B.22 Maximum strain in north column spirals at each run (plastic hinge zone: CN3, CN4, CN5)

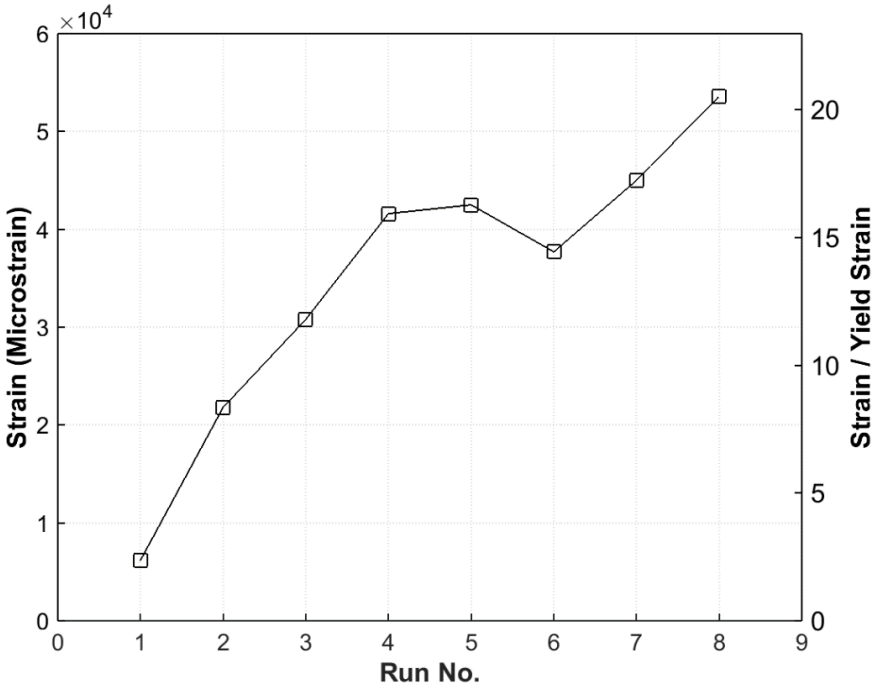

Figure B.23 Maximum strain in south rebar hinge longitudinal bars at each run – (CS1, CS2)

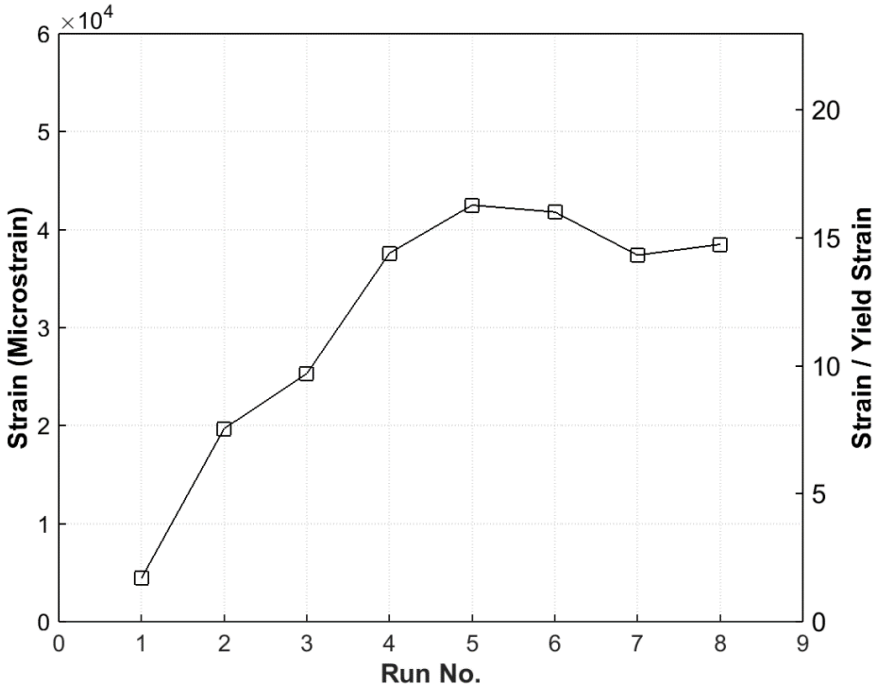

Figure B.24 Maximum strain in north rebar hinge longitudinal bars at each run – (CN1, CN2)

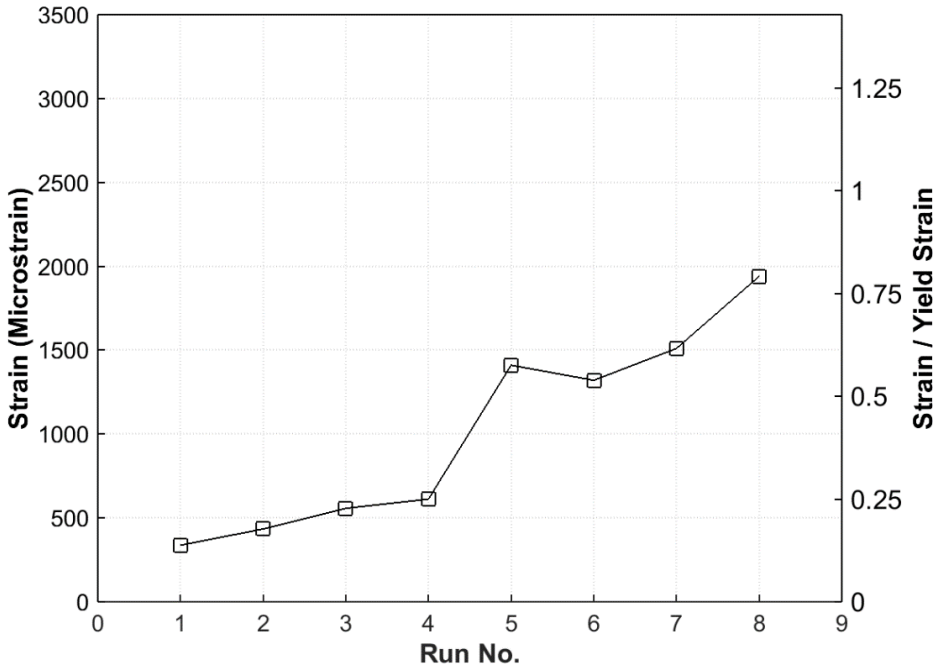

Figure B.25 Maximum strain in south rebar hinge spiral at each run – (CS1, CS2)

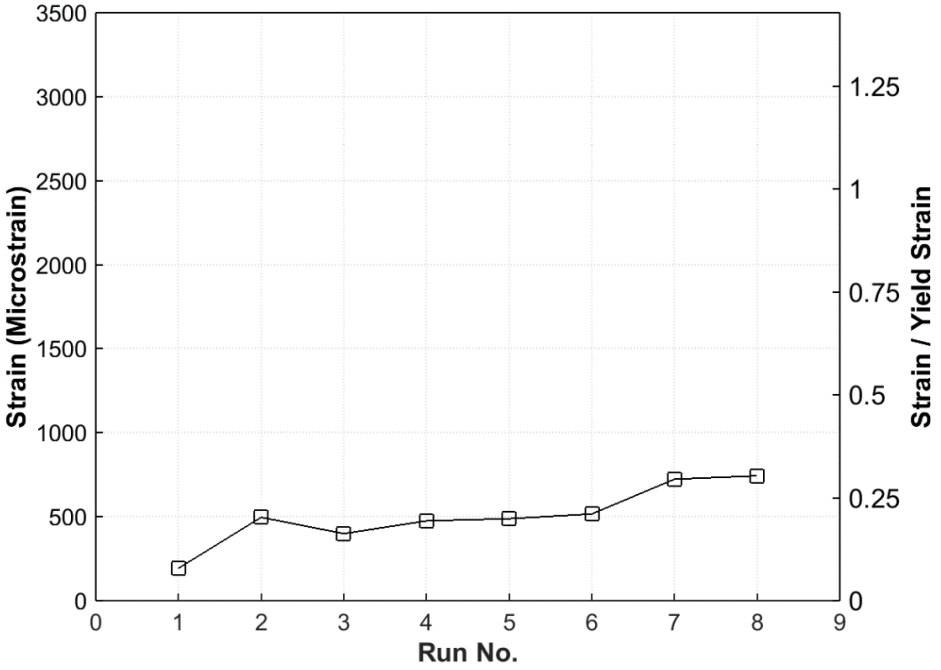

Figure B.26 Maximum strain in north rebar hinge spiral at each run – (CN1, CN2)

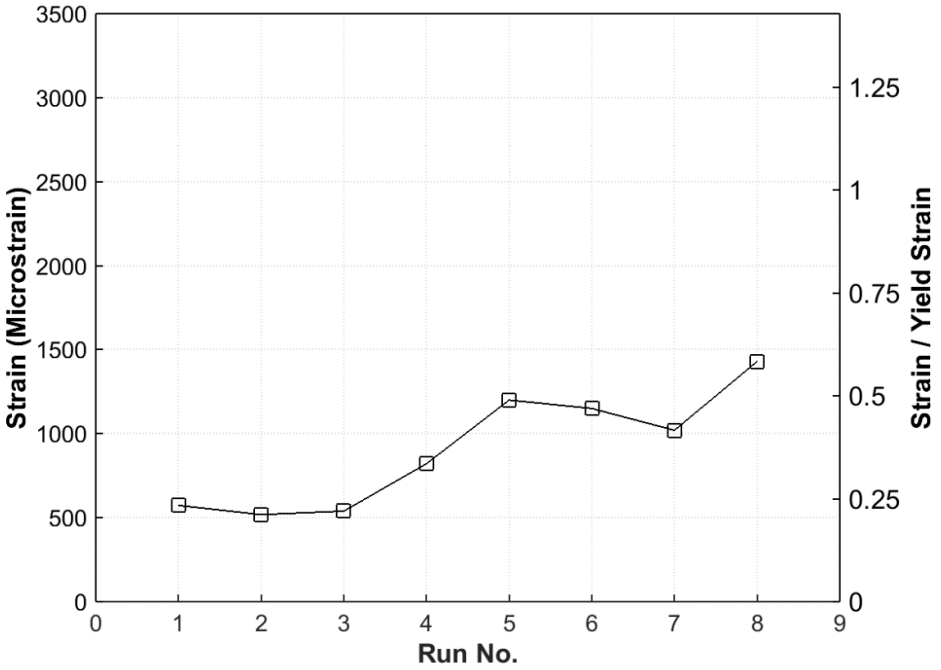

Figure B.27 Maximum strain in cap beam longitudinal bars at each run – section CB-1

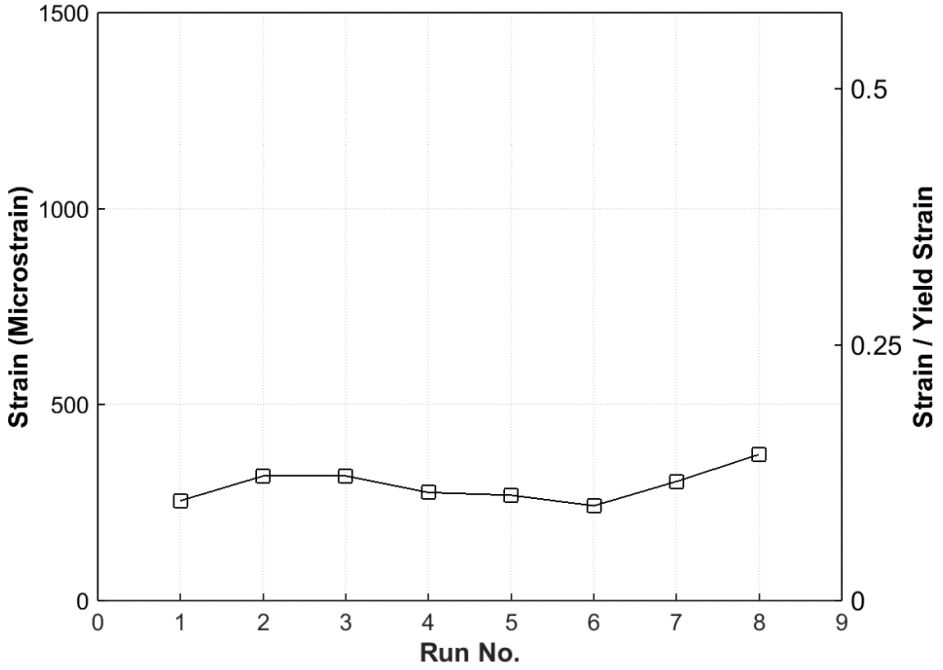

Figure B.28 Maximum strain in cap beam longitudinal bars at each run – section CB-2

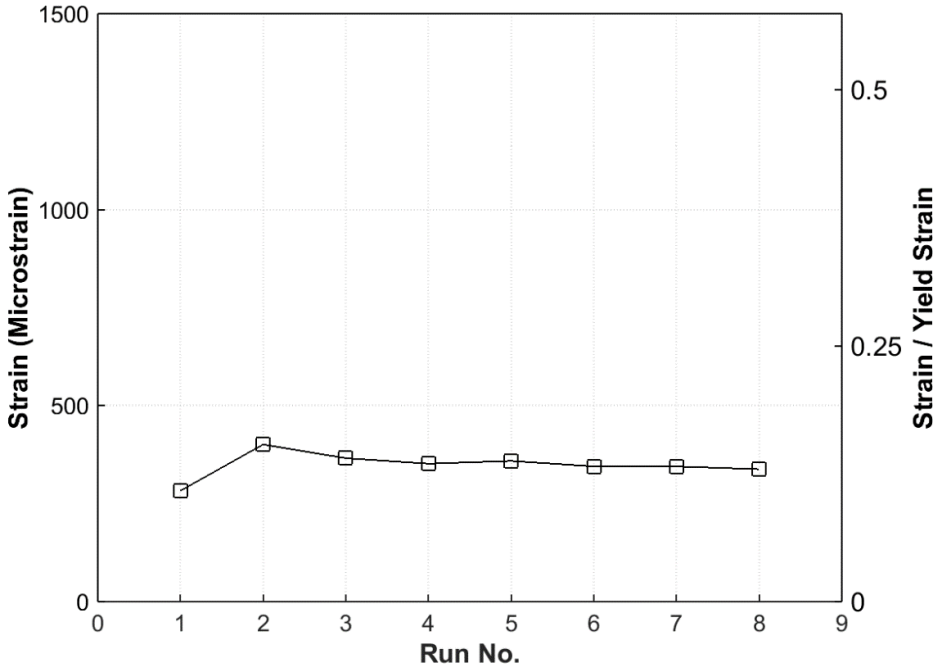

Figure B.29 Maximum strain in cap beam longitudinal bars at each run – section CB-3

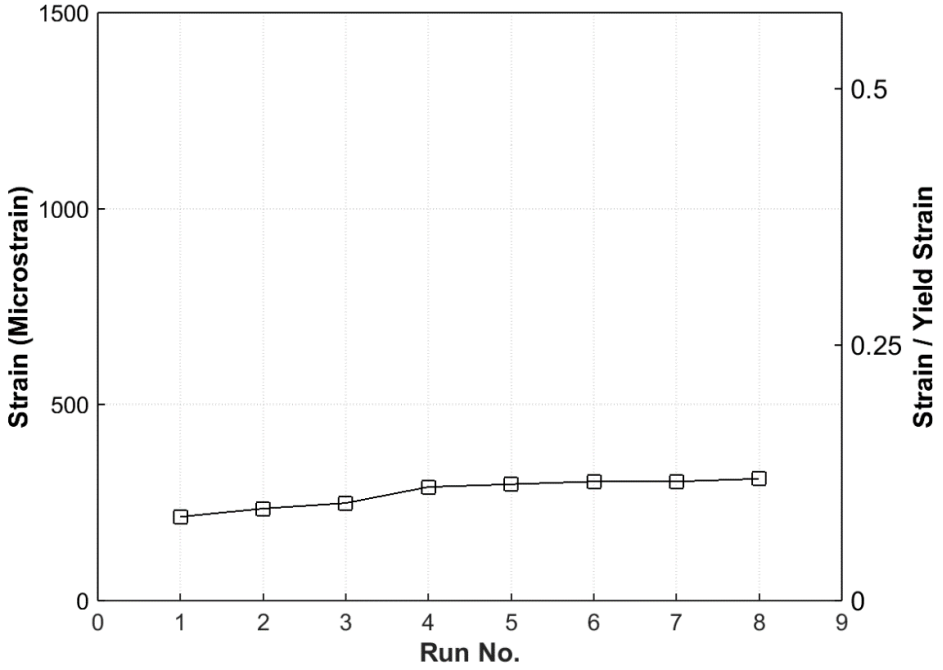

Figure B.30 Maximum strain in cap beam longitudinal bars at each run – section CB-4

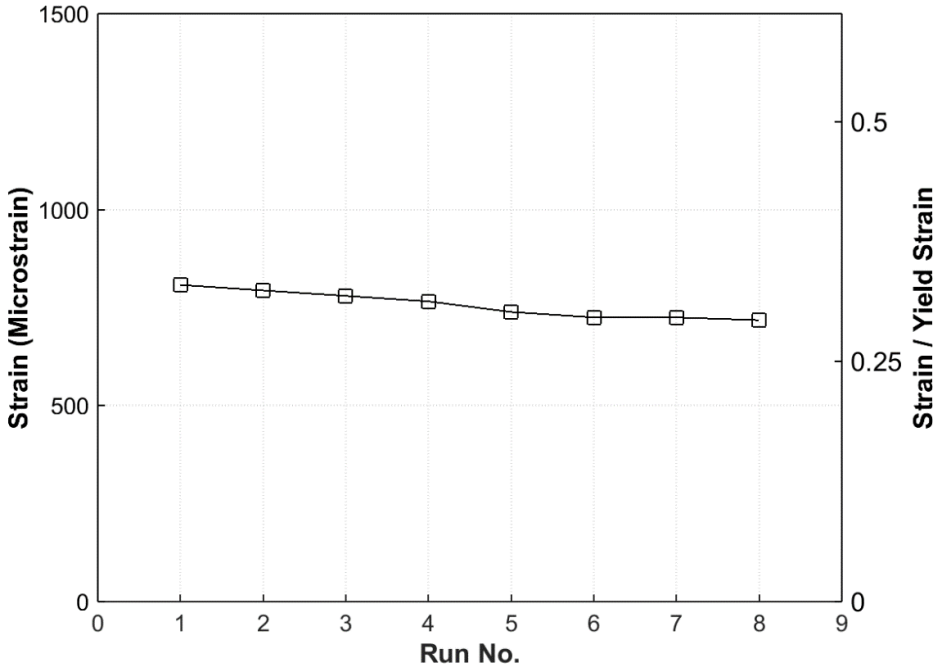

Figure B.31 Maximum strain in cap beam stirrups at each run – section CB-5

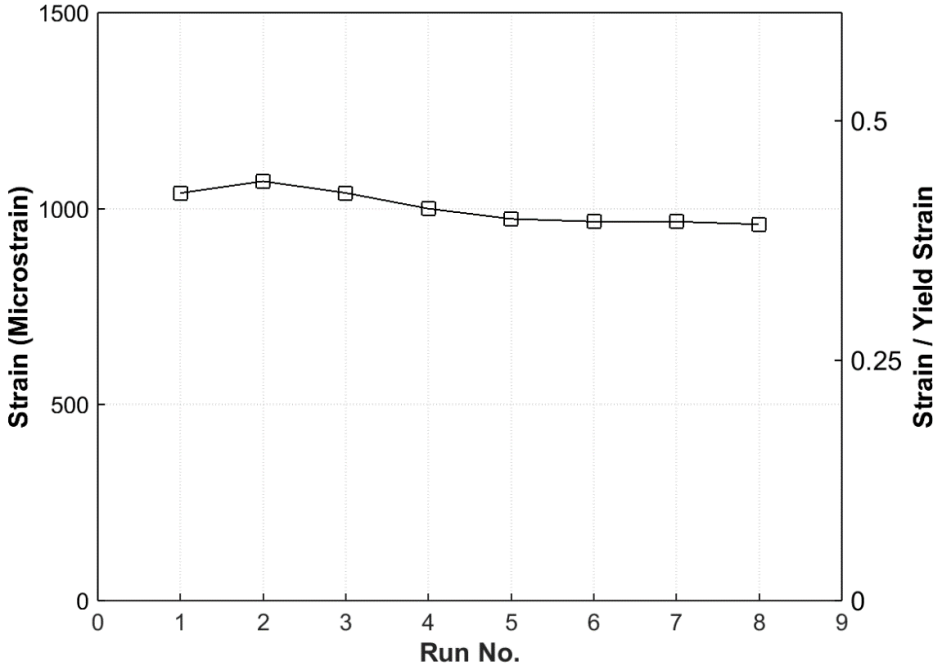

Figure B.32 Maximum strain in cap beam stirrups at each run – section CB-6

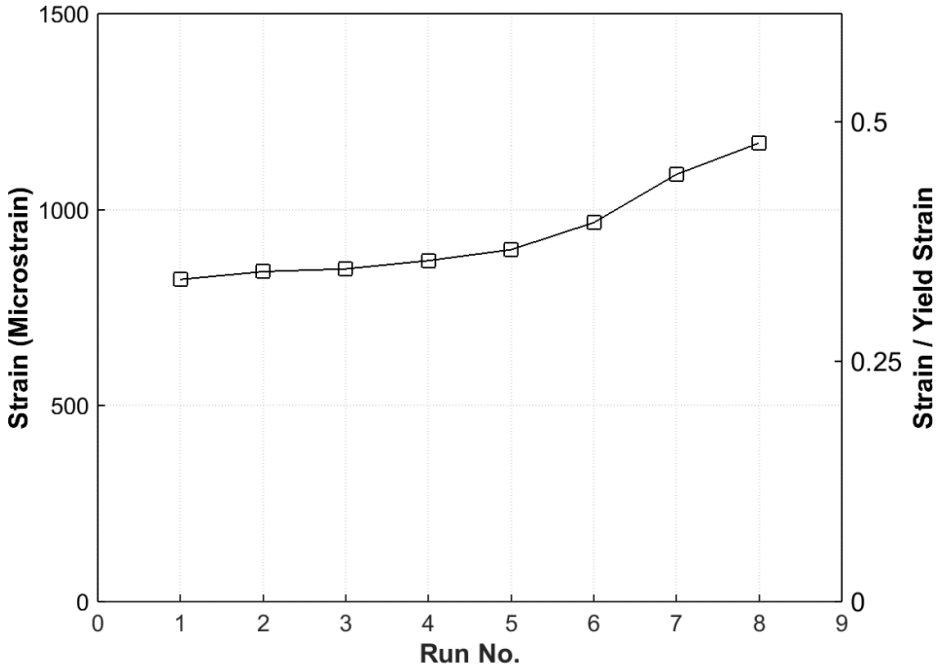

Figure B.33 Maximum strain in cap beam stirrups at each run – section CB-7

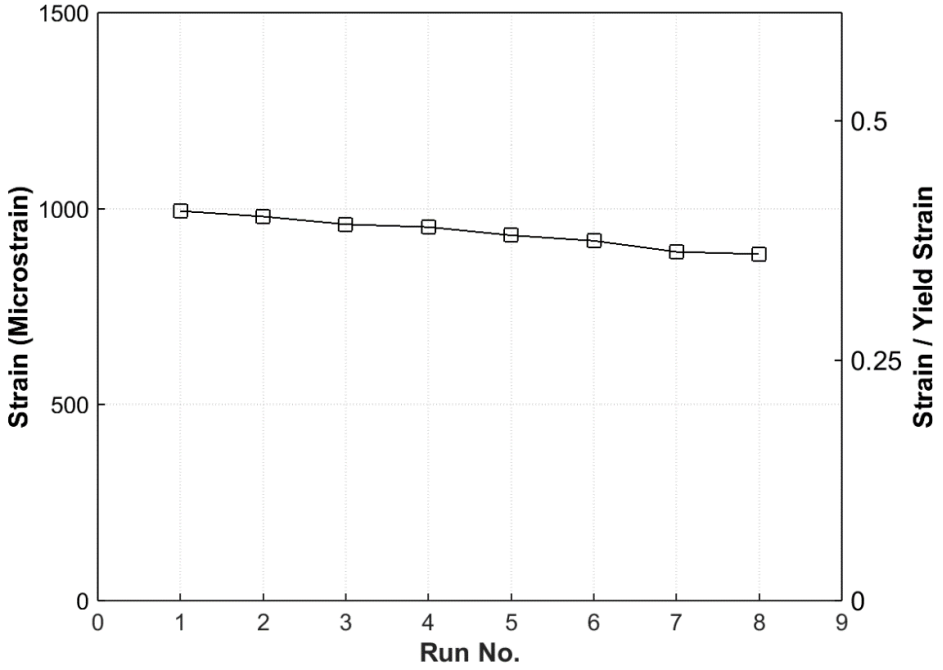

Figure B.34 Maximum strain in cap beam stirrups at each run – section CB-8

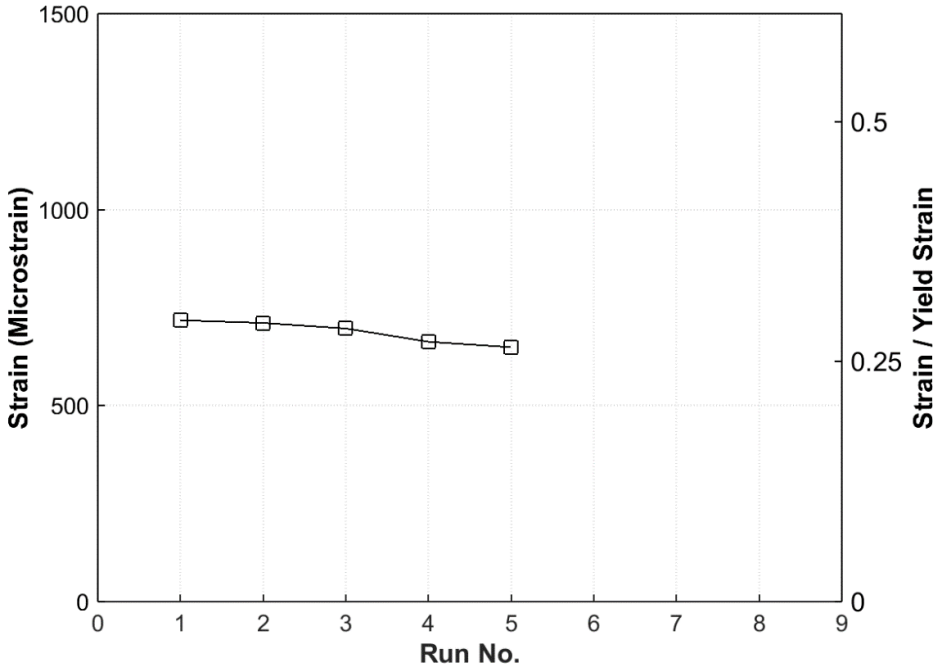

Figure B.35 Maximum strain in cap beam stirrups at each run – section CB-9

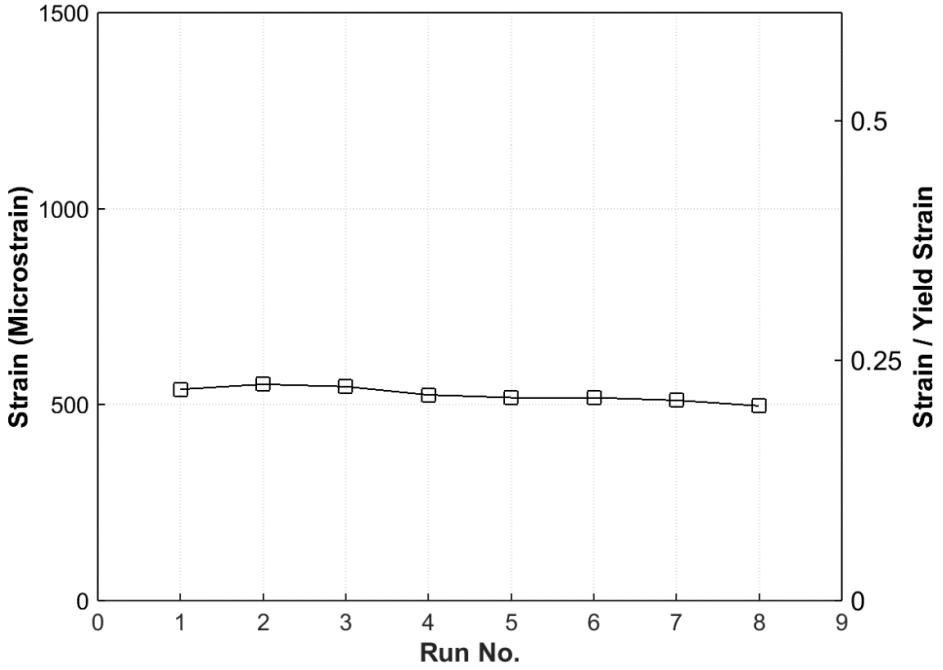

Figure B.36 Maximum strain in cap beam stirrups at each run – section CB-10

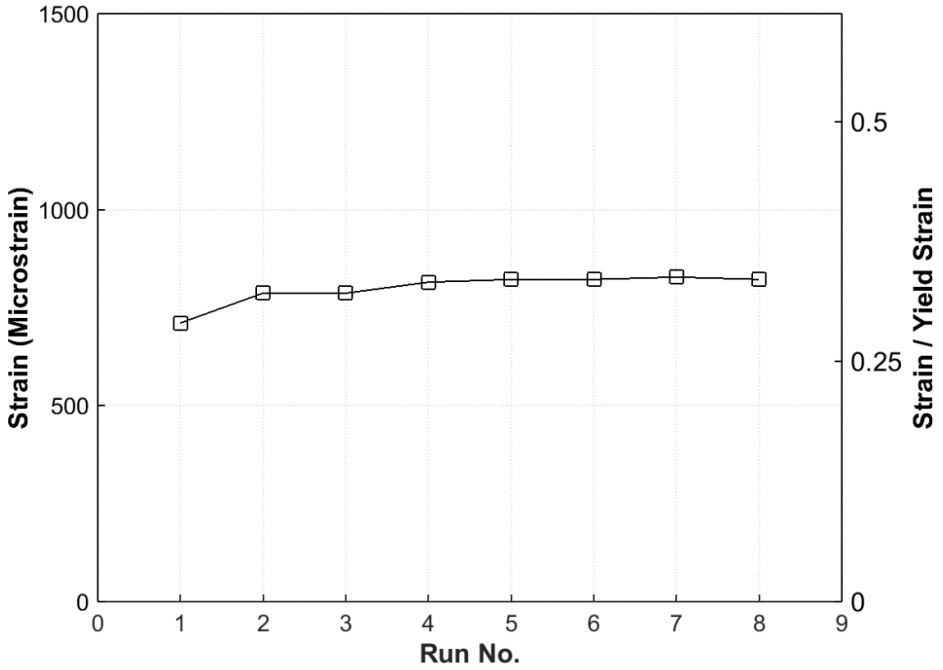

Figure B.37 Maximum strain in cap beam stirrups at each run – section CB-11

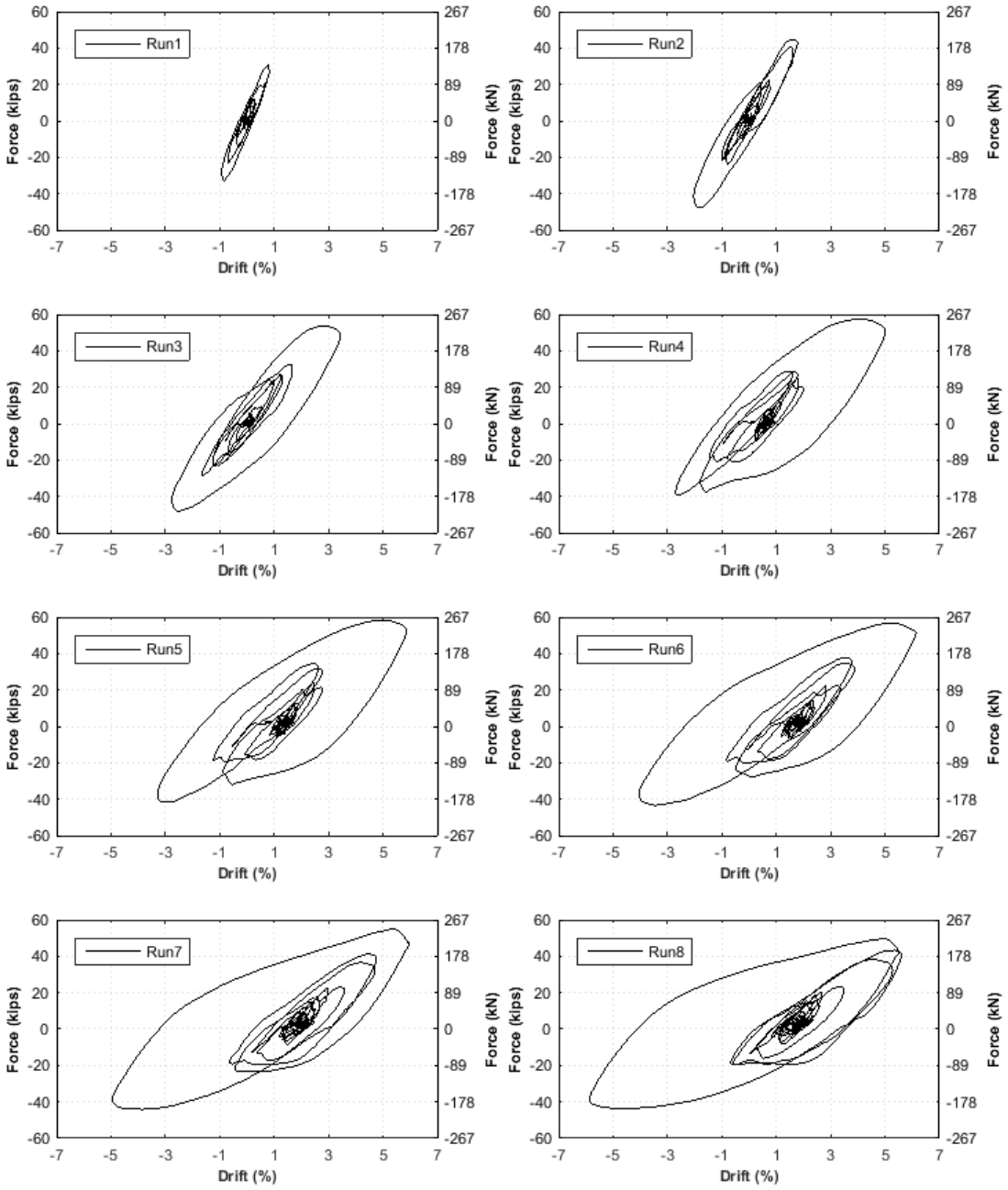

Figure B.38 Measured force-displacement hysteresis curves at each run - Longitudinal direction

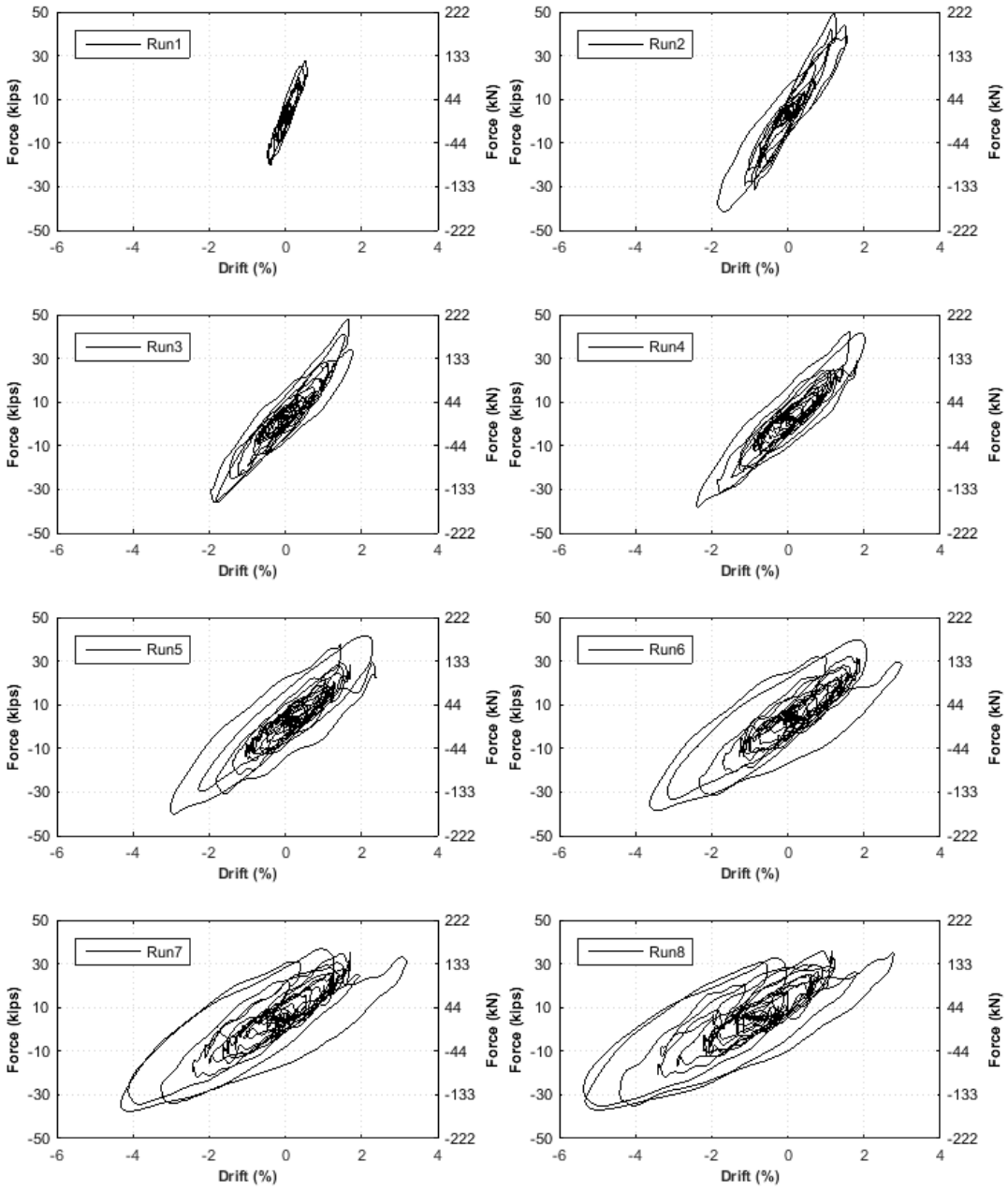

Figure B.39 Measured force-displacement hysteresis curves at each run – Transverse direction

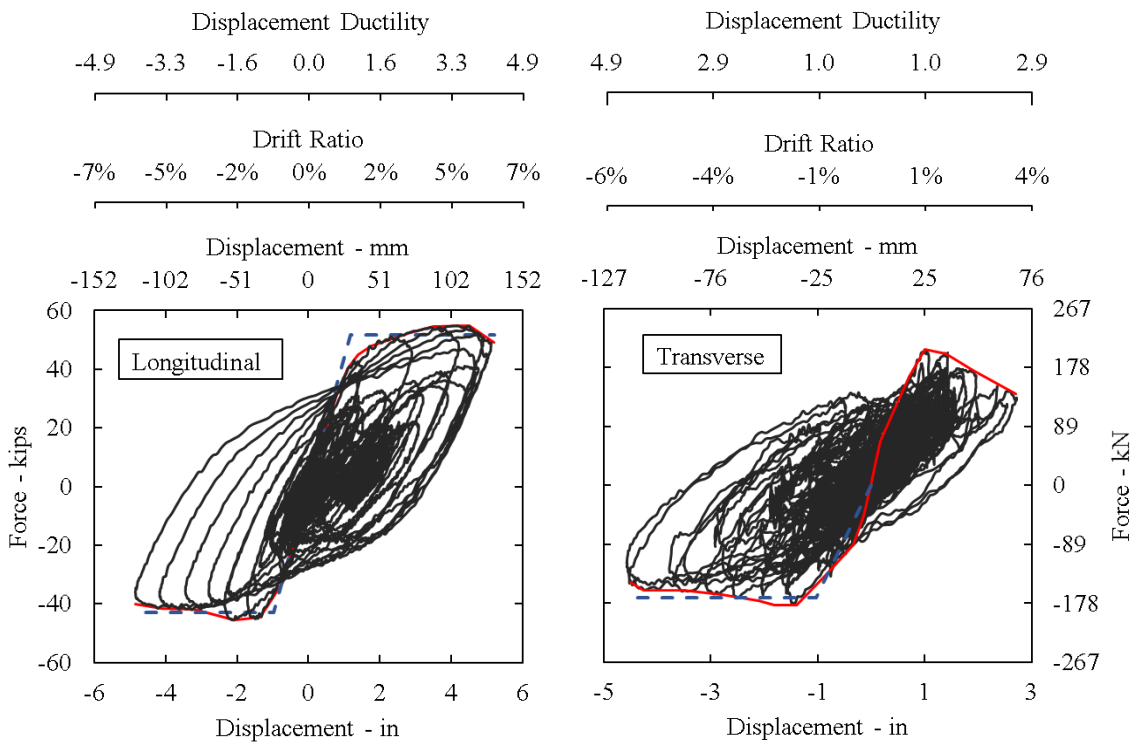

Figure B.40 Cumulative measured force vs. displacement, envelopes (red), and idealized (blue dashed line) curves

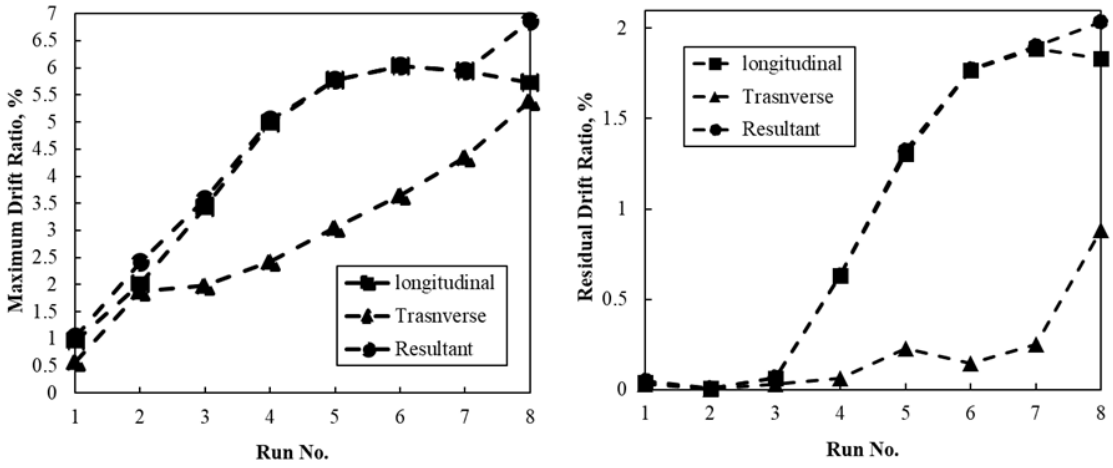

Figure B.41 Bent peak and residual drift ratios

B.3. Transverse displacement histories

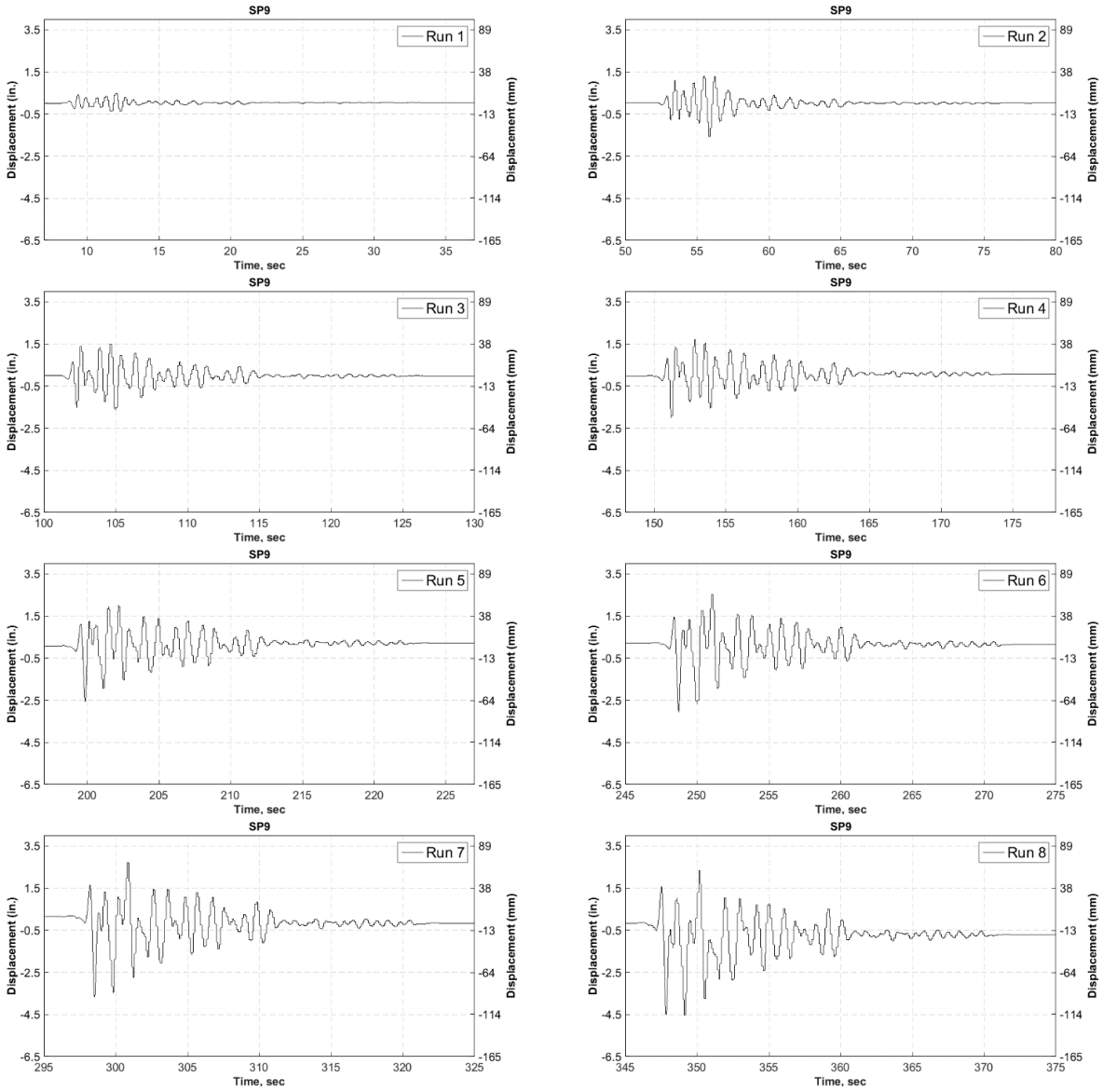

Figure B.42 Bent transverse displacement histories (SP09)

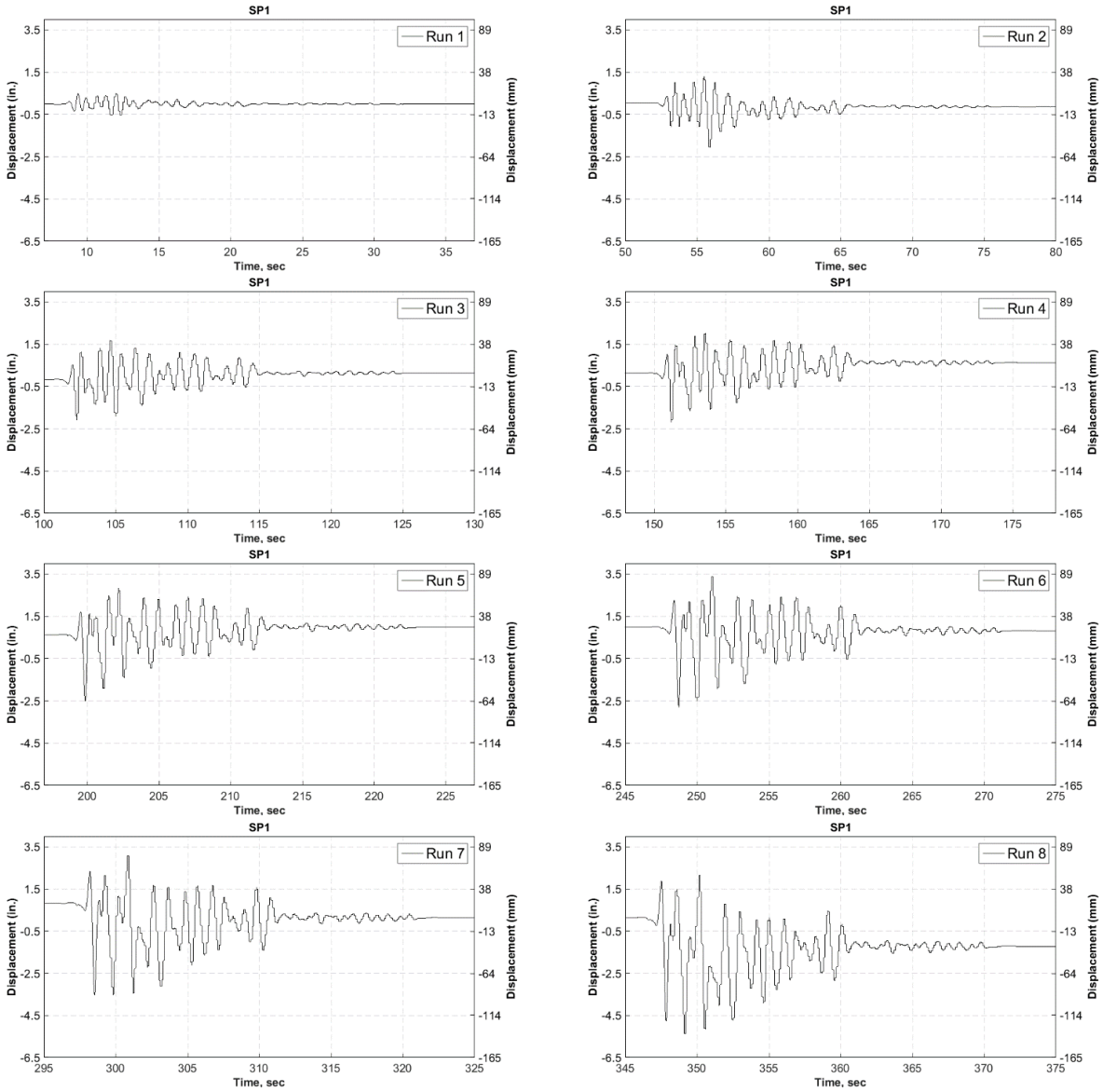

Figure B.43 West abutment transverse displacement histories (SP01)

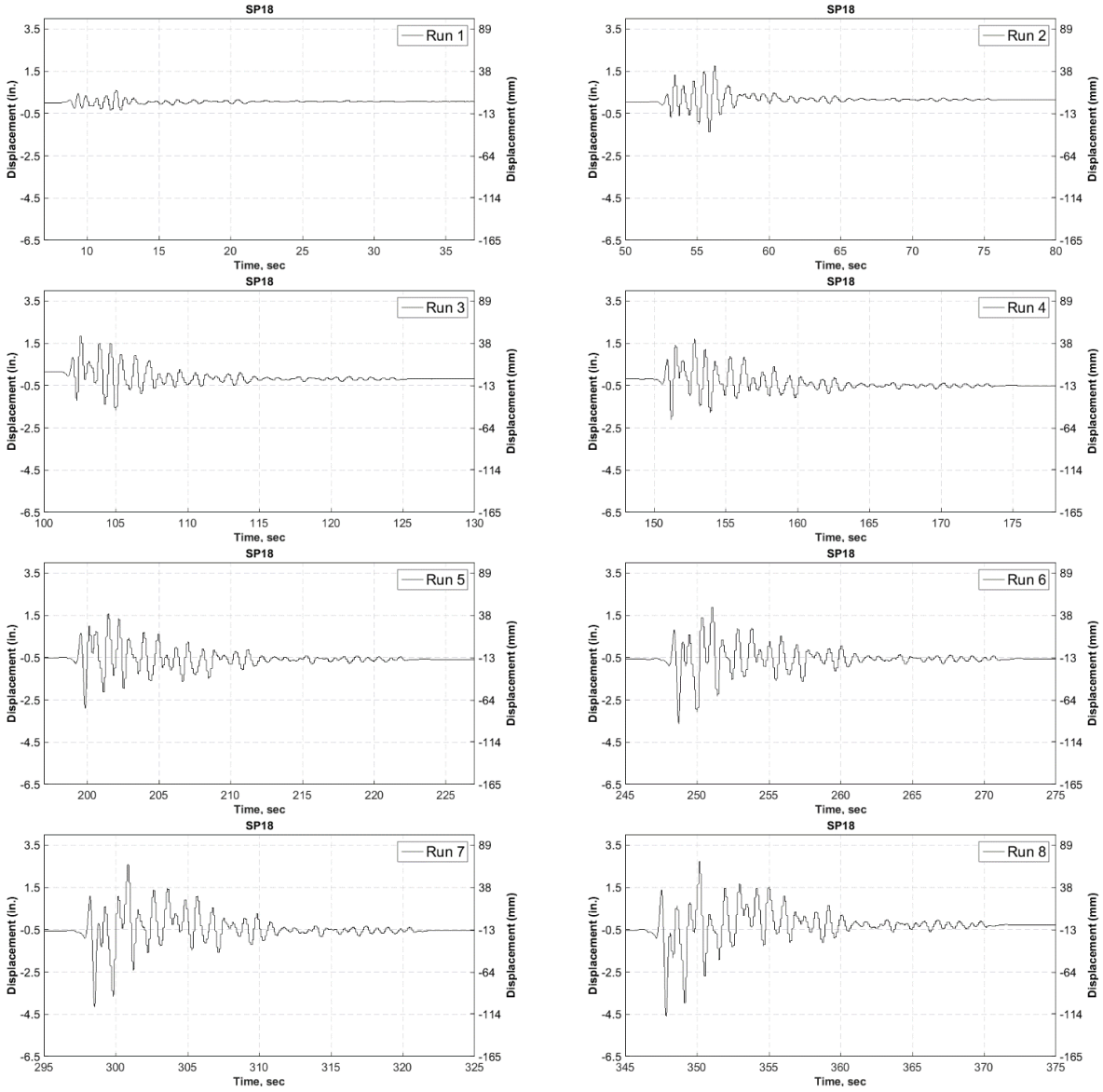

Figure B.44 East abutment displacement histories (SP18)

B.4. Longitudinal displacement histories

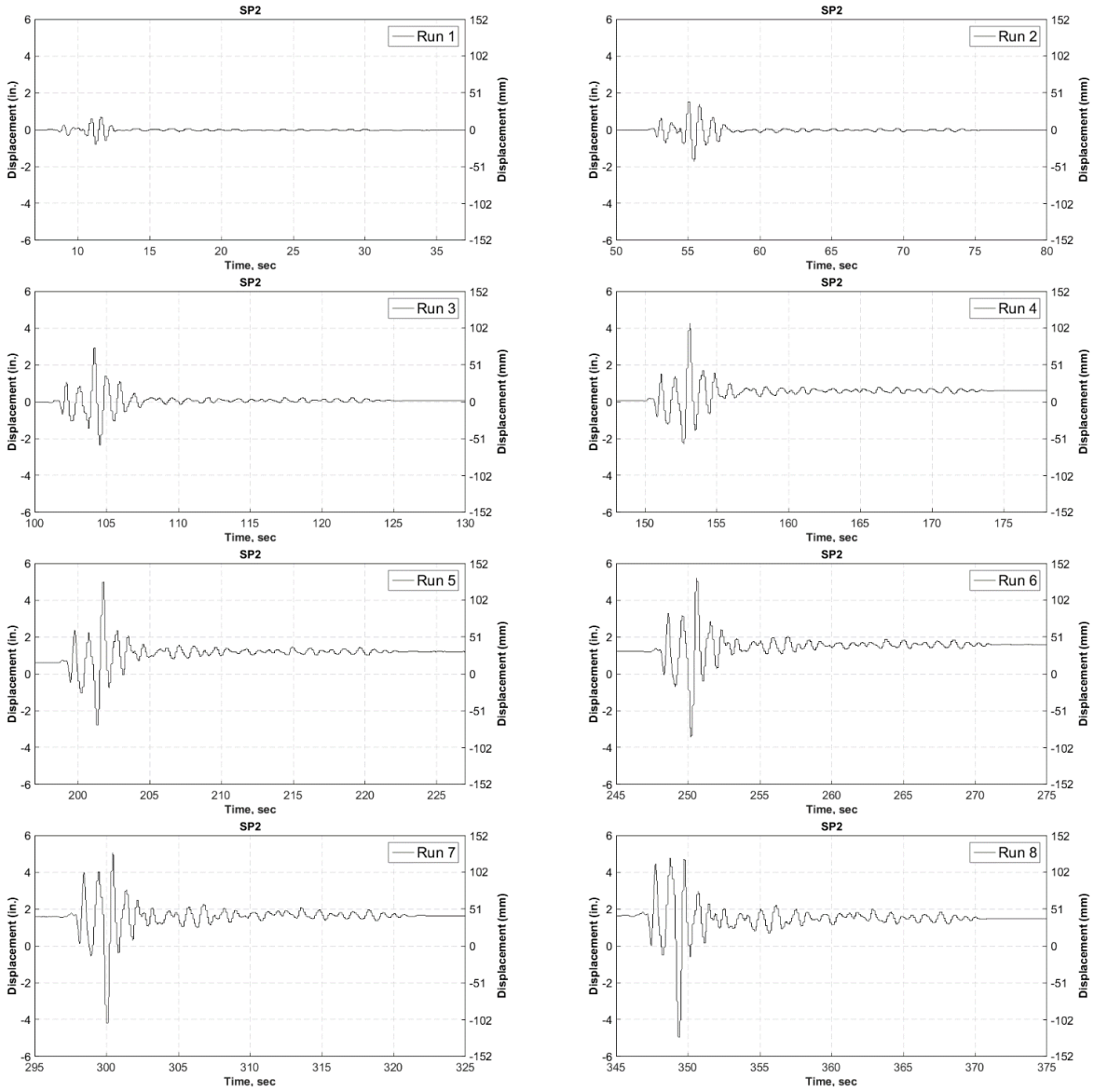

Figure B.45 West abutment longitudinal displacement histories (SP02)

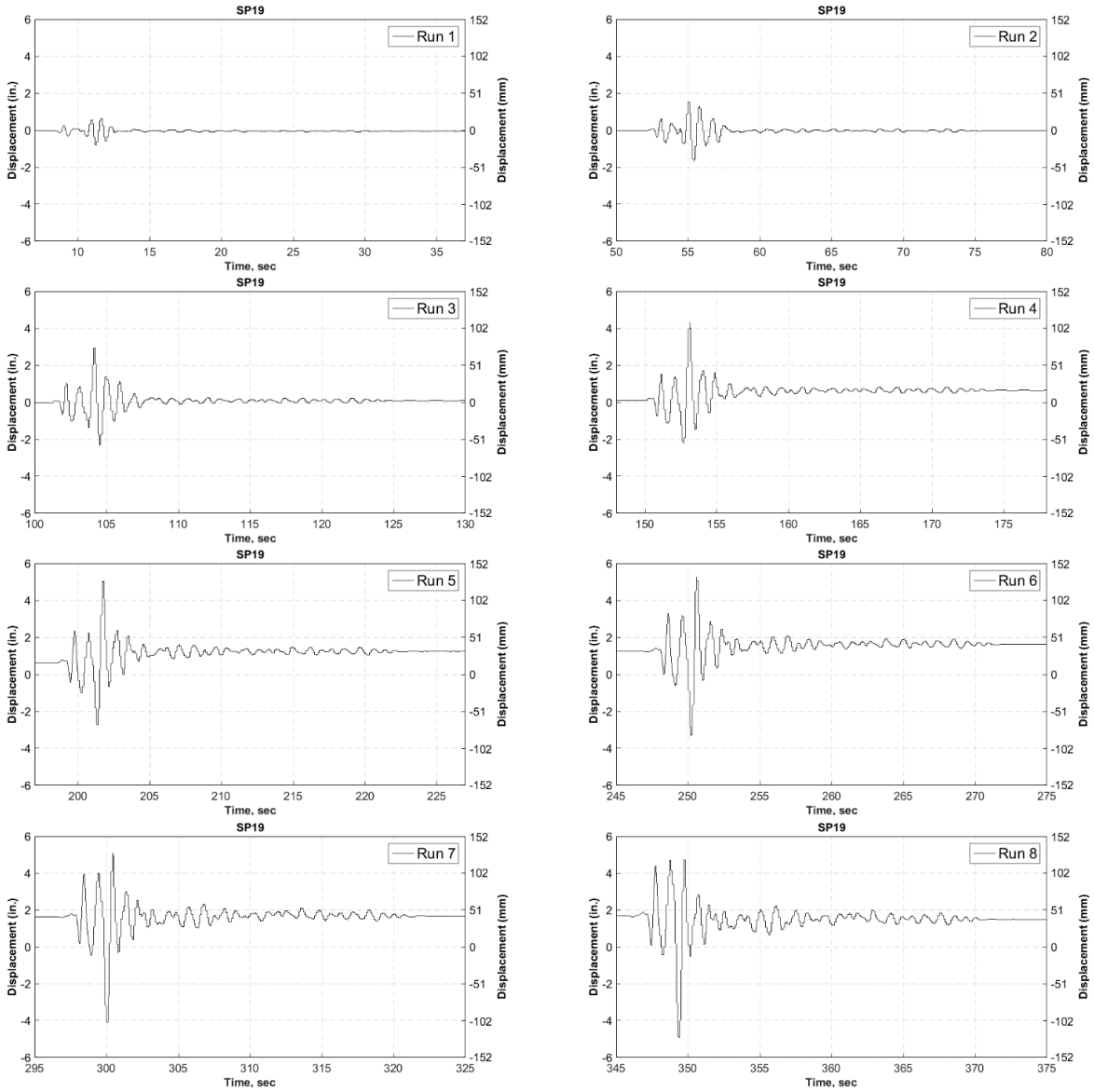

Figure B.46 East abutment longitudinal displacement histories (SP19)

B.5. Bent resultant displacement histories

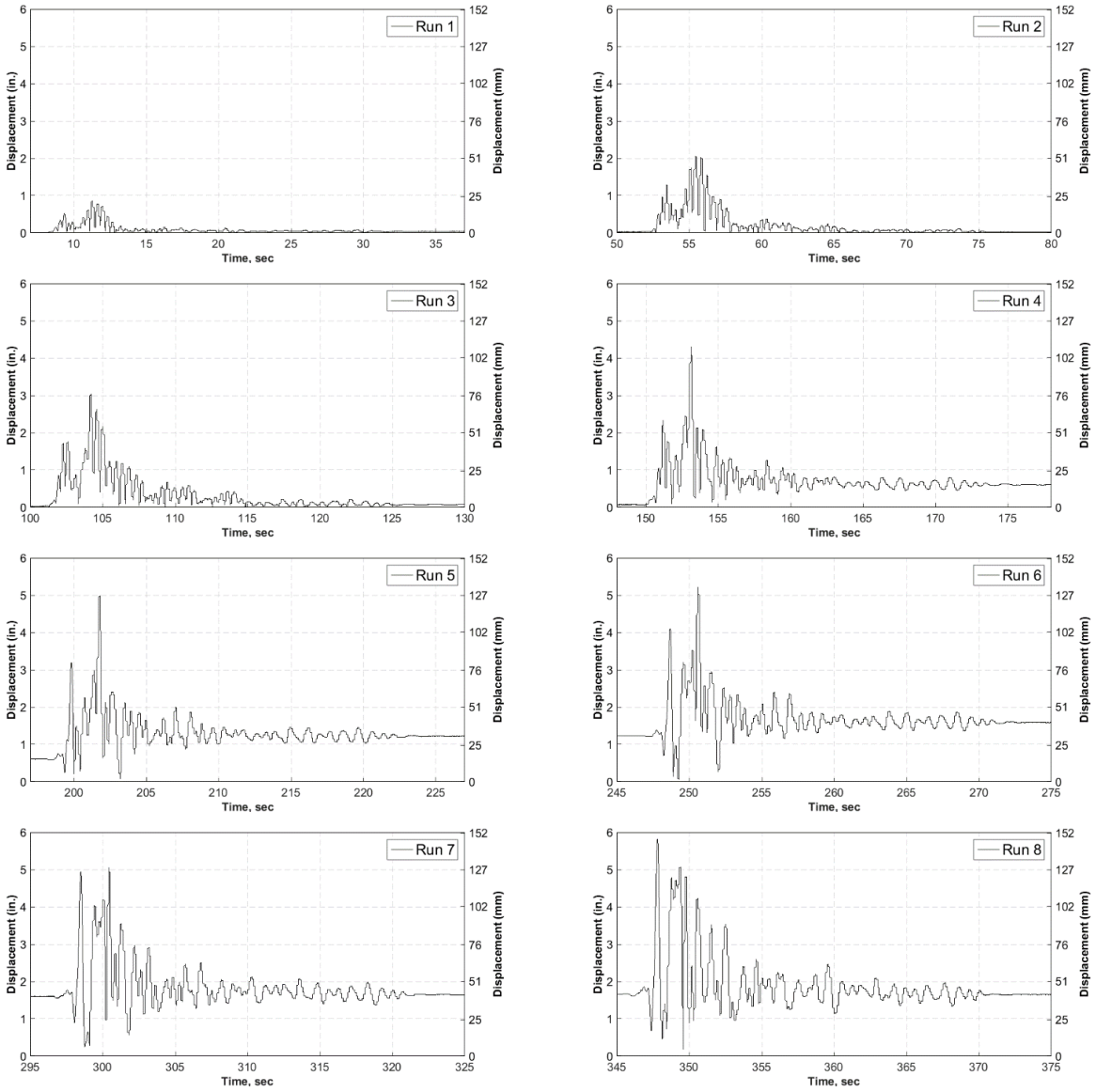

Figure B.47 Bent resultant displacement histories

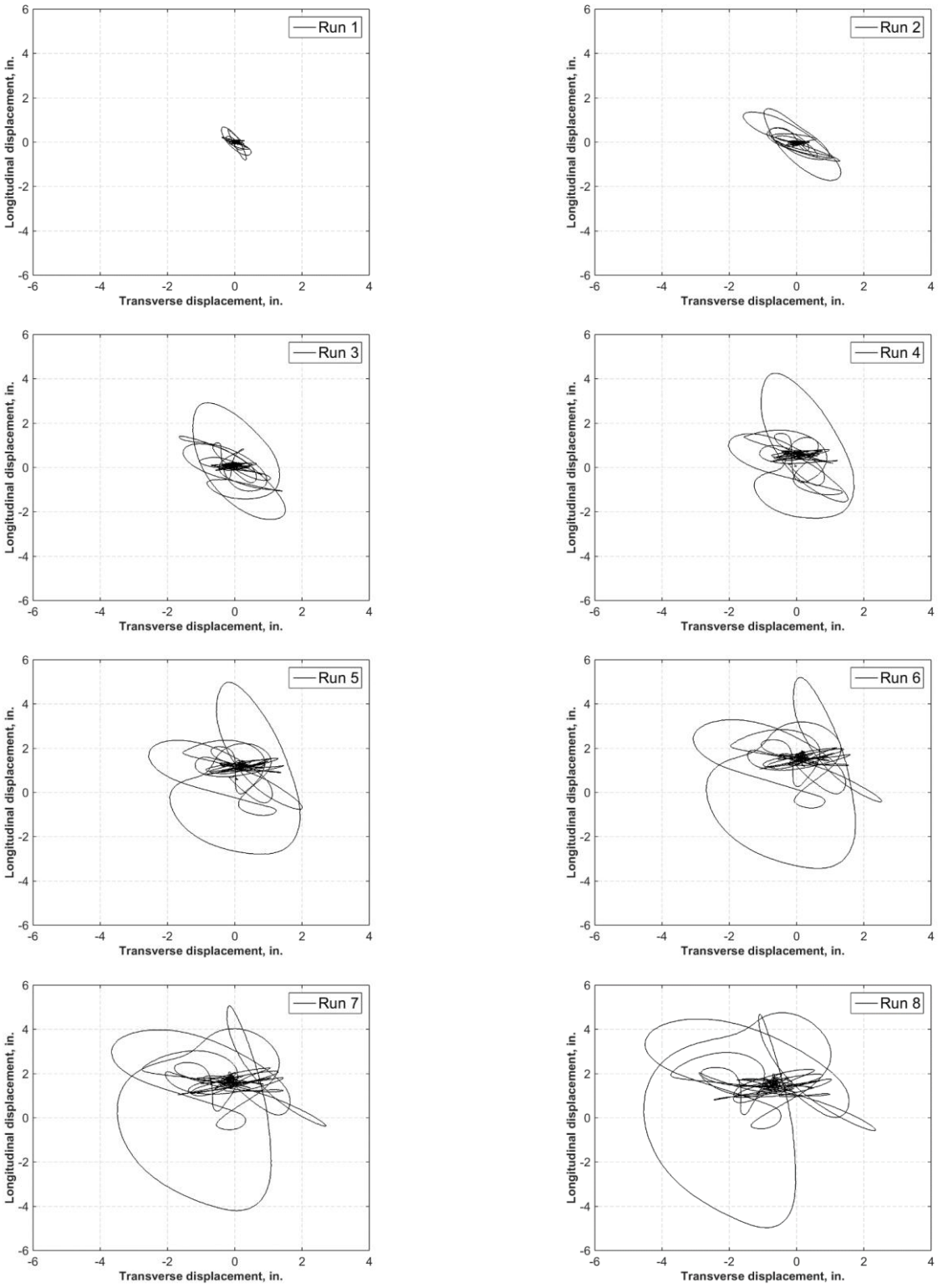

Figure B.48 Bent top particle movement in the horizontal plane relative to the shake table

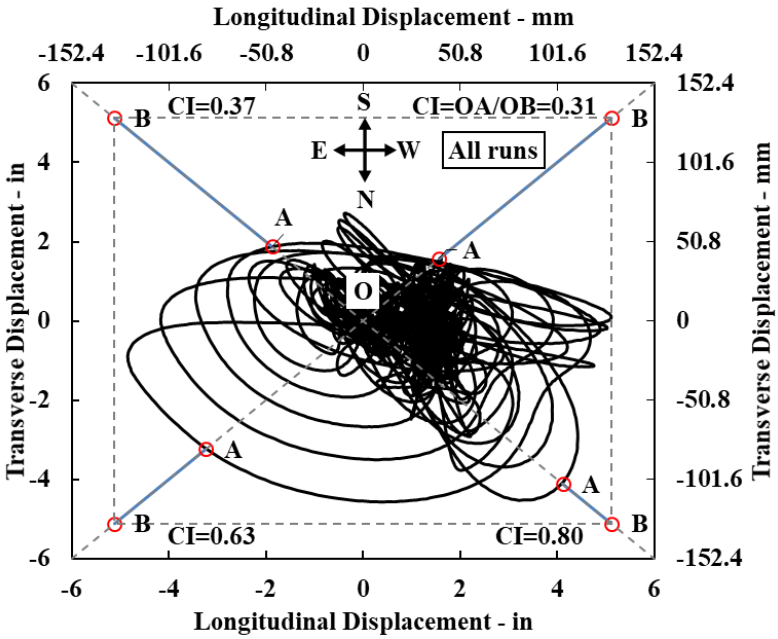

Figure B.49 Bent top particle movement in the horizontal plane relative to the shake table

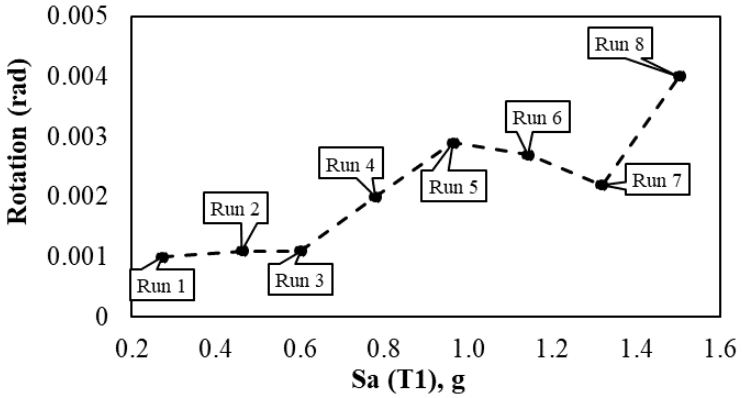

Figure B.50 Maximum in-plane rotation in each run

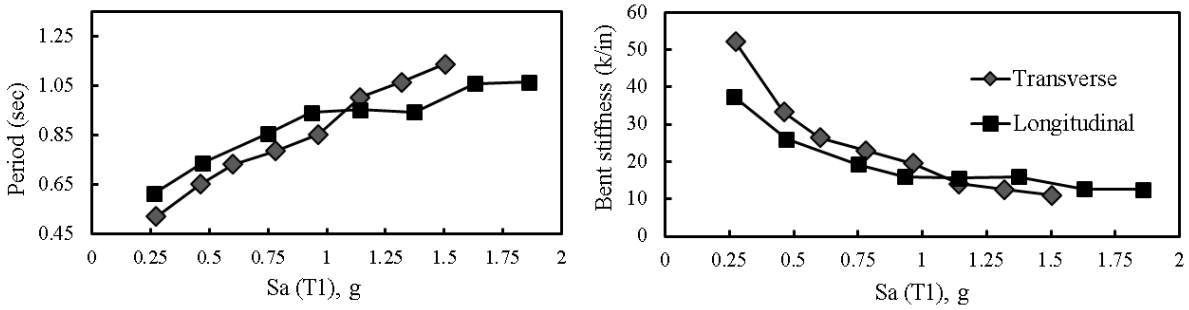

Figure B.51 Variation of the bent secant stiffnesses and periods throughout seismic tests

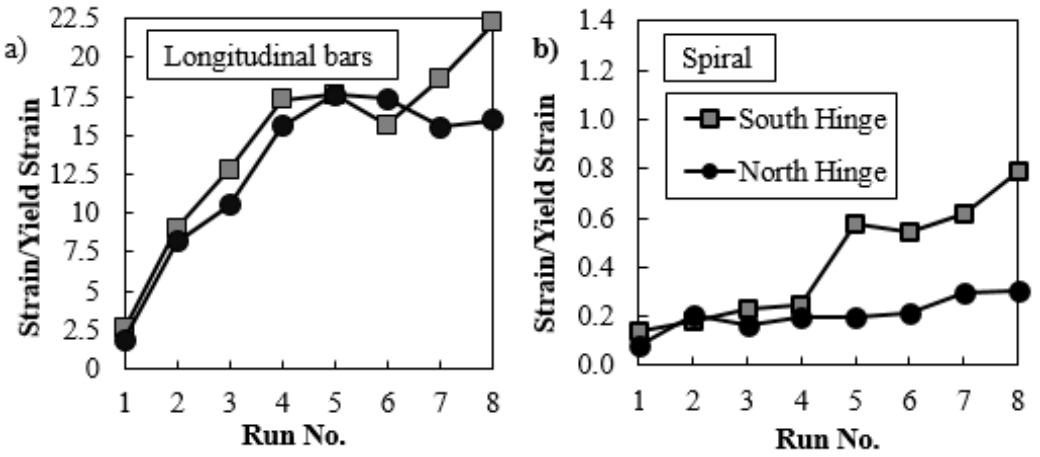

Figure B.52 Peak tensile strains in rebar hinge a) longitudinal bars, b) spiral

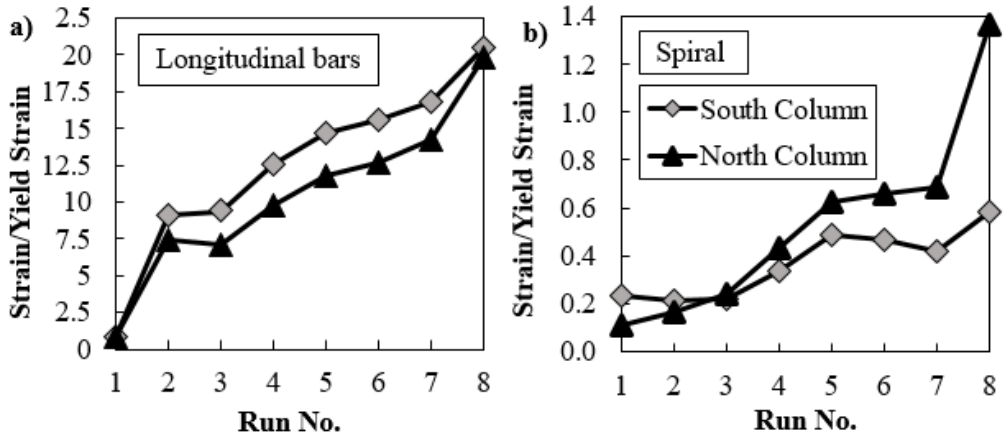

Figure B.53 Peak tensile strains in column plastic hinge a) longitudinal bars, b) spiral

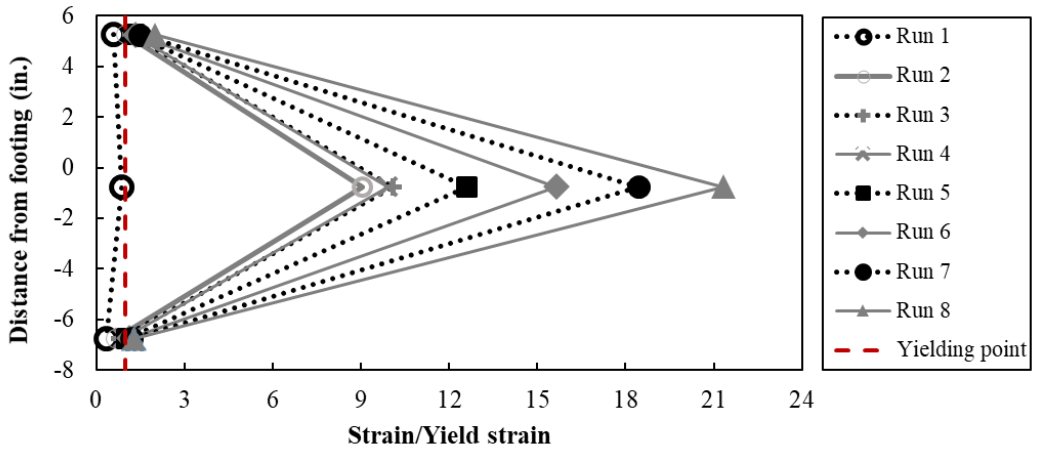

Figure B.54 Strain profile for the extreme rebar hinge longitudinal bar (South column, west bar)

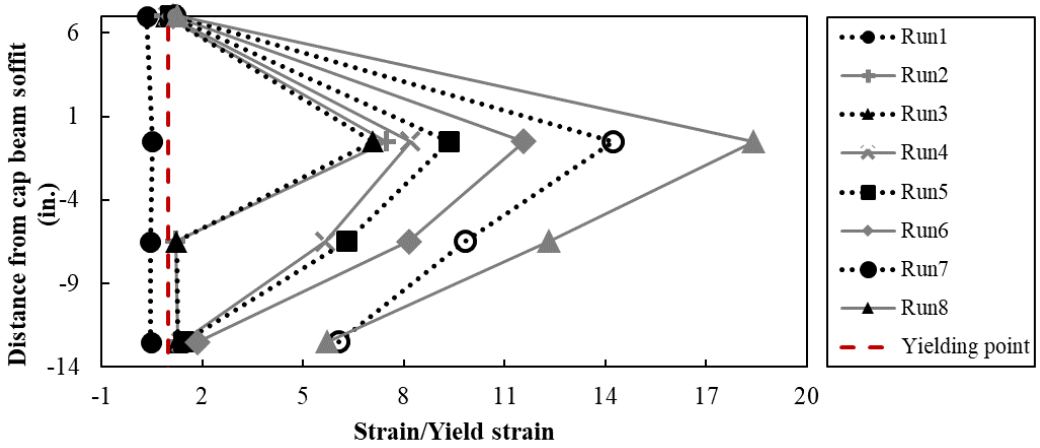

Figure B.55 Strain profile for the extreme column longitudinal bar (North col., north bar)

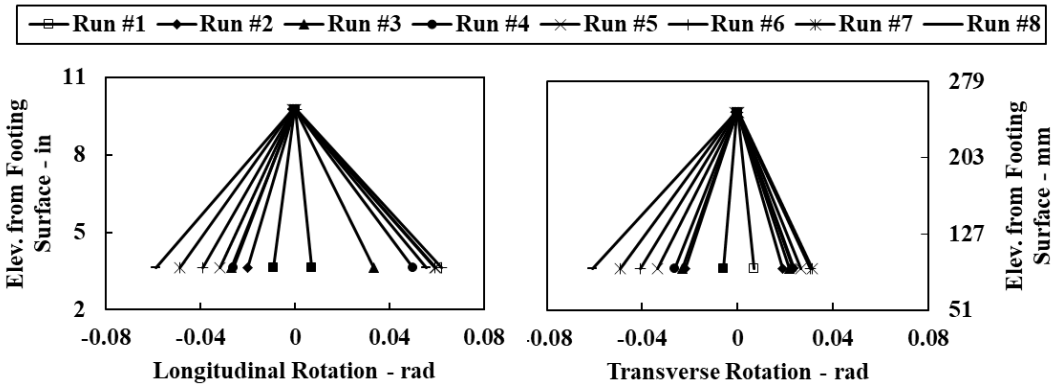

Figure B.56 Rotation profile along the height for north base hinge

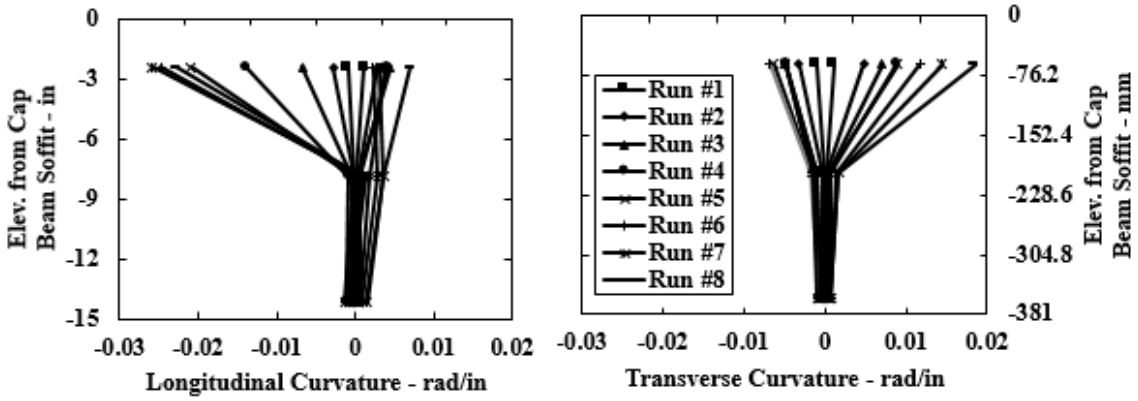

Figure B.57 Curvature profiles along the height, for north column top moment connection

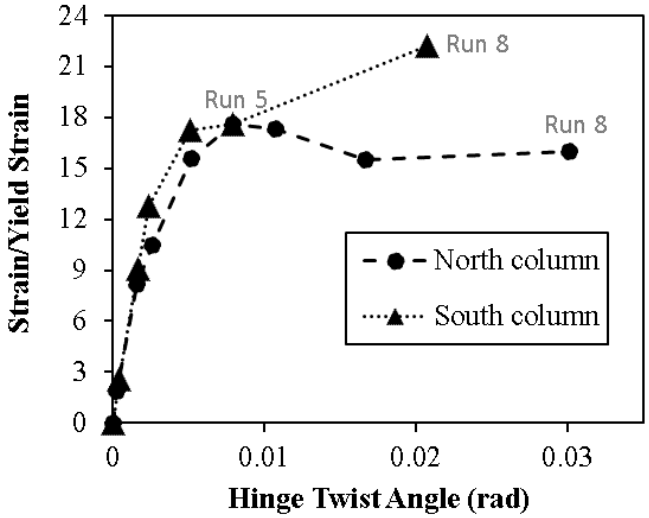

Figure B.58 Maximum hinge longitudinal bar strain versus hinge in-plane rotation

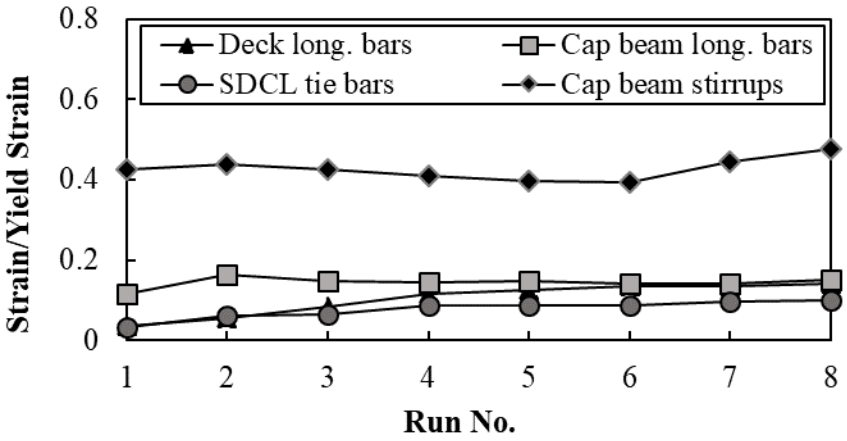

Figure B.59 Peak tensile strains in cap beam long. bars, stirrups, and tie bars, and deck long. bars

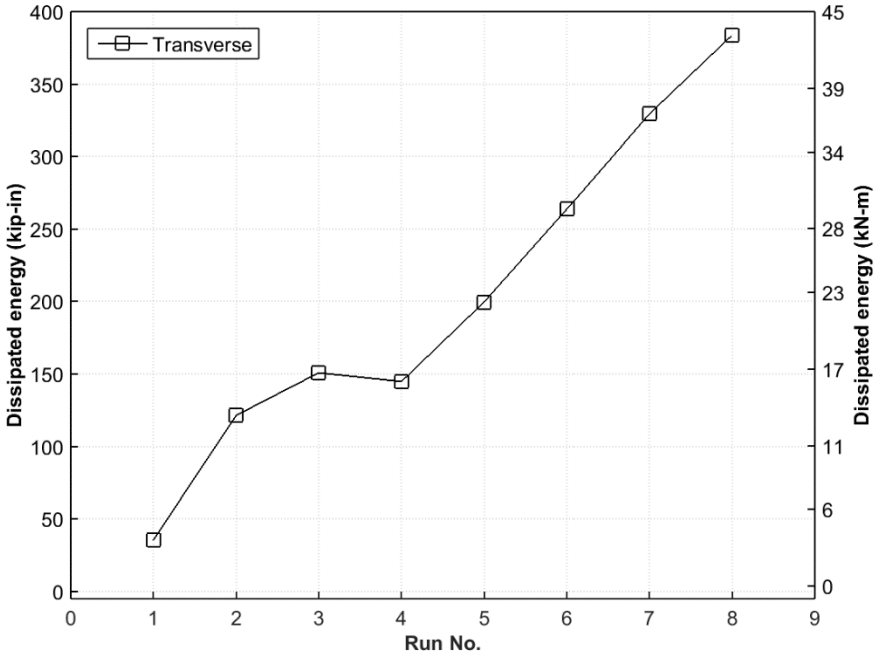

Figure B.60

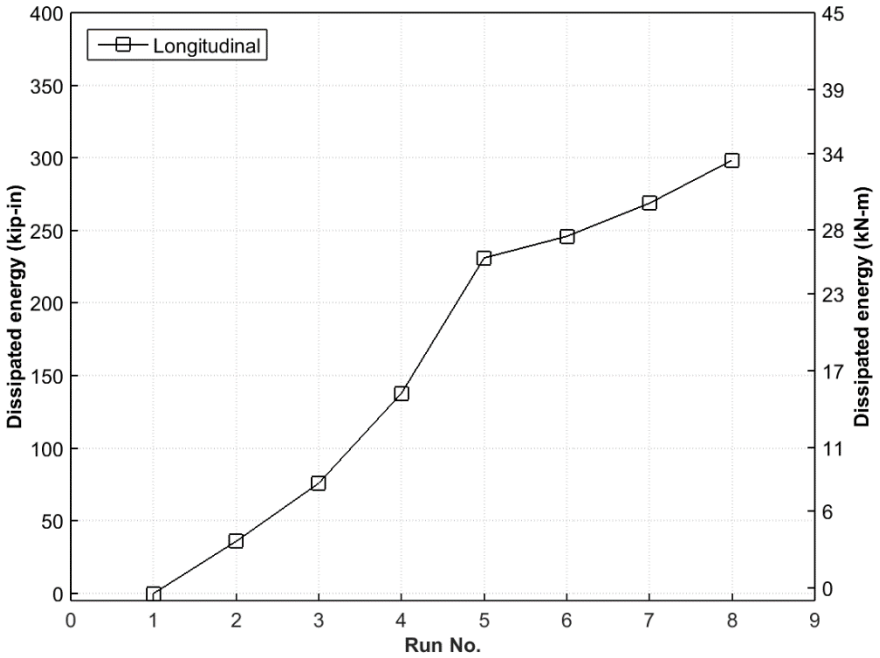

Figure B.61

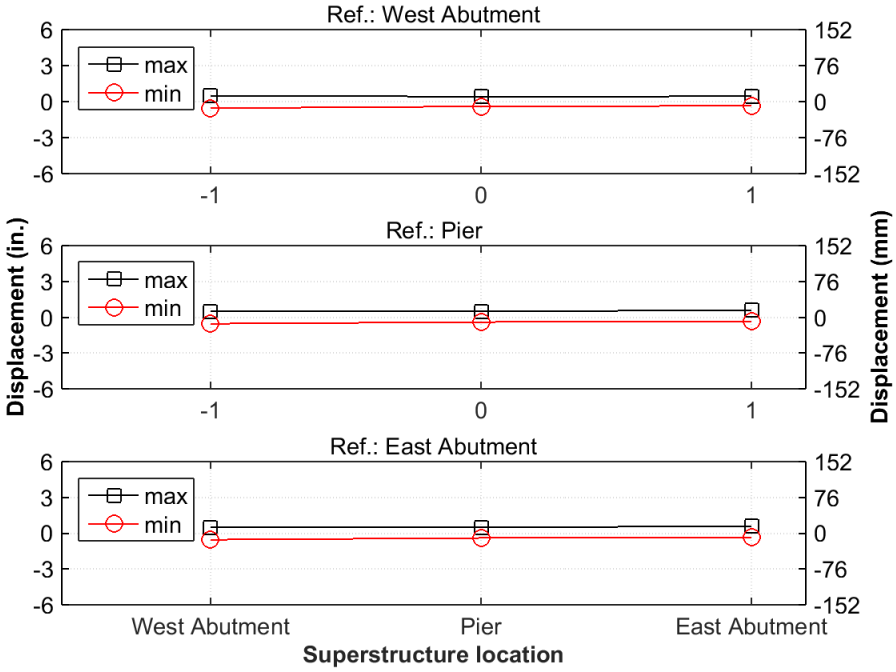

Figure B.62 Transverse displacement envelope (Run 1)

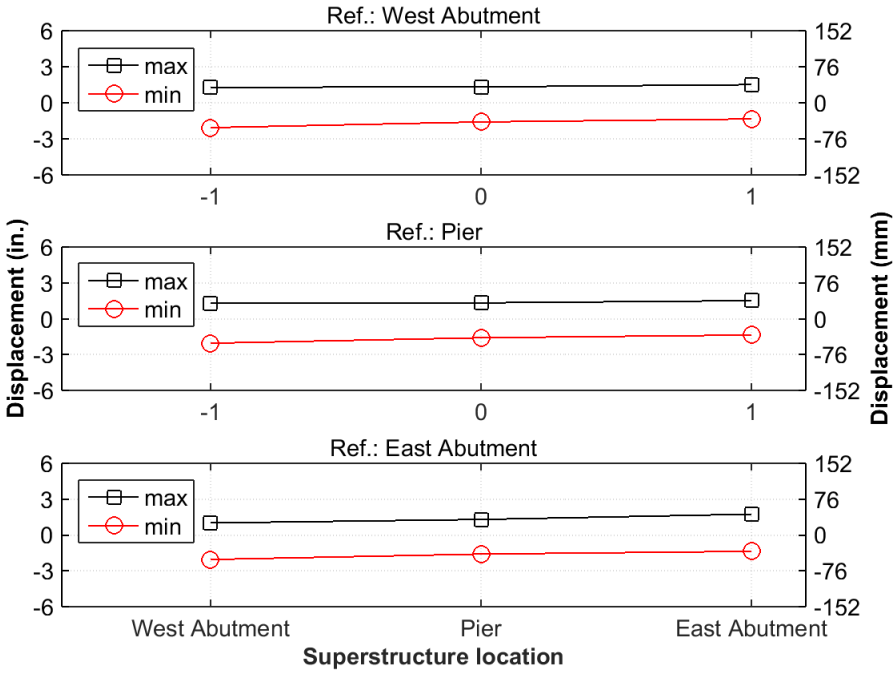

Figure B.63 Transverse displacement envelope (Run 2)

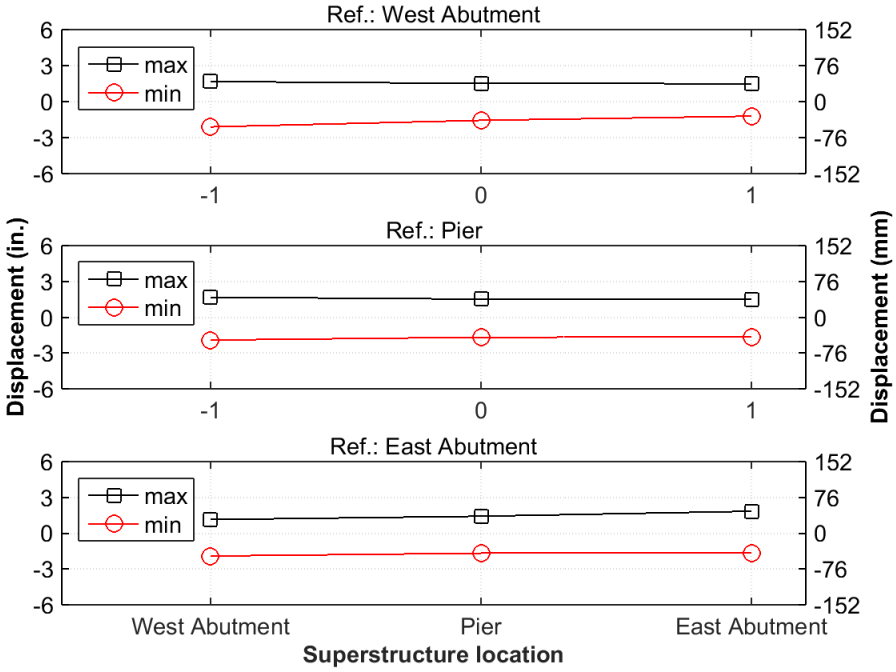

Figure B.64 Transverse displacement envelope (Run 3)

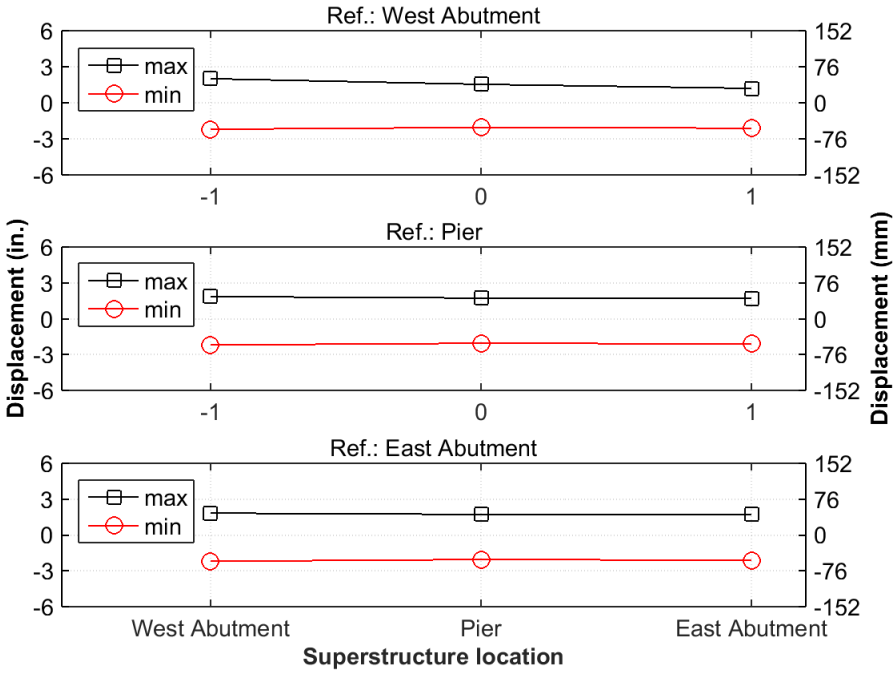

Figure B.65 Transverse displacement envelope (Run 4)

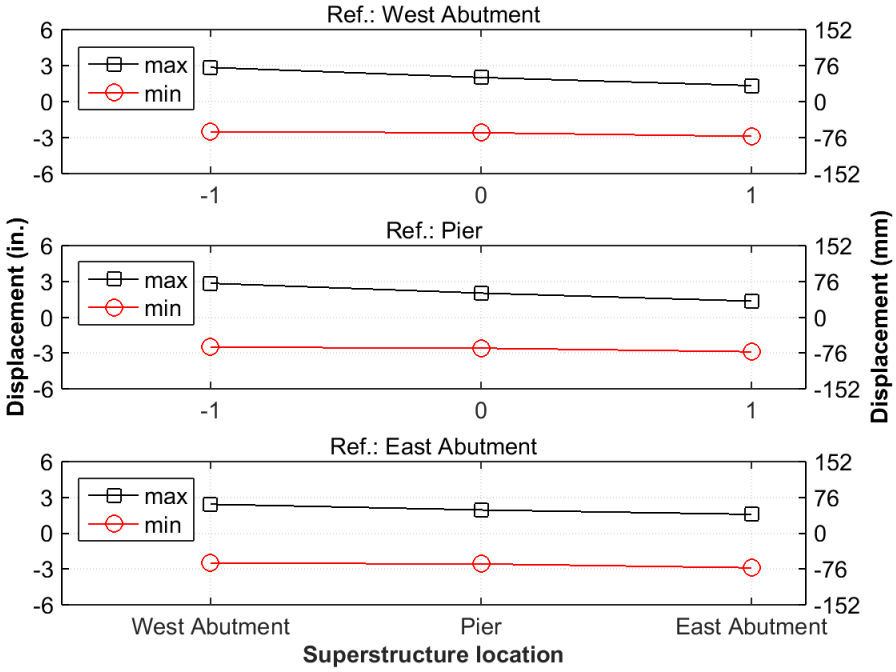

Figure B.66 Transverse displacement envelope (Run 5)

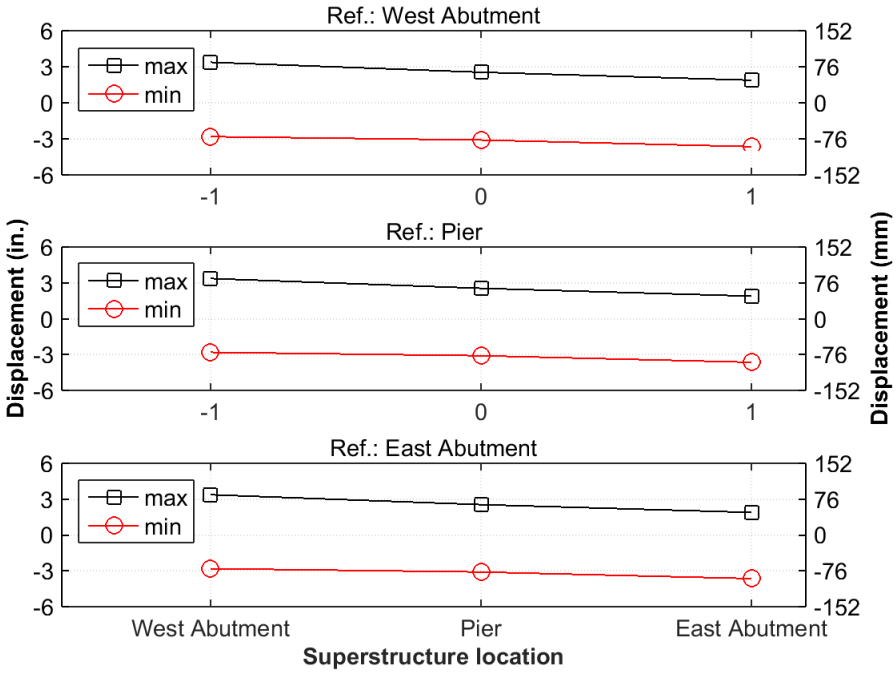

Figure B.67 Transverse displacement envelope (Run 6)

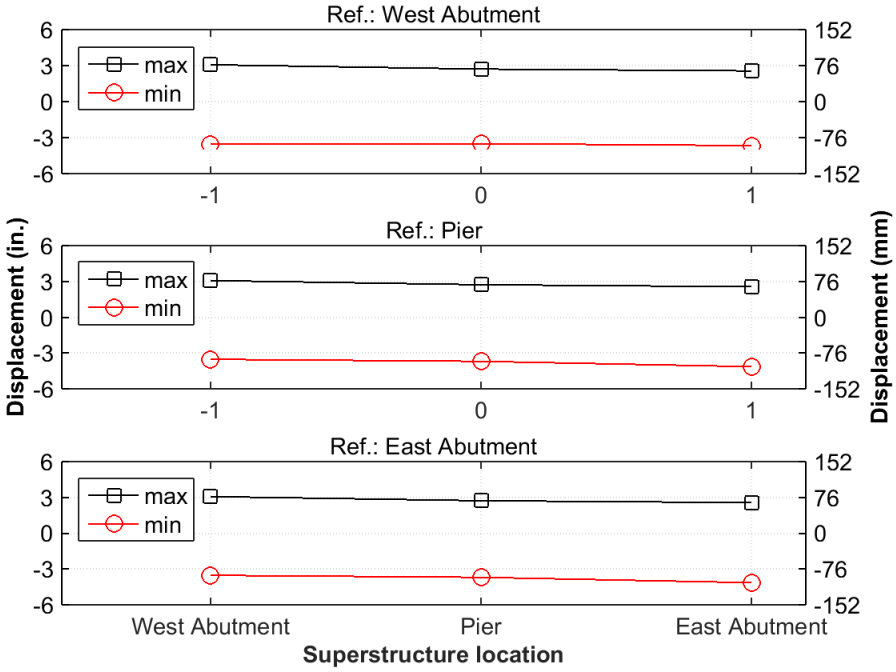

Figure B.68 Transverse displacement envelope (Run 7)

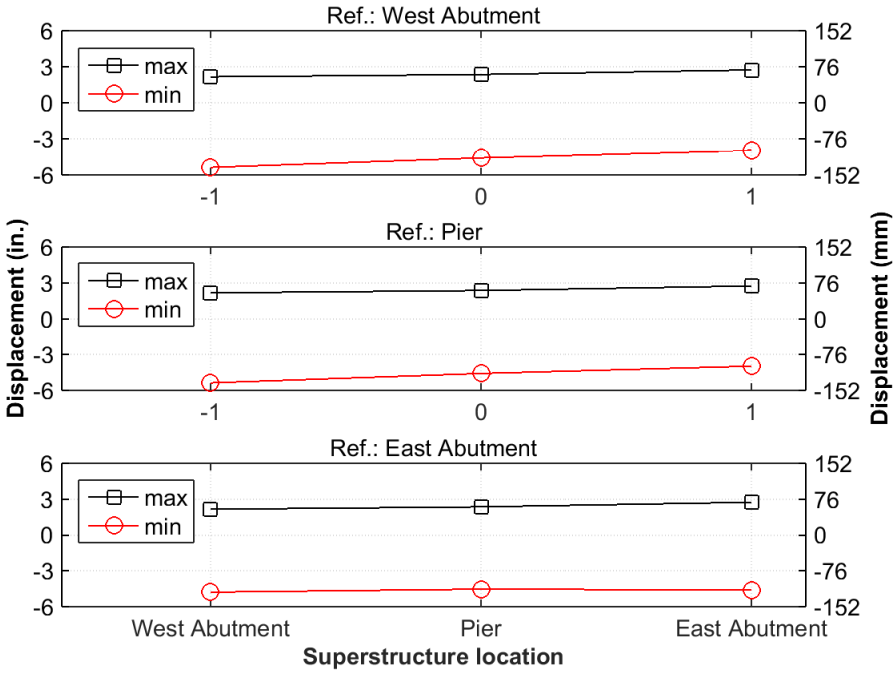

Figure B.69 Transverse displacement envelope (Run 8)

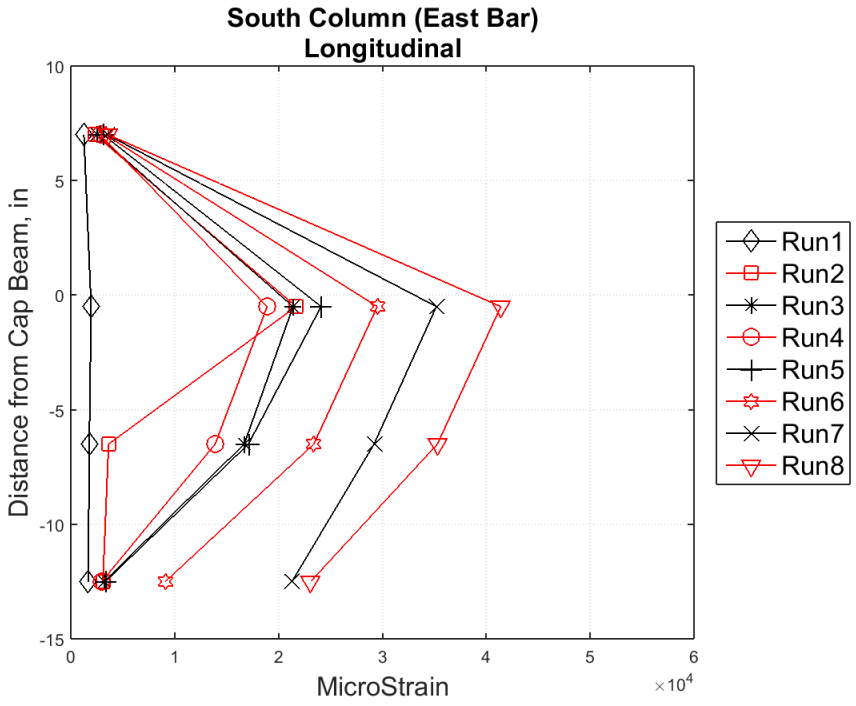

Figure B.70 Strain profile along the plastic hinge of south column – East bar

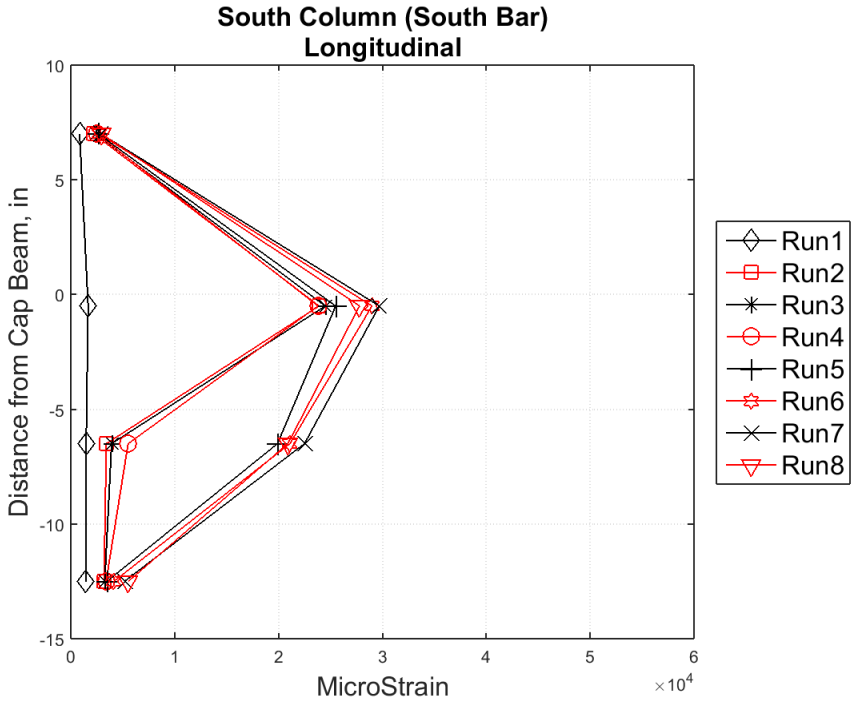

Figure B.71 Strain profile along the plastic hinge of south column – South bar

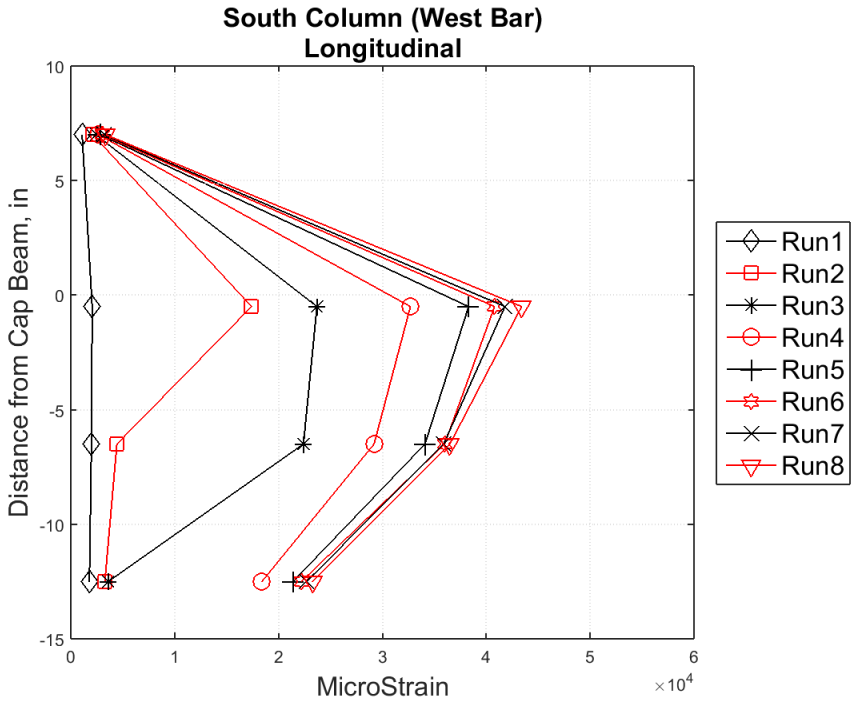

Figure B.72 Strain profile along the plastic hinge of south column – West bar

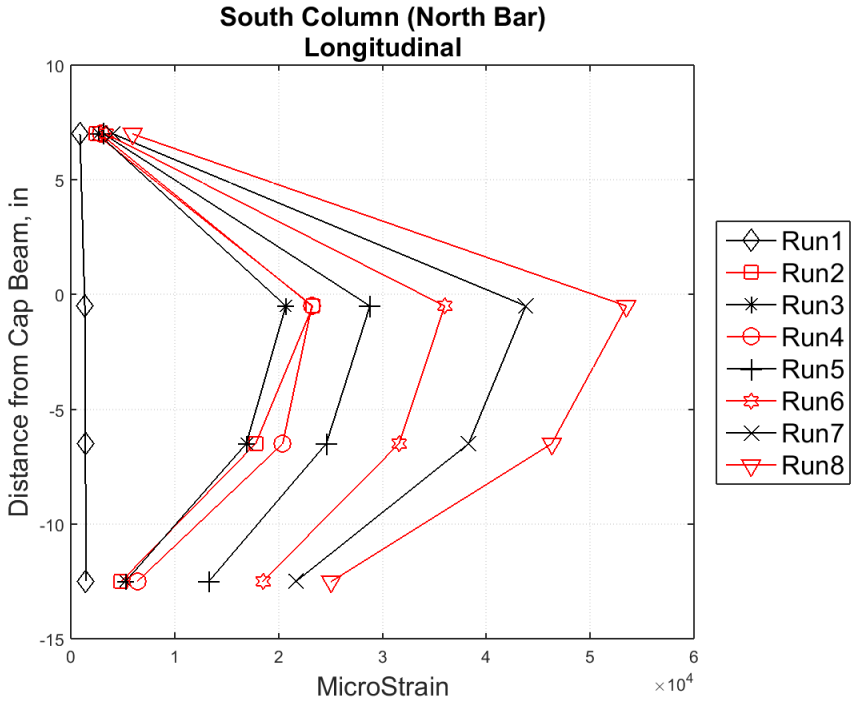

Figure B.73 Strain profile along the plastic hinge of south column – North bar

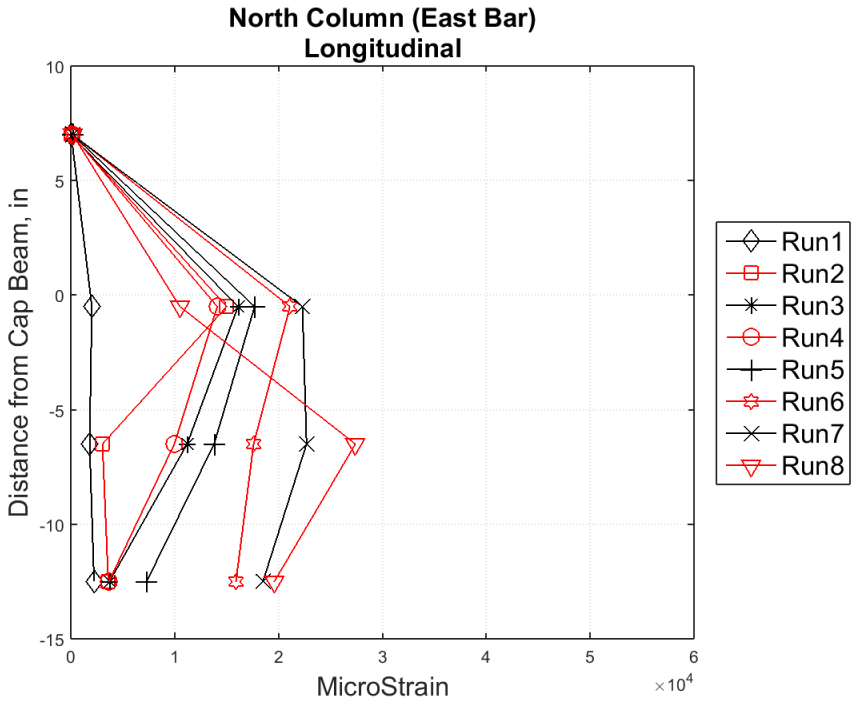

Figure B.74 Strain profile along the plastic hinge of north column – Esat bar

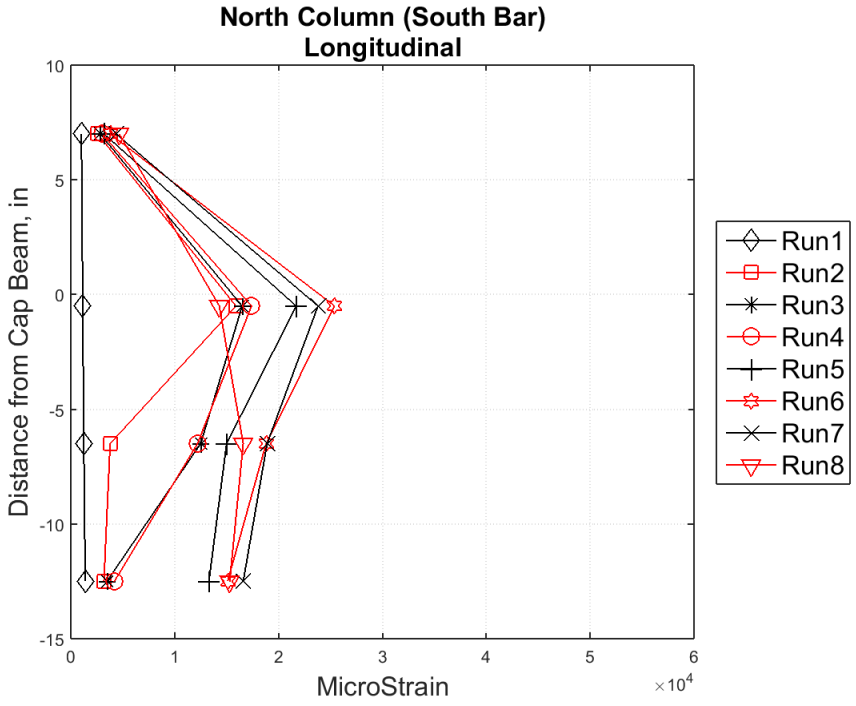

Figure B.75 Strain profile along the plastic hinge of north column – South bar

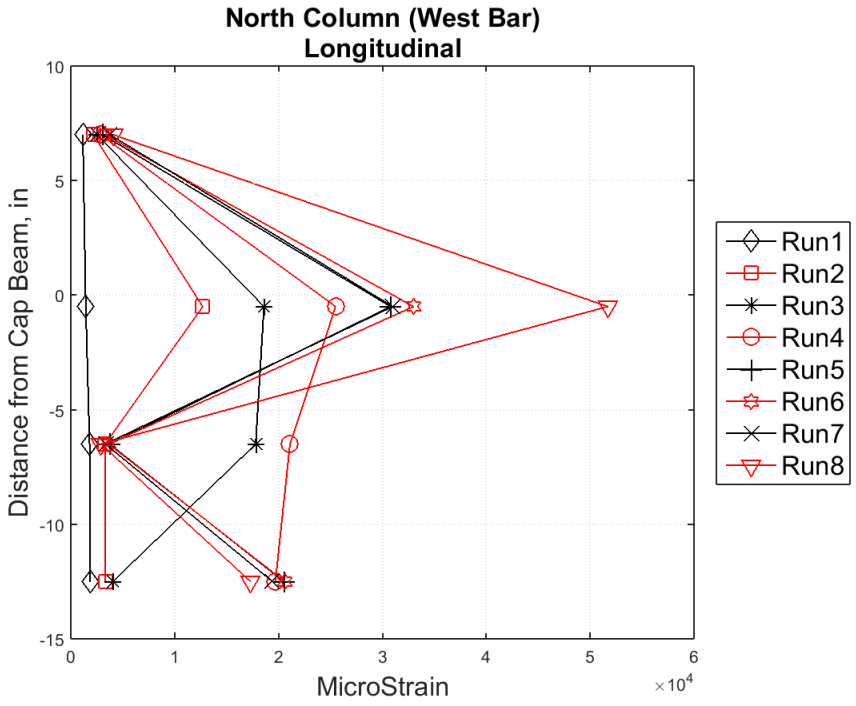

Figure B.76 Strain profile along the plastic hinge of north column – West bar

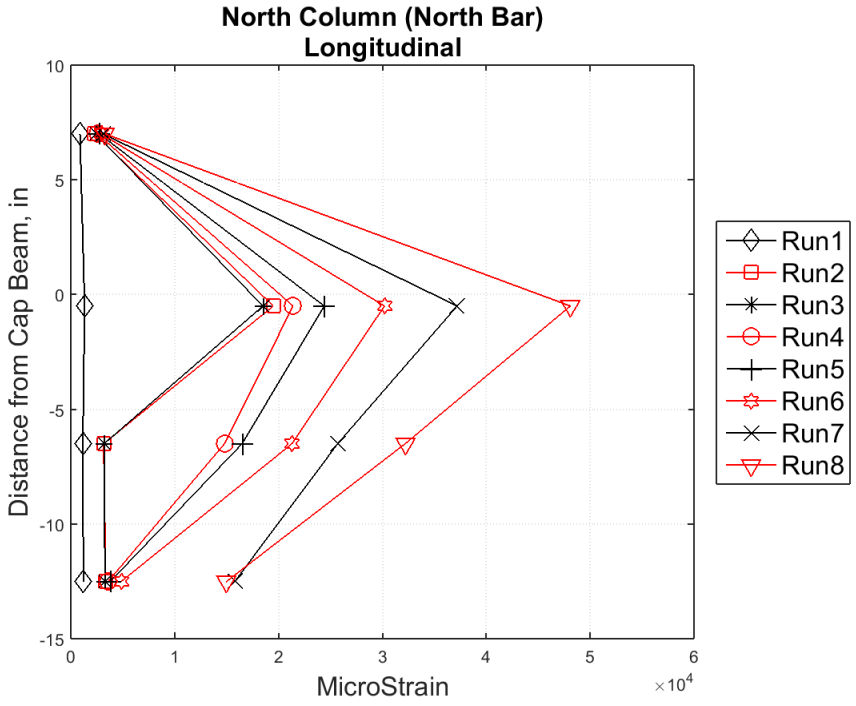

Figure B.77 Strain profile along the plastic hinge of north column – North bar

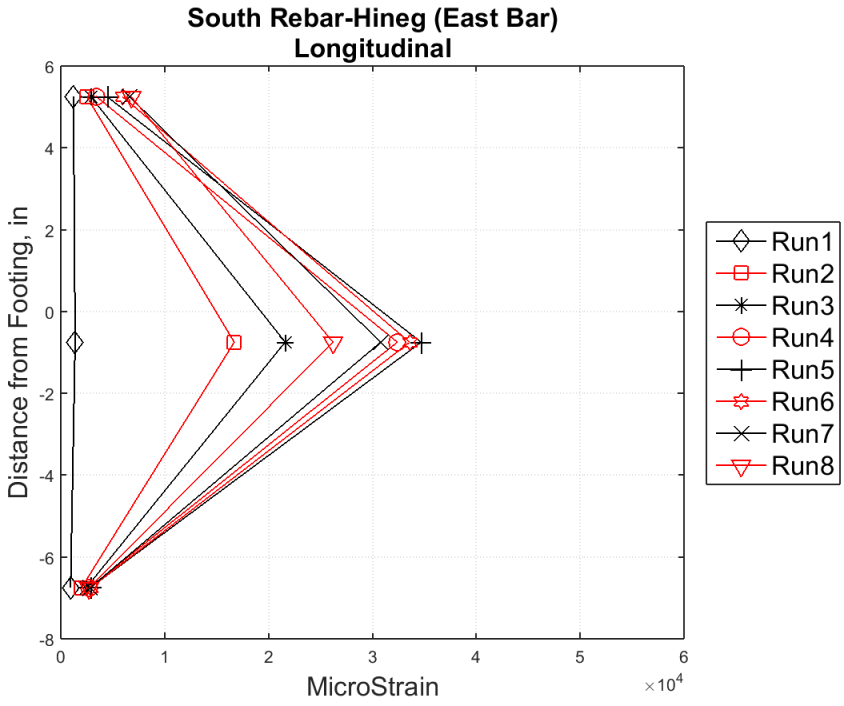

Figure B.78 Strain profile along the rebar hinge of south column – East bar

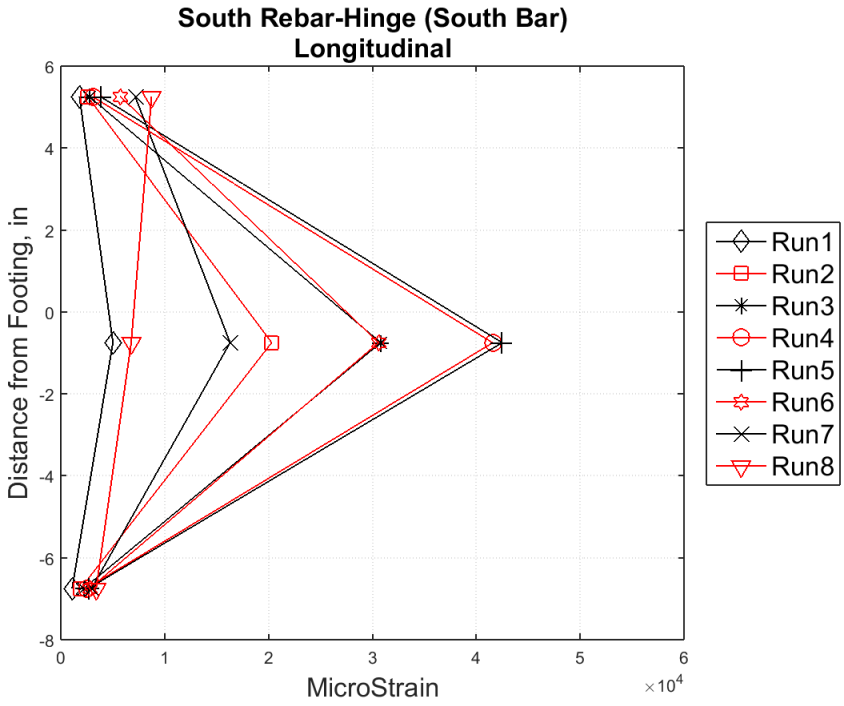

Figure B.79 Strain profile along the rebar hinge of south column – South bar

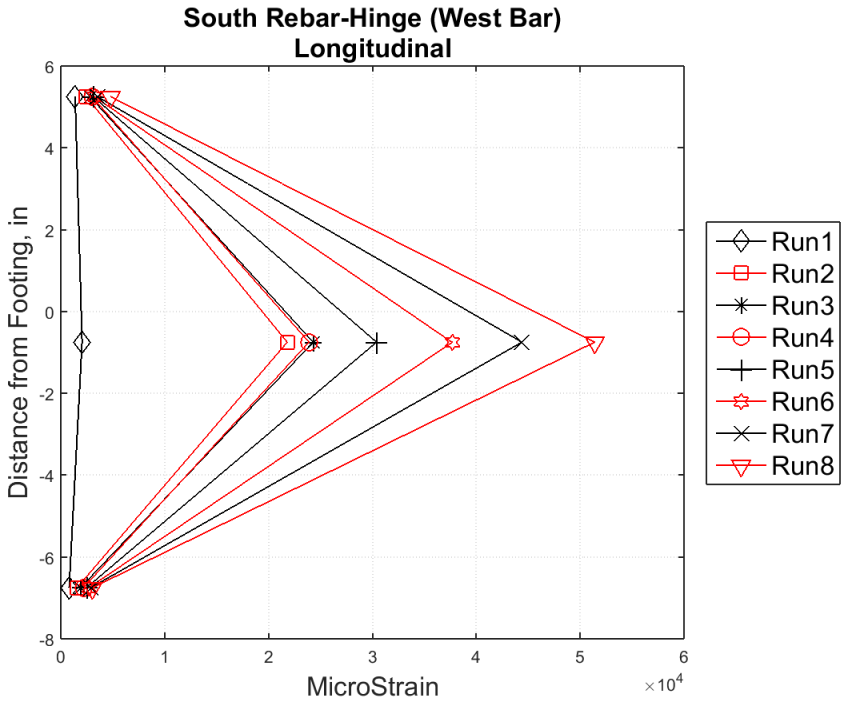

Figure B.80 Strain profile along the rebar hinge of south column – West bar

Figure B.81 Strain profile along the rebar hinge of south column – North bar

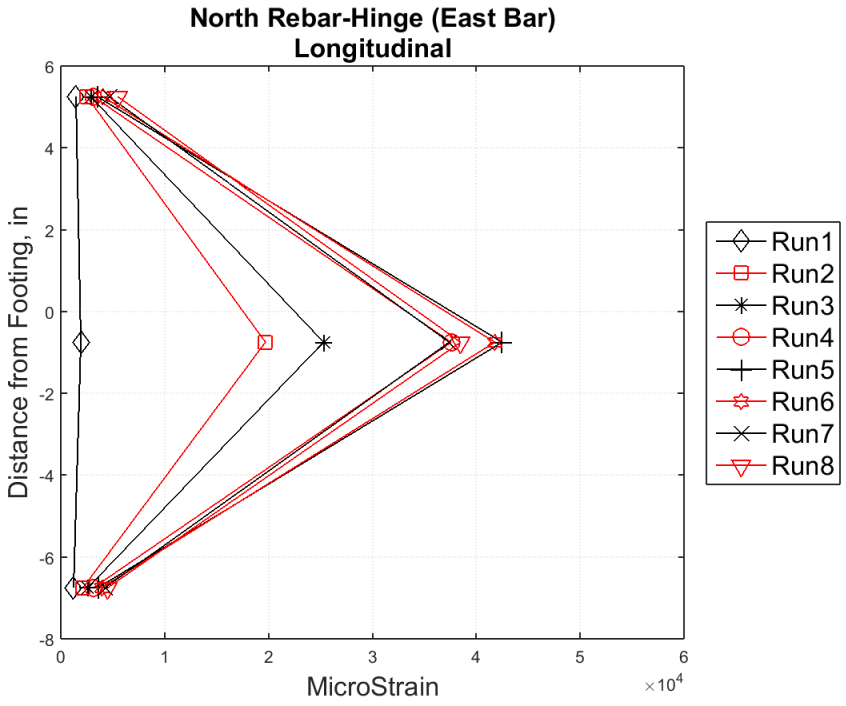

Figure B.82 Strain profile along the rebar hinge of north column – East bar

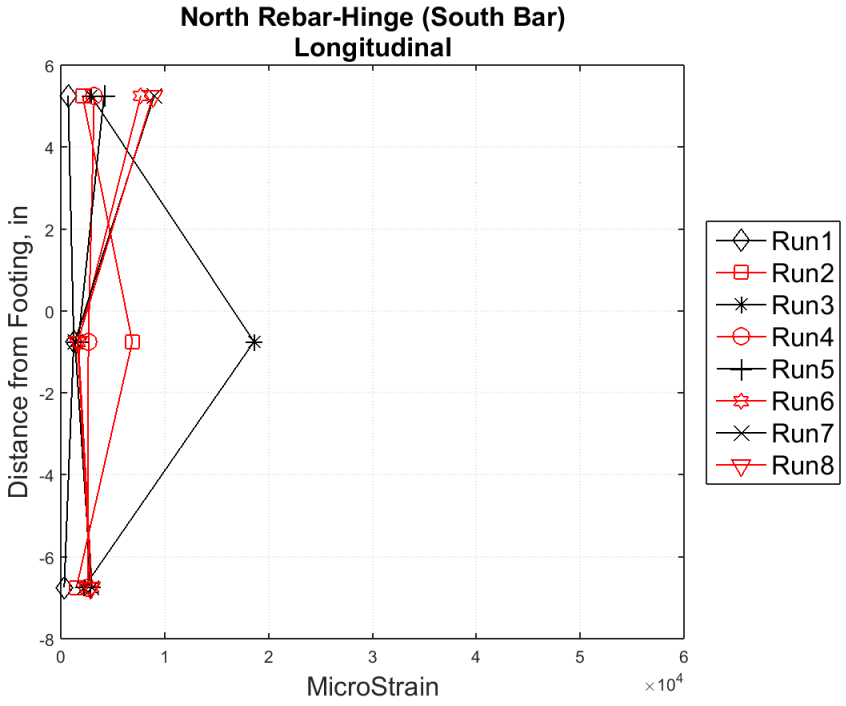

Figure B.83 Strain profile along the rebar hinge of north column – South bar

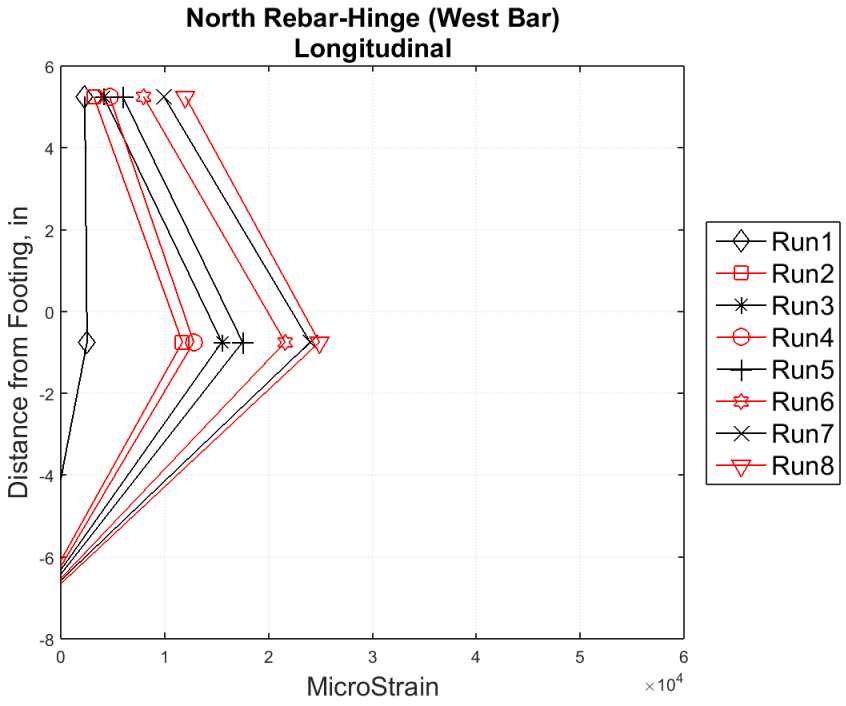

Figure B.84 Strain profile along the rebar hinge of north column – West bar

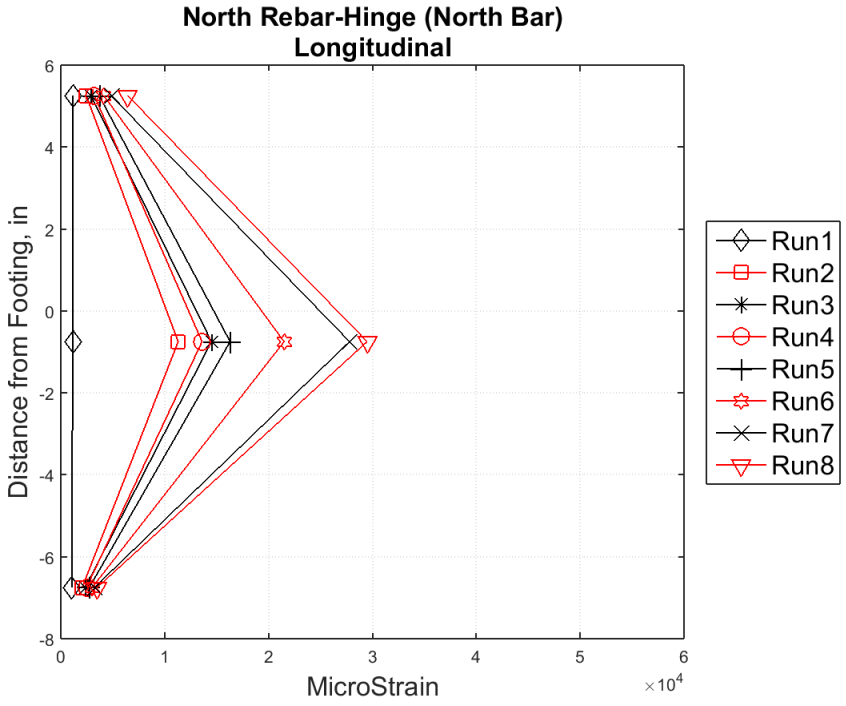

Figure B.85 Strain profile along the rebar hinge of north column – North bar

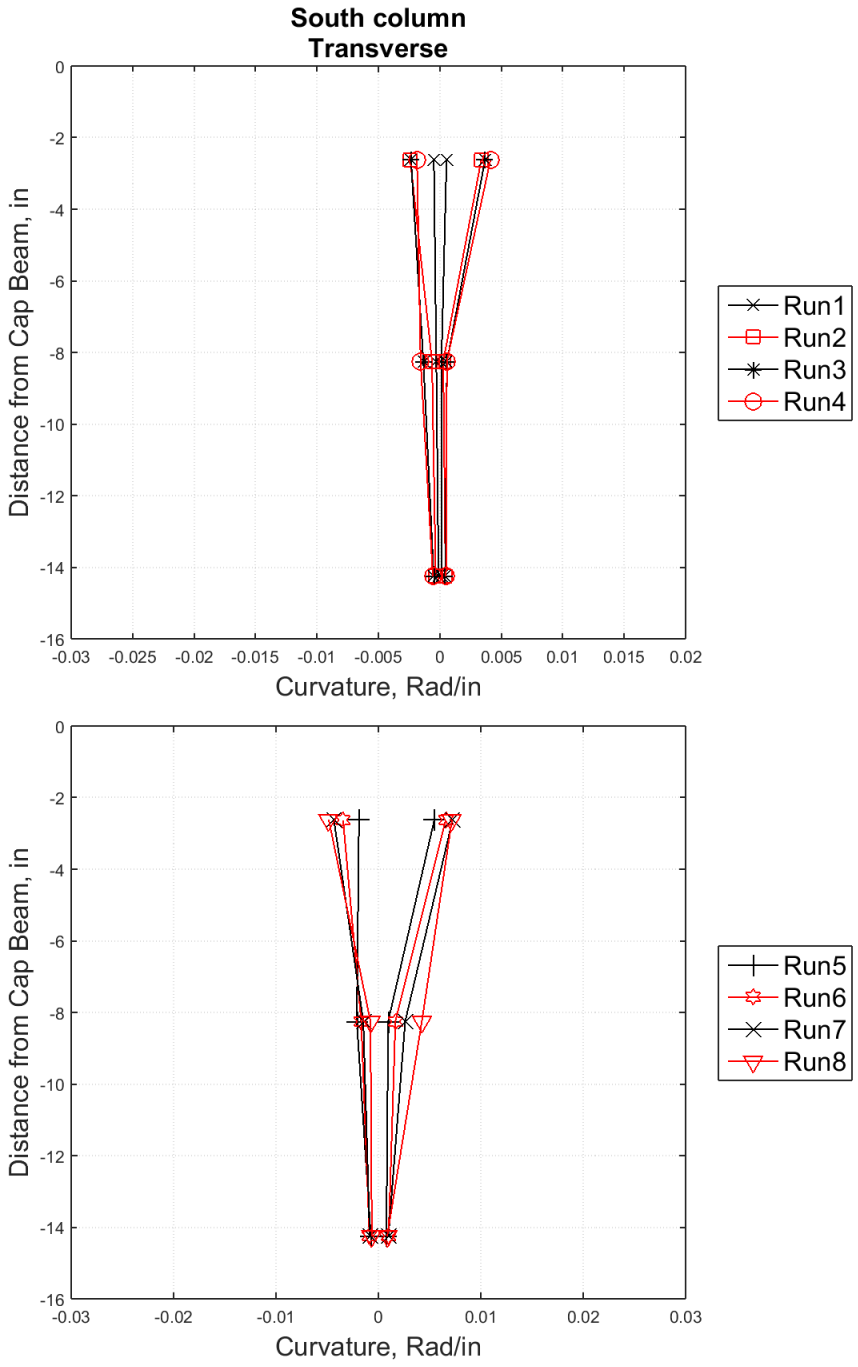

Figure B.86 Curvature profile along the plastic hinge of south column in trans. direction

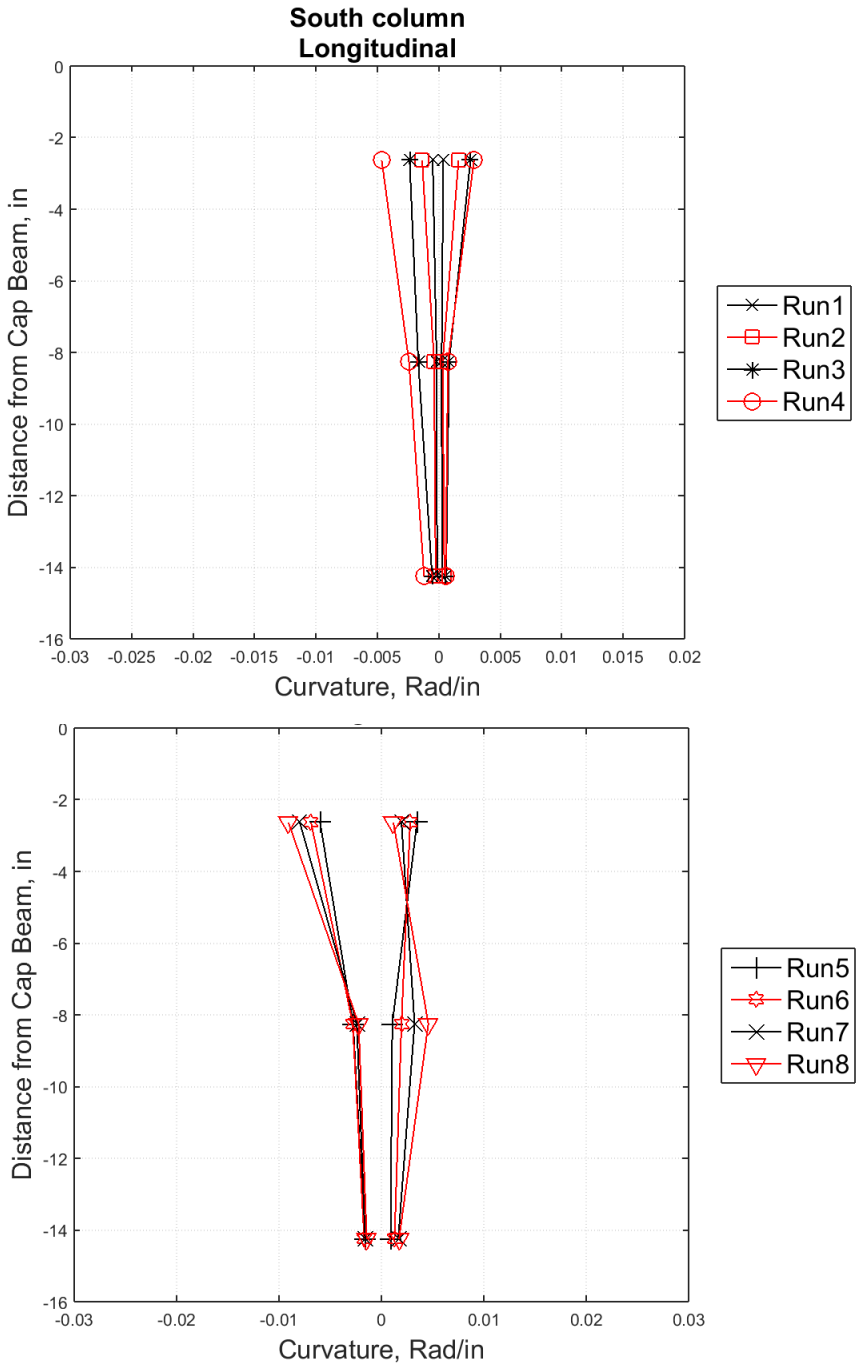

Figure B.87 Curvature profile along the plastic hinge of south column in long. direction

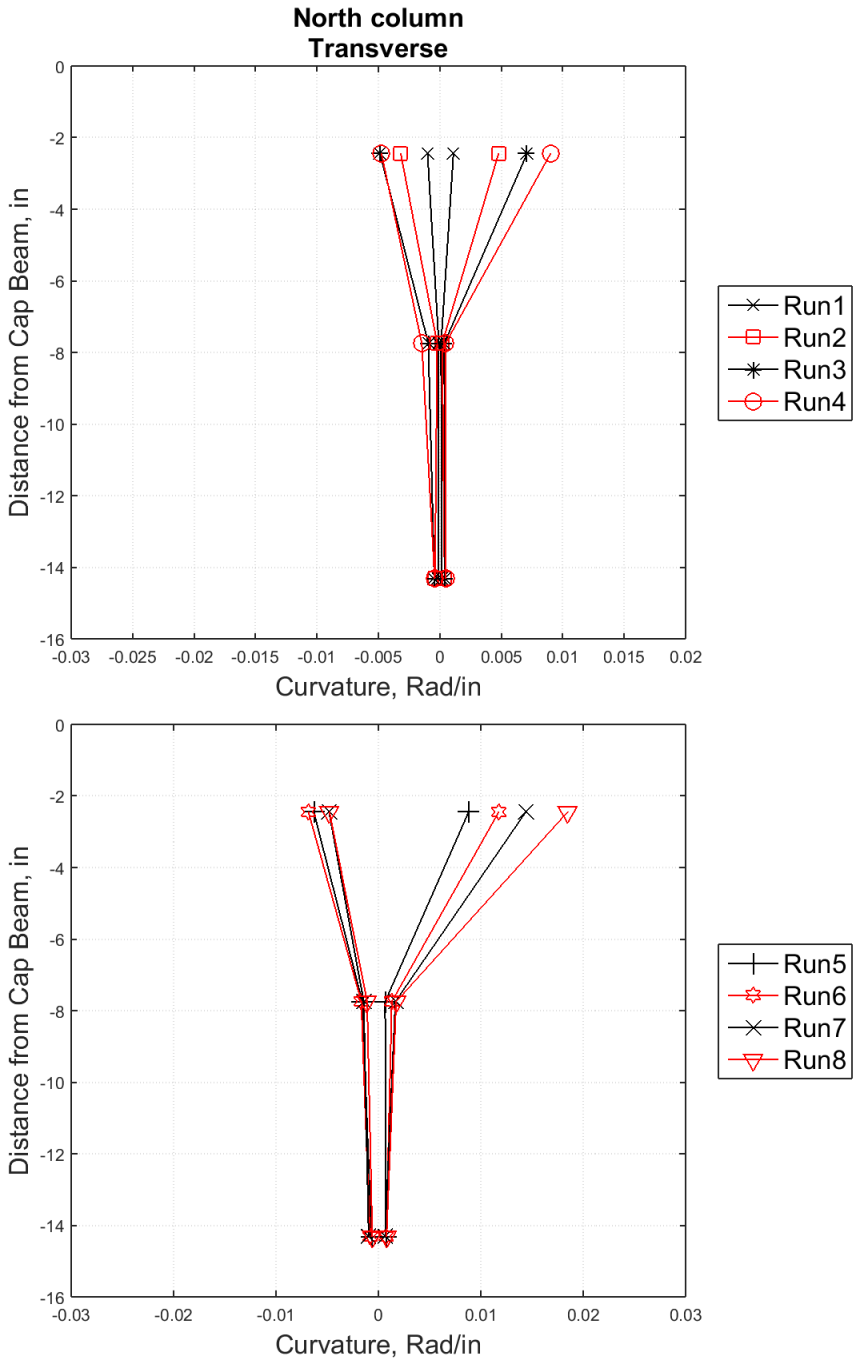

Figure B.88 Curvature profile along the plastic hinge of north column in trans. Direction

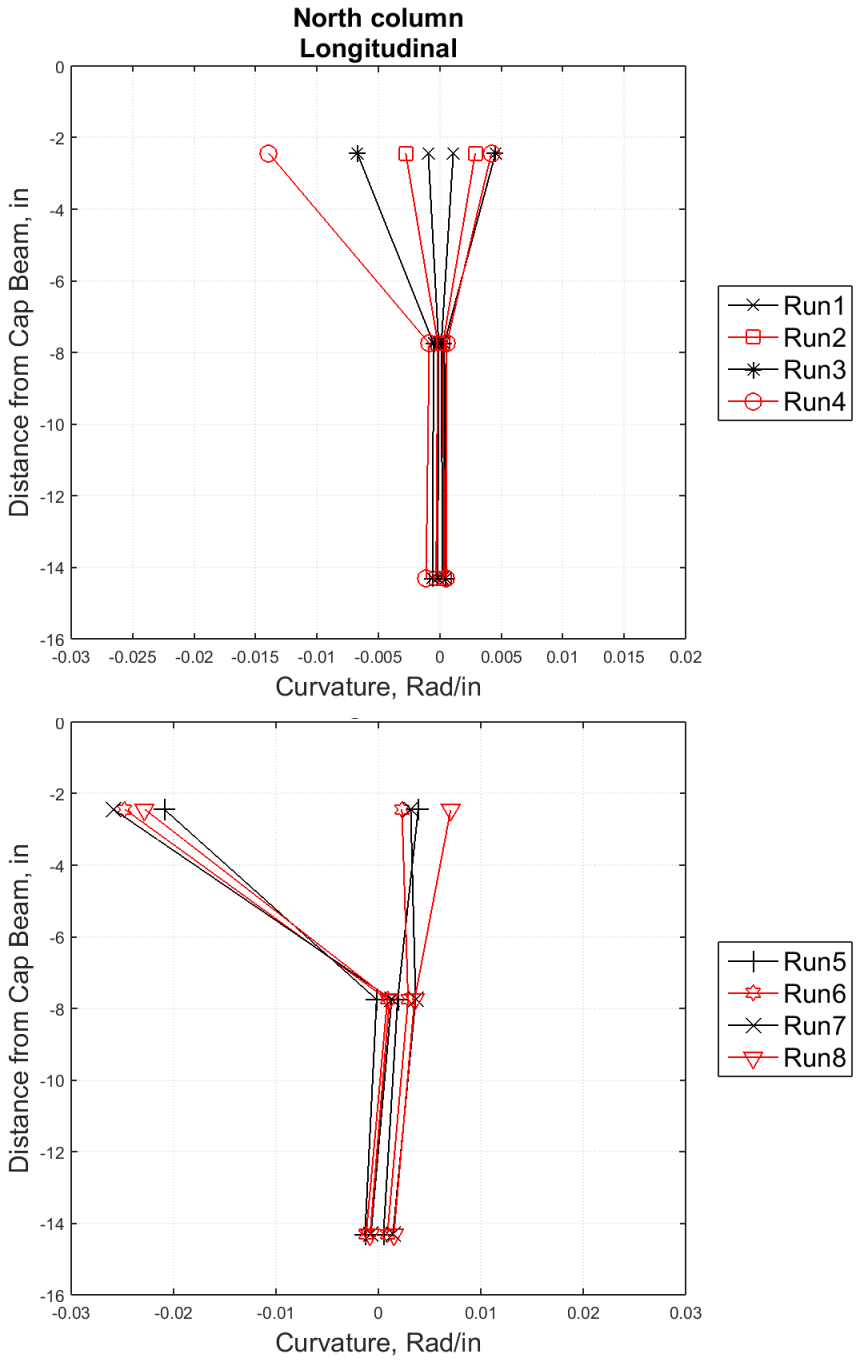

Figure B.89 Curvature profile along the plastic hinge of north column in long. Direction

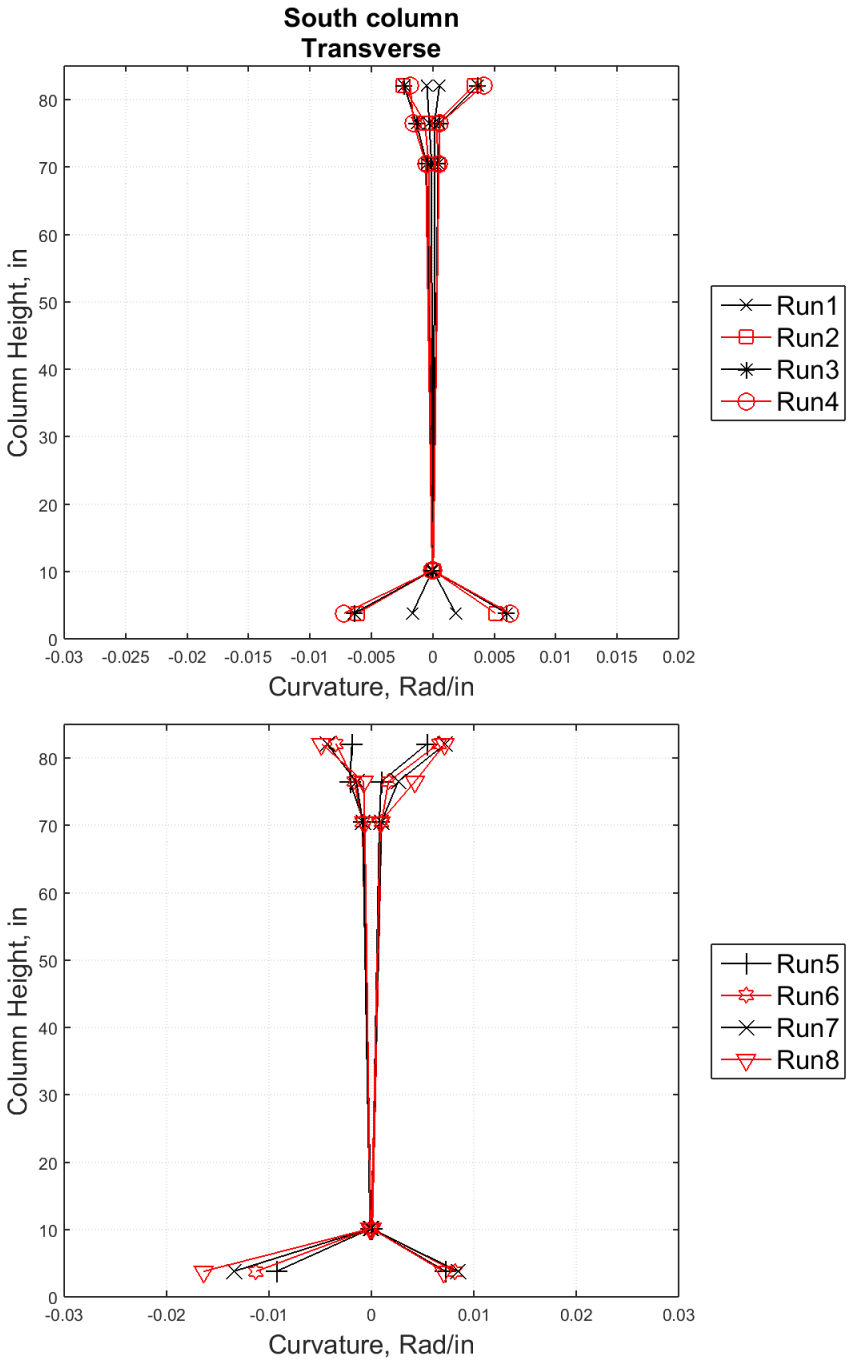

Figure B.90 Curvature profile along the south column in transverse direction

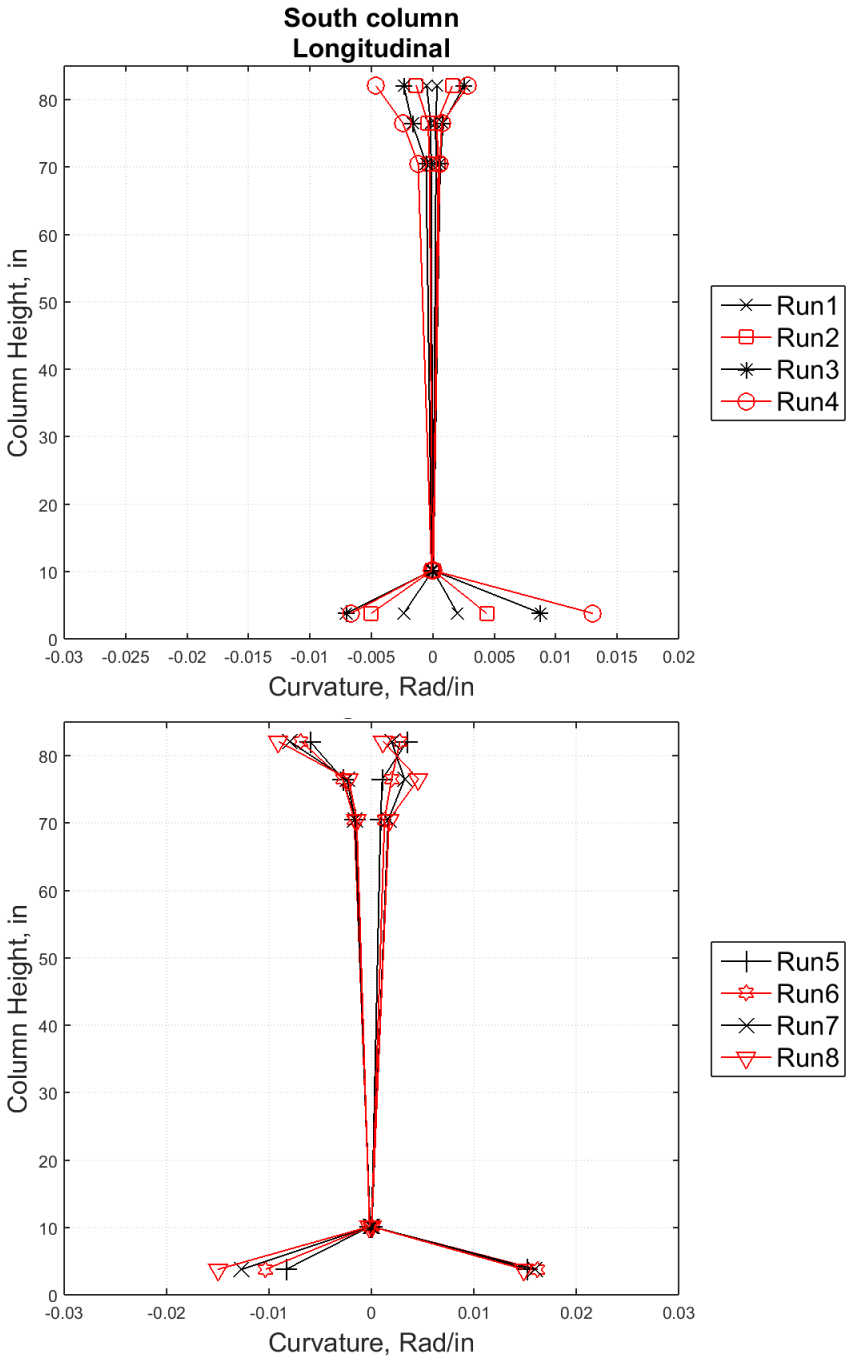

Figure B.91 Curvature profile along the south column in longitudinal direction

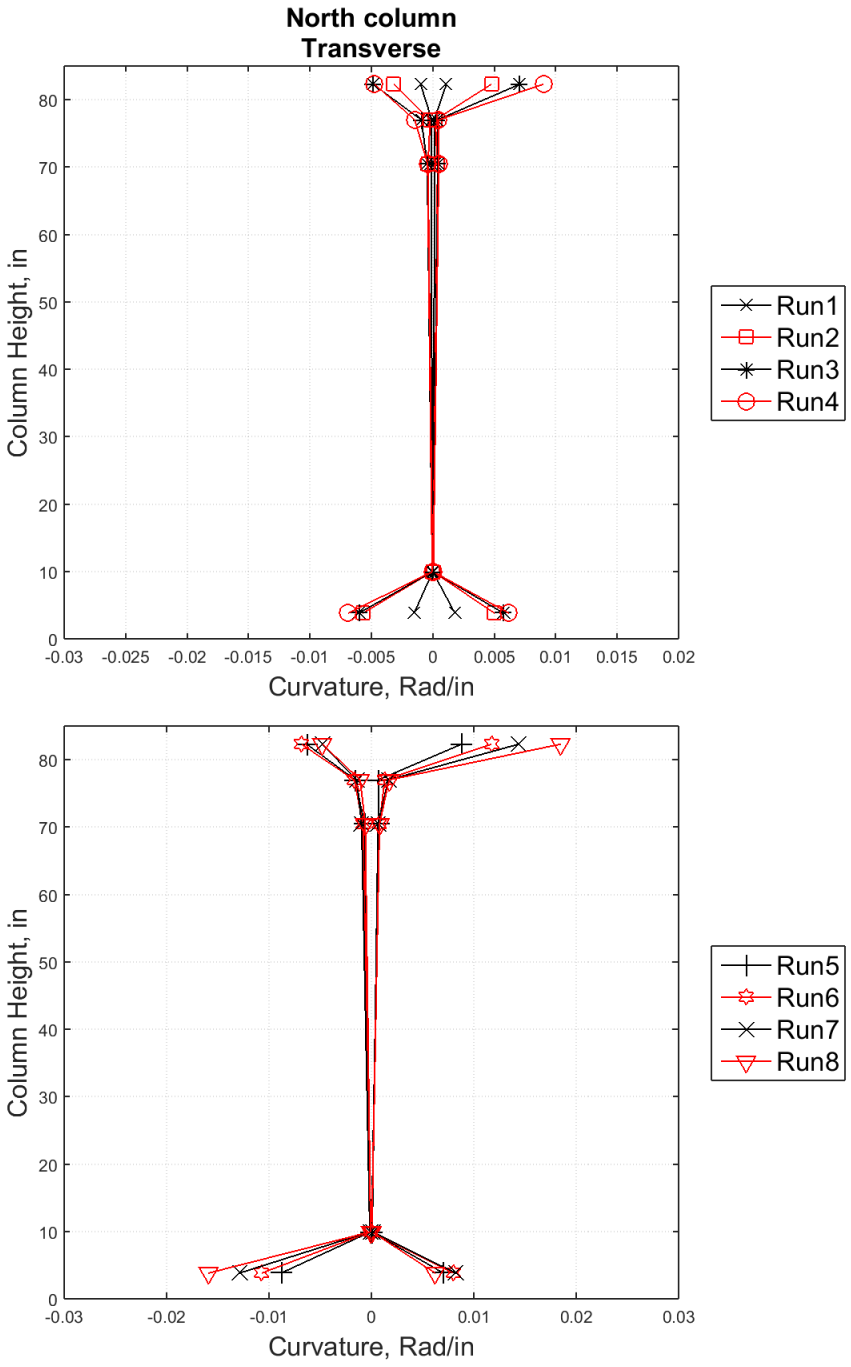

Figure B.92 Curvature profile along the north column in transvers direction

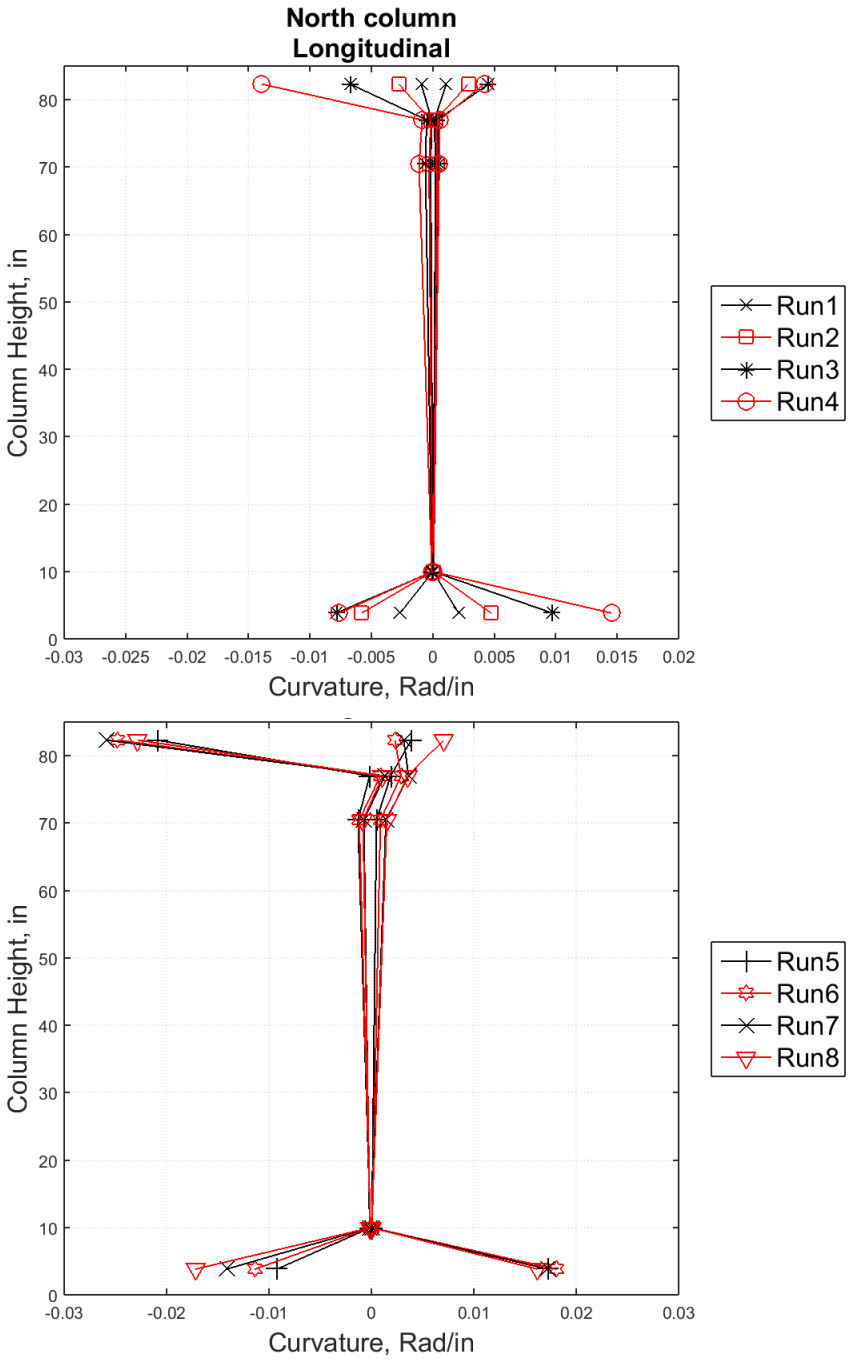

Figure B.93 Curvature profile along the north column in longitudinal direction